



SCUOLA DI DOTTORATO  
UNIVERSITÀ DEGLI STUDI DI MILANO-BICOCCA

Dipartimento di Scienze dell'Ambiente e della Terra - DISAT

Dottorato di Ricerca in Scienze Chimiche, Geologiche e Ambientali

Ciclo XXXV

Curriculum in Chemical Sciences

# Physico-Chemical Characterization of Emissions from Braking Operation

Mancini Alessandro

Matricola n° 862695

Tutor:	Prof. Claudio Greco
Academic Supervisor:	Prof. Ezio Bolzacchini
Company Supervisor:	Dr. Federico Bertasi
Coordinator:	Prof. Marco Giovanni Malusà

ANNO ACCADEMICO 2021/2022

## Preface

This thesis collects all the experimental work carried out in the three past years of research on the physico-chemical characterization of the non-exhaust emissions generated by brakes. These three years represented for me the extraordinary chance to leave for and live in a new terrific journey, once again. For this reason, in spite of (hopefully) maintaining the suitable and necessary scientific rigor, I have approached, lived, felt and developed this project as a travel exploration: in the end, exploration and research are synonymous. For every travel to begin, a mix of previous little knowledge, great curiosity towards a place and peculiar fortuity is always necessary. My personal mixture was brewed in the R&D Department of Brembo S.p.A., where I arrived in 2016, leaving the academy shortly after a PhD in Chemistry. Since my arrival in the company, I had the opportunity to work at the chemical characterization of emissions generated by braking devices, through the participation to EU-funded research projects such as LOWBRASYS and ECOPADS. In the previous years, the research related to the brakes emissions was mainly focused on the definition of reproducible protocols for reliable collection of particulates and the determination of the variables influencing the emission level of the braking devices. These projects started to shift the general interest towards a deeper characterization of the physico-chemical properties of the brakes emissions, with the final aim of finding clearer correlations with their toxicological behavior and environmental impact. These projects, together with several other internal development activities, represented my first contacts with the air quality topic and the corresponding research community. They both prepared the substrate and create the spark to ignite my curiosity. Therefore, the random event necessary to align all the pieces happened in 2019 in form of a regional program of research collaboration between companies and universities of Regione Lombardia, providing to companies the possibility to set industrial PhD projects for their employees. In my case, everything began as a mere joke with a younger colleague of mine, who was interested in the program, but doubtful. I still clearly remember the coffee break we were discussing about the possibility and his doubts: I was really convinced that it would have been a great opportunity for him, but the conversation eventually landed in the same deadlock as the previous ones. Thus, in that moment, I decided to raise the pot to make him call my bluff: "If you do it, I'll do it, too. We will pass through it together". Few days later, we started our respective registration procedures to the Environmental Science and Mechanical Engineering Doctorate schools. A couple of months later, my colleague eventually decided to pursue a new career path moving to a different institution: I was left alone just before the journey beginning. Even if it started as a pure joke, I decided to go on, even by myself alone. Indeed, that is because actually there was hiding in the background another reason pushing me to jump in this new adventure. It was more personal, painful and obscure. During my previous academic experience, the guy who happened to be my best friend during my youth decided to reach our common equilibrium state as human beings but following a wrong -too fast- kinetic, due to an incurable disease. He died by leukemia at the age of 27. Being him perfectly aware of my extremely poor capability to manage feelings (especially if bad) and not having time to improve his negative chess record against me, he decided to leave me with a final spectacular checkmate: "Don't you dare to stop living, since from now you have to live twice, also for me". I never had the courage to make it explicit, since somehow I have always been afraid to fail or to quit this new project, which

I slowly started to consider my best “twice” option to his memory. In the end, I can finally confess the little burden of his curse, which actually turned out into a real benediction. Because as every great exploration journey, together with the fear, the fatigue and the confrontation with the shadows from the past, they arrive also new skills, new perspectives, new travel mates and plenty of wonder for new landscapes and discoveries. For each of these things, which I found in abundance in the last three years, I am infinitely grateful. At the same time, I really hope to pay off the debt of such fortune with the studies and the results reported in this thesis, providing my personal little brick to the creation of a better home for all the living beings. This is the genesis and the spirit of this thesis work.

# Index

## 1. Introduction

1.1. Air Quality: Why Being Interested?	1
1.2. Air Pollutants: What is the (Particulate) Matter?	4
1.3. Sources of PMs: Road Transport and Brakes Wear	8
1.4. Tribological Interface: a Closer Look	10
1.5. From Brake Wear to Brake Emissions: Hints on Generation Mechanisms	16
1.6. Aim of the Thesis: Gap Analysis & Concept Map	19
1.7. Remarks: What cannot be Found in the Thesis	22
References	23

## 2. Experimental

2.1. Introduction	28
2.2. Brakes Emissions Generation and Collection	28
2.3. Sample Preparation	34
2.4. SEM/EDXS Analysis	35
2.5a. Particle Size Distribution – SEM Image Analysis	37
2.5b. Particle Size Distribution – Laser Diffraction Analysis	39
2.6. X-Ray Diffraction (XRD) Analysis	39
2.7. X-Ray Absorption Near-Edge Structure (XANES) Analysis	42
2.8. Raman Spectroscopy	43
References	44

## 3. Reproducibility Studies

3.1. Aim of the Study	46
3.2. Experimental	48
3.2.1. <i>Materials</i>	48
3.2.2. <i>Samples Collection and Experimental Design</i>	48

3.2.3. Analytical Protocol	50
<b>3.3. Intra Bench Assessment</b>	<b>50</b>
3.3.1. Investigation Design	50
3.3.2. Elemental Composition	51
3.3.3. Phase Composition	56
3.3.4. Particle Size Distribution	61
<b>3.4. Inter Benches Assessment</b>	<b>63</b>
3.4.1. Elemental Composition	64
3.4.2. Phase Composition	67
3.4.3. Particle Size Distribution	69
<b>3.5. Summary</b>	<b>72</b>
<b>References</b>	<b>74</b>
<b>4. Elemental Composition Maps</b>	
4.1. Aim of the Study	76
4.2. Materials	77
4.2.1 Braking Discs (BDs)	77
4.2.2. Friction Materials (FMs)	81
4.2.3. Friction Couples	82
4.3. Experimental	83
4.4. Results	84
4.4.1. Category 1: GCI BDs + LS/LM FMs ( <b>LS/LMs</b> )	84
4.4.2. Category 2: GCI BDs + IN FMs ( <b>INs</b> )	85
4.4.3. Category 3: GCI BDs + NAO FMs ( <b>NAOs</b> )	89
4.4.4. Category 4: CTD BDs + LS/LM FMs ( <b>CTDs</b> )	92
4.4.5. Category 5: CC BDs + LS/LM FMs ( <b>CCs</b> )	94
4.5. Summary	96
4.5.1. Main Elements	99

4.5.2. <i>Secondary and Minor Elements</i>	102
4.5.3. <i>Overall Summary for Introduction to Next Investigations</i>	107
4.6. <i>Elemental Composition Maps</i>	109
<b>References</b>	<b>113</b>
<b>5. Speciation in Brake Emissions</b>	
<b>5.1. Aim of the Study</b>	<b>115</b>
<b>5.2. Experimental Techniques</b>	<b>116</b>
<b>5.3. Crystalline Fraction</b>	<b>117</b>
5.3.1. <i>Category 1 (GCI BDs + LS/LM FMs)</i>	118
5.3.2. <i>Category 2 (GCI BDs + IN FMs)</i>	122
5.3.3. <i>Category 3 (GCI BDs + NAO FMs)</i>	126
5.3.4. <i>Category 4 (CTD BDs + LS/LM FMs)</i>	129
5.3.5. <i>Category 5 (CC BDs + LS/LM FMs)</i>	131
5.3.6. <i>Crystalline Fraction Summary</i>	132
<b>5.4. Oxidation States in d-Block Metals</b>	<b>134</b>
5.4.1. <i>Titanium K-edge</i>	135
5.4.2. <i>Vanadium K-Edge</i>	138
5.4.3. <i>Chromium K-Edge</i>	140
5.4.4. <i>Manganese K-Edge</i>	143
5.4.5. <i>Iron K-Edge</i>	146
5.4.6. <i>Copper K-Edge</i>	151
5.4.7. <i>Zinc K-Edge</i>	152
5.4.6. <i>Summary of Oxidation States in d-Block Metals</i>	154
<b>References</b>	<b>155</b>
<b>6. Size Distributions</b>	
<b>6.1. Aim of the Study</b>	<b>157</b>

<b>6.2. Experimental</b>	<b>158</b>
<b>6.3. Particle Size Distribution (PSD)</b>	<b>159</b>
6.3.1. <i>Category 1 (GCI BDs + LS/LM FMs)</i>	159
6.3.2. <i>Category 2 (GCI BDs + IN FMs)</i>	162
6.3.3. <i>Category 3 (GCI BDs + NAO FMs)</i>	164
6.3.4. <i>Category 4 (CTD BDs + LS/LM FMs)</i>	166
6.3.5. <i>Summary</i>	168
<b>6.4. Conclusions</b>	<b>171</b>
<b>References</b>	<b>172</b>
<b>7. Dimensional Profiles and Chemical Composition</b>	
<b>7.1. Aim of the Study</b>	<b>174</b>
<b>7.2. Ultra-fine vs. Micrometric Particulates</b>	<b>176</b>
7.2.1. <i>Experimental</i>	176
7.2.2. <i>Qualitative Assessment of the PSD</i>	179
7.2.3. <i>Elemental Composition</i>	179
7.2.4. <i>Phase Composition</i>	186
7.2.5. <i>Summary</i>	188
<b>7.3. Debris vs. Micrometric Particulates</b>	<b>189</b>
7.3.1. <i>Experimental</i>	189
7.3.2. <i>Particle Size Distributions (PSD)</i>	189
7.3.3. <i>Elemental Composition</i>	191
<b>7.4. Summary</b>	<b>196</b>
<b>References</b>	<b>197</b>
<b>8. Influence of the Driving Conditions</b>	
<b>8.1. Aim of the study</b>	<b>199</b>
<b>8.2. Experimental</b>	<b>201</b>

8.2.1. <i>Materials</i>	201
8.2.2. <i>Braking Cycles</i>	202
8.2.3. <i>Samples Collection and Preparation</i>	203
8.2.4. <i>SEM/EDXS Analysis</i>	203
8.2.5. <i>XRD Analysis</i>	204
<b>8.3. Results</b>	<b>205</b>
8.3.1. <i>Elemental Composition</i>	205
8.3.2. <i>Phase Composition</i>	209
<b>8.4. Discussion</b>	<b>211</b>
<b>8.5. Summary</b>	<b>213</b>
<b>References</b>	<b>215</b>
<b>Annexes</b>	
<b>Annex 1: List of Abbreviations</b>	<b>217</b>
<b>Annex 2: List of Crystallographic References</b>	<b>219</b>
<b>Annex 3: Data Sets for Reproducibility Studies</b>	<b>220</b>



# 1. Introduction

*Non-Exhaust Emissions (NEE) produced by disc-brake systems are introduced in this chapter as subject of this thesis. Their link to the general air quality topic is described reporting and summarizing results from most recent source apportionment studies and air quality guidelines. Therefore, a summary of the generation mechanisms of these emissions is provided, together with their possible interactions with the environment. With specific reference to the study of their chemical composition and the currently available information in the scientific literature, several fields of investigation are identified and stated as aim of this work.*

## 1.1. Air Quality: Why Being Interested?

Air quality and its influence on the human life have gained worldwide the increasing attention of the general public since the late '80s, when the World Health Organization (WHO) started to issue periodical guidelines, since the most recent version published in the 2021.<sup>[1]</sup> These air quality guidelines identify the most dangerous and diffuse pollutants, suggesting governments and civil society to reduce the human exposure to specific threshold values and estimating their adverse effects on human health, economy and society. Following this, an increasing number of international institutions and national governments adopted air pollutants monitoring programs as well as dedicated reduction policies.<sup>[2-3]</sup> Therefore, in the past decades, a growing body of scientific evidences has been collected to corroborate how air pollution has adverse effects on health and, more in general, on well-being. As a matter of fact, nowadays air pollution is globally perceived as a serious problem by citizens all around the world: good air quality is a necessary condition for healthy life. Indeed, air pollution in both indoor and outdoor environment is currently one of the major health risk for human beings, similarly to unwholesome diets and tobacco smoking.<sup>[4]</sup> It represents the single most dangerous environmental threat to human health: every year, the exposure to polluted ambient air is estimated to cause 4 to 9 million of deaths<sup>[4-6]</sup> and hundreds of millions of lost years of life through increased morbidity and mortality in a wide range of non-communicable diseases (NCDs) affecting mainly respiratory, cardiovascular and neurological systems.<sup>[7,8]</sup> In addition, air pollution represents also a significant economic problem, since it increases medical costs and generate loss of working days, therefore reducing the global welfare and productivity in the order of trillions and hundreds of billions, respectively.<sup>[9]</sup> Furthermore, it is also source of strong geographical and social inequality, since it affects disproportionately developing countries, people living in urban environment and the most vulnerable population groups, such as children, elderly and individuals with chronic illnesses.<sup>[1-3,7]</sup> Finally, air pollution has a profound impact on the environment. In first place, air pollutants are also detrimental and hazardous for the life

of all the other living beings. Moreover, they can stimulate climate change, which in turn can furthermore worsen the air quality on both local and regional scale.<sup>[2]</sup>

The problems related to air pollution are vast and complex. Thus, it is evident that a global, evidence-informed and long-term policy-making approach is necessary condition in order to implement suitable corrective actions to mitigate effects due to the current situation and to set the basis to improve air quality in the future. However, in spite of all the well testified critical issues linked to air pollution and the current availability of several air quality guidelines and standards on both international and local level, they are far to be adopted worldwide. For instance, several nations do not even have active monitoring programs.<sup>[1]</sup> Table 1.1 summarizes the distribution of countries having guidelines or standards for at least one air pollutant (60%), countries with no standards (27%) and countries where air quality information is completely lacking (12%).<sup>[10]</sup>

WHO Region	Countries with standards / %	Countries without standards / %	Countries with no information / %
Africa (47)	36	45	19
Americas (35)	57	37	6
South-East Asia (11)	64	27	9
Europe (53)	94	4	2
East Mediterranean (21)	52	5	43
Western Pacific (27)	44	48	7
<b>Total</b>	<b>60</b>	<b>27</b>	<b>12</b>

**Table 1.1:** Adoption of air quality guidelines and standards in different world regions.<sup>[10]</sup> The number of countries for each region is reported within brackets.

Looking at the geographical distribution of the nations showing the highest level of interest towards the air quality topic, it is evident that Europe is currently the region with the widely diffused and most structured approach to the air quality issue. This is mainly due to the policy-making action carried out by the European Union (EU), following the referencing of the WHO guidelines in the Ambient Air Quality Directive<sup>[1]</sup> in 2008. In addition, EU air quality policies are constantly updated and driven by a comprehensive report on air quality produced every year by the European Environmental Agency (EEA).<sup>[3]</sup> All the legislation activity and the countermeasures adopted in EU in the two past decades resulted in an overall continuous improvement of the air quality in the continent. Notably, the constant reduction of air pollutions in the recent past years came together a period of continuous good economic performances, therefore testifying the compatibility between environmental-driven policies and a growing and healthy economy. This can be observed by the clear decoupling of the Gross Domestic Products (GDP) and several air pollutants trends showed in Figure 1.1.<sup>[3]</sup>

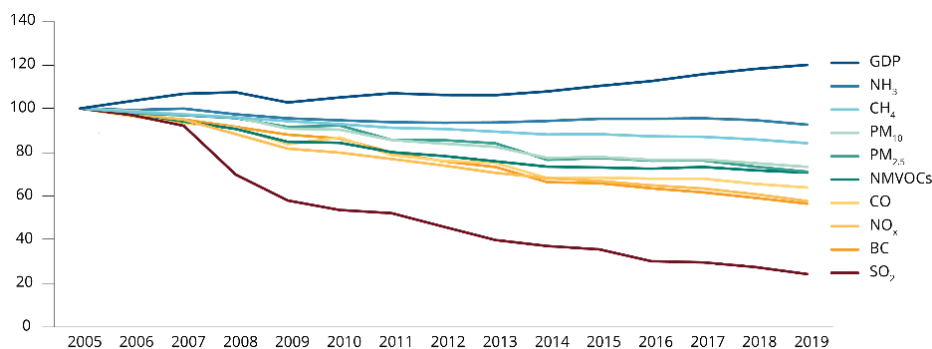


**Figure 1.1:** Global emission trend of several air pollutants in the 27 EU countries set against their global Gross Domestic Product (GDP). Reprinted from EEA – 2021 Air Quality Report.<sup>[3]</sup>

In spite of a gradual improvement of the air quality in most EU and other high-income countries in the American and West Pacific Region, pollutants concentrations still frequently exceed suggested threshold values in many of these areas, exposing a significant fraction of the population to hazardous levels of air pollution. For example in the EU, this is particularly evident: *i)* around the most densely populated areas, such as the bigger cities, mainly due to the heavy traffic conditions; *ii)* in the east of the Union, where the combustion of fossil fuels for domestic heating and energy production for industrial activity is more diffuse; and *iii)* in those areas where high density of population and productive activities combine with peculiar geographical and meteorological conditions, such in the northern Italy or the Catalan region in Spain.<sup>[3]</sup> Therefore, it is reported that in 2019 in EU, a significant percentage of the urban population still remained exposed to concentrations of air pollutants exceeding the EU standards. Notably, this percentage turns in the vast majority if considering the most recent threshold values suggested in the WHO guidelines, as shown in Figure 1.2.<sup>[3]</sup>

Conversely, developing and low-income countries are currently facing significant air quality deterioration, following the combination of large scale urbanization, economic development mainly based on the consumption of fossil fuels, poor dedicated legislation and limited interest in the policy-makers.<sup>[1]</sup> Therefore, it is possible to conclude that, in spite of the spark of hope represented by the most recent notable improvements of the air quality in some areas of the world, plenty of work still remain to be carried out to reduce air pollution and mitigate its effects on the human health on a global basis. Since the air motion is typically not particularly affected by national borders, spatially heterogeneous or even remote air problems tend to have ubiquitous impacts on the long-term perspective. Fortunately, most recent scientific evidences and technological development clearly demonstrated that successful interventions are feasible, effective and compatible with economic growth.<sup>[1-3]</sup>

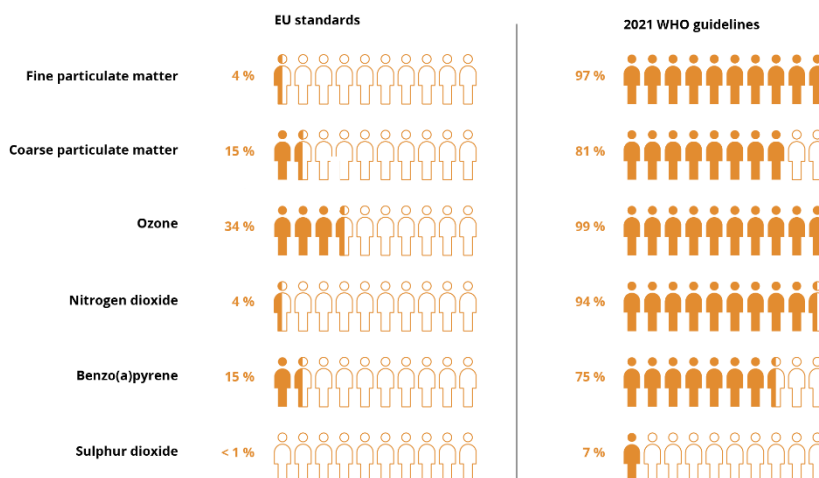


**Figure 1.2:** Share of the EU urban population exposed to air pollutant concentrations above EU standards (left side) and WHO guidelines (right side), in 2019. Reprinted from EEA – 2021 Air Quality Report.<sup>[3]</sup>

## 1.2. Air Pollutants: What is the (Particulate) Matter?

In general, pollutants can be defined as external substances introduced in an environment which have the functional capability of being hazardous or harmful towards that specific environment. They acquire relevance when being introduced at a rate exceeding the absorptive capacity of the affected system or in concentrations sufficient to manifest acute and/or long-term negative impacts. Referring to the air, there exist a wide and heterogeneous range of different pollutants having both natural and anthropogenic origin, with the latter ones being dominant since the beginning of industrialization. They can be single substances in all the physical states as well as be composed by more species mixed or interacting together. These pollutants can be emitted directly in air from their origin source (primary pollutants), but can be also formed in the air through a wide range of complex physico-chemical processes and interactions (secondary pollutants). Typically, they are categorized depending on their source origin. The major contribution to the air pollution is the combustion process, in particular of fossil fuels for energy generation and domestic heating. In addition, outdoor combustion sources include also the transport sector and, secondary, fires, agricultural burnings and volcanic activity. Other important contributions to the air pollution are the resuspension of surface dust, construction activity and mid-to-long range atmospheric transportation in natural events (such as sand storms). Finally, also biogenic emissions from agriculture and live-stocks contribute appreciably to the generation of air pollutants.<sup>[1,2,11]</sup> The WHO guidelines reports on six different major air pollutants, which are particulate matter, Ozone, Carbon monoxide, Sulfur oxides,

Nitrogen oxides and Lead.<sup>[1]</sup> On this basis, the US Environmental Protection Agency (EPA), as well as other national environmental agencies, nowadays monitors and reports mainly on these suggested air pollutants.<sup>[2]</sup> More extensively, the European Environment Agency annual Air Quality report takes also into consideration other species, such as Black Carbon (BC), Ammonia, volatile organic compounds, Methane, Benzo- $\alpha$ -Pyrene and additional heavy metals (Arsenic, Cadmium, Mercury and Nickel).<sup>[3]</sup> All this pollutants show detrimental effects on both the environment and the health of living beings, which are widely documented and supported by an extensive amount of scientific evidences.

Among all of these pollutants, particulate matters (PMs) are usually the most poorly affected by the countermeasures adopted to limit their presence in air, showing at the same time extremely severe effects on the human health.<sup>[1-3,12-19]</sup> Therefore they are commonly considered among the most hazardous air pollutants. PMs are particles with aerodynamic diameter lower than 10  $\mu\text{m}$ . In environment, they are typically mixtures of solid and liquid material formed in atmosphere as the result of physico-chemical processes occurring between different pollutants emitted by a whole variety of specific emission sources. Most often these particulates are categorized following their size dimensional distribution: *i*) PM<sub>10</sub> includes particle with diameter lower than 10  $\mu\text{m}$ ; *ii*) finer PM<sub>2.5</sub> includes particles with diameter lower than 2.5  $\mu\text{m}$ ; *iii*) ultra-fine particulates (UFP), including particles with nanometric dimensions ( $d \leq 100 \text{ nm}$ ). As far as their environmental impact and toxicological behavior is assessed, the finer fractions are progressively more dangerous and penetrate deeper into the biological systems, exhibiting at the same time a stronger chemical and bio-chemical reactivity due to their higher surface area. Figure 1.3 and Table 1.2 show respectively a size comparison between different PMs and their size-related capability to penetrate progressively the whole human respiratory system.<sup>[3,11]</sup> Numerous epidemiological studies have been performed on the health effects of PMs, demonstrating positive correlations between both short and long –term exposure to these pollutants and several pathologies affecting respiratory<sup>[15,20-25]</sup>, cardiovascular<sup>[26,27]</sup>, neurological<sup>[28,29]</sup> systems, as well as other apparatuses such as the skin<sup>[30]</sup> and the eyes<sup>[31,32]</sup>. In general, their toxic effects are strongly dependent on their physico-chemical properties: the chemical composition is typically the defining factors, while size distributions and morphologies of the constituting particles strongly modulate the behaviors. In addition, PMs tends to be significantly persistent in air: due to their small dimensions and weight, they can remain in suspension in the atmosphere for long time, therefore increasing their chance to be transferred and spread also to locations distant from their origin.<sup>[33]</sup> This phenomenon is typically related to long-scale transport effects in natural event, such as example dust storms, fires and volcanic activity, but can easily apply to industrial and other anthropogenic particulate emissions.

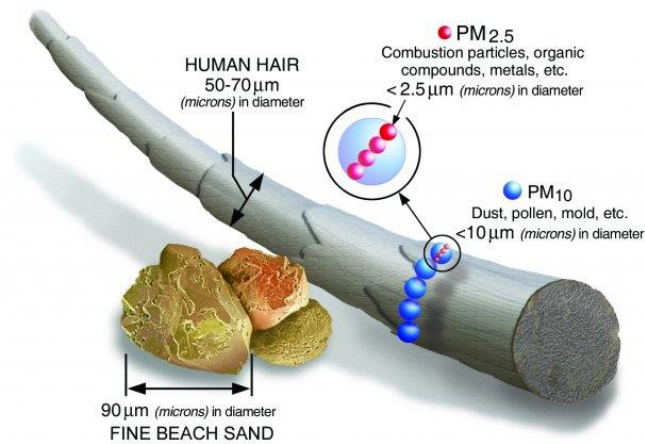


**Figure 1.3:** Dimensional comparison of PM<sub>10</sub> and PM<sub>2.5</sub>. Reprinted from US Environmental Protection Agency - Internet database and report.<sup>[2]</sup>

Particle Size / $\mu\text{m}$	Penetration in human respiratory system
> 11	Nostrils and upper respiratory system
7 - 11	Nasal cavity
4.7 - 7	Larynx
3.3 - 4.7	Trachea-bronchial area
2.1 - 3.3	Secondary bronchial area
1.1 - 2.1	Terminal bronchial area
0.65 - 1.1	Bronchioles
0.43 - 0.65	Alveoles

**Table 1.2:** PMs penetrability in the human respiratory system in function of the dimensional distribution of the particulates.

The excessive exposure to particulate matters is a problem affecting a wide share of the global population: in 2019, more than 90% of the global population lived in areas with PM<sub>2.5</sub> already exceeding previous 2005 WHO guidelines of 10  $\mu\text{g}/\text{m}^3$ . Highest concentrations were recorded in the South-East Asia, Mediterranean and Africa regions, while general decreasing trends are observed in Europe, America and West Pacific. Looking more in detail at the European situation, in 2019 the 97% and 81% of the urban population in EU was exposed respectively to PM<sub>10</sub> and PM<sub>2.5</sub> concentrations exceeding the WHO guideline values.<sup>[3]</sup> Similar exposure levels (96% and 71%) were recorded in 2020, in spite of the strong limitations related to the surge of the Covid-19 pandemic.<sup>[3]</sup> Congruently, in the same year, the 61% and 68% of the PMs reporting monitoring stations registered PM<sub>10</sub> concentrations exceeding respectively the daily and the annual WHO guideline values (16% and 5% if the EU limits are considered). The situation is even

worse when looking at the PM<sub>2.5</sub>, with almost all the reporting monitoring stations exceeding both the daily and the annual WHO guideline values, as showed in Figure 1.4.

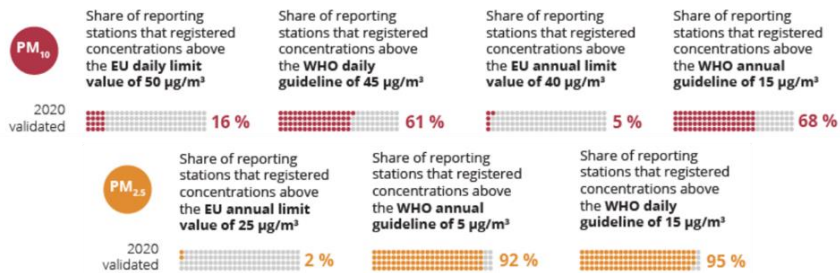


**Figure 1.4:** Percentage of reporting monitoring stations registering PM<sub>10</sub> and PM<sub>2.5</sub> concentrations above EU limits and WHO guidelines in 2020. Reprinted from EU Air Quality Status online report.<sup>[3]</sup>

Notably, all the 36 countries participating in the EEA monitoring activity registered PM<sub>10</sub> concentrations above the daily WHO guideline targets, while only the Iceland was able to limit the annual suggested limit.<sup>[3]</sup> The strongest exceedances are typically recorded in Italy, mainly localized along the Po valley, in eastern countries and in other densely populated and industrialized areas, such as close to many national capitals (Figure 1.5). Similar trends are observed when considering PM<sub>2.5</sub>: all the 33 EEA reporting countries registered annual and daily concentrations exceeding the most recent WHO guidelines values, with the only exception of Estonia.<sup>[3]</sup>

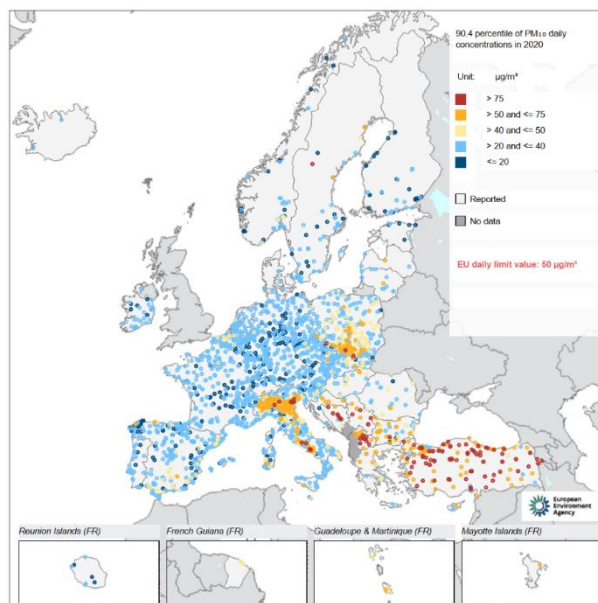


**Figure 1.5:** Concentrations of PM<sub>2.5</sub> in relation to the EU annual limit value and the WHO annual guideline, 2020 validated data. Reprinted from EU Air Quality Status online report.<sup>[3]</sup>

For all these reasons, the legislation activity focused on the improvement of the air quality is moving towards new and more ambitious objectives. For instance, under the European Green Deal's Zero Pollution Action Plan, the European Commission set the goal of reducing the number of premature deaths caused by fine particulate matter, by at least 55% compared with 2005 levels, within the 2030. To this end, the European Commission started the revision of the ambient air quality directives, aiming to align the air quality standards more closely with WHO recommendations. In parallel, stricter requirements are also foreseen to tackle air pollution at source, such as pollution from agriculture, industry, transport<sup>§</sup> and buildings<sup>#</sup> and energy supply sectors (§, # = see *Notes* on the following legislation paragraph at *Pag. 24*).

### 1.3. Sources of PMs: Road Transport and Brakes Wear

As already introduced, air pollutants and PMs can have several different origins, both from natural and anthropogenic sources. The former ones can be considered as a sort of natural background with a stochastic pattern of mostly unpredictable peak events, for which little limitations or countermeasures can be adopted on standard basis. Conversely, the latter ones are consequence of the human activity, and therefore they can be more easily controlled and tackled, if there exists the will to do so. First of all, it is of pivotal importance to map all the possible anthropogenic source and to understand their relative contribution to the total, in order to select the most widely affecting, effective and convenient policies and countermeasures. At this aim, a huge body of knowledge based on source apportionment studies was produced in the last decades.<sup>[1-3]</sup> For example, Figure 1.6 shows the most updated picture of contribution of several human activity sector to the global generation of air pollutants in Europe.<sup>[3]</sup>

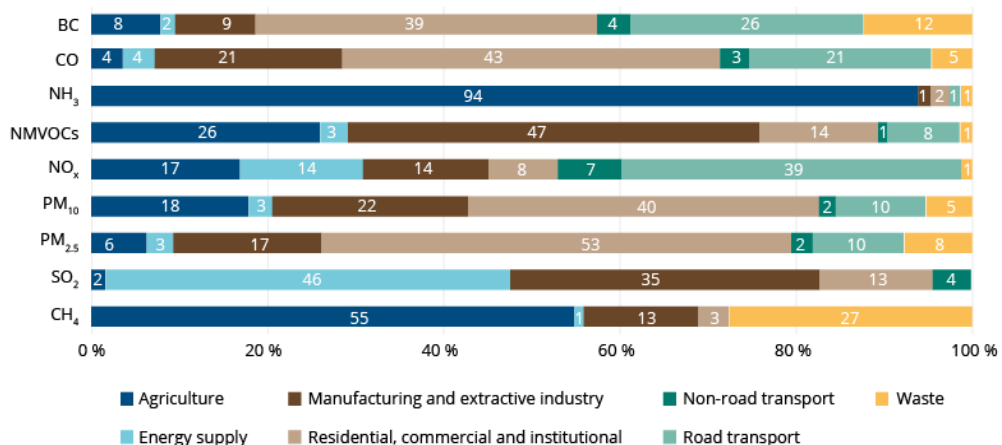


**Figure 1.6:** Contribution to anthropogenic emissions of several air pollutants from the main source sectors in 2019 in the EU-27 countries. Reprinted from EU Air Quality Status online report.<sup>[3]</sup>



As can be observed from the reported graph, the road transport sector is recognized as significant source for the emission of several pollutants, such as Black Carbon (BC), Carbon monoxide (CO), Non-Methane Volatile Organic Compounds (NMVOCs), Nitrogen oxides (NO<sub>x</sub>) and particulates matters (both PM<sub>10</sub> and PM<sub>2.5</sub>). With particular reference to the latter ones, the transport sector is estimated to produce the 10% of both the PM<sub>10</sub> and the PM<sub>2.5</sub> generated by anthropogenic sources on global basis in EU.<sup>[3]</sup> However, these figures can easily increase up to six times when the urban environment is specifically considered.<sup>[34]</sup> The road transport emissions are commonly divided into the two following categories: *i)* Exhaust, referring to mixtures of gases and particulates generated by combustion engines; and *ii)* Non-Exhaust, accounting for particulates generated by the wear occurring at brakes, clutches and tires-to-road interfaces, together with material (road dust) resuspended in air by the motion of circulating vehicles. The former ones have been historically dominant since the introduction of specific legislations dedicated to their reduction in the first '90s, such as the European Emission Standards.<sup>[35,36]</sup> Notably, within this framework, particulates matters (PMs) have been inserted officially as controlled pollutants starting from the 2011: since that moment, continuous and steady reduction of PM emissions from exhaust sources have been reported.<sup>[3]</sup> Therefore, following the continuous improvement in the exhaust emissions treatment, the non-exhaust counterpart has progressively gained relative weight and it is currently estimated to contribute equally to the exhaust fraction. Furthermore, it is expected to become dominant in the next years, due to the increasing electrification of road mobility.<sup>[37,38]</sup>

With particular reference to the non-exhaust emissions, brake wear is currently assessed as one significant source of particulate generated from traffic, being estimated to contribute respectively by the 55% and 21% to the total PM<sub>10</sub> and PM<sub>2.5</sub>.<sup>[37,39,40]</sup> Braking is in fact the operation of slowing down or stopping the motion of a vehicle by conversion of kinetic energy into heat. This process is commonly pursued by the friction generated by two rubbing surfaces. In the case of the automotive sector, this operation is commonly performed by disc brake systems (Figure 1.7): the driver pushes the brake pedal or pinches the brake lever, delivering pressure to the calipers via hydraulic or electro-mechanical actuation. Then the calipers transmit the pressure to a couple of braking pads, which are finally pushed against a rotor joint to the wheel. Thus, a braking torque is generated, which is responsible of slowing down or stopping the vehicle motion. The conversion of kinetic energy via heat dissipation is intrinsically accompanied by undesired side effects, such as the generation of sound vibrations (noise) and the loss of mass (wear) occurring at the tribological interface, *i.e.* the contact surface between the braking disc (BD) and the friction material (FM) from the braking pads.<sup>[39,40]</sup> Since the tribological interface represents the place where the brake emissions are actually

generated, the interplay between its features and the physico-chemical properties of the corresponding generated emissions will be widely discussed along this thesis work.

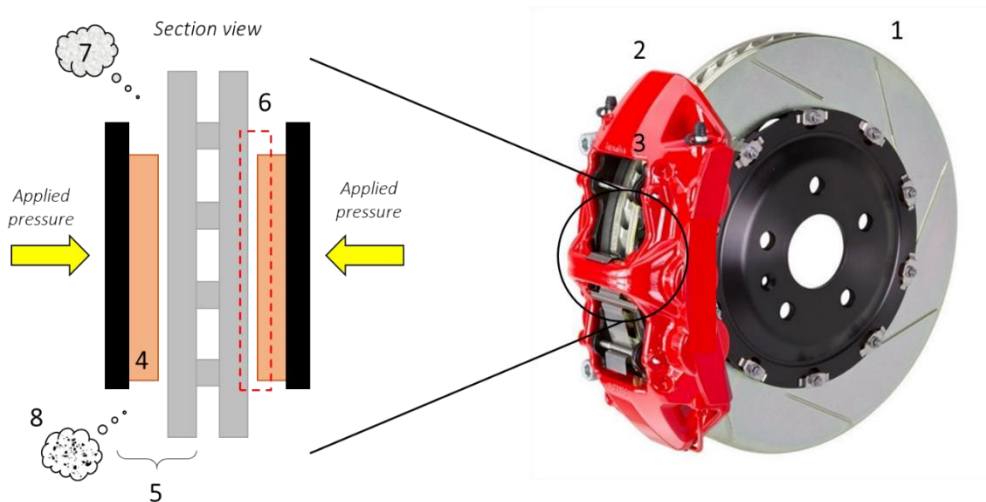


**Figure 1.6:** Schematic representation of a brake disc system and the tribological interaction between braking discs and pads producing brake emissions. **1-** Braking Disc (BD); **2-** Caliper; **3-** Braking Pads; **4-** Friction Material (FM); **5-** Friction Couple (FC = BD+FM); **6-** Tribological Interface (TI); **7-** Particulate Matter (PM); **8-** Wear Debris.

#### 1.4. Tribological Interface: a Closer Look

In the disc-brake system, the objects composing the friction couple are typically made by complex materials. On one side of the friction couple there is the rotor, which is typically composed by pearlitic grey cast iron (GCI), *i.e.* a Fe-based alloy containing floccular graphitic structures called lamellae. Its microstructure is typically finely tuned through the addition of secondary alloying elements to obtain the desired mechanical properties. Figure 1.7 shows the microstructure of one typical GCI used for the production of most of the BDs used in this research work, while Table 1.3 summarizes its nominal chemical composition.

Element	C	Si	Mn	Cu	Cr	Fe	Others
wt%	3.8	1.8	0.5	0.2	0.1	<i>balance</i>	<i>traces</i>

**Table 1.3:** Elemental composition of a GCI typically used for braking discs production. *Traces* indicates concentrations below 0.1 wt%, while *balance* represents the remaining amount of material to close the mass balance.

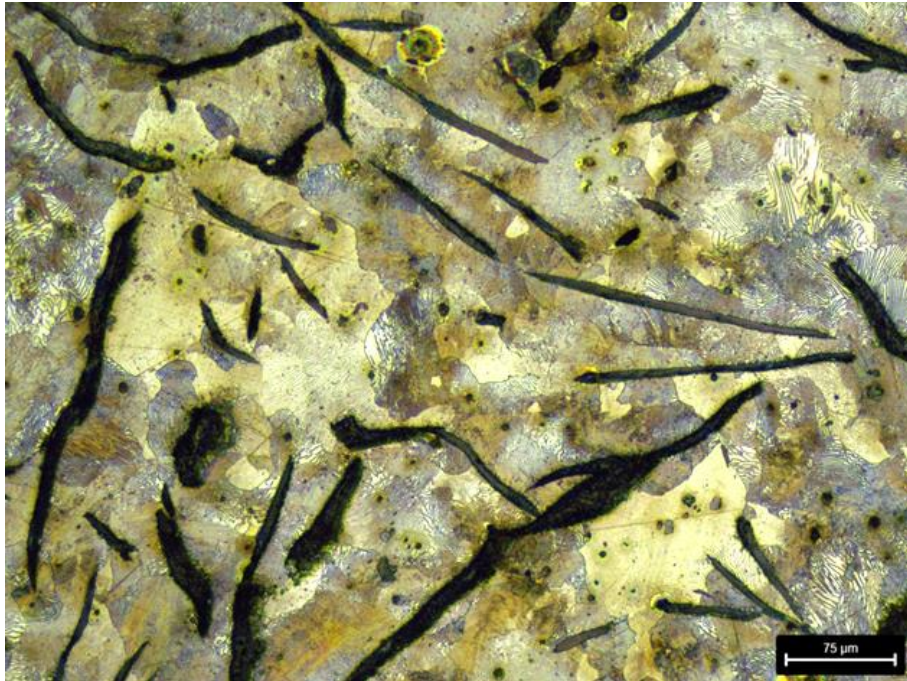


**Figure 1.7:** Microstructure of pearlitic GCI after Nital etching under the metallographic microscope. It is possible to appreciate different phases composing the alloy (ferrite, cementite, lamellar graphite and precipitates such as inter-metallics and sulfides).

As can be observed in Table 1.3, the elemental composition of GCI for BDs production is usually characterized by relatively high concentrations of Carbon and Silicon, while all the other elements are found in minor or trace amounts, typically lower than 0.5 wt%. These elements are in general ubiquitous impurities of Iron (such as Mn, Cr and Cu) or can be voluntarily added in the production phase as alloying elements in order to modify the microstructure, thus increasing GCI physico-mechanical properties such as hardness, wear resistance and corrosion resistance (Al, Ti, V, Nb, Mo).<sup>[41-45]</sup> However, on the market can be found rotors based on other metallic alloys, such Steel (mainly for motorbike and light vehicles) and Al or Ti -based alloys.

In addition, also Carbon-ceramic composites can be used to produce braking discs, typically exhibiting superior mechanical properties in respect with the GCI counterparts. They are typically made by infiltrating carbon fiber preforms with metallic Silicon at very high temperatures. Therefore they are composites featuring the coexistence of the three following main phases: *i*) Silicon carbides (matrix); *ii*) elemental Carbon in form of Carbon fibers; and *iii*) unreacted Silicon from the infiltration process, constituting a minor component of the matrix. Figure 1.8 shows a SEM image of the braking surface of a carbon ceramic BD.

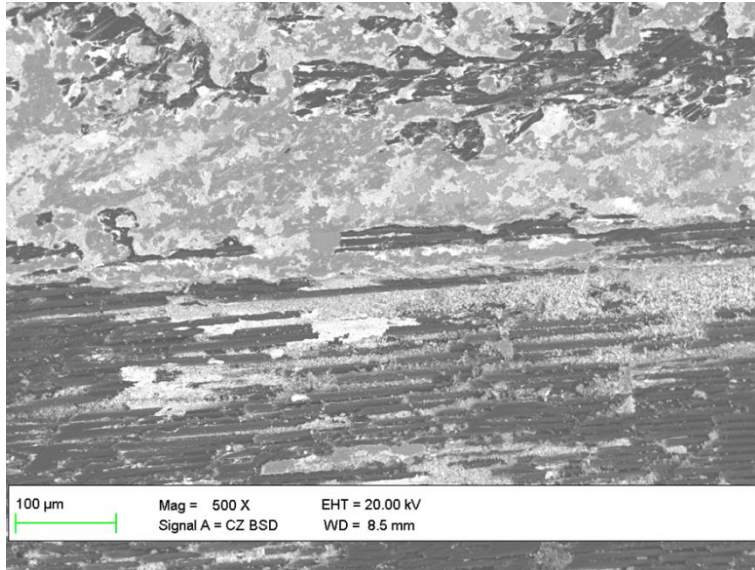


**Figure 1.8:** SEM image of the braking surface of a carbon-ceramic disc. Back-scattered electrons (BSE) are used in order to highlight phase contrast between the Carbon fibers and the SiC/Si matrix.

Silicon carbides, the main matrix component, assures great hardness for the composite material, while carbon fibers guarantee high mechanical strength resistance and providing fracture toughness required for braking rotors. Thus, these discs are characterized by having overall superior mechanical and thermal properties (hardness, wear resistance, thermal shock resistance) and significantly lower weight in respect with the GCI counterpart. However, all these excellent functional properties are obtained through expensive production and surface refinement processes. Therefore, they find natural application in high-performance braking systems, such as for racing and high-end vehicles.

Finally, new BD products, namely “coated” braking discs, are currently under development aiming to obtain improved wear and corrosion resistance. Notably, since the overall wear of the brake device is strictly related to its emission level, coated discs are nowadays considered as one of the most promising hardware solution to reduce particulates generated by brakes.<sup>[46-48]</sup> More in detail, they are GCI BDs whose braking surfaces are covered or clad with coatings being composed by a wide range of different materials with the specific aim of improving their functional properties. They are a relatively young technology, which in most cases rarely dates back more than 10-15 years and are currently positioned between the prototypal and the small pre-series production stage. However, coated discs are expected to diffuse very quickly into the market in the next years, mainly due to possible future legislations targeting NEE in the road transport sector. Since they are more expensive in respect with the uncoated

counterparts, they will likely diffuse first in the medium to high BD market segments. The coatings for BDs can be single layer as well as ensemble of more layers with the most external one representing BD side of the tribological interface. Their thickness is calibrated in order to endure the working life of the BDs, and depending on the material composing the coating, can vary between few tenth to few hundreds of microns. They can be deposited with a wide range of different techniques, such as cold-spraying, high-velocity air/oxygen fuel (HVOF or HVAF) depositions, laser cladding (LC) or laser melting deposition (LMD). An example of BD coating can be observed in Figure 1.9.

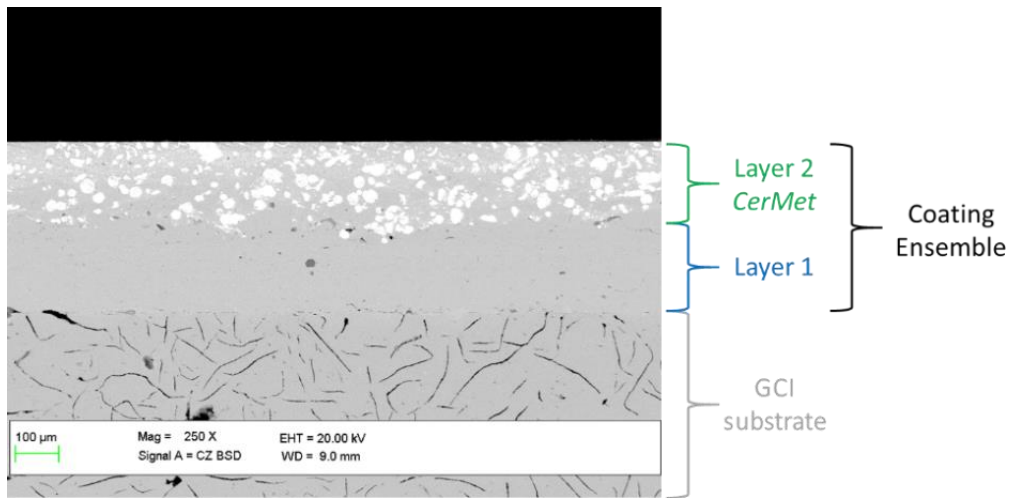


**Figure 1.9:** SEM section image of a coated BD. Detail of the coating ensemble, composed by two different layers deposited on the GCI braking surface.

The materials deposited on the braking surface must exhibit superior physico-mechanical properties in respect to the GCI. In particular, higher hardness, wear resistance and corrosion resistance are specific targets for BD coatings. At the same time, they are required to closely match the thermal properties of the substrate to avoid thermal shock or thermal stress –induced cracking of the braking surface, eventually leading to delamination of the structure and potential safety failure of the braking system. For the same reason, they must assure optimal adhesion with the substrate, with the linking interface being able to sustain significant compressive and shear forces. Therefore, materials typically suitable to be applied as BDs coatings are *CerMet* composites, *i.e.* dispersions of ceramic powders (carbides, oxides, nitrides and borides) in a metallic or intermetallic matrix, with relative ratio between *Cer* and *Met* fractions suitably tuned to match all the desired functional properties. In particular, the *Cer* components typically provide high hardness and wear resistance to the braking surface, while the *Met* fraction assure the overall integrity of the ensemble and the adhesion to the GCI substrate.

On the other side of the tribological interface lays the friction material (FM), *i.e.* a composite material being usually made by a complex mixture of up to thirty/forty different compounds of both organic and inorganic nature. Figure 1.10 shows a section image of a friction composite, in which is possible to appreciate the presence of several different phases.

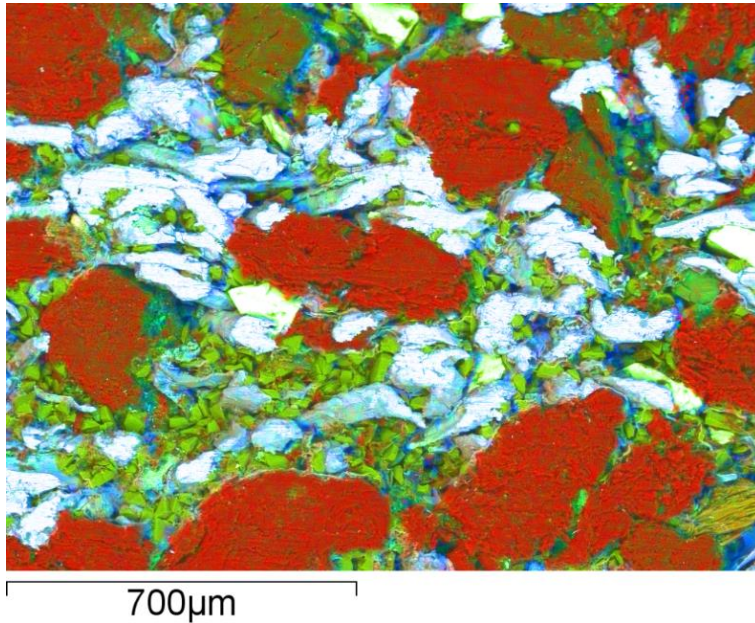


**Figure 1.10:** SEM section image of a friction composite (false color reconstruction, based on differences in electron density). It is possible to appreciate several different granulometries and morphologies, thus testifying the presence of a variegated ensemble of different compounds.

Their formulation is typically finely tuned in order to match specific requirements in terms of safety, comfort, performances, environmental concerns and target costs. Therefore, they should exhibit: *i)* good mechanical properties; *ii)* good thermal resistance; *iii)* adequate, stable and reproducible friction coefficient over a wide range of different braking conditions (temperature, pressure, speed, environment, etc.); and *iv)* high wear resistance and good coupling against the rubbing BD counterpart. In addition, since it was recognized in the recent past as fundamental in determining the emission profile of the friction couple, it is nowadays more and more frequently formulated with great attention to the replacement of potentially hazardous ingredients (such as Cu, Sn, antimony trisulfide, and whisker materials).<sup>[50-53]</sup>

According to the terminology conventionally accepted in the automotive industry, which indeed is particularly ancient and obscure, brake materials typically used in the same industry are categorized as NAO (non-asbestos organic), low metallic (LM) or low steel

(LS), semi-metallic (SM). These friction materials can be considered organic-inorganic composites, since their matrix is formed by one or more organic polymers. In addition, a new class of emerging prototypal friction materials started to appear, which is based on inorganic binders such as cements and geopolymers. For this reason they can be referred as inorganic bound (IN) friction materials. They are being developed at the aim of completely eliminating the gaseous emissions related to the thermal decomposition of the organic binders contained in all the other FMs families. Since the SM formulations have progressively lost large share in the automotive market, remaining essentially related only to the motorbike (or train) counterpart, they are not considered in the investigations reported in this thesis work. Therefore, three different typologies of FMs are used in the following investigations: *i*) Non Asbestos Organic (NAO); *ii*) Low Steel or Low Metallic (LS/LM) FMs; and *iii*) Inorganic bound (IN) FMs.

The compounds constituting the friction material can be classified on the basis of their functional properties and several different classifications exist in literature accordingly to various authors, while the relative ratio or the use of specific components usually define the membership to a particular family (with a high degree of subjective discretion). Following the classification reported in reference [49], all the compounds typically constituting the friction material can be divided in the following four classes:

- 1- **Reinforcements:** compounds giving mechanical strength to the composite. They are typically metallic fibers and powders (Fe, Steel, Cu, Cu-alloys, Sn, etc.), ceramic and mineral fibers and polymer fibers or pulp (aramid or acrylic fibers).
- 2- **Friction Modifiers:** compounds determining and modulating the friction coefficient. They are divided in abrasives (typically inorganic oxides and carbides) and solid lubricants (Graphites, cokes and inorganic sulfides).
- 3- **Binders:** compounds linking and holding together all the composite compounds. They are typically phenolic resins, but inorganic binders such as cements and geopolymers are being currently under extensive development.
- 4- **Fillers:** thermally/mechanically stable and inexpensive compounds, increasing volume of the composite while exhibiting minimum impact on the performances. They are typically materials from geological origin and insoluble inorganic carbonates, hydroxides and sulfates.

Typical general compositions for materials of the three different typologies of composites selected for the following investigations are reported in Table 1.4, together with other parameters of interest. As can be observed in the table, NAO friction materials exhibit overall higher content of binder and lower content of friction modifiers (strong abrasives and lubricants) in respect with the LS/LM formulations. In particular, metals are frequently absent and, where present, they are always non-ferrous. Conversely, NAO friction materials usually contain significantly higher amount of

compounds which can be classified as fillers or mild abrasives. All these compositional features are well coherent with overall slightly lower friction coefficient values (0.33-0.35) and gentler tribological behavior showed by these formulations when coupled against standard GCI BDs. They are relatively soft materials, particularly sensitive to elevated temperatures and exhibiting overall low friction performances. Conversely, they tend to generate low level of abrasion (and consequently lower emissions) and noise. LS/LM and IN formulations are in general characterized by slightly higher binder content and significantly higher metals and friction modifiers concentrations. The higher presence of metals and strong abrasives determines a more aggressive tribological behavior towards the standard GCI braking discs and, consequently, higher friction performances and durability in respect with the NAO counterparts. More lubricants are usually needed in these formulations in order to stabilize and module their friction coefficient ( $\mu = 0.35-0.38$ ).<sup>[49,54]</sup> Finally, IN formulations share overall similar characteristics with the LS/LM family, with a couple of main differences. In particular, these composites are currently being developed in order to minimize the emissions of organic compounds, thus they are not bound with soft organic resins. Instead, inorganic binders such as glasses, cements and geopolymers, are most frequently used. Notably, these binders show in general also significant abrasive capability at the same time. For this reason, they usually contain low amounts of strong abrasives and fillers, while maintaining significant concentrations of lubricants.

wt%	NAO	LS/LM	IN
<b>Binder</b>	10-25	5-15	10-20
<b>Metals</b>	0-10	15-30	20-30
<b>Abrasives</b>	20-30	25-40	5-15
<b>Lubricants</b>	5-15	20-35	15-25
<b>Fillers</b>	20-40	5-15	0-10
<b>Hardness (HRR)</b>	80-100	100-150	>150
<b>Friction Coefficient (<math>\mu</math>)</b>	0.33-0.35	0.35-0.38	0.38-0.42
<b>Normalized Emission</b>	0.2-0.3	1	0.8-0.9

**Table 1.4:** Compositional detail and mechanical properties of different typology of friction materials. Hardness is reported in HRR. Friction coefficient ( $\mu$ ) is reported considering the coupling with standard GCI braking discs.

### 1.5. From Brake Wear to Brake Emissions: Hints on Generation Mechanisms

Every typology of braking friction process leads to the wear of both the rubbing surfaces from the BD and FM side of the tribological interface. As already introduced, this wear is responsible of the release of particles (and eventually liquid and gases) into the surrounding environment. However, this process is not completely instantaneous, at least not for all the released material. If part of the asperities located at the tribological interface of the brake system can be quickly detached by direct mechanical



abrasion and immediately released in environment, a consistent part of the tribological event is characterized by the redeposition of the wear debris material onto the rubbing friction surfaces. This material adhering to the braking surfaces forms a very thin and inhomogeneous layer, partially covering and shielding its substrates. This behavior further modulates the friction process, since it favors the sliding of the rubbing surfaces. In the case of brakes, this layer is usually referred as *friction layer*, but it is also commonly named as *transfer layer* or *third-body layer*.<sup>[49]</sup> In spite of being widely recognized as the most important feature in determining the efficiency, the performances and also the comfort of the braking event, the mechanisms underlying its formation are still not fully understood and characterized. This is mainly due to the very complex nature of the tribological interface, as briefly introduced in the previous paragraph.<sup>[49,55-57]</sup> Nevertheless, the friction layer can be considered at all extent as newly formed matter, composed by an extremely complex mixture of material detached from the friction surfaces by direct mechanical abrasion, whose composition and granulometry start to vary depending on the intensity (*i.e.* temperature, velocity and pressure) of the following braking events. If more stable constituents of the friction composite, such inorganic oxides and fillers from geological origin, can hardly modify even at the higher temperatures possibly experienced by the braking device (around 700-800°), there exist also a wide range of components which can easily undergo thermal degradation (organic binders, Graphites, sulfides), oxidize (metals from both BD and FM) and possibly react together.<sup>[49,56]</sup> Therefore the friction layer can be imagined as an ensemble of localized reaction pools, from which part of the material detached by mechanical abrasion is continuously grinded, mixed and undergoes tribo-oxidative modifications before being released in the environment on stochastic base. Thus, brakes emissions are composed by an ensemble of materials which is generated by the interplay of different mechanisms, ranging from direct mechanical wear to a combination of adhesive and tribo-oxidative action.<sup>[56]</sup> The correspondingly induced modifications have extremely important implications not only in the modulation of the brakes performances, but also considering the amount of the wear material generated, its dimensional and compositional profiles and its environmental and toxicological behavior.<sup>[49,56]</sup> However, the stochastic nature of the braking process, the high-energy conditions, and the complex mechano-chemical and tribo-chemical interactions occurring at the friction surface during braking events, make substantially impossible to predict the level of particle emission, even if it is generally recognized to increase with the increasing temperature.<sup>[49,56]</sup> It is similarly impossible also to predict the particle size of newly formed species. However, it is generally observed that their size distributions strongly shift towards smaller dimensions in function of the increasing temperature, while direct abrasion usually leads to particles of bigger dimensions.<sup>[49,56]</sup> Finally, also the predictive assessment of their chemical composition is extremely complicated.<sup>[49,56]</sup> Thus, even if the tribological interface is designed in conformation with environmental and toxicological considerations or

standards, it might be possible to obtain emissions exhibiting undesired chemical characteristics.

## 1.5. Brakes Emissions: State of the Art

Taking together all the considerations previously reported, it is possible to summarize the following points related to the non-exhaust brakes emissions. The material worn by braking device has wide dimensional and shape distribution and variegated chemical composition. This is due to the fact that the released materials is produced by the interplay of at least two different wear mechanisms, involving both the mechanical abrasion and the tribo-oxidation of the material deposited at the tribological interface as transfer layer. Both the dimensional and the compositional features are strongly dependent of a wide range of different factors, including: *i)* the intensity of the brake event (sliding speed and contact pressure); *ii)* the materials composing the friction couple (*i.e.* the physico-chemical characteristics of the braking discs and pads); *iii)* the wear mechanism (abrasion, adhesion, fatigue wear and tribo-oxidation), and *iv)* the driving and the environmental conditions (temperature, humidity, etc.).<sup>[39,40,49,56-61]</sup> Braking wear constituents can indeed range from objects with characteristic dimensions of millimeters to ultra-fine nanometric particles. Depending on their dimensions, braking wear products follow different emission paths: the objects with bigger dimensions usually fall directly to the ground while conversely the finer fractions are more suitable to be directly emitted in air. As far as particulate matter is concerned, particles from the finer fractions (*i.e.* with aerodynamic diameter  $\leq 10 \mu\text{m}$ ) are the ones of specific interest for their contribution to the total non-exhaust PM emissions.<sup>[39,40,49]</sup> In addition, when environmental interactions with ground or water systems are concerned, the coarser fractions (Wear Debris) acquire more interest. For all of these reasons, in the past decade, consistent scientific and technological efforts have been performed in order to correlate braking operations to the corresponding particulate emissions. More in detail, significant work has been specifically carried out in developing robust particles collection protocols, validating reliable analytical methods for determination of particulate number (PN) and mass (PM) in controlled conditions, correlating various braking conditions to different emissive profiles and estimating their emission factors (EFs) in real-world conditions to apportion their contribution to the NEE produced by extended vehicles fleets.<sup>[39,40,49,61-68]</sup> Recently, several observational studies focused in deeper detail on the chemical composition of the brake emissions have also appeared in the literature, aiming at providing deeper insight into the correlation with their environmental and toxicological behavior.<sup>[60,61,69-73]</sup>

When characterizing in detail the brake emissions, both the particle count for the emission factor determination and the collection of material for chemical characterizations have to be necessary performed in controlled environment to avoid

spurious contribution from sources other than the tested braking system itself. Nowadays, one of the most convenient option to obtain samples made exclusively by brake emissions is to collect them at a dedicated dynamometric bench (DB), while performing a standard sequence of braking events, *i.e.* a standard braking test cycle.<sup>[74-76]</sup> Inertia DBs are mechanical test platforms built to simulate one braking corner module for a specific vehicle application, commonly used to study selected properties of the braking devices, such as wear, friction performances or vibration behavior over selected braking sequences. They avoid the use of a whole vehicle, limiting the investigated system at a single braking device kept in laboratory environment. In addition, the braking sequences can be highly automated and standardized in respect with road testing on real vehicles. Parameters such as vehicle inertia and energy indexes of a real vehicle can be maintained, which is not usually the case for other typical tribological test platforms such as the Pin-on-Disc (PoD) benches.<sup>[77-80]</sup> Finally, a further advantage specifically related to the particulate collection, is the possibility to easily enclose the whole testing system in a suitable chamber, in order to create a highly controlled environment in terms of air fluxes, temperatures and contaminations. For all these reasons, such typology of test platforms are nowadays commonly used to determine the emission factors of selected friction couples.<sup>[81,82]</sup> Moreover, emission tests at the DB are more and more frequently exploited also to collect emissions for their physico-chemical characterization, cyto-toxicological studies and environmental assessment.<sup>[83]</sup>

## 1.6. Aim of the Thesis: Gap Analysis & Concept Map

This thesis work is specifically meant to integrate the previously cited observational studies on the chemistry of the brakes emissions, creating a wider and more comprehensive ensemble of compositional information. The main subject of the work are brakes non-exhaust PM<sub>10</sub> emissions, since they can be collected in suitable amounts for the chemical characterization in reasonable time and with affordable economical effort. Nevertheless, coarser and finer particulates fractions are also investigated, depending on the reported investigations. The final aim of this work is to provide a wide, reliable and updated set of physico-chemical data as input source for future environmental assessments, toxicological characterizations and source apportionment studies. An overall summary of the main objectives of this thesis is listed in Table 1.5: they are reported with specific reference to the main knowledge or literature gaps which they are meant to fill.

Along the whole thesis, particular attention is paid in drawing the widest possible set of correlations between the chemical composition of disc brake emissions and several determining or influencing factors, such as the origin friction couple and the driving conditions, which are usually less considered or explored in the current literature.

Knowledge/Literature Gap	Objectives	Section
No information on the reproducibility level of brakes emissions chemical composition and granulometry as sampled in laboratory conditions	Assess the <i>intra bench</i> and <i>inter benches</i> variability of elemental composition, phase composition and dimensional profiles of particulates generated by the same friction couple in the same test conditions	<i>Chapter 3</i>
Limited knowledge of elemental composition of brake emissions, mostly derived by punctual and observational studies	Study the influence of the starting material composing the friction couple on the elemental composition of the brakes emissions. Provide correlation with geographical and market distribution of different friction couples categories.	<i>Chapter 4</i>
Extremely limited information on the phase composition of the brakes emissions	Provide a wide characterization of compounds constituting the brakes emissions and correlate their generation with the compositional characteristics of the origin friction couple	<i>Chapter 5</i>
Friction couple category not commonly recognized as influencing factor of brake emissions granulometry	Characterize the influence of the starting material composing the friction couple on the dimensional profile of the brakes emissions.	<i>Chapter 6</i>
No information available on the correlation between chemical composition and different dimensional profiles of brakes emissions	Assess the compositional differences in different dimensional fraction of brakes emissions generated by the same friction couple	<i>Chapter 7</i>
Extremely limited information on the influence of the driving conditions on the chemical composition of brake emissions	Understand how energy indexes from different braking cycles modulates the chemical composition of brakes emissions	<i>Chapter 8</i>

**Table 1.5:** Summary of thesis objectives in relation with identified knowledge and literature gaps.

At this aim, the chemical composition of PM<sub>10</sub> particulate emissions generated by a wide range of different materials couplings is widely characterized in terms of both elemental and phase composition, respectively in *Chapter 4. Elemental Composition Maps* and *Chapter 5. Speciation*. In particular, the chemical features of the investigated emissions are put in correlation with the compositional features of the starting materials composing five different categories of couplings, representative for both the current standards in the automotive original equipment market and prototypal or pre-series innovative solutions representing the next future developments in the friction industry. In addition, the correlation with the corresponding geographical, market and future diffusion of the same categories of couplings is also discussed. Similarly, also the eventual correlations between the materials composing the tribological interface and the particulates dimensional distributions are investigated and discussed in *Chapter 6. Size Distributions*.

Each of the emissions analyzed in *Chapter 4 to 6* and, more in general, along all the thesis are obtained at the dynamometer bench with a limited number of test repetitions (typically three for each sample) due to time and cost reasons. In spite of representing simplified systems in comparison to real vehicles, DBs still remain complex mechanical devices whose performances can be affected by several variables. Therefore, if the tribological interaction in the friction couple and the experimental environment are not kept constant over different tests, significantly different wear mechanisms and local temperatures might be expected at the tribological interface. This can translate into the generation of particulates exhibiting higher variability in different physico-chemical characteristics, even if originated by the same braking rotor and pads and in the same test conditions. At this regard, the first experimental investigation reported in this thesis work (*Chapter 3. Reproducibility Studies*) widely explores the topic of the reproducibility of the physico-chemical composition of braking emissions generated at the DBs, in order to investigate the capability of these systems to ensure the generation of reproducible particulates. This was thought to be of pivotal importance and interest in order to assure reliable and consistent comparative assessments between particulates generated by different friction couple and to provide univocal chemical information as input for toxicological and environmental assessments as well as for source apportionment studies.

As reported in the previous paragraphs, the physico-chemical characteristic of the brakes emissions are complex and largely dependent on several variables. The investigations reported in *Chapter 4* and *5* demonstrate that the most determining for the compositional features are the material composing the friction couple which generate the corresponding emissions. However, other factors are found to exhibit remarkable influence at least in modulating the assessed physico-chemical

characteristics. In particular, the different dimensional fractions in which the particulates are produced and the driving conditions (*i.e.* the overall energy density dissipated by the braking system) are demonstrated to be able to significantly shift the compositional profile of a specific emission. The corresponding results are reported in *Chapter 7. Dimensional Profiles vs. Chemical Composition* and *Chapter 8. Influence of the Driving Conditions*, respectively.

## **1.7. Remarks: What cannot be Found in the Thesis**

This thesis is primarily focused on the physico-chemical characterization of non-exhaust emissions generated during braking. Thus, all the chemical information reported are kept disaggregated in respect with the emission factors and therefore expressed in relative terms. For this reason, even if qualitative considerations are sporadically reported on the emission level of different friction couples, no systematic data or point to point correlations are provided. Nevertheless, several information can be found in the dedicated literature, which is reported for each chapter. In addition, the generation of a specific emission inventory for disc-brakes devices is currently under development and will be largely based on the results reported in this thesis. It will become available once the collection and measurement protocols will be fixed and validated on a legislative level.

All the emissions characterized in the following chapters are produced by car disc-brake systems, as described in *Paragraph 1.3* and *1.4*. Therefore, no other emissions are taken into consideration. In particular, no emissions from motorbikes, heavy trucks or other sources within and outside the road transport sector are assessed.

The dominant mass contribution to the brakes emissions is represented by solid particle compounds, while liquid and gaseous species represent a far minority fraction. In addition, most recent trends of product development in the friction material market are focused on the substitution of the organic binders with inorganic compounds. For these reasons, the chemical investigations reported in the next chapters are mainly devoted to the characterization of the solid state fractions and, accordingly, to the inorganic fractions. Nevertheless, since the organic fraction concur to determination of the toxicological behavior of the brakes emissions, other internal research projects are currently ongoing in Brembo S.p.A. to characterize more in detail the presence and the distribution of these compounds.

Finally, no specific correlations or data on the toxicological characterization of the investigated emissions are reported. However, a new PhD research project specifically dedicated to these characterizations is starting exactly in the moment of the delivery of this thesis, based on the collaboration between Brembo S.p.A., Politecnico di Milano and

Istituto Ricerche Farmacologiche Mario Negri. This new research project will be based on the results reported in this thesis as starting point to individuate most interesting environmental and toxicological trends to be investigated and characterized in the next four years.

## Notes

§ = This thesis has been written just before the expected delivery of the EURO 7 new regulation proposal (November 2022).

# = This thesis has been written slightly before the expected delivery of the new EU Energy Performance of Building directive (January 2023).

## References

[1] World Health Organization, “WHO Global Air Quality Guidelines: Particulate Matter (PM<sub>2.5</sub> and PM<sub>10</sub>), Ozone, Nitrogen Dioxide, Sulfur Dioxide and Carbon Monoxide”, *World Health Organization*, **2021**, <https://apps.who.int/iris/handle/10665/345329>.

[2] US Environmental Protection Agency, “Air Quality System Data Mart”, internet database and report, 2022 <https://www.epa.gov/outdoor-air-quality-data>.

[3] European Environmental Agency, “Europe’s Air Quality Report - 2021”, *EEA*, **2021**, Online Version; European Environmental Agency, “Europe’s Air Quality Status - 2022”, *EEA*, **2022**, Online Version.

[4] GBD 2019 Risk Factors Collaborators, “Global Burden of 87 risk Factors in 204 Countries and Territories, 1990–2019: a Systematic Analysis for the Global Burden of Disease Study 2019”, *Lancet*, 396, **2020**, 1223-1249, [https://doi.org/10.1016/S0140-6736\(20\)30752-2](https://doi.org/10.1016/S0140-6736(20)30752-2).

[5] R. Burnett, H. Chen, M. Szyszkowicz, N. Fann, B. Hubbell, *et al.*, “Global Estimates of Mortality Associated with Long-term Exposure to Outdoor Fine Particulate Matter”, *PNAS*, 115(38), **2018**, <https://doi.org/10.1073/pnas.1803222115>.

[6] K. Vohra, A. Vodonos, J. Schwartz, E.A. Marais, M.P. Sulprizio, L.J. Mickleyd, “Global Mortality from Outdoor Fine Particle Pollution Generated by Fossil Fuel Combustion: Results from GEOS-Chem”, *Environmental Research*, 195, **2021**, 110754, <https://doi.org/10.1016/j.envres.2021.110754>.

[7] World Health Organization, “Burden of Disease from Ambient Air Pollution for 2016”, version 2, *WHO*, **2018**, Geneva.

[8] A.J. Cohen, M. Brauer, R. Burnett, H.R. Anderson, J. Frostad, *et al.*, “Estimates and 25-year Trends of the Global Burden of Disease Attributable to Ambient Air Pollution: an Analysis of Data from the Global Burden of Diseases Study 2015”, *Lancet*, 389, **2017**, 1907-1918, [https://doi.org/10.1016/S0140-6736\(17\)30505-6](https://doi.org/10.1016/S0140-6736(17)30505-6).

[9] World Bank, “The cost of air pollution : strengthening the economic case for action”, World Bank Group, 2016, Washington (DC), <https://documents.worldbank.org/en/publication/documents-reports/documentdetail/781521473177013155/the-cost-of-air-pollution-strengthening-the-economic-case-for-action>.

- [10] M. Kutlar Joss, M. Eeftens, E. Gintowt, R. Kappeler, N. Künzli, “Time to harmonize national ambient air quality standards”, *Int. J. Public Health*, 62, **2017**, 453–462, [doi:10.1007/s00038-017-0952-y](https://doi.org/10.1007/s00038-017-0952-y).
- [11] I. Manisalidis, E. Stavropoulou, A. Stavropoulou, E. Bezirtzoglou, “Environmental and Health Impacts of Air Pollution: a Review”, *Frontiers in Public Health*, 8(14), **2020**, 1-13, [doi:10.3389/fpubh.2020.00014](https://doi.org/10.3389/fpubh.2020.00014).
- [12] European Environment Agency, Unequal exposure and unequal impacts: Social Vulnerability to Air Pollution, Noise and Extreme Temperatures in Europe, EEA Report N°22/2018, **2018**, Luxembourg.
- [13] World Health Organization, Economic Cost of the Health Impact of Air Pollution in Europe: Clean air, Health and Wealth, WHO, **2015**, Geneva.
- [14] World Health Organization, Burden of Disease From the Joint Effects of Household and Ambient Air Pollution for 2016, WHO, **2018**, Geneva.
- [15] C.A. Pope, R.T. Burnett, M.J. Thun, E.E. Calle, D. Krewski, K. Ito et al., Lung Cancer, Cardiopulmonary Mortality and Long-Term Exposure to Fine Particulate Air Pollution, *J. Am. Med. Assoc.*, **2002**, 287, 1132-1141
- [16] C.A. Pope, D.D. Dockery, Health Effect of Fine Particulate Air Pollution: Lines that Connect, *J. Air Waste Manage. Assoc.*, **2002**, 56, 709-742.
- [17] A. Valavanidis, K. Fiotakis, T. Vlachogianni, Airborne Particulate Matter and Human Health: Toxicological Assessment and Importance of Size and Composition of Particles for Oxidative Damage and Carcinogenic Mechanisms, *J. Environ. Sci. and Health*, **2008**, 26, 4, 339-362.
- [18] D. Loomis, Y. Grosse, B. Lauby-Secretan, F.E. Ghissassi, V. Bouvard, L. Benbrahim-Tallaa et al., The Carcinogenicity of Outdoor Air Pollution, *Lancet. Oncol.*, **2013**, 14, 1262-1263.
- [19] K.H. Kim, E. Kabir, S. Kabir, A Review on the Human Health Impact of Airborne Particulate Matter, *Environ. Int.*, **2015**, 74, 136-143.
- [20] Ref.#56 in [11]; [21] Ref.#58 in [11]; [22] Ref.#59 in [11]; [23] Ref.#97 in [11]; [24] Ref.#98 in [11]; [25] Ref.#99 in [11]; [26] Ref.#100 in [11]; [27] Ref.#101 in [11]; [28] Ref.#105 in [11]; [29] Ref.#107 in [11]; [30] Ref.#111 in [11]; [31] Ref.#113 in [11]; [32] Ref.#114 in [11]. [33]Ref.#53 in [11].
- [34] P. Pant, R.M. Harrison, “Estimation of the Contribution of Road Traffic Emissions to Particulate Matter Concentrations from Field Measurements: A Review”, *Atmos. Environ.*, 77, **2013**, 78-97, <http://dx.doi.org/10.1016/j.atmosenv.2013.04.028>.
- [35] European Council, Directive 2008/50/EC, **2008**, Bruxelles.
- [36] European Commission, Commission Regulation (EU) N°459/2012, **2012**, Bruxelles.
- [37] A. Suleiman, M.R. Tight, A.D. Quinn, “Assessment and Prediction of the Impact of Road Transport on Ambient Concentrations of Particulate Matter PM10”, *Transp. Res. Part D*, 49, **2016**, 301-312, [doi:10.1016/j.trd.2016.10.010](https://doi.org/10.1016/j.trd.2016.10.010).
- [38] W.J. Requia, M. Mohamed, C.D. Higgins, A. Arain, M. Ferguson, “How Clean are Electric Vehicles? Evidence-based Review of the Effects of Electric Mobility on Air Pollutants, Greenhouse Gas Emissions and Human Health”, *Atmospheric Environment*, 185, **2018**, 64–77, <https://doi.org/10.1016/j.atmosenv.2018.04.040>.



- [39] T. Grigoratos, G. Martini, "Brake Wear Particle Emissions: a Review", *Environ. Sci. Pollut. Res.*, **22**, **2015**, 2491-2504, doi: [10.1007/s11356-014-3696-8](https://doi.org/10.1007/s11356-014-3696-8).
- [40] B.D. Garg, S.H. Cadle, P.A. Mulawa, P.J. Groblicki, "Brake Wear Particulate Matter", *Environ. Science & Tech.*, **34**(21), **2000**, 4463-4469, <https://doi.org/10.1021/es001108h>.
- [41] S.K. Rhee, "Influence of Rotor Metallurgy on the Wear of Friction Materials in Automotive Brakes", *SAE Transactions*, **80**(2), **1971**, 992-998.
- [42] D.M. Stefanescu, "Classification and Basic Metallurgy of Cast Iron", *ASM Handbook*, Volume 1: Properties and Selection: Irons, Steels, and High-Performance Alloys ASM Handbook Committee, **1990**, p 3-11, doi: [10.31399/asm.hb.v01.a0009206](https://doi.org/10.31399/asm.hb.v01.a0009206).
- [43] J.M., Radzikowska, "Metallography and Microstructure of Cast Iron", *ASM International*, **2004**, 565-587, <https://doi.org/10.31399/asm.hb.v09.a0003765>.
- [44] F. Bertasi, B. Dudzik, A. Mancini, M. Bandiera, *et.al.*, "Rust Is Not a Must. Improvement of Discs Corrosion Resistance by Tuning of Grey Cast Iron Alloying Elements and Microstructure", *SAE Technical Paper 2020-01-1624*, **2020**, <https://doi.org/10.4271/2020-01-1624>.
- [45] S. Weitao, W. Bin, L. Xiaoliang, W. Yuqian, Z. Jian, "Controlling the Tribology Performance of Gray Cast Iron by Tailoring the Microstructure", *Tribology International*, **167**, **2022**, 107343, <https://doi.org/10.1016/j.triboint.2021.107343>.
- [46] G. Perricone, V. Matějka, M. Alemani, G. Valota, A. Bonfanti, *et. al.*, "A Concept for Reducing PM10 Emissions for Car Brakes by 50%", *Wear*, 396–397, **2018**, 135–145, doi: <http://dx.doi.org/10.1016/j.wear.2017.06.018>.
- [47] O. Aranke, W. Algenaid, S. Awe, S. Joshi, "Coatings for Automotive Gray Cast Iron Brake Discs: A Review", *Coatings*, **2019**, **9**, 552; doi:10.3390/coatings9090552.
- [48] M. Federici, G. Perricone, S. Gialanella, G. Straffellini, "Sliding Behaviour of Friction Material Against Cermet Coatings: Pin-on-Disc Study of the Running-in Stage", *Tribology Letters*, **2018**, **66**:53, <https://doi.org/10.1007/s11249-018-1004-3>.
- [49] J. Kukutschova, P. Filip, "Review of Brake Wear Emissions, in: F. Amato (Ed.), Non Exhaust Emissions: an Urban Air Quality Problem for Public Health", *Academic Press*, Elsevier, San Diego, **2018**.
- [50] N. Aranganathan, J. Bijwe, "Development of Copper-free Eco-friendly Brake-Friction Material Using Novel Ingredients", *Wear*, 352–353, **2016**, 79-91, <https://doi.org/10.1016/j.wear.2016.01.023>.
- [51] V. Mahale, J. Bijwe, S. Sinhab, "Efforts towards Green Friction Materials", *Tribology International*, **136**, **2019**, 196–206, <https://doi.org/10.1016/j.triboint.2019.03.049>.
- [52] M. Leonardi, "Development of Novel Eco-Friendly Friction Materials for Disc Brake Systems", Doctoral Thesis, 2020, Università di Trento.
- [53] N. Kalel, B. Bhatt, A. Darpe, J. Bijwe, "Copper-free brake-pads: A Break-Through by Selection of the Right Kind of Stainless Steel Particles", *Wear*, 464-465, **2021**, 203537, doi:10.1016/j.wear.2020.203537.
- [54] R.C. Dante, "Handbook of Friction Materials and Their Applications", 1st Ed., Elsevier, The Woodhead Publishing, **2015**.

- [55] P. Chandra Verma, L. Menapace, A. Bonfanti, R. Ciudin, S. Gialanella, et.al, “Braking Pad-Disc System: Wear Mechanisms and Formation of Wear Fragments”, *Wear*, **2015**, 322– 232, 251–258, <https://doi.org/10.1016/j.wear.2014.11.019>.
- [56] G. Straffellini, S. Gialanella, “Airborne Particulate Matter from Brake Systems: An assessment of the Relevant Tribological Formation Mechanisms”, *Wear*, **2021**, 478-479, 203883, <https://10.1016/j.wear.2021.203883>.
- [57] P. Filip, Z. Weiss, D. Rafajac, “On friction layer formation in polymer matrix composite materials for brake applications”, *Wear*, 252(3-4), 2002, 189-198, [https://doi.org/10.1016/S0043-1648\(01\)00873-0](https://doi.org/10.1016/S0043-1648(01)00873-0).
- [58] H. Niemann, H. Winner, C. Asbach, H. Kaminski, G. Frenzt, R. Milczarek, “Influence of Disc Temperature on Ultrafine, Fine and Coarse Particle Emissions of Passenger Car Disc Brakes with Organic and Inorganic Pad Binder Materials”, *Atmosphere*, **2020**, 11(10), 1060.
- [59] A.P. Gomes Nogueira, D. Carlevaris, C. Menapace, G. Straffellini, “Tribological and Emission Behavior of Novel Friction Materials”, *Atmosphere*, **2020**, 11(10), 1050.
- [60] A. Mancini, B. Tsyupa, S. Pin, M. Bandiera, et al., “Chemistry of the Brake Emissions: Influence of the Test Cycle”, *SAE Technical Paper*, 2021-01-1300, **2021**, [doi:10.4271/2021-01-1300](https://doi.org/10.4271/2021-01-1300).
- [61] J. Park, B. Joo, H. Seo, W. Song, J.J. Lee, W.K. Lee, H. Jang, “Analysis of Wear Induced Particle Emissions from Brake Pads During the Worldwide Harmonized Light Vehicle Test Procedure (WLTP)”, *Wear*, 466-467, **2021**, 203539.
- [62] M. Alemani, O. Nosko, I. Metinoz, U. Olofsson, “A Study on Emission of Airborne Wear Particles from Car Brake Friction Pairs”, *SAE International J. of Materials and Manufacturing*, **2016**, 1, 147-157.
- [63] J. Kukutschova, P. Moravec, V. Tomasek, V. Matejka, J. Smolik, J. Schwarz, et. al., “On Airborne Nano/Micro-Sized Wear Particles Released from Low-Metallic Automotive Brakes”, *Environmental Pollution*, **2011**, 159(4), 998-1006.
- [64] P.C. Verma, M. Alemani, S. Gialanella, L. Luterotti, U. Olofsson, G. Straffellini, “Braking Pad-Disc System: Wear Mechanism and Formation of Wear Fragments”, *Wear*, **2015**, 322-323, 251-258.
- [65] J.H.J. Hulskotte, G.D. Roskam, H.A.C. Denier von der Gon, “Elemental Composition of Current Automotive Braking Materials”, *Atmospheric Environment*, **2014**, 99, 436-445.
- [66] F. Amato, F.R. Cassee, H.A.C. Dener von der Gon, R. Gehrig, M. Gustafsson, et. al., “Urban Air Quality: The Challenge of Traffic Non-Exhaust Emissions”, *J. of Hazard. Mat.*, **2014**, 275, 31-36, [doi: 10.1016/j.jhazmat.2014.04.053](https://doi.org/10.1016/j.jhazmat.2014.04.053).
- [67] C.A. Alves, M. Evtugina, A.M.P. Vicente, E.D. Vicente, T.V. Nunes, et. Al., “Chemical Profiling of PM10 from Urban Road Dust”, *Sci. of Total Environ.*, **2018**, 634, 41-45, [doi:10.1016/j.scitotenv.2018.03.338](https://doi.org/10.1016/j.scitotenv.2018.03.338).
- [68] S.L. Goddard, K.R. Williams, C. Robins, R.J.C. Brown, “Determination of Antimony and Barium in UK Air Quality Samples as Indicators of Non-Exhaust Traffic Emissions”, *Environ. Monit. Assess*, **2019**, 191:641, 1-12, [doi:10.1007/s10661-019-7774-8](https://doi.org/10.1007/s10661-019-7774-8).
- [69] A. Liati, D. Schreiber, D. Lugovyy, S. Gramstat, P. Dimopoulos Eggenschwiler, “Airborne Particulate Matter Emissions from Vehicle Brakes in Micro- and Nano- Scales: Morphology, and Chemistry by Electron Microscopy”,

- [70] C. Menapace, A. Mancini, M. Federici, G. Straffellini, S. Gialanella, "Characterization of Airborne Wear Debris Produced by Brake Pads Pressed against HVOF-Coated Discs", *Friction*, **2020**, 8(2), 421-432.
- [71] M. Figliuzzi, M. Tironi, L. Longaretti, A. Mancini, F. Teoldi, F. Sangalli, A. Remuzzi, "Copper-dependent biological effects of particulate matter produced by brake systems on lung alveolar cells", *Archives of Toxicology*, **2020**, 94, 2965-2979.
- [72] A. Volta, S. Sforzini, C. Camurati, F. Teoldi, S. Maiorana, *et.al.*, "Ecotoxicological Effects of Atmospheric Particulate Produced by Braking Systems on Aquatic and Edaphic Organism", *Environ. Int.*, **2020**, 137, 105564.
- [73] A. Mancini, B. Tsyupa, S. Pin, F. Bertasi, M. Bandiera, M. Federici, G. Perricone, A. Bonfanti, E. Bolzacchini, "Novel Approaches for Physico-Chemical characterization of Brake Emissions", EuroBrake2021, **2021**, EB2020-EBS-031.
- [74] M. Mathissen, J. Grochowicz, C. Schmidt, R. Vogt, *et.al.*, "A novel Real-World Braking Cycle for Studying Brake Wear Emissions", *Wear*, 414-415, **2018**, 219-226.
- [75] M. Mathissen, T. Grigoratos, T. Lahde, R. Vogt, "Brake Wear Particle Emissions of a Passenger Car Measured on a Chassis Dynamometer", *Atmosphere*, **2019**, 10(9), 556.
- [76] G. Perricone, M. Alemani, I. Methiöz, V. Matějka, J. Wahlström, U. Olofsson, "Towards the Ranking of Airborne Particle Emissions from Car Brakes – a System Approach", *Proc. Inst. Mech. Eng. Part D: J. Automob. Eng.*, **2016**, 230(11), 1–17.
- [77] N. Perzborn, C. Agudelo, G.P. Ostermeyer, "On Similarities and Differences of Measurements of Inertia Dynamometer and Scale Testing Tribometer for Friction Coefficient Evaluation", *SAE Int. J. Mater. Manf.*, 8(1), **2015**, [doi:10.4271/2014-01-2523](https://doi.org/10.4271/2014-01-2523).
- [78] M. Federici, M. Alemani, C. Menapace, S. Gialanella, G. Perricone, G. Straffellini, "A Critical Comparison of Dynamometer Data with Pin-on-Disc Data for the Same two Friction Material Pairs – A Case Study", *Wear*, 424-425, **2019**, 40-47, <https://doi.org/10.1016/j.wear.2019.02.009>.
- [79] N. Perzborn, C. Agudelo, G.P. Ostermeyer, "On Similarities and Differences of Measurements of Inertia Dynamometer and Scale Testing Tribometer for Friction Coefficient Evaluation", *SAE Int. J. Mater. Manf.*, 8(1), **2015**, [doi:10.4271/2014-01-2523](https://doi.org/10.4271/2014-01-2523).
- [80] M. Federici, M. Alemani, C. Menapace, S. Gialanella, G. Perricone, G. Straffellini, "A Critical Comparison of Dynamometer Data with Pin-on-Disc Data for the Same two Friction Material Pairs – A Case Study", *Wear*, 424-425, **2019**, 40-47, <https://doi.org/10.1016/j.wear.2019.02.009>.
- [81] P.G. Sanders, T.M. Dalka, N. Xu, M.M. Maricq, R.H. Basch, "Brake Dynamometer Measurement of Airborne Brake Wear Debris", *SAE Transactions*, 111(6), **2002**, 1693-1699.
- [82] H. Hagino, M. Oyama, S. Sasaki, "Laboratory Testing of Airborne Brake Wear Particle Emissions Using a Dynamometer System under Urban City Driving Cycles", *Atmospheric Environment*, 131, **2016**, 269-278, <http://dx.doi.org/10.1016/j.atmosenv.2016.02.014>.
- [83] G. Perricone, V. Matějka, M. Alemani, G. Valota, A. Bonfanti, *et. al.*, "A Concept for Reducing PM10 Emissions for Car Brakes by 50%", *Wear*, 396–397, **2018**, 135–145, [doi: http://dx.doi.org/10.1016/j.wear.2017.06.018](http://dx.doi.org/10.1016/j.wear.2017.06.018).

## 2. Experimental

*This chapter is meant to collect all the analytical procedures adopted along this thesis work. In particular, great attention is paid in the description of the chemical characterization of the brakes emissions particulates. Nevertheless, also the corresponding collection and preparation procedures are described.*

### 2.1. Introduction

As already stated, this section describes all the procedures adopted for the collection, the preparation and the physico-chemical characterization of the particulates which are the subject of this thesis. A short description of the experimental procedures related to specific investigations reported in the next chapters is always reported at their beginning. Nevertheless, this section collects the most detailed information.

The experimental procedures specifically related to the collection of the brakes emissions are not treated as a central topic in this work, since they have been widely reported and discussed in the literature, thanks also to previous PhD projects developed within the R&D department of Brembo.<sup>[1,2]</sup> Nevertheless, a detailed description of the devices used for the generation of brakes wear particulates is provided. In addition, procedures for the suitable preparation of the particulates in relation to specific analytical techniques adopted for their characterization are also discussed. Finally, a wide description of all the analytical protocols adopted for the physico-chemical characterization of the brakes emissions is reported as main topic of this chapter.

Generally speaking, the rationale behind the choice of the adopted analytical protocols is always to maximize the amount of obtainable physico-chemical information, reducing the number of test probes, with preferential attention to non-destructive techniques. Indeed, brakes emissions in form of PM<sub>10</sub>, PM<sub>2.5</sub> or ultra-fine particulates (UFP) are usually collected in very low amounts (*i.e.* few milligrams to few micrograms) after prolonged emissions tests (up to weeks) carried out on complex mechanical devices which are used in industrial context for the development and the validation of series products. Thus, the collected emission samples are obtained as a results of significant investments in terms of both machine and human working time. Therefore, the intrinsic high cost of these samples has to be properly compensated trying to extract as much physico-chemical information as possible.

### 2.2. Brakes Emissions Generation and Collection

Most of the samples investigated in this thesis are generated during emissions tests carried out at brake dynamometric benches. These testing platforms are mechanical devices simulating a braking corner for a selected application (vehicle). They

are able to recreate the inertia and the speed, *i.e.* the kinetic energy, of a target vehicle and are usually programmed in order to perform predetermined sequences of brake events. These sequences are usually referred as braking cycles, whose aim is to mimic specific driving conditions. Therefore, their main advantages in respect with real vehicles are: *i)* the lowest level of complexity; *ii)* the capability of generating and withstanding comparable energies (differently from other typologies of tribometers, such as the Pin-on-Disc benches); *iii)* the possibility of operating in laboratory (controlled) conditions, thus strongly limiting environmental variables; and *iv)* an elevate degree of automation. They have been historically used in the brake industry to test brakes performances and comfort (*i.e.* noise and vibration), during both the development and the validation phases in the production of new brakes.<sup>[3]</sup> Nowadays, they are also frequently used as tool to measure and rank brakes emission factors.<sup>[4,6]</sup> Conveniently, they can be also exploited to collect brakes emissions to the specific aim of their physico-chemical characterization, as proposed in this thesis. The major part of the emissions analyzed in the following chapters are collected at a brake inertia dynamometer bench suitably designed and optimized for brakes particulates collection and measurement. This specific bench is currently located at the Testing Department of Brembo S.p.A. and a detailed description of its features is already reported in the literature.<sup>[7]</sup> Nevertheless, the next lines provide a summary of its most important characteristics, while Figure 2.1 and 2.2 report respectively a schematic diagram and a picture of the bench.

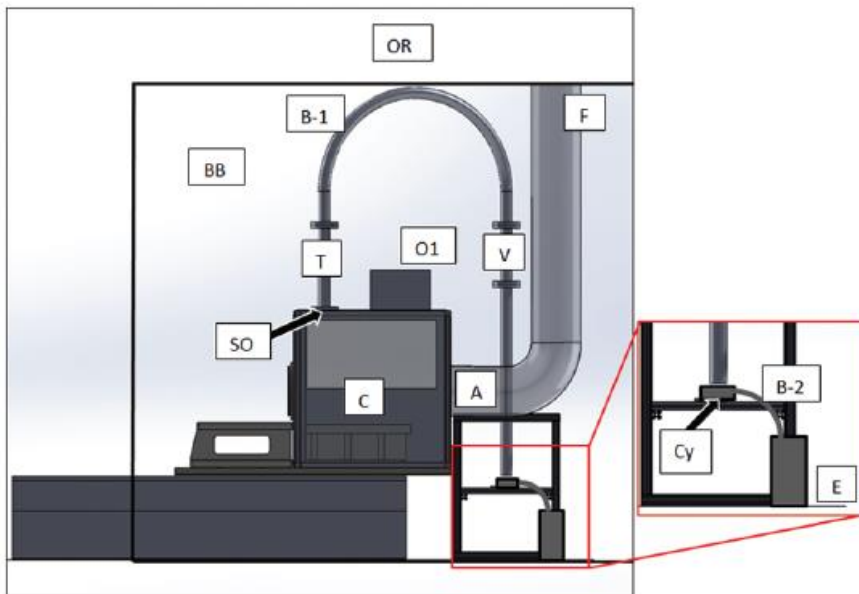


**Figure 2.1:** Schematic representation of the test stand. **OR:** Outdoor room; **B-1:** bend tube 1; **F:** flow measurement point and filter; **BB:** bigger box; **T:** tube; **O1:** first outlet gap; **V:** Venturi flow measurement

tube; **SO**: sampling outlet; **C**: dust box chamber; **A**: air inlet opening; **Cy**: cyclone; **B-2**: bend tube 2; **E**: emission collection and measurement devices.

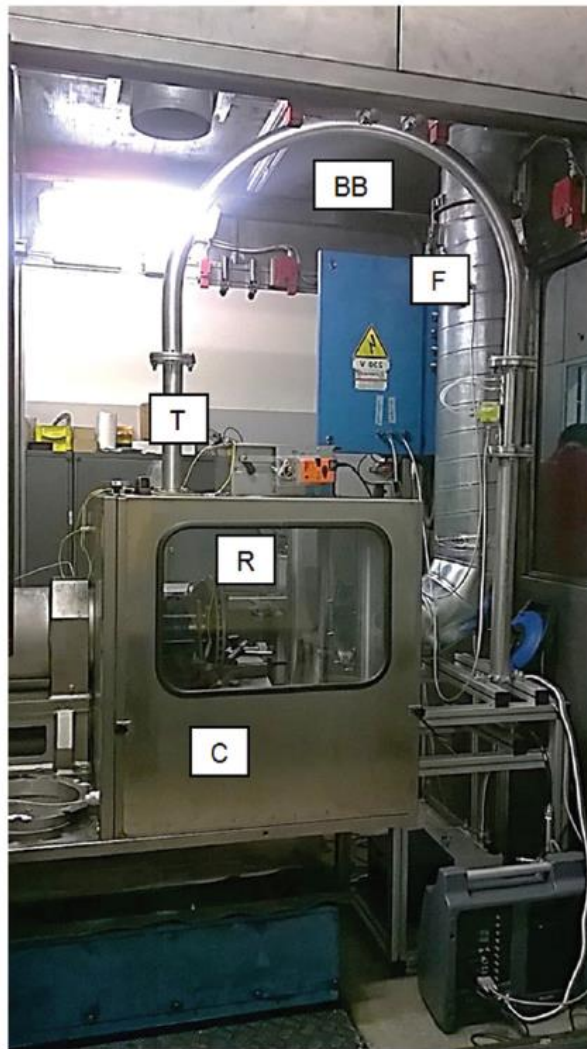


**Figure 2.2:** Picture of the test stand. **BB**: bigger box (door open); **T**: tube; **F**: flow measurement point and filter; **C**: dust box chamber; **R**: rotor ensemble.

As can be observed in both Figure 2.1 and 2.2, one of the main characteristics of this bench is the enclosure which surrounds the braking corner. This is necessary in order to: *i*) isolate the system from other spurious contributions from the environment; and *ii*) to maintain the system in controlled conditions, with temperature and relative humidity respectively fixed at 20°C and 50%. Another important feature is represented by the inlet air flux, which is purified by a HEPA-H13 filter ensuring an average filtration efficiency of the incoming air higher than 99.95%. Finally, the sampling outlet is

specifically designed to maximize the efficiency of the aerosol samples extraction for the full range of expected particle sizes. In order to do so, isokinetic sampling is obtained by the use of a Dekati™ IP probe of 7.62 mm, equipped with four sharp edged nozzles to ensure a high efficiency sampling. The isokinetic probe is positioned parallel to the air stream with its tip inserted 5 cm inside the outlet sampling tube (T). This sampling line ends into several different measurement and collection devices, prior dimensional selection carried out by a Dekati™ PM<sub>10</sub> cyclone. Therefore the probe can be simultaneously connected to measurement instrument such as the Dekati™ ELPI+ and DGI impactors, CPC and OPC counters. As far as the particulates presented in this work are concerned, most of them were collected through a 47 mm diameter filter holder, hosting high efficiency cellulose filters (Whatman™ RC58: diameter = 47 mm, pores < 0.20 μm) which collects together all the particles with aerodynamic diameter lower than 10 μm thanks to dimensional selection carried out by the cyclone, as showed in Figure 2.3. Therefore, most of the particulates collected for the studies presented in the next chapter are PM<sub>10</sub> emissions. However, for some specific studies, also materials with different dimensional distribution profiles were collected (*Chapter 7. Dimensional Profiles and Chemical Composition*). To do so, both Aluminum and Polycarbonate collection substrates for ELPI+ and DGI impactors were exploited. In addition, also coarser material (wear debris) falling to the cabin floor during the test is collected by means of a metallic tray simply positioned directly under the braking corner.

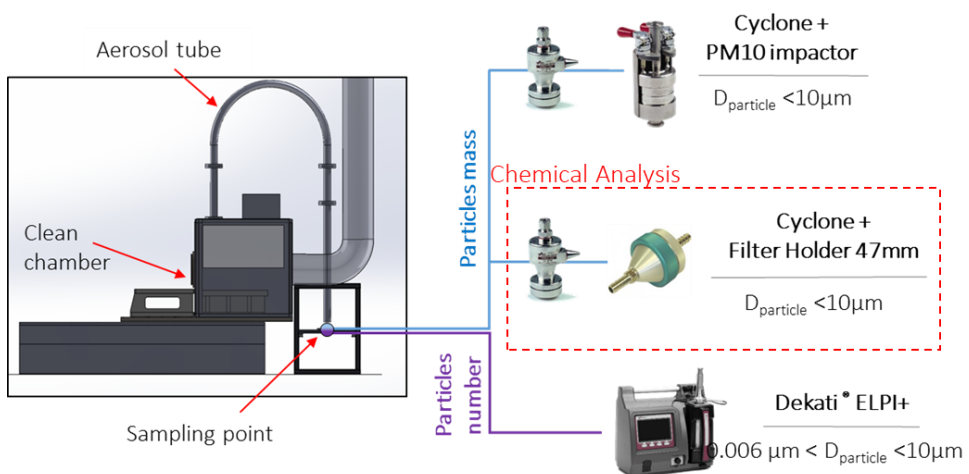


**Figure 2.3:** Schematic representation of the sampling line.

*Chapter 3. Reproducibility Studies* reports an assessment of the variability of the chemical composition of particulates collected at three different dynamometer benches in the same experimental conditions. To do so, in addition to the just described bench, other two test platforms were employed. One of the additional bench is an updated and

upgraded version of the platform described in the previous lines, which is recently arrived and installed at the same Testing Department of Brembo S.p.A. This second stand differs from the main one for the volume of the enclosure surrounding the braking corner. In particular its enclosure has volume approximately one third of the first stand enclosure. Due to this, air fluxes are typically increased in order to obtain suitable cooling to match the temperature requirements of the adopted braking cycle. Finally, another minor difference is represented by the relative orientation of the caliper in respect to the air flux, which is optimized for the specific aerodynamic of the enclosure. The third platform is located in the testing laboratory of another company, market leader for the production of braking pads. For this bench, few details are reported for proprietary reasons. This platform differs from the main one for the two following main features: *i)* the air is taken prior HEPA-H13 filtration directly from indoor but not from controlled environment, with temperature and relative humidity parameters possibly varying respectively in the 18-25°C and 40-60% ranges; and *ii)* PM<sub>10</sub> particulate is collected on a 47 mm filter located inside an eFilter™ (Dekati) instrument for the determination of the particulate mass. For all the other relevant features, the three testing platforms are closely similar and always compliant with the guidelines provided by the Particle Measurement Programme (PMP) Informal Working Group for the generation, the collection and the measurement of the brakes emissions.<sup>[8]</sup>

As already introduced, dynamometric benches are programmed for executing series of predetermined braking events composing a braking cycle. These routines are usually created to mimic overall driving conditions in ensembles of different situations, such as urban, sub-urban, rural and highway traffic situations. As far as the particulates analyzed in this work are concerned, most of the them were collected during emission bench tests carried out when executing the “Worldwide-harmonized Light-duty vehicle Test Procedure for Brakes” cycle, more conveniently abbreviated in WLTP-Brake along this thesis.<sup>[9]</sup> the WLTP-Brake is a time-controlled cycle composed by 303 brake events divided into ten trips. The emission test duration is about 7.5 hours, comprehensive of the cooling phases between trips. It is nowadays most commonly used for sake of reference in the study of brake emissions, since it is based on a wide database of traffic behavior in the European region, thus being considered extremely representative of a global ensemble of braking profiles simulating standard driving conditions in EU. In *Chapter 6. Influence of the Driving Conditions*, it is reported a comparative assessment of the chemical composition of brake emissions generated by the same friction couple but in different driving (*i.e.* braking) conditions. To do so, particulates produced also during a different braking cycle are compared with the corresponding one generated during the WLTP-Brake cycle. In particular, the other used cycle is the 3h-Los Angeles City Traffic routine, abbreviated from this moment on in 3h-LACT.<sup>[10]</sup> This is a temperature driven test, accounting for 217 braking events performed in a unique run



during approximately 3 hours. It is historically one of the first cycles proposed in the dedicated literature as reference cycle to compare and rank emissions generated by different braking devices. Table 2.1 and Figure 2.4 report respectively a comparative summary of the main characteristics of the two cycles and the comparison of their speed profiles. As can be appreciated mainly by the data reported in Table 2.1, the 3h-LACT cycle is overall more energy demanding in respect with the WLTP-Brake counterpart.

	3h-LACT	WLTP-Brake
<b>Duration</b>	approx. 3h	approx. 7.5h
<b>Average Initial Speed</b>	53.6 km/h	41.5 km/h
<b>Deceleration</b>	0.2-2.9 m s <sup>-2</sup>	0.49-2.18 m s <sup>-2</sup>
<b>IBT</b>	54-187°C	30-175°C
<b>Number of Stops</b>	217	303
<b>Total Distance</b>	145 km	192 km

**Table 2.1:** Comparative summary of parameters of interest for 3h-LACT and WLTP-Brake cycles.

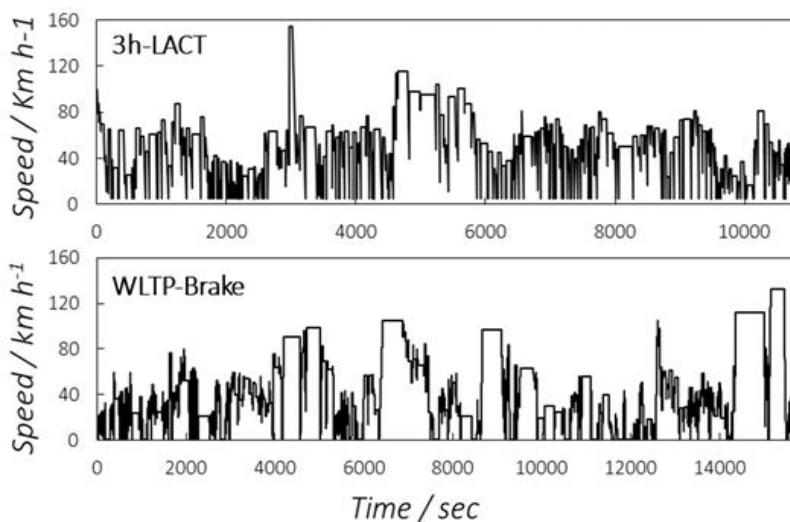


**Figure 2.4:** Speed profiles of the two braking cycles used for the generation of brake emissions.

Independently from the cycle, the braking corner is composed by: *i*) a four piston fixed Aluminum caliper with pistons diameter of 44 mm; *ii*) a fully pearlitic vented cast-iron braking disc with diameter of 342 mm and 32 mm height (distance between internal and external braking surfaces); and *iii*) a couple of pads with surface of 89.1 cm<sup>2</sup>. Thus, the combination of the pads and braking disc geometry leads to an effective radius of 136.5 mm.

## 2.3. Sample Preparation

Most of the collected particulates are obtained in form of powder deposited on collection substrates. For some probes, no additional manipulation of the sample is needed to proceed to the analysis. In particular, XRD, XANES,  $\mu$ -Raman analysis can be carried out directly on the samples as collected. The composition of the collection substrate should be taken into account to avoid spurious analytical contribution from the substrate itself. For example, amorphous or highly disordered material are used for the XRD analysis: target collection substrate for this probe are cellulose and polycarbonate filters, while Teflon, Aluminum and inorganic filters are highly not recommended due to their partial or complete crystalline nature. When assessing the elemental composition of the samples, high purity filters are preferred, while Aluminum or ceramic substrates are obviously not suitable due to their inorganic composition. Similarly, when looking at the oxidation state of *d-block* metals by means of XANES probe, high purity polymeric based filters have to be used. Therefore, emission samples undertaking characterization by means of X-Ray probes were preferentially collected on cellulose or polycarbonate substrates (respectively, RC58 Whatman™ and 23006 Sartorius™). Other analytical probes requires detachment of the collected particles in order to obtain samples in form of free powders or to redeposit them on more suitable substrates. The detachment is usually performed by sonication in suitable solvent (usually isopropyl alcohol or acetone) and following recovery by centrifugation. Typically, the collection filters are positioned inside a 2 or 5 mL glass vial and covered with the solvent. Then the samples are sonicated at 35 kHz for times in the range between 1-10 minutes, depending on the specific collection substrate. Then, the collection substrate is removed and the vial is put in centrifuge, typically at 3000 rpm for 3 minutes. After the centrifugation step, most of the solvent is gently removed by hand, using a micro-pipette. Finally, the remaining solvent is left overnight at room temperature in mild vacuum conditions (20 mbar) to evaporate. In the end, a free powder of brakes emissions is obtained. Then, the free powder can be used without any further manipulation or, alternatively, it can be redeposited on other substrates. For instance, in the case of SEM/EDXS characterization, a compact layer of emission powder is taken with a fine tip metallic spatula and deposited by hand on an Aluminum stub covered with carbon tape for electron microscopy. In the case of SEM image analysis for granulometric characterization, the emission powder is resuspended in few mL of isopropyl alcohol by sonication at 35 kHz for 10 minutes to obtain a diluted suspension. Then, the dispersed particulates are slowly deposited by micro-pipette on polycarbonate filters, in order to achieve the maximum possible separation between particles. Debris samples were always analyzed without any specific manipulations, with the only exception of a mild grinding homogenization of the collected material, which is carried out by hand in an agate mortar.

## 2.4. SEM/EDXS Analysis

Scanning electron microscopy is used as probe to assess qualitatively the morphology and the granulometry of the collected samples. It is used in first place as quick check control of the coherency of the dimensional distributions obtained in respect with the sampling prior the chemical analysis. Then, the elemental composition of the collected samples is investigated by the mean of the coupling with the Energy Dispersive X-Ray Spectroscopy (EDXS) probe. In particular, a *Zeiss EVO MA10* electron microscope equipped with an Oxford Instrument INCA X-act silicon-drift detector (SDD) with 10 mm<sup>2</sup> active area is used (Figure 2.5).



**Figure 2.5:** EVO MA10 Scanning Electron Microscope used for the morphological and chemical analysis. The EDXS detector can be observed on the left side (front image).

SEM images are acquired first with secondary electrons (SE) in order to highlight the morphological details of the particulates. Therefore, back scattered electrons (BSE) are used in order to highlight the phase contrast and maximize the interaction volume between the particles and the electronic beam during the acquisition of the EDXS spectra. An example of typically collected images is reported in Figure 2.6.

All the measurements are performed using the following power parameters:  $V = 20$  kV and  $I = 300$  pA. When chemical analysis is performed on PM<sub>10</sub> samples, five different areas of 400 x 300  $\mu\text{m}$  are usually measured, and the obtained results are averaged in order to obtain final concentration values together with the corresponding variability index (standard deviation over five independent observations). Each emission spectrum is acquired within the 0.1 – 20 keV energy range for 540 s, maintaining the detector dead-time lower than 15%. All the emission spectra are acquired at the ideal working distance (gun to sample surface) for the specific system configuration, at  $8.5 \pm 0.1$  mm.

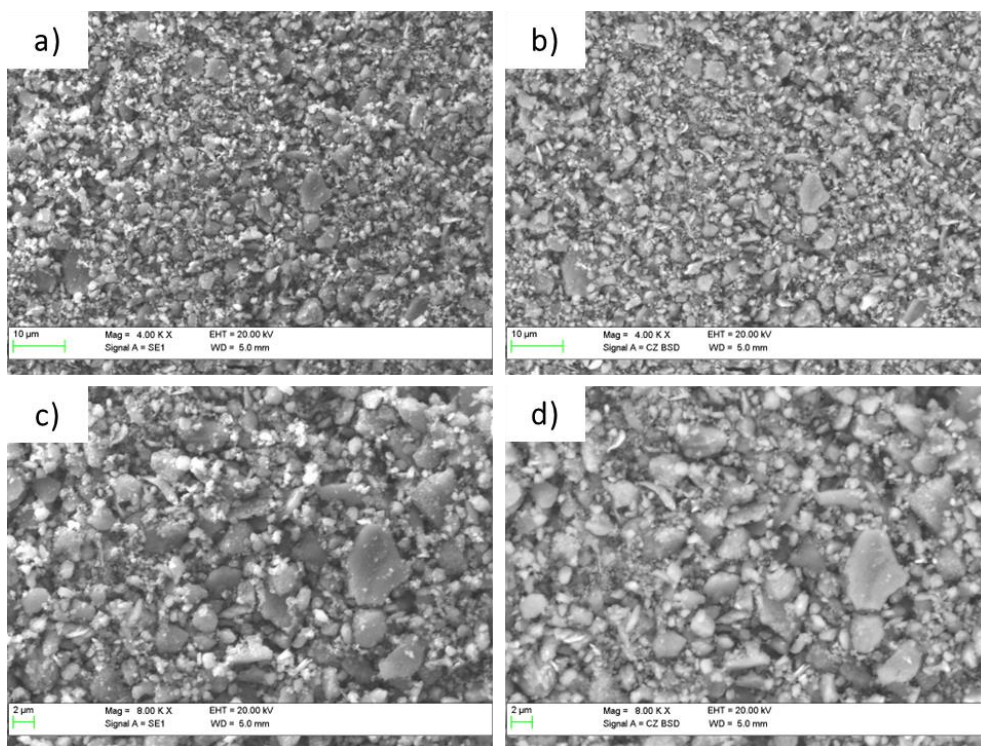


**Figure 2.6:** Comparison of SEM images acquired on a brake PM<sub>10</sub> sample by mean of secondary electron (SE) and back-scattered electrons (BSE) detection at two different magnification (4000x and 8000x). **a), c)** SE images, detail on the morphology of the particles; **b), d)** BSE images, detail on the phase contrast.

The SEM/EDXS probe is selected as tool for the development of all the comparative assessments reported in this thesis, since it can provide analytical information on both the granulometry, the morphology and the elemental composition of the investigated samples. At the same time, as far as the elemental analysis is concerned, it is possible to assess simultaneously a wide range of elements, ranging from Beryllium up to the Uranium. In particular, the possibility of measuring also the lighter elements (Carbon and Oxygen in particular) is one of the most important feature of the technique. However, the accurate determination of elements with low atomic number ( $Z < 10$ ) is always problematic with energy-dispersive spectroscopy (EDS) probes. This is particularly true, if considering samples exhibiting also significant concentrations of heavier elements possibly overlapping with their M- or L-peaks the K transitions of the lighter elements. This is due to several reasons, including: *i)* the intrinsically low resolution of the SDD-EDXS in the lower energies region; *ii)* the complexity of the spectral background in the low photon energy region; and *iii)* the low fluorescence yield in the lower energies region, leading intrinsically to corresponding low signal to noise ratio. Therefore, in order to limit as much as possible the possible sources of error and

to maximize both the reliability, the accuracy and the sensitivity of the method, the developed protocol try to overlap as much as possible the guidelines provided by NIST for good practices in EDXS micro-analysis.<sup>[11]</sup> In particular, great attention is paid in prepare measurement surfaces as compact, flat and even as possible (as shown in Figure 2.6), in order to minimize specimen geometry effects. Then, the measurement geometry and conditions are always kept constant as reported in the previous lines. Finally, the beam current is chosen to provide detector deadtime approximatively of 10% to minimize the occurrence of pulse coincidence (*i.e.* sum peaks). The voltage is kept at minimum possible values to assure correct production of emission X-ray for all the interested transitions, while obtaining suitable penetration depth (estimated in the order of 2  $\mu\text{m}$  for the system under investigation). The quantification is performed via standard-less methods previously validated by empirical comparison with other direct or standardized analytical methods (such as  $\mu\text{-ED-XRF}$ , ICP-OES, ICP-MS and C,O-Elemental Analysis). In particular, for most of the elements investigated, variabilities between standardized and standardless measurements are typically maintained below the 10%, including the Carbon. The element which is observed to exhibit the highest level of variability is typically the Oxygen, which can reach relative errors in the order of the 20%.

### 2.5a. Particle Size Distribution – SEM Image Analysis

The granulometry, or particle size distribution (PSD), of the collected  $\text{PM}_{10}$  samples is investigated via Scanning Electron Microscopy Image Analysis (SEM-IA) by means of the ImageJ software suite to minimize the amount of material needed for the dimensional characterization.<sup>[12]</sup> More in detail, the particulates are characterized for their maximum Feret diameter ( $D_{\text{max}}$ ). First of all, the investigated sample is suitably prepared at the specific aim of obtaining redeposition of non-overlapping particles, as diffusely described in *Paragraph 2.3*. The procedure is developed in following steps (Figure 2.7). As first, SEM images of high quality, *i.e.*, with particles well separated, proper resolution and contrast between particles and background are acquired. Once suitable images are obtained, the scale bar is registered in the ImageJ software. Then, a fixed value of Threshold is fixed for each set of image to empathize the difference between the objects of interest and the background. This step is followed by the image binarization and dimensional analysis carried out by the mean of the Analyze Particles function to obtain  $D_{\text{max}}$  values as parameter of interest.  $D_{\text{max}}$  more precisely is calculated as the longest distance between any two points along the particle selection boundary. In order to obtain relevant statistics, at least five SEM images acquired at 4000x magnification are analyzed with the ImageJ software following the procedure described above. As the final result, at least more than 3500 particles, and typically more than 5000 particles, are in analyzed for each sample.

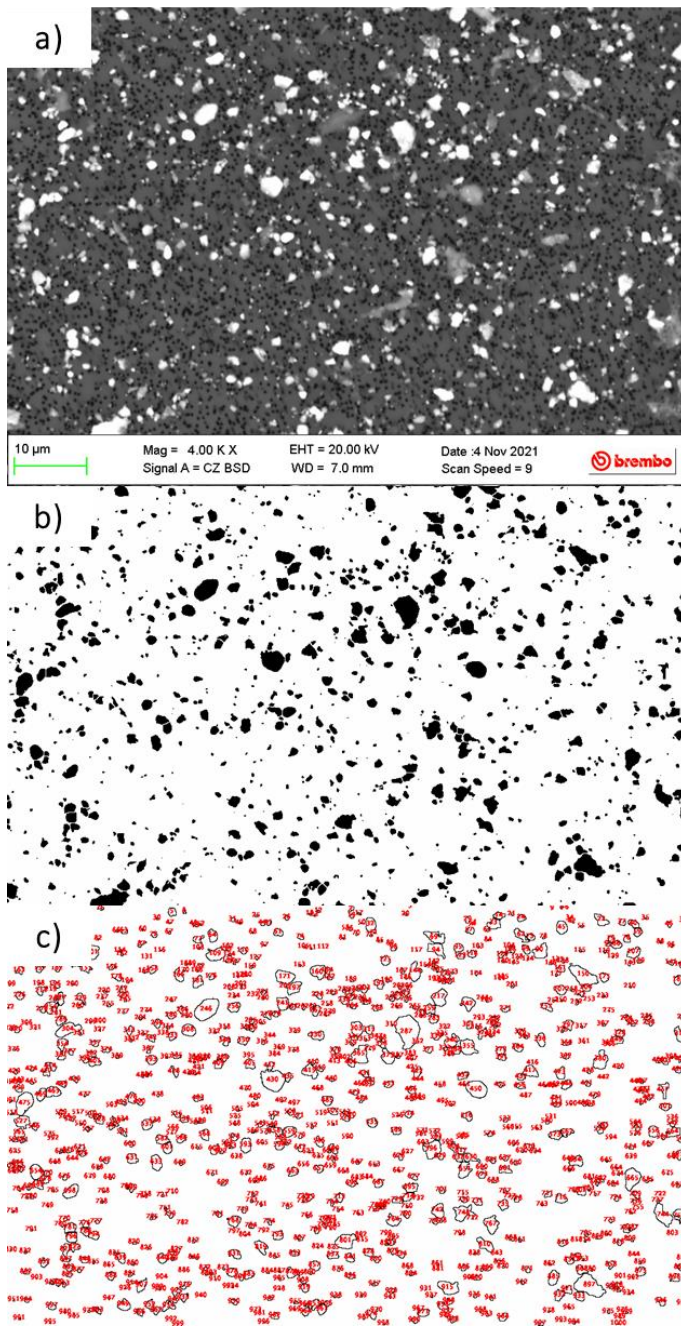


Figure 2.7: SEM-Image Analysis procedure; **a)** acquisition of SEM image; **b)** Binarization; **c)** Particle recognition and analysis.

## 2.5b. Particle Size Distribution – Laser Diffraction Analysis

The granulometry of the Debris samples is investigated in terms of Particle Size Distribution (PSD), via Laser Diffraction (LD) analysis. The technique is applied to those samples, since they are typically collected in far higher amount in respect with the PM<sub>10</sub> counterparts. The LD measurements are carried out by the mean of the Fritsch *Analysette 22 NanoTec Plus* laser particles sizer, equipped with one infrared and two green lasers. Previously to the measurements the instrument is calibrated with standard reference materials, in the dimensional range of interest (0.01 – 500 μm). For each sample, at least 10 mg of Debris powder are necessary to perform a single repetition of analysis. For each sample, three measurement repetitions are carried out and averaged. The analysis is performed in wet media (water), prior suitable stabilization of the suspension by the mean of the addition of diluted solution of surfactants (Triton X). Debris powders are dispersed and suspended in water via sonication and the final PSD profile is calculated using on the basis of Fraunhofer model.<sup>[13]</sup>

## 2.6. X-Ray Diffraction (XRD) Analysis

X-Ray Diffraction (XRD) analysis is used as probe to investigate the phase composition of the crystalline fraction of the collected particulates. The analysis is performed directly on the samples as collected, without any further manipulation. Collection filters are mounted over an polycarbonate hollow filter-holder, in order to avoid any possible spurious contribution from the sample-holder itself in the collected diffraction patterns. The major part of the reported XRD measurements are carried out by the mean of the *Rigaku SmartLab* diffractometer, equipped with a 9 kW rotating anode and Copper target ( $K_{\alpha 1Cu} = 0.154$  nm), as shown in Figure 2.8. For all the measurements, the maximum available power is used ( $V = 45$  kV,  $I = 200$  mA) and the 5-90° 2θ angular range is typically investigated in Bragg-Brentano configuration, with scan steps of 0.02°. The collected particulates are measured with scan speed ranging between 0.025°/min and 0.1°/min, depending on the amount of sample deposited on filters (14 up to 56 h of measurement), aiming to collect at least 1000 counts for the most intense diffraction peaks observed. All the samples are spinned during the acquisition at the speed of 20 rpm in order to limit eventual preferential orientation effects. The phase identification and analysis are performed by the mean of the ICDD PDF4+ 2022 crystallographic database and the Rigaku PDXL 2 software.<sup>[14,15]</sup> The list of the crystallographic references selected for the phase identification and analysis is reported in the *Annex 2*. Phase analysis and quantification are performed only on those samples exhibiting XRD patterns with minimum intensity of 1000 counts on the most intense peaks. When this condition is not fulfilled due to the low amount of material collected on the collection substrate, then only the phase identification is performed.

Phase analysis is carried out by means of Whole Powder Pattern Fitting (WPPF) method [16], using as refinement variables zero and scale parameters, lattice parameters, profile parameters, crystal structures and preferential orientation factors.

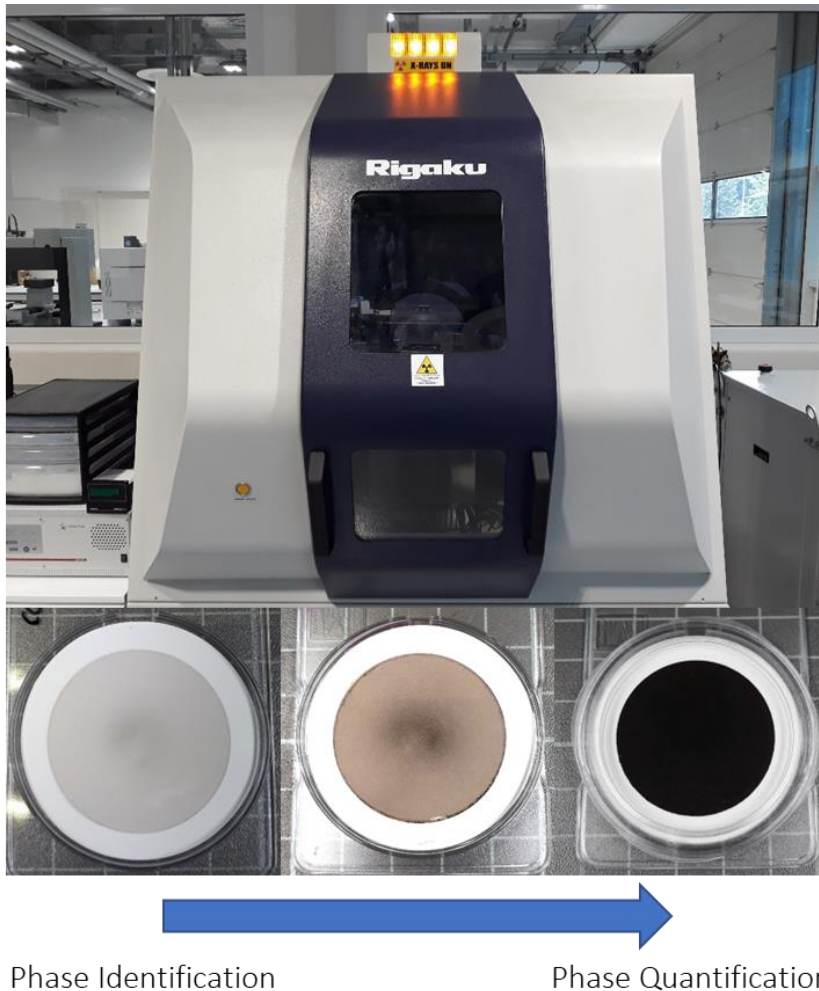


**Figure 2.8:** XRD analysis performed on laboratory diffractometer directly on the collected samples, without any additional manipulation. Depending on the amount of material collected on the filters, different levels of analysis are possible.

A minor part of the XRD analysis reported in the following studies were carried out at MCX beamline<sup>[17]</sup> of the ELETTRA synchrotron during ring operation at 2.4 GeV (Figure 2.9). XRD patterns are acquired at 15 keV and  $\lambda = 0.0826(1)$  nm, in Debye-Scherrer geometry, with beam spot kept at 1.0 x 0.3 mm. About 1 mg of PM<sub>10</sub> powders are gently inserted and compacted inside standard glass Mark-tube for XRD diffraction



experiments with external diameter of 0.2 mm and wall thickness of 0.01 mm (Hilgenberg™), filling the capillaries for at least 15 mm in height. The capillaries are centered inside a 4-circle Huber goniometer and spun at 3000 rpm during the measurements. The detection of the diffracted beam is carried out by a high-count rate fast scintillator counter equipped with a pair of slits with a vertical aperture of 0.3 and 0.4 mm, respectively. XRD patterns are acquired in the  $2\theta$  angular range of 3-45°, with 0.01° steps and acquisition speed of 1 sec/step. Phase identification and quantification are performed following the same protocol as described for laboratory XRD measurements.

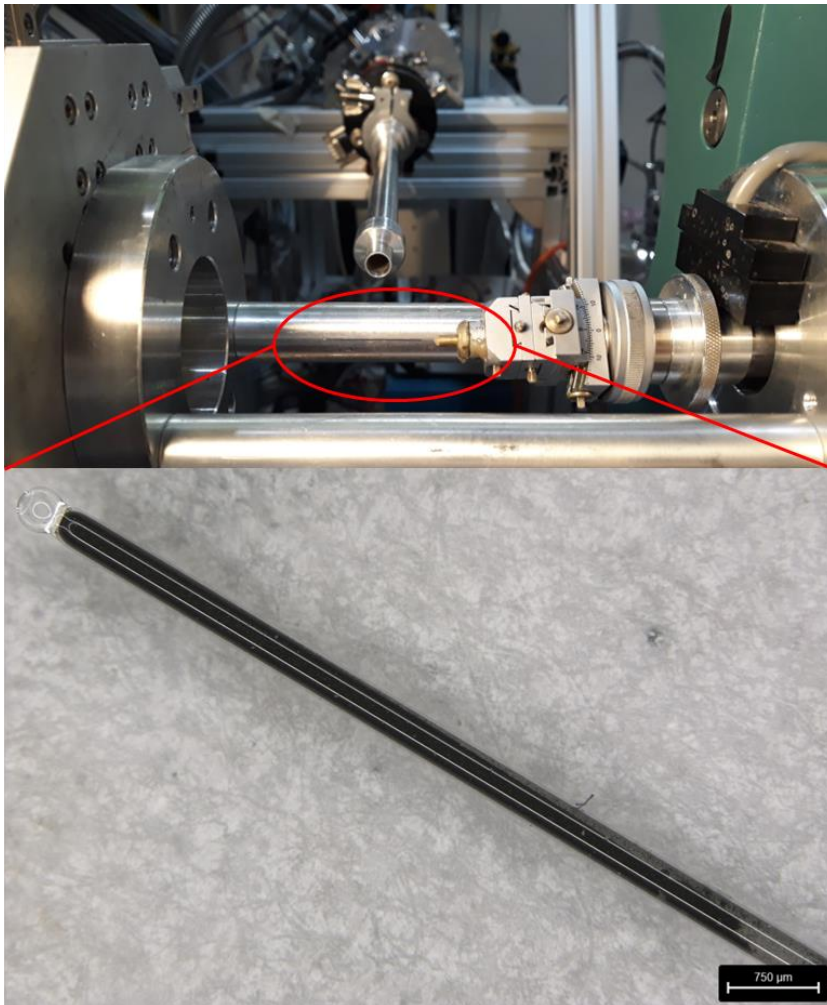


**Figure 2.9:** XRD analysis performed at the MCX beamline of ELETTRA Synchrotron.  $\text{PM}_{10}$  samples are prepared in capillary for the analysis.

## 2.7. X-Ray Absorption Near-Edge Structure (XANES) Analysis

XANES analysis is used as probe to investigate the oxidation state of several *d-block* metals of environmental and biological interest and assess their speciation. In particular, X-Ray Absorption spectra are acquired at the K-edge of the following metals: Ti (4966.4 eV), V (5465.1 eV), Cr (5989.2 eV), Mn (6539.0 eV), Fe (7112.0 eV), Cu (8978.9 eV) and Zn (9658.6 eV). The measurement of the selected K-edges was carried out in the UHV chamber<sup>[18]</sup> available at the XRF beamline<sup>[19]</sup> at the ELETTRA Synchrotron in two different experiments. PM<sub>10</sub> samples are inserted directly into the measurement system as collected, without any particular manipulation except of covering them with a thin layer of transparent polycarbonate film in order to avoid the loss of powder inside the high vacuum chamber (Figure 2.10).

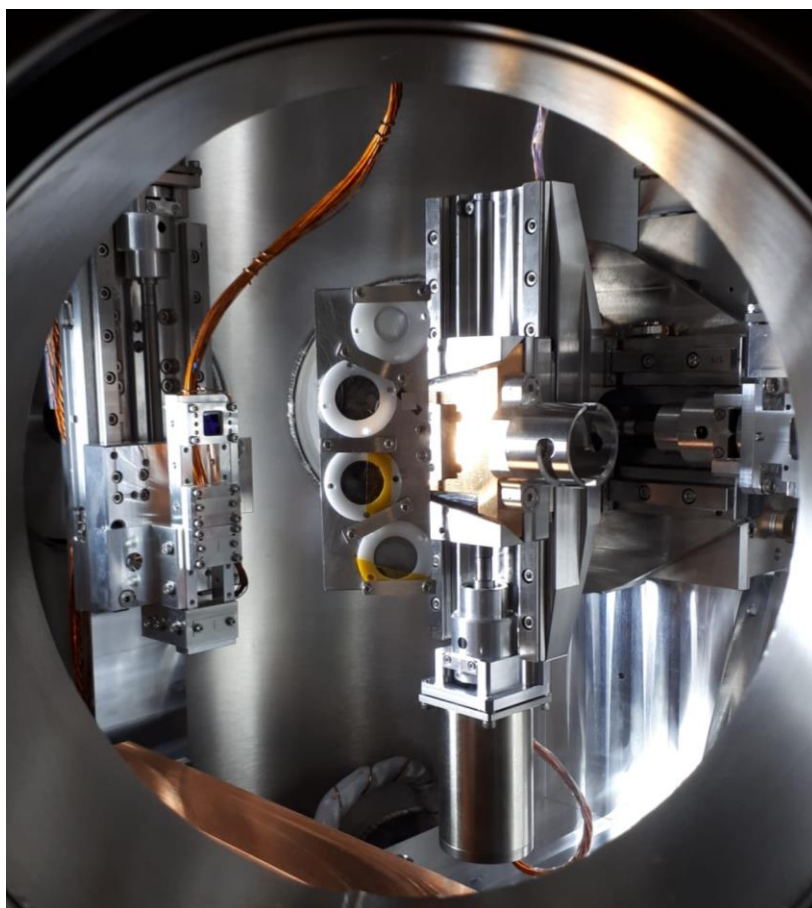


**Figure 2.10:** PM<sub>10</sub> samples inside the measurement chamber at the XRF beamline of ELETTRA Synchrotron.

The raw data are processed using the procedures reported in Reference [20] for XAFS data treatment including: *i)* pre-edge background subtraction, *ii)* post-edge bare ion model definition; and *iii)* edge jump normalization. The data analysis is performed in two following steps. First, a qualitative evaluation is performed by the mean of direct comparison of the experimental XAS spectrum of a specific elements with those from reference standard compounds of the same elements. When acceptable matching is found, Linear Combination Fit (LCF) analysis is carried out with the best matching standard compounds profiles in order to assess the relative abundance of the oxidation states. Data treatment and analysis are performed by the mean of the Athena software.<sup>[21]</sup>

## 2.8. Raman Spectroscopy

Raman Spectroscopy (RS) is used in order to obtain some information on the phase composition of the collected emissions when the ultra-fine particulates (UFP:  $d < 100\text{nm}$ ) are investigated. Raman analysis is carried out by the mean of the Horiba LabRAM HR, equipped with a solid-state laser source ( $\lambda = 473 \text{ nm}$ ), as shown in Figure 2.11. The analysis is carried out directly on the collected samples, without any preventive manipulation needed. The laser power is set nominally to 12.5 mW, since higher power values are frequently found to damage the samples, leaving burnt micro-area after the measurements. All the spectra are acquired with the 50x objective, which is found to be the best magnification in order to maximize the signal to noise ratio. The acquisition range is typically set in the range of  $50\text{-}2000 \text{ cm}^{-1}$ , and the high intensity grating ( $600 \text{ gr mm}^{-1}$ ) is used to maximize the collected signal. For each spectrum, five to ten acquisition integrations of 10-30 sec are merged together along the whole investigated frequency range, to obtain suitable signal to noise ratios.



**Figure 2.11:** Raman spectrometer used for the characterization of the phase composition in UFP samples.

The Raman probe is chosen after the X-Ray Diffraction (XRD) analysis for the assessment of samples exhibiting low degree of long-range order (*i.e.* nano-particulates) which are collected in very low amounts. The reason for this choice is to overcome the two main limitations of the XRD probe as an analytical probe, which are: *i)* the insensitivity to amorphous materials; and *ii)* the relatively low detection limits, most of all when low amounts of material are available. The phase identification is performed by direct comparison with standard reference spectra in the RRUFF database.<sup>[22]</sup>

## References

- [1] M. Alemani, "Particle Emissions from Car Brakes: the Influence of Contact Conditions on the Pad-to-Rotor Interface", Doctoral Thesis, KTH - Machine Design Dept., **2017**.
- [2] G. Perricone, "Laboratory Measurements of Airborne Emissions from Car Brakes for Clean Air", Doctoral Thesis, KTH - Machine Design Dept., **2020**.
- [3] J.D. Preston, "Inertia Dynamometer Evaluation of Brake Lining Materials", *SAE Transactions*, 82(1): **1973**, 755-761.
- [4] P.G. Sanders, T.M. Dalka, N. Xu, M.M. Maricq, R.H. Basch, "Brake Dynamometer Measurement of Airborne Brake Wear Debris", *SAE Transactions*, 111(6), **2002**, 1693-1699.
- [5] G. Perricone, V. Matějka, M. Alemani, G. Valota, A. Bonfanti, *et.al.*, "A Concept for Reducing PM10 Emissions for Car Brakes by 50%", *Wear*, 396-397, **2018**, 135-145, doi: <http://dx.doi.org/10.1016/j.wear.2017.06.018>.
- [6] G. Perricone, M. Alemani, I. Metinoz, V. Matejka, *et.al.*, "Towards the Ranking of Airborne Particle Emissions from car Brakes – a System Approach", *Proc. I. Mech. E., Part D: J. Automobile Engineering*, **2016**, 1-17, doi: [10.1177/0954407016662800](https://doi.org/10.1177/0954407016662800).
- [7] G. Perricone, J. Wahlstrom, U. Olofsson, "Towards a Test Stand for Standardized Measurements of the Brake Emissions", *Proc. I. Mech. E., Part D: J. Automobile Engineering*, **2015**, 1-8, doi: [10.1177/0954407015616025](https://doi.org/10.1177/0954407015616025).
- [8] Particle Measurement Programme (PMP) Informal Working Group, Informal document GRPE\_81\_12, 81st GRPE, 9-11 June **2020**, Agenda Item 7.
- [9] M. Mathissen, J. Grochowicz, C. Schmidt, R. Vogt, *et.al.*, "WLTP-based Real World Brake Wear Cycle", *Mendeley*, **2019**, doi: [10.17632/dkp376g3m8.1](https://doi.org/10.17632/dkp376g3m8.1).
- [10] M. Mathissen, C. Evans, "Lowbrasy Brake Wear Cycle – 3h LACT", *Mendeley*, **2019**, doi: [10.17632/4cgs6myx9d.1](https://doi.org/10.17632/4cgs6myx9d.1).
- [11] D.E. Newbury, N.W.M. Ritchie, "Performing Elemental Microanalysis with High Accuracy and High Precision by Scanning Electron Microscopy/Silicon Drift Detector Energy-Dispersive X-Ray Spectrometry (SEM/SDD-EDS)", *J. Mater. Sci.*, 50, **2015**, 493-518, doi: [10.1007/s10853-014-8685-2](https://doi.org/10.1007/s10853-014-8685-2).
- [12] J. Schindelin, I. Arganda-Carreras, E. Frise, V. Kaynig, M. Longair, *et.al.*, "Fiji: an open-source platform for biological-image analysis", *Nature Methods*, 9(7), **2012**, 676-682, doi: [10.1038/nmeth.2019](https://doi.org/10.1038/nmeth.2019).

- [13] G.B.J. de Boer, C. de Weerd, D. Thoenes, N.W.J. Goossens, H. W. J., "Laser Diffraction Spectrometry: Fraunhofer diffraction versus Mie scattering", *Particle Characterization*, 4(1-4), **1987**, 14-19, <https://doi.org/10.1002/ppsc.19870040104>.
- [14] S. Gates-Rector, T. Blanton, "The Powder Diffraction File: a Quality Materials Characterization Database", *Powder Diff.*, 34(4), **2019**, 352-360.
- [15] Rigaku, "PDXL Software", ver. 2.8.4.0, **2018**.
- [16] H. Toraya, "Whole Powder Pattern Fitting Without Reference to a Structural Model: Application to X-Ray Powder Diffraction Data", *J. Appl. Cryst.*, 19(6), **1986**, 440-447, <https://doi.org/10.1107/S0021889886088982>.
- [17] L. Rebuffi, J.R. Plaisier, M. Abdellatif, A. Lausi, A., et. al., "MCX: a Synchrotron Radiation Beamline for X-Ray Diffraction Line Profile Analysis", *Z. Anorg. Allg. Chem.*, 640, **2014**, 3100-3106, [doi:10.1002/zaac.201400163](https://doi.org/10.1002/zaac.201400163).
- [18] A. Germanos Karydas, M. Czyzycski, J.J. Leani, A. Migliori, J. Osan, "An IAEA Multi-Technique X-ray Spectrometry Endstation at Elettra Sincrotrone Trieste: Benchmarking Results and Interdisciplinary Applications", *J. Synchrotron Rad.*, 25, **2018**, 189-203, [doi: 10.1107/S1600577517016332](https://doi.org/10.1107/S1600577517016332).
- [19] W. Jark, D. Eichert, L. Luehl, A. Gambitta, "Optimisation of a Compact Optical System for the Beamtransport at the X-Ray Fluorescence Beamline at Elettra for Experiments with Small Spots", *Proceedings of SPIE*, 9207G, **2014**, [doi: 10.1117/12.2063009](https://doi.org/10.1117/12.2063009).
- [20] G. Bunker, "Introduction to XAFS", **2010**, Cambridge University Press.
- [21] B. Ravel, M. Newville, "ATHENA, ARTEMIS, HEPHAESTUS: Data Analysis for X-ray Absorption Spectroscopy Using IFEFFIT", *Journal of Synchrotron Radiation*, 12, **2005**, 537-541, [doi:10.1107/S0909049505012719](https://doi.org/10.1107/S0909049505012719).
- [22] B. Lafuente, R.T. Downs, H. Yang, N. Stone, "The Power of Databases: the RRUFF Project", in *Highlights in Mineralogical Crystallography*, T. Armbruster, R.M. Danisi, eds. Berlin, Germany, W. De Gruyter, **2015**, 1-30.

### 3. Reproducibility Studies

*Reproducible generation, collection and physico-chemical characterization of brakes emissions are necessary when comparing particulates generated by different friction couples, brake designs or driving conditions. Furthermore, they are pivotal in order to provide reliable chemical information for source apportionment studies as well as for toxicological and environmental assessments. Non-exhaust particulates generated by brakes are nowadays commonly collected at suitably designed variable inertia dynamometer benches, during selected braking test cycles in controlled conditions to avoid other contributions from the environment. In spite of being simplified models of a single real car semi-axis corner, dynamometric benches for brakes emissions collection still remain elaborate mechanical devices used for testing complex materials. Such systems, when not carefully set and calibrated, can generate highly variable particulates: if the tribological interaction is not kept constant over different tests, significantly different local forces and temperatures might be expected at the tribological interface. This can eventually result in the generation of particulates with different granulometry and chemical composition, even if originated by the same braking device components. Similarly, a good level of reproducibility in the chemical composition of brakes emissions generated at different test benches is needed in order to assure that different laboratories can provide univocal information. At this regard, the work here presented explores for the first time the capability of a brake dynamometer bench dedicated to emission tests to generate reproducible particulates. More in detail, the assessment of both intra bench reproducibility over an extended period of time and inter bench reproducibility between three different dynamometers are discussed. The reported results are meant to provide a critical assessment on the variability of both the size distribution and the chemical composition of the emissions generated by brakes in the controlled environments typically used for their generation, measurements and collection.*

#### 3.1. Aim of the Study

Brakes dynamometer benches are mechanical devices simulating a braking corner for a selected application. They are able to recreate the inertia and the speed, *i.e.* the kinetic energy, of a target vehicle and are usually programmed in order to perform a predetermined sequence of brake events, composing a braking cycle to mimic specific driving conditions. Therefore, their main advantages are: *i)* the lowest level of complexity in respect to a real vehicle; *ii)* the capability of generating and withstanding energies comparable to those developed by real vehicles (differently from other tribometers such as the Pin-on-Disc benches); *iii)* the possibility of operating in laboratory controlled conditions, therefore strongly limiting environmental variables;

and *iv*) an elevated degree of automation.<sup>[1-3]</sup> They have been historically used in the brake industry to test brakes performances and comfort (*i.e.* noise and vibration), during both the development and the validation phases in the production of new brakes.<sup>[4-7]</sup> In the recent past, they have been progressively used more and more frequently also for fundamental studies, mainly related to tribology and emissions topics.<sup>[8-10]</sup> In particular, they have been widely employed to generate brakes emissions with the aim of characterizing the emission factors of automotive disc brake systems.<sup>[11-18]</sup> At this regard, they are expected to become an even more fundamental tool in the development and certification of brake solutions targeting low emission levels in the next future. Nowadays, they are also used more frequently as tool to collect sufficient amounts of brakes emissions for environmental assessment and toxicological studies.<sup>[19-23]</sup> For all these reasons, referring to a specific friction couple, the generation of brake particulate and its physico-chemical characteristics have to be assured as constant and stable as possible over time and different testing benches or laboratories. Indeed, a good level of reproducibility in the generation and the collection of brakes emissions is fundamental to obtain reliable and univocal information on both the emission factors and the chemical composition of particulates generated by brakes. However, in spite of being simplified models of single braking corners, variable inertia dynamometric benches still remain complex mechanical devices testing heterogeneous materials. They have to be properly set and calibrated to ensure optimal working: indeed, if the tribological interactions are not kept constant over different tests performed on the same components, significantly different local forces and temperatures might be expected at the tribological interface, possibly leading to the generation of different amounts of particulates exhibiting different granulometries and chemical compositions. In addition, other levels of complexity to be taken into account in the case of emission tests carried out at the dynamometric bench are the laboratory environment as well as the collection devices, which have to assure constant sampling efficiency and reproducibility. For all these reasons, this chapter is meant to provide detailed insights into the topic of the reproducibility of brakes emissions physico-chemical characteristics, such as their elemental composition, phase composition and granulometry. More in detail, both *intra bench* variability over extended period of time and *inter benches* variability over three different test platforms are investigated and discussed in the next paragraphs. Thus, the study reported here is meant to provide a critical assessment on the reproducibility of both the size-distribution and the chemical composition of the emissions generated by brakes in controlled environments typically used for their generation, measurements and collection. Therefore, the final aim of this section is to understand if statistically limited number of independent observations can be used in order to: *i*) draw general comparative assessments between particulates generated from different materials composing the friction couple or particulates obtained in different braking conditions;

and *ii*) obtain univocal chemical information as input for source apportionment, environmental and toxicological studies, when assessing a specific brake emission.

### 3.2. Experimental

The next paragraphs briefly describe all the experimental details of interest for the reported study. In particular, description of the starting materials, the collection procedures, the different test bench and a short summary of the adopted analytical protocol are provided. More detailed description of the procedures for the sample preparation and the physico-chemical analysis can be found in *Chapter 2: Experimental*.

#### 3.2.1. Materials

The friction couple used for this investigation is composed by a full pearlitic gray cast-iron (GCI) braking disc (BD) and a Low-Steel (LS) and Copper-free friction material (FM) compliant with the ECE R90 regulation. The nominal elemental composition of the cast-iron, as well as of the selected friction material, is reported in Table 3.1.

GCI BD		LS FM	
Element	wt%	Element	wt%
C	3.7	C	50.8
Si	1.9	O	22.3
Mn	0.5	Mg	4.3
Cu	0.2	Al	2.3
Cr	0.1	Si	1.1
Fe	<i>balance</i>	S	1.9
Others	<i>traces</i>	Ca	0.7
		Cr	1.1
		Fe	11.6
		Zn	0.7
		Sn	2.9
		Others	<i>traces</i>

**Table 3.1:** Summary of the nominal elemental composition of the materials composing the friction couple. Elements with concentration lower than 0.1 wt% are not reported for sake of brevity.

#### 3.2.2. Samples Collection and Experimental Design

Emission samples are collected on suitable substrates in form of PM<sub>10</sub> particulates at variable inertia dynamometric benches designed for emissions collection during tests performed in controlled conditions at three different testing platforms. The three benches are labeled as **B1**, **B2** and **B3** along the next paragraphs. More in detail, the particulates are sampled during the execution of the Worldwide harmonized Light-duty vehicles Test Procedure for brakes, namely WLTP-Brake cycle, featuring 303 brake



events divided into ten different sectors. The emission test duration is about 7.5 hours, comprehensive of the cooling phases between different sections.<sup>[24]</sup> For all the performed tests, the braking corner is composed by: *i)* a four pistons fixed Aluminum caliper, with pistons diameter of 44 mm; *ii)* a vented braking disc with diameter of 342 mm and thickness of 32 mm; and *iii)* a couple of brake pads with surface of 89.1 cm<sup>2</sup>. Tests are performed with inertia of 72.67 kg m<sup>2</sup>.

The *intra bench* variability study is performed on the **B1** test platform, located at the Testing Department of Brembo, which is also the one used for the generation and the collection of the vast majority of the particulates investigated in the entire thesis. A more detailed description of this bench can be found in *Chapter 2*. The *inter bench* variability study is carried out comparing particulates coming also from the other two dynamometric benches. In particular, **B3** platform is an updated and upgraded version of **B1** bench, recently arrived and installed at the same department of Brembo. Finally, **B2** platform is located in the testing laboratory of another company, market leader for the production of braking pads.

As far as the **B1** platform is concerned, during the emission test, a controlled particle-free air flux of 65 m<sup>3</sup> h<sup>-1</sup> enters the brake enclosure in order to fulfill the temperature targets, as suggested by the more recent guidelines from the Particle Measurement Programme (PMP) Informal Working Group<sup>[25]</sup>, prior a specifically tailored calibration run carried out before the bedding phase. The air flux is filtered through a HEPA-H13 filter which ensures an average filtration efficiency higher than 99.95%, while all the bench ensemble is kept in controlled environment at temperature of 20°C and relative humidity of 50%. The collection of the PM<sub>10</sub> emissions is carried out by an isokinetic sampling-probe, equipped with sharp edged nozzles to ensure a high efficiency sampling. This sampling line ends into a filter holder which hosts a high efficiency cellulose filter (diameter = 47 mm, pores < 0.20 µm), which collects together all the particles with aerodynamic diameter lower than 10 µm thanks to dimensional selection carried out by a cyclone. **B2** platform differs from the **B1** counterpart in the two following main features: *i)* the air is taken prior HEPA-H13 filtration directly from indoor but not from controlled environment, with temperature and relative humidity parameters possibly varying respectively in the 18-25°C and 40-60% ranges; and *ii)* PM<sub>10</sub> particulate is collected on a 47 mm filter located inside an eFilter™ (Dekati) instrument for the determination of the particulate mass. Finally, **B3** test platform differs from the **B1** counterpart for the volume of the enclosure surrounding the braking corner. In particular **B1** enclosure has volume approximately three times higher in respect with **B3**. Due to this, air flux in **B3** is increased to the value of 350 m<sup>3</sup> h<sup>-1</sup> in order to obtain suitable cooling to match the temperature requirements of the WLTP-Brake cycle. In addition, another slight difference in **B3** is the orientation of the caliper in respect to the air flux,

which is optimized for the specific aerodynamic of the enclosure. For all the other relevant features, including sampling probes and measurement devices, **B1** and **B3** platforms are closely similar.

### 3.2.3. Analytical Protocol

The obtained samples are analyzed in order to characterize their granulometry and chemical composition by the mean of different techniques. In particular, the elemental composition of the collected PM<sub>10</sub> samples is investigated by the mean of the Energy Dispersive X-Ray Spectroscopy (EDXS) probe, following the procedures already described in *Chapter 2*. The phase composition of the crystalline fraction of the investigated emissions is evaluated by the mean of X-Ray Diffraction (XRD) and the phase quantification is carried out by means of the Whole Powder Profile Fitting (WPPF) method. Finally, the granulometry of the collected material is investigated by the mean of Scanning Electron Microscopy Image Analysis (SEM-IA). XRD analysis is carried out directly on the collection filters, without any further manipulation of the samples. Conversely, SEM/EDXS/IA analysis are performed after suitable sample preparation. More in detail, the collected PM<sub>10</sub> powders are stripped from the collection substrates by sonication in 5 mL of isopropyl alcohol at 35 kHz for 10 minutes. The suspended particles are then recollected by centrifugation at 3000 rpm for 3 minutes and finally dried overnight in mild vacuum conditions (20 mbar) before the analysis. When analyzed for the elemental composition, the free emission powders are deposited well compacted on carbon-tape for electron microscopy analysis. Conversely, when image analysis is performed, 1 mg of emission powder is resuspended in isopropyl alcohol via sonication and then deposited on polycarbonate filters by mean of a micro-pipette in order to maximize the dispersion of the particles on the substrate.

## 3.3. Intra Bench Assessment

This paragraph describes in detail the study of the variability of PM<sub>10</sub> particulates granulometry and chemical composition generated on the **B1** test platform over an extended period of time and a significant number of tests. The results here reported are meant to sustain and corroborate the validity of the comparative assessments of emissions generated from different starting materials and in different driving (*i.e.* braking) conditions, which are discussed in the next chapters.

### 3.3.1. Investigation Design

The selected friction couple is tested fourteen times in three distinct test blocks over a period of six months. Both the BDs and the FMs are picked from a unique production batch and each emission test is performed starting with new components, following all the guidelines from the PMP Informal Working Group.<sup>[25]</sup> Each test

generates one particulate sample collected on 47 mm diameter cellulose filter (labeled as PM<sub>10</sub>-*n*). As summarized in Table 3.2, ten samples are used for the chemical analysis (EDXS and XRD), while four samples are used for the assessment of the particle size distribution (PSD) via image analysis (IA).

Block 1				Block 2						Block 3			
Months 1-2				Months 3-4						Months 5-6			
PM <sub>10</sub> -1	PM <sub>10</sub> -2	PM <sub>10</sub> -3	PM <sub>10</sub> -4	PM <sub>10</sub> -5	PM <sub>10</sub> -6	PM <sub>10</sub> -7	PM <sub>10</sub> -8	PM <sub>10</sub> -9	PM <sub>10</sub> -10	PM <sub>10</sub> -11	PM <sub>10</sub> -12	PM <sub>10</sub> -13	PM <sub>10</sub> -14
EDXS	EDXS	-	EDXS	EDXS	-	EDXS	EDXS	-	EDXS	EDXS	EDXS	-	EDXS
XRD	XRD	-	XRD	XRD	-	XRD	XRD	-	XRD	XRD	XRD	-	XRD
-	-	IA	-	-	IA	-	-	IA	-	-	-	IA	-

**Table 3.2:** Summary of the collected samples and corresponding performed characterizations.

### 3.3.2. Elemental Composition

Figure 3.1 reports the elemental distribution as observed for the PM<sub>10</sub>-1 sample as representative example for all the analyzed particulates, while all the measured elemental concentrations are reported in *Annex 3*.

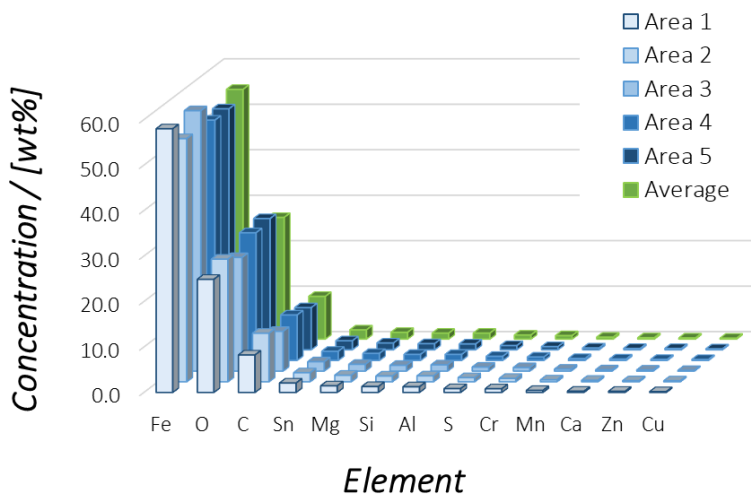


**Figure 3.1:** Elemental distribution in PM<sub>10</sub>-1 sample. Blue histograms represent the distributions obtained in the five measured areas, while the green histogram is the average of the independent observations.

For each particulate, five independent observations are carried out, and their average values are reported together with the corresponding standard deviations along this chapter. As can be observed in Figure 3.1, the particulate generated by the selected FC (GCI BD + LS FM) is mainly composed by three dominant elements: Iron, Oxygen and

Carbon. They account together for about the 90% of the total particulate mass. The remaining 10% is composed by a wide dispersion of secondary elements, which are found in minor amounts (typically between 2 and 0.01 wt%). As can be guessed by looking at the nominal composition of the materials composing the friction couple (Table 3.1), Iron likely arises preferentially from the wear and the tribo-oxidation of the brake disc. However, significant contribution can be due to the friction material, too. Similarly, Oxygen has double origin: for sure, part of it arises from the consumption of the friction material, and more in detail from inorganic oxides, alumino-silicates, carbonates, *etc.*, typically used as fillers or abrasives; on the other side, significant amount of Oxygen can be expected to be due to the tribo-oxidation occurring at the interface between BD and FM. Carbon, represents a more specific marker for the consumption of the friction material, since it is largely contained in form of organic binders (phenolic resins), elemental fraction (Graphite and Cokes as solid lubricants) and inorganic compounds (such as carbides and carbonates, respectively used as abrasives and fillers). However, a minor but not negligible contribution from the Graphite of the BD grey cast-iron has also to be taken into account. Finally, secondary and trace elements are mainly due to the consumption of the friction material, with only few exceptions. In particular, among these elements, only Si, Cr and Cu can be due to the consumption of both BD and FM.

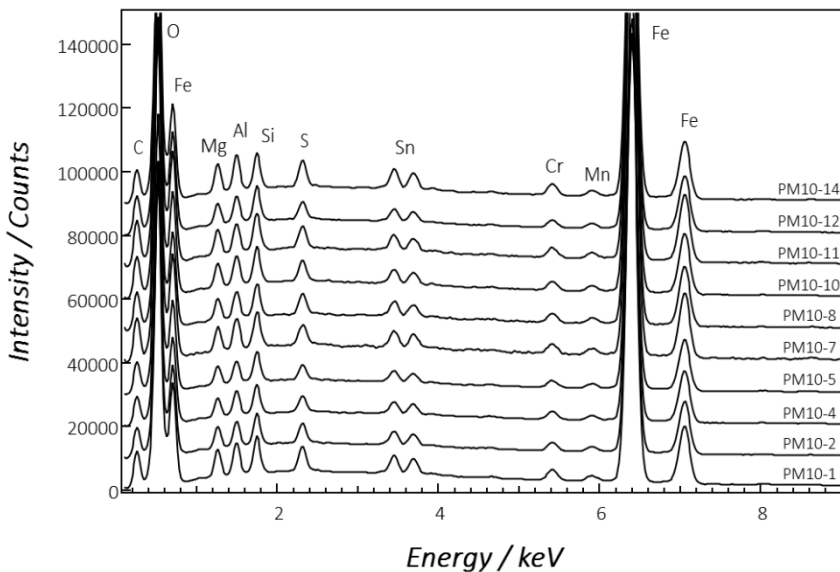


**Figure 3.3:** Elemental distribution over the ten investigated PM<sub>10</sub> samples.

Figure 3.2 shows one EDXS spectrum for each investigated particulate. In addition, Table 3.3 and Figure 3.3 summarize the elemental concentration and distribution of the main constituents of the collected particulates, *i.e.* Fe, O, C and the sum of all the other elements (labeled as “Others” from here to the end of the chapter).

wt%	1	2	4	5	7	8	10	11	12	14	Av.	SD	v%
Fe	54.9	55.3	56.1	55.1	53.9	54.9	55.3	54.1	54.7	54.6	54.6	1.8	3.3
O	26.8	27.3	26.6	27.7	27.6	28.0	27.0	27.9	27.5	27.5	27.4	1.2	4.4
C	9.4	9.4	9.7	10.1	10.8	9.9	10.1	10.5	11.0	9.6	10.1	0.8	7.9
Others	8.9	8.0	7.6	7.1	7.7	7.2	7.6	7.5	6.9	8.2	-	-	-

**Table 3.3:** Summary of the measured elemental concentrations for the main constituents. Concentrations values are expressed in wt%. **Av.** = average; **SD** = standard deviation; **v%** = percentage variability. Since it is an aggregated data, statistical parameters of **Others** are not evaluated in this section.

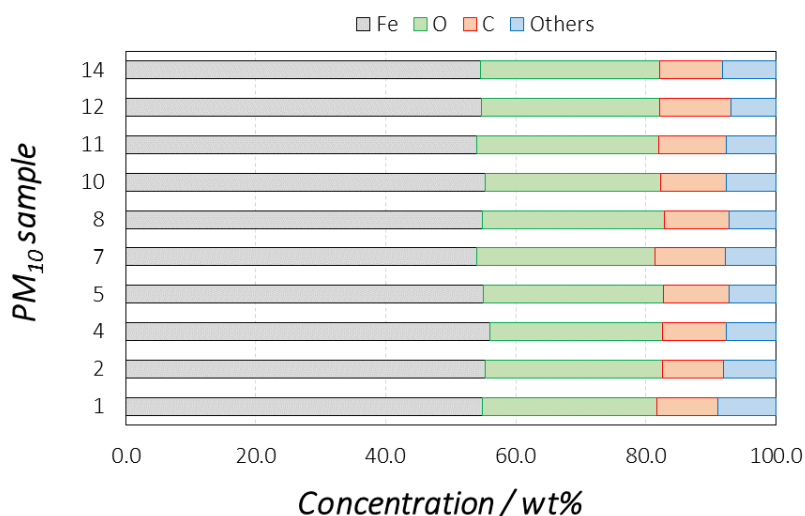


**Figure 3.3:** Elemental distribution over the ten investigated PM<sub>10</sub> samples.

As can be qualitatively observed, the overall variability of the main components along the different tests is limited. Consequently, their relative abundance within the particulates remain stable and reproducible along all the tests. For sake of a more detailed and statistical evaluation, box plots reporting the comparison of the measured concentrations for all the investigated particulates are also showed in Figure 3.4. In addition, Anova assessment of the average elemental concentrations is proposed in the following tables 3.4-3.6 for Iron, Carbon and Oxygen. As can be observed from all the reported data, no statistical differences are found in the case of the Iron and Oxygen concentrations. These two elements exhibit overall variability well below the 5% of their global average concentrations. Conversely, modest statistical differences in the Carbon concentrations are highlighted by the corresponding Anova analysis. However, the observed differences are extremely limited, with overall variability representing approximately the 8% of the global average concentration.

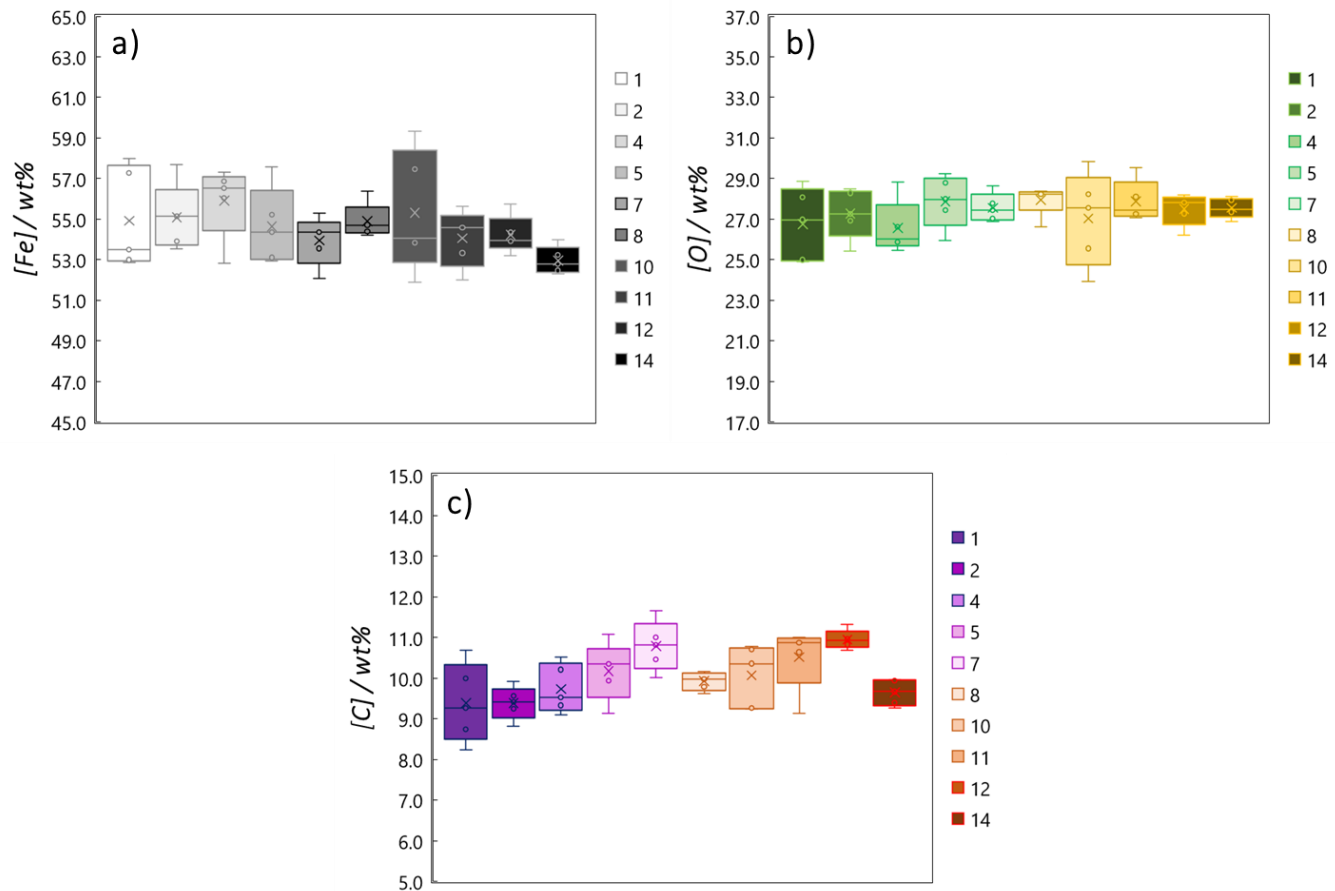


**Figure 3.4:** Box plots for the comparison of the elemental concentrations measured for the ten investigated PM<sub>10</sub> samples. **a)** Iron; **b)** Oxygen; **c)** Carbon.

ANOVA Test Table - Iron						
Variation Source	Sum Sq	DF	Mean Sq	F-Value	P-Value	F-Crit
Between	31.315	9	3.479	1.150	0.352	2.124
Within	120.999	40	3.025			
Total	152.314	49				

**Table 3.4:** One way ANOVA test table for Iron concentrations. Since F-Value parameter is found lower than the F-Critic value, the stated hypothesis (Fe concentrations statistically equivalent along all the particulates) is accepted.

ANOVA Test Table - Oxygen						
Variation Source	Sum Sq	DF	Mean Sq	F-Value	P-Value	F-Crit
Between	10.454	9	1.162	0.704	0.701	2.124
Within	65.950	40	1.649			
Total	76.403	49				

**Table 3.5:** One way ANOVA test table for Oxygen concentrations. Since F-Value parameter is found lower than the F-Critic value, the stated hypothesis (O concentrations statistically equivalent along all the particulates) is accepted.

ANOVA Test Table - Carbon						
Variation Source	Sum Sq	DF	Mean Sq	F-Value	P-Value	F-Crit
Between	13.760	9	1.529	4.038	0.000973	2.124
Within	15.144	40	0.379			
Total	28.904	49				

**Table 3.6:** One way ANOVA test table for Carbon concentrations. Since F-Value parameter is found higher than the F-Critic value, the stated hypothesis (C concentrations statistically equivalent along all the particulates) is rejected.

Looking more in detail at the other elements, it is possible to appreciate a similar situation in respect with the main constituents. With only few exceptions, all the secondary elements qualitatively exhibit overall stable and constant concentrations in all the investigated particulates, as can be observed in Figure 3.5 and Table 3.7. However, with the only exception of Mg, all the other secondary elements are found to exhibit one average concentration statistically different along the ten investigated particulates at the ANOVA evaluation. Nevertheless, the vast majority of these secondary elements exhibits extremely limited variability, well below the 10%. The only elements exceeding this value is Sn, with relative variability approximately around the 12%, therefore being the element with the overall lower degree of reproducibility in the *intra* bench assessment here reported.

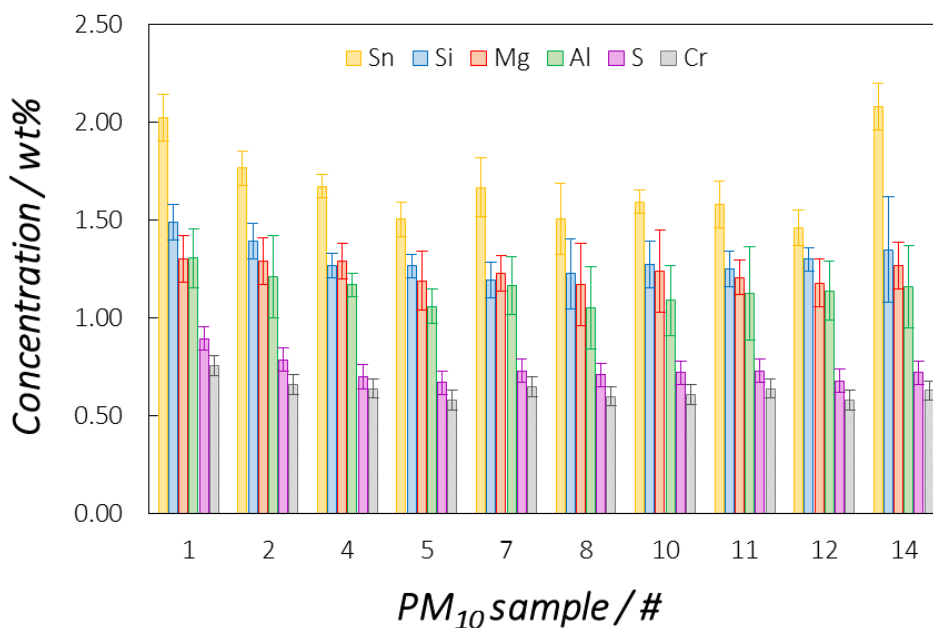


**Figure 3.5:** Average elemental concentrations in wt% of secondary and minor elements in the investigated particulates. Only elements with concentration higher than 0.5 wt% are showed. Error bars intervals are expressed by the corresponding standard deviations in form of **average  $\pm$  standard deviation**.

wt%	1	2	4	5	7	8	10	11	12	14	Av.	SD	v%
Sn	2.0	1.8	1.7	1.5	1.7	1.5	1.6	1.6	1.5	2.1	<b>1.7</b>	<b>0.2</b>	<b>12.1</b>
Si	1.49	1.39	1.27	1.27	1.20	1.23	1.28	1.25	1.30	1.35	<b>1.30</b>	<b>0.08</b>	<b>6.3</b>
Mg	1.30	1.29	1.29	1.19	1.23	1.17	1.24	1.21	1.18	1.27	<b>1.24</b>	<b>0.05</b>	<b>3.8</b>
Al	1.31	1.21	1.17	1.06	1.17	1.05	1.09	1.13	1.14	1.16	<b>1.15</b>	<b>0.07</b>	<b>6.3</b>
S	0.89	0.79	0.70	0.67	0.73	0.71	0.72	0.73	0.68	0.72	<b>0.73</b>	<b>0.06</b>	<b>8.4</b>
Cr	0.76	0.66	0.64	0.58	0.65	0.60	0.61	0.64	0.58	0.63	<b>0.63</b>	<b>0.05</b>	<b>7.6</b>

**Table 3.7:** Summary of the measured elemental concentrations for secondary elements with concentration higher than 0.5 wt%. Concentrations values are expressed in wt%. **Av.** = average; **SD** = standard deviation; **v%** = percentage variability. The complete dataset is reported in *Annex 3*.

### 3.3.3. Phase Composition

Moving towards the phase composition, XRD analysis was selected as investigation probe. Since the major part of the investigated particulate (90 wt%) is made by Iron, Oxygen and Carbon, and due to the specific composition of the tribological interface, a significant presence of Iron oxides and elemental carbon might be expected within this brake emission. Figure 3.6 shows the experimental XRD pattern measured for



each investigated PM<sub>10</sub> particulate, following the analytical protocol reported in the corresponding section in *Chapter 2*. As can be clearly observed, several diffraction peaks can be spotted in the investigated angular range, testifying the presence of crystalline phases. Notably, the positions of the diffraction peaks and their relative intensity ratios are well reproducible in all the investigated samples. For this reason, as far as the crystalline fraction is concerned, it is possible to state an overall reproducible phase composition of the collected emissions. Another interesting observation is related to the width of the diffraction peaks, which are mostly broad with the only main and constant exceptions of two narrower peaks at about 25.5, 26.5 and 44.6°. This testifies the reproducible presence of at least two crystalline phases having coherent diffraction domains (*i.e.* powder grains) characterized by different crystallinity: lower for the phase(s) with broader peaks and higher for the phase(s) with narrower peaks.

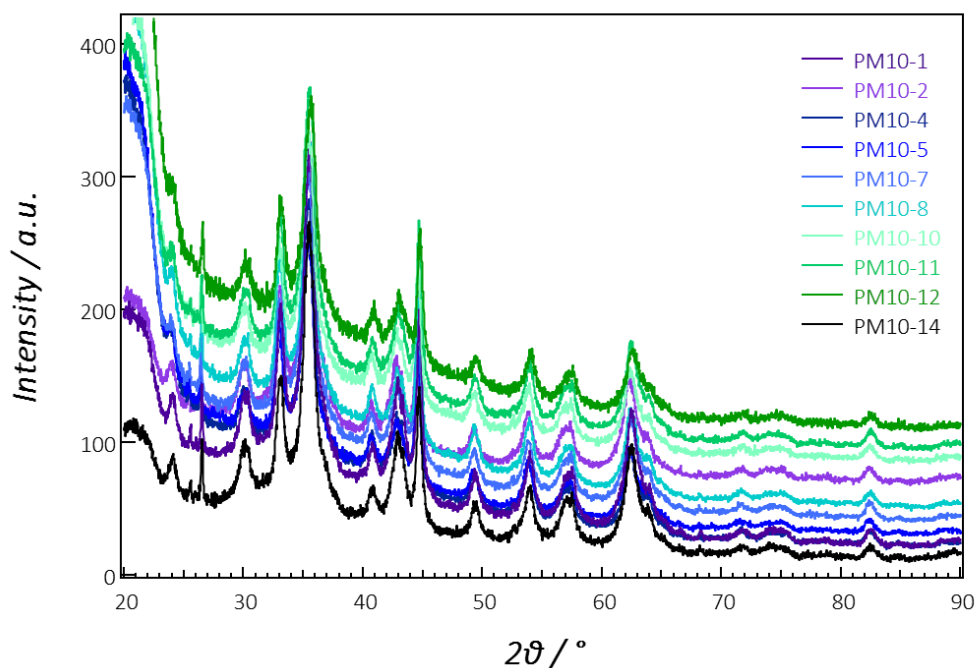


**Figure 3.6:** Experimental XRD pattern measured for the PM<sub>10</sub> particulates collected for the *intra* bench variability study.

Phase identification performed on the collected XRD pattern unveils that the crystalline fraction of the investigated emissions is composed by a mixture of the following phases: *i*) Fe<sub>3</sub>O<sub>4</sub> (Magnetite, main phase); *ii*) Fe<sub>2</sub>O<sub>3</sub> (Hematite, main phase); *iii*) α-Fe (metallic iron, secondary phase); *iv*) Graphite (secondary phase); and *v*) SnS (Tin sulfide, trace phase). The attribution of each diffraction peak is reported in Figure 3.7, while the

corresponding crystallographic references from ICDD Database PDF4+ 2022<sup>[26]</sup> are reported in Table 3.8. To be highlighted that the same references and crystallographic models are used in every XRD phase analysis reported in this thesis, whenever Iron, Iron oxides, Graphite and Tin sulfide are observed. As can be observed, metallic Iron, Graphite and Tin Sulfide are characterized by narrower peaks in respect with the Iron oxides polymorphs. This observation infers a lower degree of crystallinity for those compounds which are generated by thermal modification (*i.e.* the oxidation occurring at the tribological interface), in respect to particles generated by direct abrasion.

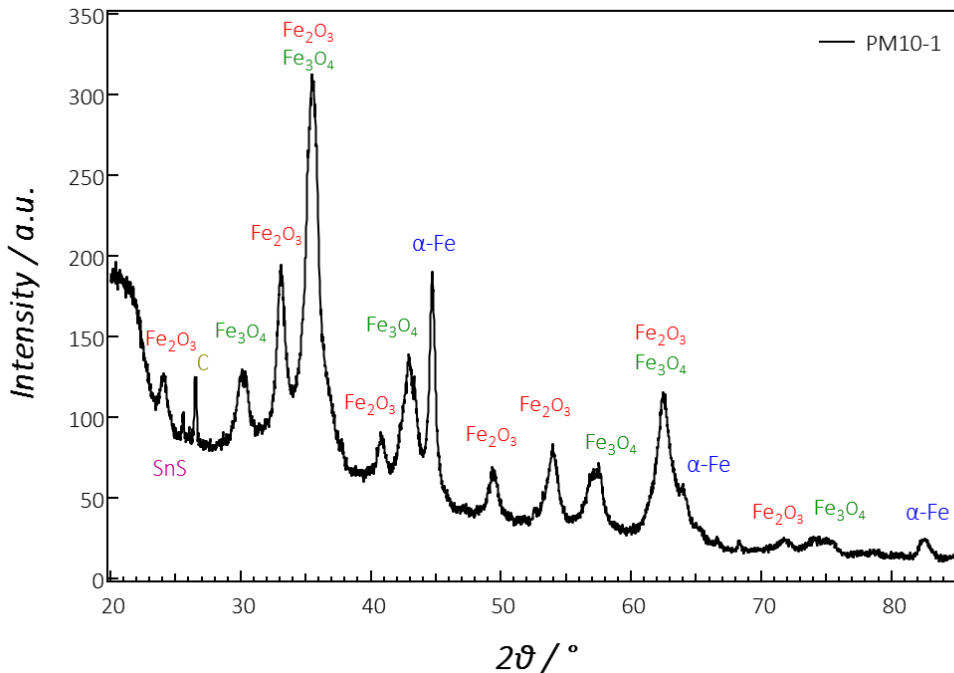
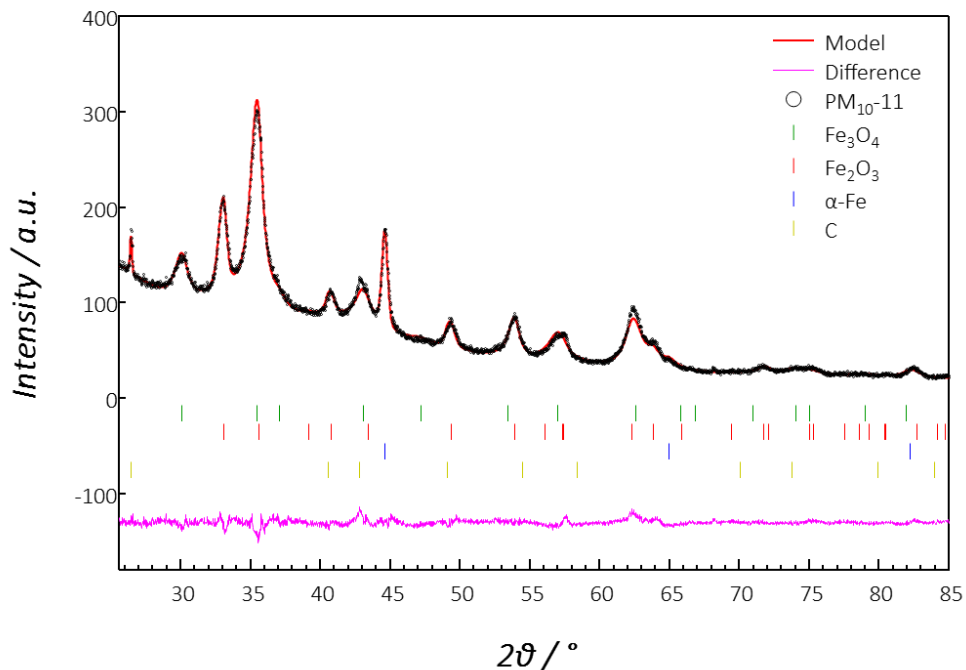


**Figure 3.7:** Identification of the phases composing the crystalline fraction of the investigated PM<sub>10</sub> particulates generated by the selected friction couple.

Phase	Compound	Crystallographic Reference (ICDD)
Fe <sub>3</sub> O <sub>4</sub>	Magnetite	04-015-9120
Fe <sub>2</sub> O <sub>3</sub>	Hematite	04-015-7029
α-Fe	Ferrite	04-014-0360
C	Graphite	00-041-1487
SnS	Tin Sulfide	04-016-6156

**Table 3.7:** Crystallographic references from ICDD database PDF4+ 2022, as used in phase identification and phase analysis.

Finally, the crystallographic references reported in Table 3.7 are used as starting models to fit the collected XRD experimental data for phase analysis by means of the WPPF method, following the procedure described in the corresponding section of *Chapter 2*. Figure 3.8 reports an example of fit as obtained for the PM<sub>10-1</sub> sample.



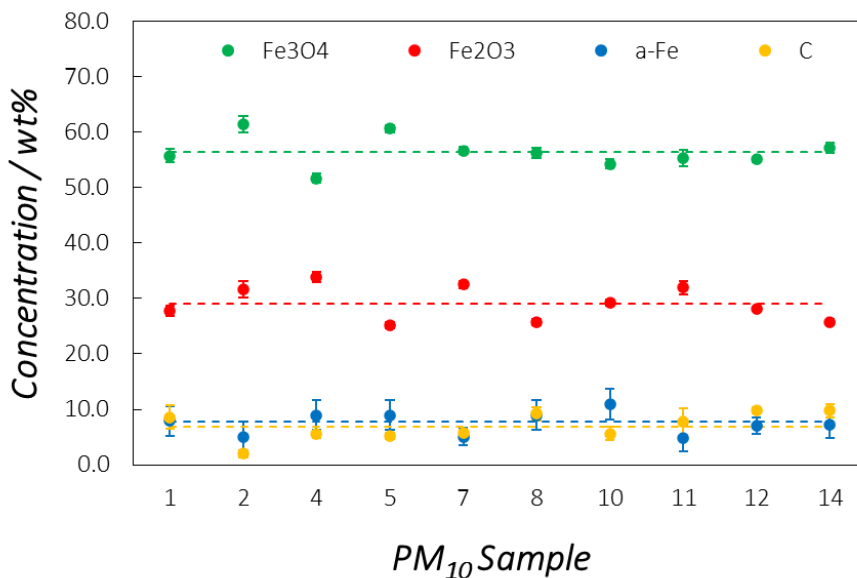
**Figure 3.8:** XRD pattern refinement for PM<sub>10-1</sub> sample via WPPF method. *i)* Black profile: experimental pattern; *ii)* red profile: calculated model; *iii)* pink profile: residuals between experimental data and calculated model; *iv)* vertical bars: crystallographic references. α-Fe, Fe<sub>3</sub>O<sub>4</sub>, Fe<sub>2</sub>O<sub>3</sub> and C reference bars are respectively reported in blue, green, red and yellow.

Table 3.8 summarizes the obtained results in terms of relative abundance of the identified phases. SnS is not reported since it is always found in between the detection and quantification limit of the technique, around the 0.5 wt%. Figure 3.9 helps in visualizing schematically the variability of the main and secondary phases. As can be observed in both the summary table and the following graph, the two Iron oxides (Magnetite and Hematite) are the dominant phases. Conversely, metallic Iron and Graphite are found in secondary amounts, while the Tin sulfide is always observed in trace amounts. The overall absolute variability obtained by phase analysis for all the assessed compounds is found to be around in the 2-3 wt% range. This translates in an extremely limited percentage variability when looking at the main phases (around 6 and 11% for Magnetite and Hematite, respectively). Conversely, the secondary phases

suffers of higher percentage variability, being around the 30% of their overall concentration for both the metallic Iron and the Graphite.

PM <sub>10</sub> -n	Fe <sub>3</sub> O <sub>4</sub> /wt%	Fe <sub>2</sub> O <sub>3</sub> /wt%	α-Fe/wt%	C/wt%	R <sub>wp</sub> /%
1	55.7	27.8	7.9	8.6	5.32
2	61.4	31.6	5.0	2.0	7.67
4	51.7	33.9	8.9	5.5	3.69
5	60.6	25.2	8.9	5.2	5.08
7	56.7	32.5	5.1	5.7	3.88
8	56.2	25.7	8.9	9.2	4.36
10	54.3	29.2	10.9	5.6	4.20
11	55.3	32.0	4.9	7.8	4.80
12	55.1	28.2	7.0	9.8	6.06
14	57.2	25.7	7.3	9.8	4.38
Average	56.4	29.2	7.5	6.9	4.94
SD	2.9	3.2	2.0	2.5	
v%	5.1	10.8	27.1	36.6	

**Table 3.7:** Summary table of the phase concentration along the PM<sub>10</sub> samples generated in the different tests. Average concentrations are also reported together with the corresponding standard deviations (SD) and percentage variability (v%).



**Figure 3.9:** Variability of the phase concentration along the different investigated particulates. Dashed lines represent the overall averages and are reported for sake of comparative evaluation.

Notably, all these findings are in excellent agreement with those obtained from the elemental analysis, reporting the dominant presence of Iron, Oxygen and Carbon. Therefore it can be stated that the phase composition of the crystalline fraction of the investigated emissions fits very well their elemental composition. In addition, phase analysis unveils further interesting details anyway not obtainable. For instance, it is clearly possible to observe that the vast majority of the generated Iron is oxidized, while only an overall minor fraction still exhibits metallic character after its emission in environment. Looking at the Carbon concentration, it is possible to observe that Graphite is found around the 7 wt% on a global basis, while slightly higher amounts of Carbon are detected at the elemental analysis (around 10 wt%). This is coherent with the additional presence of Carbon in the PM<sub>10</sub> emissions in forms typically not detectable by the XRD probe, such for instance the organic Carbon arising from the degradation of the organic binders in the friction materials. Finally, eventual crystalline phases related to minor and trace elements are in general not observed. Indeed, their very low concentrations makes them hardly detectable at the XRD probe, most of all considering the overall extremely limited amounts of material collected on the filters (which was in the order of few milligrams for each test). Nevertheless, some exceptions might be expected in the cases of particularly crystalline compounds and/or materials having high electronic density, such in the case of several sulfides typically used as lubricants in the friction composites. For instance, the Tin sulfide reported in these emissions represents a good example of what just stated: in spite of being hardly quantifiable with precision and good reproducibility, it is at least possible to confirm its presence within the particulates.

#### 3.3.4. Particle Size Distribution

Finally, the particle size distribution (PSD) of the collected particulates is also evaluated. For this reason, in between the samplings of material for the chemical characterization, four tests were dedicated at the specific aim collecting material for the investigation on the reproducibility of the particulates granulometry. Samples collected at this aim are **PM<sub>10</sub>-3**, **-6**, **-9** and **-13** samples, as reported in Table 3.2. The PSD of the investigated particulates was characterized by SEM image analysis, following sample preparation and analytical protocol reported in Chapter 2. In particular, the dimensional distributions are reported following the dimensional ranges of the ELPI+ impactor, with the main difference represented by the use of the maximum diameter ( $D_{max}$ ) instead of the  $d_{50}$  parameter. To be noted that dimensional ranges lower than the resolution of the electron microscope used for the characterization are not reported. Therefore, the ultra-fine particles (UFP) are categorized in a unique dimensional range, *i.e.* below 170 nm. Table 3.8 summarizes the percentage appearance frequency of particulates in the corresponding dimensional ranges, while Figure 3.10 reports the graphical

representation of the PSD comparison carried out between the four investigated particulates.

$D_{max}/\mu m$	PM <sub>10-3</sub>	PM <sub>10-6</sub>	PM <sub>10-9</sub>	PM <sub>10-13</sub>	Average	SD
0.17	12.8	12.6	17.5	12.0	13.7	2.5
0.31	15.9	18.5	22.1	17.7	18.5	2.6
0.6	33.9	28.7	31.1	33.3	31.7	2.4
0.9	16.3	15.6	13.0	16.3	15.3	1.6
1.6	14.1	13.3	12.3	14.4	13.5	1.0
2.5	5.1	6.9	3.1	4.7	5.0	1.6
3.65	1.6	2.1	0.8	1.3	1.5	0.5
5.36	0.3	1.7	0.1	0.3	0.6	0.7
9.87	0.1	0.6	0.0	0.0	0.2	0.3
TOT	100.0	100.0	100.0	100.0	100.0	

**Table 3.8:** Summary table of frequency appearance of particles exhibiting  $D_{max}$  lower than the corresponding limit value. Average results and corresponding standard deviations (SD) are also reported for each dimensional range.

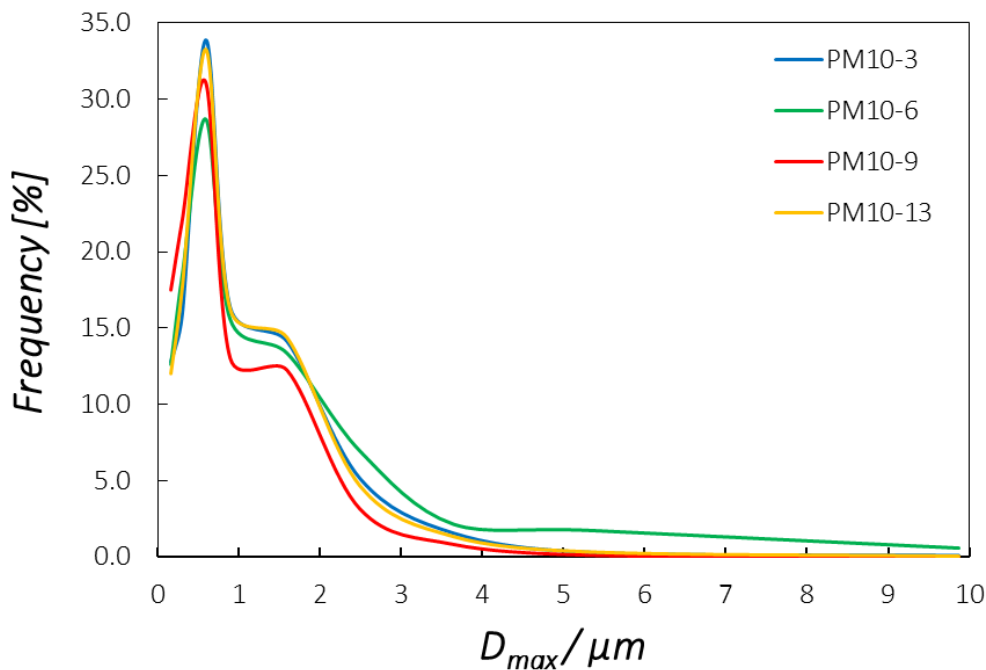


**Figure 3.10:** Comparison of the obtained PSD profiles for the investigated PM<sub>10</sub> particulates.

As can be clearly observed by the graphs reported in Figure 3.10 as well as the results reported in Table 3.8, the majority of the collected PM<sub>10</sub> particulates are composed of particles having dimensions lower than 2.5 μm (more than 95% of the observations), while only a limited amount of particles shows dimensions comprised between 2.5 and 10 microns. UFP represents in all the four investigated samples about the 15% of the total observations. More in detail, it is possible to observe that all the PSD profiles are characterized by extremely similar behavior, with the main frequency peak localized around 0.6 μm and a subsequent shoulder in the range of 0.9-1.6 μm. The overall PSD profile is reported in Figure 3.11 as average for each selected dimensional range. As can be observed, highest relative variabilities are observed in the higher dimensional ranges.

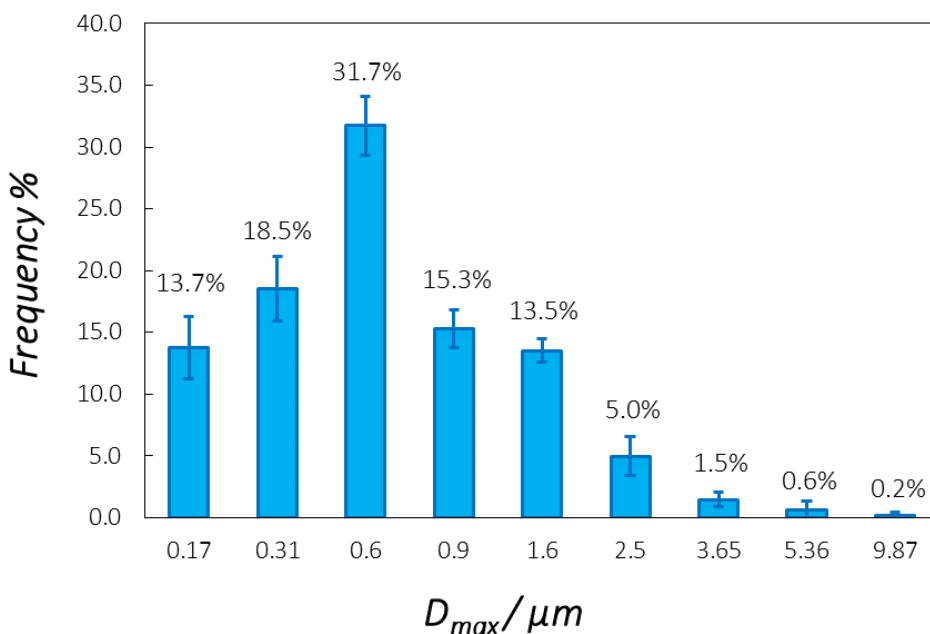


**Figure 3.11:** Overall PSD as obtained by averaging results from the four observed particulates. Error bars represents  $\pm \sigma$  (standard deviation).

### 3.4. Inter Benches Assessment

Similarly to the study carried out for the *intra* bench assessment, the chemical composition and the granulometry of the PM<sub>10</sub> brakes emissions collected at three different dynamometric benches are compared in order to assess *inter* platforms variability. The detail of the three compared benches are reported in *Paragraph 3.3.2*. The PSD profiles are compared only between particulates generated by **B1** and **B3** benches, since for the **B2** platform only one emission sample was available for the study and therefore used for the chemical characterization. For this reason, together with the

PSD profiles, also SEM images of the collected particulates are reported, in order to provide at least qualitative observation of the samples granulometry. Results from **B1** platform are always reported as the global average of the results obtained from the *intra* bench assessment study, while results from **B2** and **B3** tests arise from more limited independent observations. Thus, it is to be considered that the three datasets have different statistic weight.

### 3.4.1. Elemental Composition

Figure 3.12 shows the comparison between the average elemental concentrations of the main constituents observed for the particulates generated at the three different platforms. In order to provide a more detailed picture of the comparison, the distribution of the independent observations of the main components elemental concentrations are also reported in the box plots in Figure 3.13. Finally, the average concentration results are listed in Table 3.9. As can be observed, the overall elemental distribution profile is extremely similar in all the three cases, with very similar relative abundance ratios between the main constituents. When present, only modest differences can be observed. In particular, PM<sub>10</sub> sample collected on **B3** exhibits a slightly lower concentration of Oxygen and slightly higher of other elements in respect with the counterparts from **B1** and **B2**. Conversely, the particulate collected on the **B1** platform was found to have slightly lower average concentration of Carbon in respect with the counterparts from **B2** and **B3**.

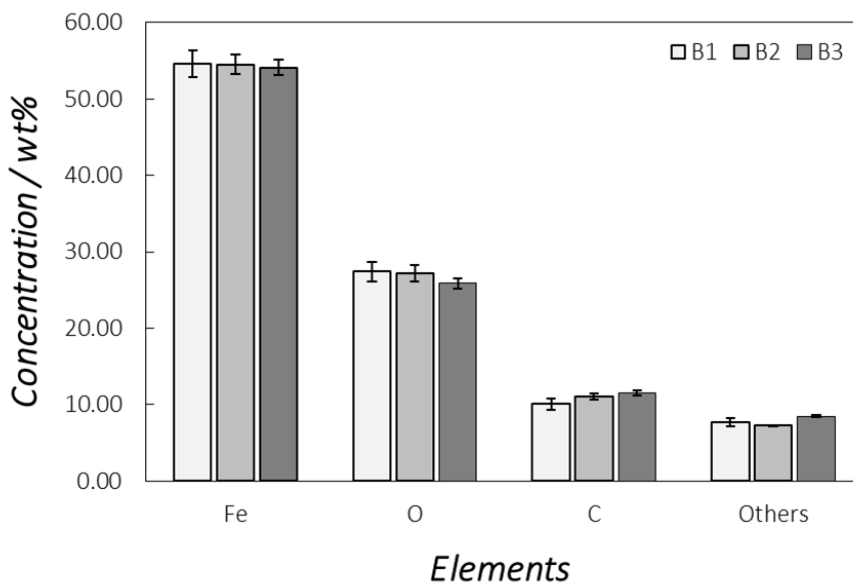
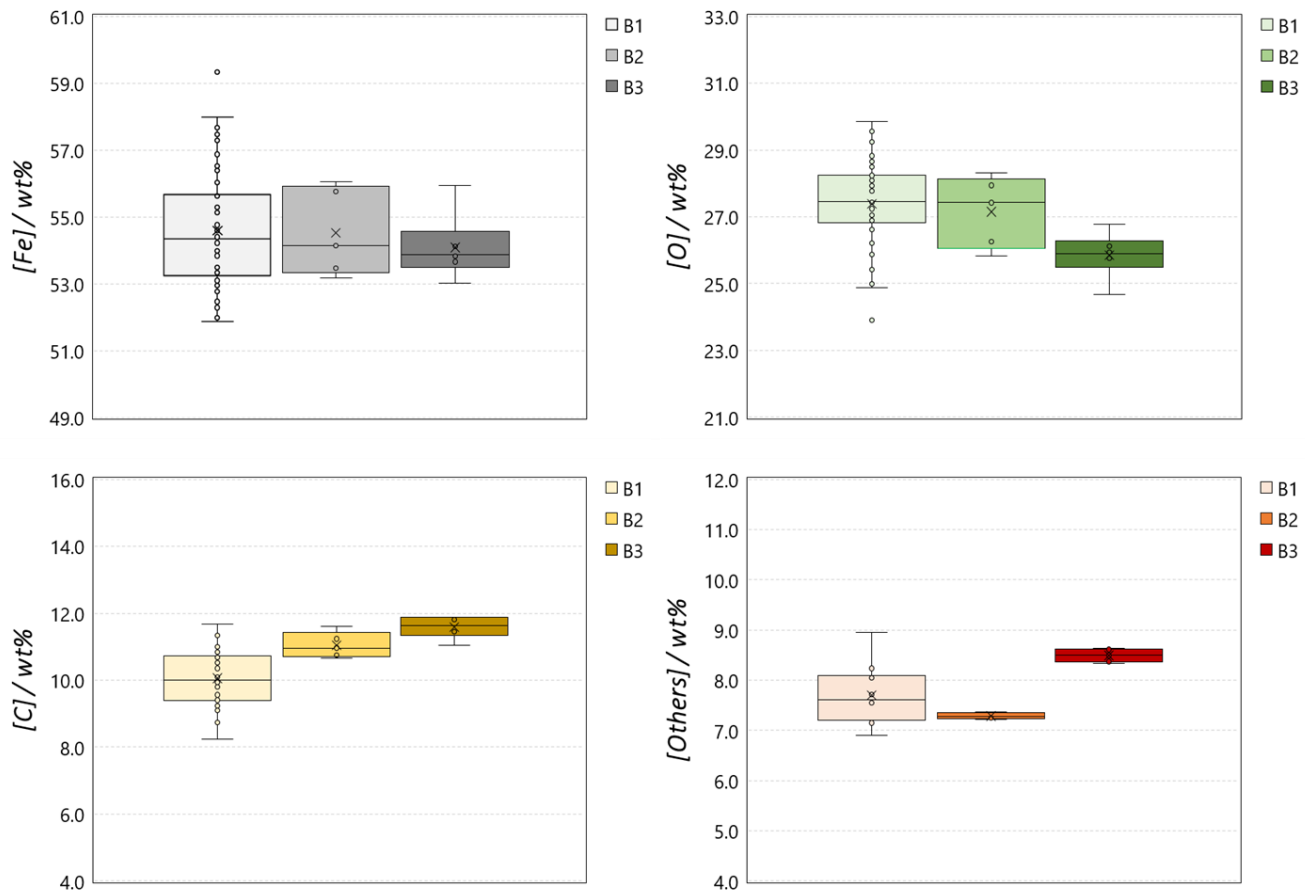


Figure 3.12: Comparison of the elemental distributions of the PM<sub>10</sub> particulates from **B1**, **B2** and **B3**.





**Figure 3.13:** Comparison of the dispersion of the main constituents elemental concentrations for the investigated PM<sub>10</sub> particulates. Box plots for Iron, Oxygen, Carbon and the sum of the other elements (Others) are reported respectively in grey, green, yellow and red scale.

Element	B1		B2		B3	
	wt%	SD	wt%	SD	wt%	SD
Fe	54.6	1.8	54.5	1.3	54.1	1.0
O	27.4	1.3	27.1	1.1	25.8	0.7
C	10.3	0.8	11.0	0.4	11.6	0.3
Others	7.7	0.6	7.4	<0.1	8.5	0.1

**Table 3.9:** Summary table of the global average concentrations for the main constituents composing the PM<sub>10</sub> emissions collected at the three different benches, together with the corresponding standard deviations (SD).

As can be spotted by visual inspection of the reported box plots, the observed variability is anyhow extremely limited. Indeed, even if the overall averages can exhibit some modest differences, most of the specific dispersions of the measured concentrations always reside within the global dispersions for each selected constituent. The only partial exception is represented by the Carbon from **B3** platform, whose higher part of the concentrations dispersion exceed both the dispersions of concentrations from the counterparts generated at **B1** and **B2** benches.

Finally, also secondary elements are evaluated. At this aim, Figure 3.14 shows the comparison between elements with concentration higher than 0.5 wt%, while Table 3.10 summarizes all the average concentrations as well as the corresponding standard deviations. The complete datasets are reported in *Annex 3*. Similarly to the main constituents, the global situation for minor components depicts an overall good level of reproducibility, with extremely similar values and relative ratios between the different assessed elements. Among all the secondary elements, only Tin shows a slightly higher level of variability. In particular, Sn as measured in **B2** sample shows a dispersion of concentration values which always lower in comparison to both the counterparts from **B1** and **B3** platforms. Sulfur and Chromium from **B3** sample exhibit concentrations dispersions which are higher than the one from **B2** sample, while remaining within the range in respect with the **B1** particulates. In turn, Sulfur and Chromium concentrations in **B2** particulate still remain within the range in the lower part of the overall concentration values dispersion of **B1** samples. Conversely, Silicon, Magnesium and Aluminum exhibit concentration values dispersions which are mostly completely overlapping. Taking all these observation together, it is possible to state an overall low level of variability also between the minor components, when assessing particulates generated by the same friction couple, during the same braking cycle, but with emission tests carried out on different dynamometric benches. More in detail, relative variabilities for secondary elements are rarely found exceeding the 10% of their corresponding average concentration values.

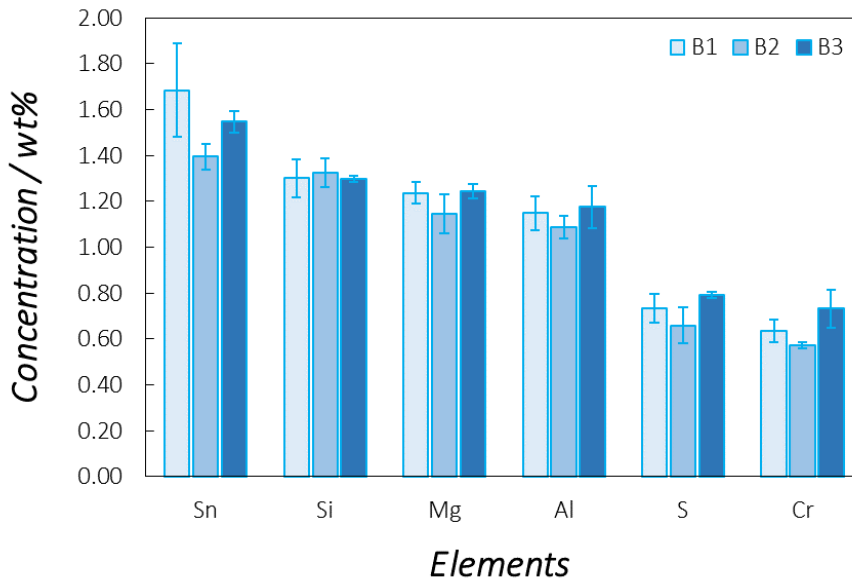


**Figure 3.14:** Comparison of the secondary element distributions of the PM<sub>10</sub> particulates generated at the **B1**, **B2** and **B3** benches.

Element	B1		B2		B3	
	wt%	SD	wt%	SD	wt%	SD
Sn	1.69	0.20	1.40	0.06	1.55	0.05
Si	1.30	0.08	1.33	0.06	1.30	0.01
Mg	1.24	0.05	1.15	0.09	1.25	0.03
Al	1.15	0.07	1.09	0.05	1.18	0.09
S	0.73	0.06	0.66	0.08	0.79	0.01
Cr	0.63	0.05	0.57	0.01	0.73	0.08

**Table 3.10:** Summary table of the global average concentrations for the minor constituents composing the PM<sub>10</sub> emissions collected at the three different benches, together with the corresponding standard deviations (SD).

### 3.4.2. Phase Composition

Figure 3.15 shows the fits carried out on the XRD experimental data collected on particulates as obtained from the three different benches, while Table 3.11 summarizes the corresponding results in terms of relative abundance of the main crystalline phases constituting the investigated emissions.

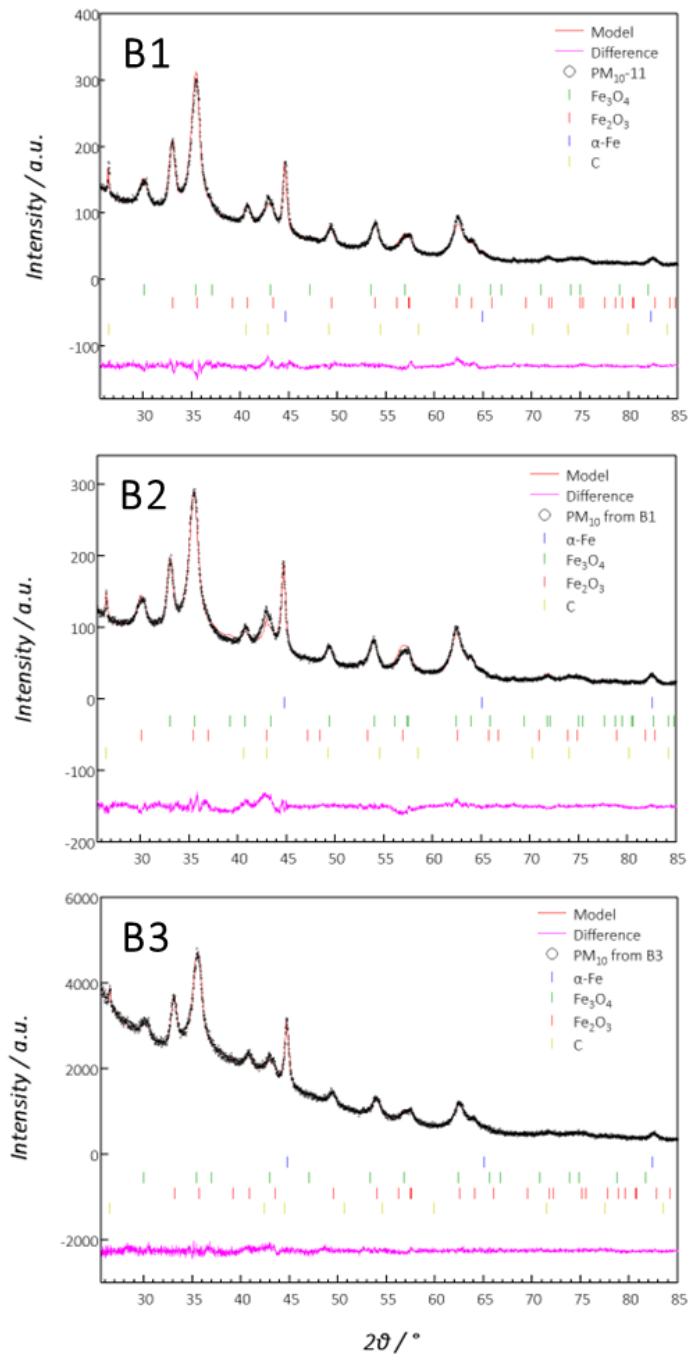


**Figure 3.15:** XRD phase analysis for  $\text{PM}_{10}$  samples collected on the three different benches (top to bottom: **B1**, **B2** and **B3**). *i)* Black profile: experimental pattern; *ii)* red profile: calculated model; *iii)* pink profile: residuals between experimental data and calculated model; *iv)* vertical bars: crystallographic references ( $\alpha\text{-Fe}$  in blue,  $\text{Fe}_3\text{O}_4$  in green,  $\text{Fe}_2\text{O}_3$  in red and C in yellow).

Phase	B1		B2		B3		Overall		
	wt%	SD	wt%	<i>esd</i>	wt%	<i>esd</i>	wt%	SD	v%
Fe <sub>3</sub> O <sub>4</sub>	56.4	2.9	59.5	0.7	60.6	0.2	58.8	2.2	3.7
Fe <sub>2</sub> O <sub>3</sub>	29.2	7.5	22.5	0.6	21.2	0.9	24.3	4.3	17.7
α-Fe	7.5	2.0	9.0	0.2	8.9	0.2	8.5	0.8	9.9
C	6.9	2.5	9.0	0.5	9.3	0.2	8.4	1.3	15.6

**Table 3.11:** Summary table of the phase concentration in PM<sub>10</sub> samples generated at different benches. Overall average concentrations are also reported together with the corresponding standard deviation (SD) and percentage variability (v%). Since B2 and B3 re obtained from the measurement of a single sample, estimated standard deviations (*esd*) from refinement software are used as variability index.

As can be expected from previous results from the elemental analysis, also the phase composition is found to be reproducible when collecting particulates generated in the same experimental condition over different benches. Notably, some of the slight differences reported from the elemental analysis are replicated also at the phase analysis. For instance, Carbon from **B1** particulate was found with overall concentration slightly lower in respect to the particulates from **B2** and **B3**. Similar trend is observed in the Graphite concentration. Similarly, the trend observed in the Oxygen concentration can be somehow observed also at the Iron oxides concentrations (mainly referred to Hematite from **B3** sample). Finally, looking at the overall picture, it is possible to observe overall good reproducibility of the phase distributions, with two phases out of four exhibiting relative variability lower than the 10% (Magnetite and metallic Iron), while the other two score percentage variability below the 20% (Hematite and Graphite).

### 3.4.3. Particle Size Distribution

As reported at the beginning of this section, only one sample from **B2** bench was available for the *inter* benches assessment. Therefore this sample was used for the characterization of the chemical composition. Thus, PSD profiles were actually collected only for particulates generated at **B1** and **B3** platforms. For this reason, Figure 3.16 shows SEM images of the particulates collected from the three assessed benches to provide at least a qualitative comparison of the investigated PM<sub>10</sub> particulates. In addition, Table 3.12 and Figure 3.17 report the comparison of the PSD profiles between samples from **B1** and **B3**. It has to be highlighted that results from **B1** particulate were obtained as the average of four independent observations, while only one particulate from **B3** was analyzed. For this reason, no variability indexes are reported for **B3** sample. As can be observed from the SEM images reported below, the granulometry of the three particulates looks very similar, with the vast majority of particles clearly exhibiting dimensions lower than 2.5 μm, as previously found in the PSD analysis carried out for the *intra* bench assessment.

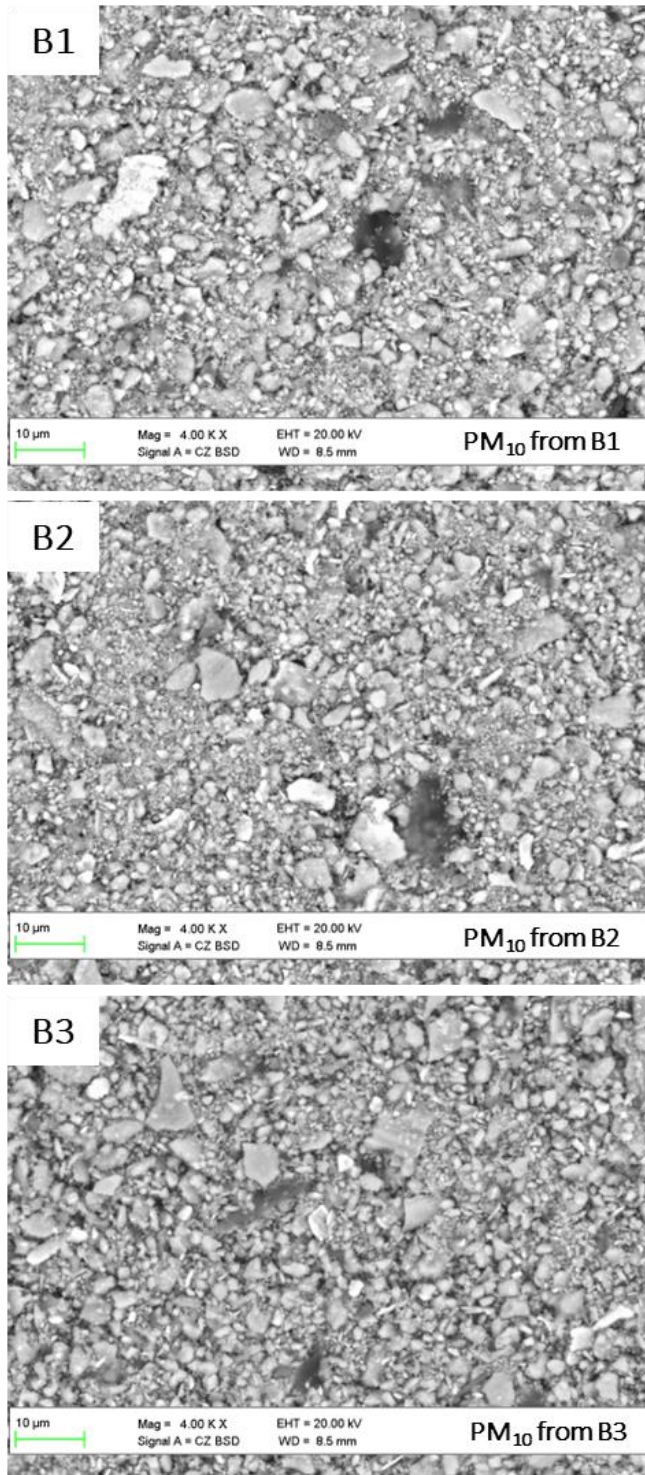


**Figure 3.16:** SEM images of the collected PM<sub>10</sub> particulates. Top to bottom: **B1**, **B2** and **B3** samples.

$D_{max}/\mu m$	0.17	0.31	0.6	0.9	1.6	2.5	3.65	5.36	9.87
B1	13.7	18.5	31.7	15.3	13.5	5.0	1.5	0.6	0.2
B1-SD	2.5	2.6	2.4	1.6	1.0	1.6	0.5	0.7	0.3
B3	9.6	12.1	30.2	19.3	16.7	8.7	2.6	0.7	0.1
SD	-	-	-	-	-	-	-	-	-

**Table 3.12:** Summary table of frequency appearance of particles exhibiting  $D_{max}$  lower than the corresponding limit value. Average results and corresponding standard deviations (SD) are also reported (when possible) for each dimensional range.

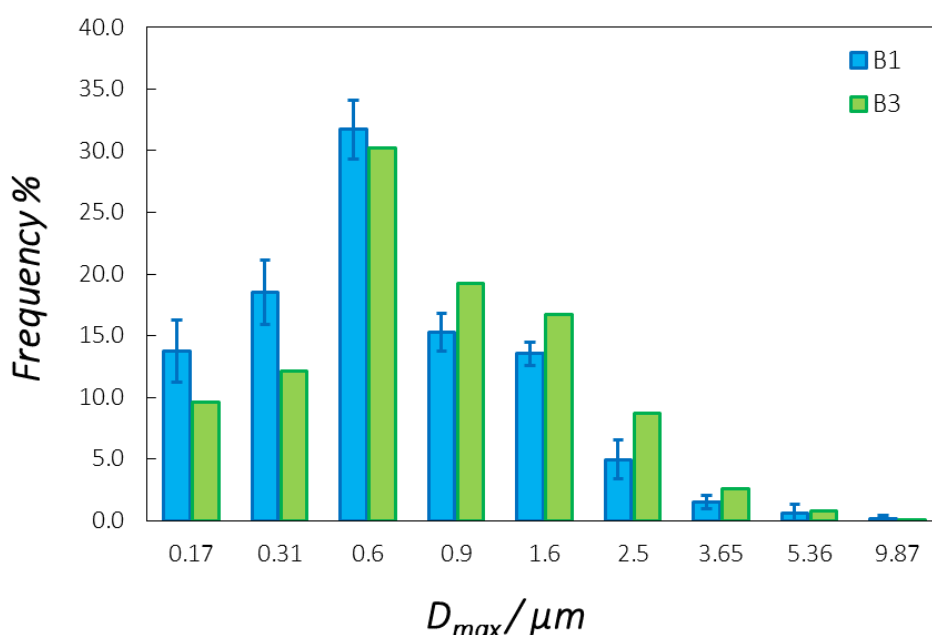


**Figure 3.17:** Comparison between PSD profiles as obtained for **B1** and **B3** particulate samples. Error bars in **B1** histogram set represent  $\pm \sigma$  (standard deviation).

Looking more in detail at the PSD profiles, it is possible to see that the overall dimensions of particulate generated at the **B3** bench are slightly higher in respect with the counterpart from **B1**. In particular, ultra-fine fractions appear to be less populated, while particles in the 1.0-2.5  $\mu m$  range are observed more frequently. Nevertheless, the frequency peak still appears around 600 nm and a shoulder is present in the 0.9 - 1.5  $\mu m$  range. In addition, as previously reported for **B1** samples, also the  $PM_{10}$  particulate generated by **B3** are dominantly composed by particles having dimensions lower than 2.5  $\mu m$ , while bigger particles represent a secondary contribution.

### 3.5. Summary

The reproducible generation of emission particulates having constant physico-chemical characteristic is fundamental in order to provide reliable and univocal input information for comparative assessments, eco/cyto-toxicological characterization and source apportionment studies. For this reason, the previous paragraphs reports two reproducibility studies, *i.e.* an *intra* bench and an *inter* benches assessment. In particular, the first study was meant in order to assess the expected variability of chemical composition and granulometry of brakes PM<sub>10</sub> emissions generated at the same bench, starting from the same materials composing the friction couple and following the guidelines from the PMP working group. The reported study unveiled extremely low variability of all the investigated properties. More in detail, as far as the elemental composition is concerned, main constituents of the emissions (Fe, O and C) were found to exhibit relative variability over ten test repetitions always significantly lower than the 10% of the corresponding average elemental concentrations. Similarly, also the relative variability of secondary elements concentration was found to reside well within the same value, with only one exception (Sn, v% = 12%). Good reproducibility of the phase composition of the crystalline fraction was also determined. In particular, the main phases (Iron oxides) were found to exhibit relative variability in the same range of that one observed in the elemental composition analysis. Conversely, higher variabilities of about 20-30% were spotted when looking at the secondary phases (metallic Iron and Graphite), likely caused the overall low amount of particulate collected on the analyzed filters in respect with the XRD probe sensitivity. Finally, also the PSD profiles were reported to exhibit modest variability along four different tests, therefore stating a good reproducibility also in the granulometry of the produced particulates. The second study reported an evaluation of the same physico-chemical characteristic investigated in the *intra* bench study, but comparing material collected from three different test platforms. Thus, the *inter* benches assessment was performed with the same starting materials composing the friction couple during the same emission test typology, but assessing the variability possibly due to different laboratory sites. Also in this case, the elemental composition was found to exhibit good reproducibility, with modest differences observed only in few cases. In particular, Carbon and Tin showed the higher relative variabilities, as already determined in the *intra* bench assessment. As far as Carbon is concerned, higher variabilities of its concentration in respect to other elements might be likely related to its abundant presence in several different forms within the friction mix, therefore being more susceptible to intrinsic variability of raw materials dispersion within different pads. Conversely, no straightforward explanation for the higher variability is easily found. Nevertheless, the fact that Sn concentration appears to be the less reproducible in both the *intra* and *inter* bench assessments seems to suggest some



systematic variability in sampling and/or measurement of Sn-based compounds. This might be due to their higher density in respect with all the other compounds composing the brake emission, which might influence their sampling efficiency. However, this hypothesis needs to be validated and corroborated by a higher number of observations in the future. Similarly, to the elemental concentration, the phase composition is also found to be similar in the particulates collected at the three different benches. In particular, good reproducibility was observed for the main phases, while Carbon showed the highest variability (about 30%). Notably, similar trends were observed in the *intra* bench assessment, and similar explanation as provided for Carbon elemental concentration can be provided to explain also the lower reproducibility of this phase among all the other crystalline compounds. Finally, looking at the comparison of the granulometry of the collected particulates, there were observed modest differences, mainly related to the ultra-fine fractions. However, in all the cases similar PSD profiles were observed, with 95% of the collected particles exhibiting dimensions lower than 2.5  $\mu\text{m}$ . In addition, the peak of appearance frequency was always observed around 0.6 micron, with consistent amount of the remaining particles being located in the 0.9-1.5  $\mu\text{m}$  range.

On the basis of the reported results, it is finally possible to state that particulates generated at the dynamometric bench during emission tests performed on the same starting materials composing the friction couple and following the same brake cycle have fairly reproducible chemical composition and dimensional profiles. In particular, most of the main constituents concentrations can be expected to suffer relative variabilities below the 10% when following the guidelines proposed by the PMP working group. Thus, a specific laboratory should be able to maintain high level of consistency in the physico-chemical information collected on brakes emissions produced at proper dynamometric bench. In addition, the *inter* benches investigation proposed in this chapter confirms that similar level of reproducibility can be expected also when looking at particulates generated at different test platforms or laboratory sites. Therefore, different laboratories testing the same friction couple in the same experimental condition should be able to obtain reasonably equivalent particulates in terms of both chemical composition and granulometry. These findings are pivotal in corroborating future comparative assessments between particulates generated from different starting materials or in different driving conditions as well as in confirming the convenient use of dynamometric benches in order to collect reproducible brakes emissions for source apportionment studies, environmental assessments and toxicological characterization.

## References

- [1] N. Perzborn, C. Agudelo, G.P. Ostermeyer, "On Similarities and Differences of Measurements of Inertia Dynamometer and Scale Testing Tribometer for Friction Coefficient Evaluation", *SAE Int. J. Mater. Manf.*, 8(1), **2015**, doi:10.4271/2014-01-2523.
- [2] M. Federici, M. Alemani, C. Menapace, S. Gialanella, G. Perricone, G. Straffellini, "A Critical Comparison of Dynamometer Data with Pin-on-Disc Data for the Same two Friction Material Pairs – A Case Study", *Wear*, 424-425, **2019**, 40-47, <https://doi.org/10.1016/j.wear.2019.02.009>.
- [3] P.G. Sanders , N. Xu, T.M. Dalka, M.M. Maricq, "Airborne Brake Wear Debris: Size Distributions, Composition, and a Comparison of Dynamometer and Vehicle Tests", *Environ. Sci. Technol.*, **2003**, 37, 4060-4069, doi:10.1021/es034145s.
- [4] E. Little, T-K. Kao, P. Ferdani, T. Hodges, "A Dynamometer Investigation of Thermal Judder", *SAE Transactions*, 107(6), **1998**, 2338-2346.
- [5] K. Lee, R.B. Dinwiddie, " Conditions of Frictional Contact in Disk Brakes and Their Effects on Brake Judder", *SAE Transactions* , 107, **1998**, 1077-1086.
- [6] L. Loader, J. Zhao, P-A. Jarnestrom, "Brake N&V Quality: Noise Dynamometer Evaluation", *SAE Transactions*, 110(6), **2001**, 2474-2480.
- [7] J.D. Preston, "Inertia Dynamometer Evaluation of Brake Lining Materials", *SAE Transactions*, 82(1): **1973**, 755-761.
- [8] L. Gudmand-Høyer, A. Bach, G.T. Nielsen, P. Morgen, "Tribological Properties of Automotive Disc Brakes with Solid Lubricants", *Wear*, 232, **1999**, 168–175.
- [9] R.J. Talib, E. Othman, R. Kasiran, "Characterisation of Semi-Metallic Brake Pads using Brake Dynamometer", *AIP Conference Proceedings* 1217, 42, **2010**, <https://doi.org/10.1063/1.3377860>.
- [10] M. Kumar, J. Bijwe., "NAO Friction Materials with Various Metal Powders: Tribological Evaluation on Full-Scale Inertia Dynamometer", *Wear*, 269, **2010**, 826–837, doi:10.1016/j.wear.2010.08.011.
- [11] P.G. Sanders, T.M. Dalka, N. Xu, M.M. Maricq, R.H. Basch, "Brake Dynamometer Measurement of Airborne Brake Wear Debris", *SAE Transactions* , 111(6), **2002**, 1693-1699.
- [12] J. Kukutschová, P. Moravec, V. Tomásek, V. Matejka, J. Smolík., *et. al.*, "On Airborne Nano/Micro-Sized Wear Particles Released from Low-Metallic Automotive Brakes", *Environmental Pollution*, 159, 2011, 998-1006, doi:10.1016/j.envpol.2010.11.036.
- [13] H. Hagino, M. Oyama, S. Sasaki, "Laboratory Testing of Airborne Brake Wear Particle Emissions Using a Dynamometer System under Urban City Driving Cycles", *Atmospheric Environment*, 131, **2016**, 269-278, <http://dx.doi.org/10.1016/j.atmosenv.2016.02.014>.
- [14] G. Perricone, V. Matějka, M. Alemani, G. Valota, A. Bonfanti, *et. al.*, "A Concept for Reducing PM10 Emissions for Car Brakes by 50%", *Wear*, 396–397, **2018**, 135–145, doi: <http://dx.doi.org/10.1016/j.wear.2017.06.018>.
- [15] L. Chasapidis, T. Grigoratos, A. Zygogianni, A. Tsakis, A.G. Konstandopoulos, "Study of Brake Wear Particle Emissions of a Minivan on a Chassis Dynamometer", *Emission Control Science and Technology*, 4, **2018**, 271–278, <https://doi.org/10.1007/s40825-018-0105-7>.

- [16] J. Park, B. Joo, H. Seo, W. Song, J.J. Lee, W.K. Lee, H. Jang, “Analysis of Wear Induced Particle Emissions from Brake Pads during the Worldwide Harmonized Light Vehicles Test Procedure (WLTP)”, *Wear*, 466-467, **2021**, 203539, <https://doi.org/10.1016/j.wear.2020.203539>.
- [17] Y. Liu, S. Wu, H. Chen, M. Federici, G. Perricone, *et.al.*, “Brake Wear Induced PM10 Emissions During the World Harmonised Light-Duty Vehicle Test Procedure-Brake Cycle”, *Journal of Cleaner Production*, 361, **2022**, 132278, <https://doi.org/10.1016/j.jclepro.2022.132278>.
- [18] S-H. Woo, H. Jang, M.Y. Na, H.J. Chang, S. Lee, “Characterization of Brake Particles Emitted from Non-Asbestos Organic and Low-Metallic Brake Pads under Normal and Harsh Braking Conditions”, *Atmospheric Environment*, 278, **2022**, 119089, <https://doi.org/10.1016/j.atmosenv.2022.119089>.
- [19] Lowbrasys Project, EU-H2020, Grant Agreement ID: 636592, [doi:10.3030/636592](https://doi.org/10.3030/636592).
- [20] H. Barosova, S. Chortarea, P. Peikertova, M.J.D. Clift, A. Petri-Fink, *et.al.*, “Biological Response of an in Vitro Human 3D Lung Cell Model Exposed to Brake Wear Debris Varies Based on Brake Pad Formulation”, *Archives of Toxicology*, 92, **2018**, 2339–2351, <https://doi.org/10.1007/s00204-018-2218-8>.
- [21] S. Maiorana, F. Teoldi, S. Silvani, A. Mancini, A. Sanguineti, *et. al.*, “Phytotoxicity of Wear Debris from Traditional and Innovative Brake Pads”, *Environment International*, 123, **2019**, 156–163, <https://doi.org/10.1016/j.envint.2018.11.057>.
- [22] M. Figliuzzi, M. Tironi, L. Longaretti, A. Mancini, F. Teoldi, *et.al.*, “Copper-Dependent Biological Effects of Particulate Matter Produced by Brake Systems on Lung Alveolar Cells”, *Archives of Toxicology*, 94, **2020**, 2965–2979, <https://doi.org/10.1007/s00204-020-02812-4>.
- [23] nPETS Project, EU-H2020, Grant Agreement ID: 954377, [doi:10.3030/954377](https://doi.org/10.3030/954377).
- [24] M. Mathissen, J. Grochowicz, C. Schmidt, R. Vogta, F.H. Farwick zum Hagen, *et.al.*, “A Novel Real-World Braking Cycle for Studying Brake Wear Particle Emissions”, *Wear*, 414–415, **2018**, 219–226, <https://doi.org/10.1016/j.wear.2018.07.020>.
- [25] Particle Measurement Programme (PMP) Informal Working Group, Informal document GRPE\_81\_12, 81st GRPE, 9-11 June 2020, Agenda Item 7.
- [26] S. Gates-Rector, T. Blanton, “The Powder Diffraction File: a Quality Materials Characterization Database”, *Powder Diff.*, 34(4), **2019**, 352-360.

## 4. Elemental Composition Maps

*Maps are always necessary to understand the geography of a place and to figure out which directions can or have to be explored. Similarly, in order to understand where directing the chemical investigation of brake emissions, general compositional maps are needed. As discussed in the introductory chapter, some observational studies reporting elemental composition of non-exhaust brake emissions are currently available in literature. However, they are mostly limited to emissions produced by a single friction couple typology and strongly decoupled to brake market considerations such as the geographical diffusion of the materials and their evolution in recent times. Therefore, a systematic characterization of these emissions is substantially lacking, while the available compositional information are partially obsolete. This chapter reports the chemical composition of thirty-eight PM<sub>10</sub> brake emissions collected during laboratory tests and generated by the coupling of different typologies of braking discs and friction materials dedicated to the original equipment (OE) automotive market. The results here reported show clearly how different starting materials composing the friction couple influence the brake emissions elemental composition. Finally, an overall assessment of elemental composition and distribution of brake emissions in function of different geographical areas, market segments and future technological developments is provided together with corresponding compositional maps.*

### 4.1. Aim of the Study

As discussed in the introduction, the emissions generated by brakes have complex chemical composition, since they are mixtures of worn and tribo-oxidized material arising from the two sides of the tribological interface, which is typically made by objects having heterogeneous and complex composition. Since different materials are used in different regions and market segments, diverse elemental compositions and distributions can be reasonably expected in different geographical areas or as function of different vehicle typologies. Furthermore, new technologies are currently developing in the brake market: materials for both the braking discs and the friction composites are evolving, mainly to address the incoming challenges imposed by the most recent emissions-related legislations and the increasing electrification of the road transport sector.<sup>[1-8]</sup> The major part of this technologies are currently in the prototypal to pre-series production stages and are expected to become dominant in the market in the next five to ten years. Therefore, the compositional profiles of the brake emissions are expected to vary significantly in the next future.

Thus, this chapter is meant to provide a global assessment of the elemental composition of brake emissions as a function of: *i*) different starting materials composing the friction couple (FC); *ii*) distribution of FCs in different regions and market segments; and *iii*)

future technological developments in the brake industry. At this aim, the emissions generated by 38 different FCs were collected and analyzed. All the particulates were sampled in standard laboratory conditions, as described in in *Chapter 2*. In particular, all of them were collected at the same enclosed dynamometric bench, during emissions tests carried out following the WLTP-Brake cycle routine.

## 4.2. Materials

In order to draw the widest possible compositional maps, several different typologies of materials composing the friction couple were involved in this study. In particular, three typologies of braking discs (BDs) from five different producers and three categories of friction materials (FMs) from six different producers were used. Both BDs and FMs groups featured the presence of products which are currently the market standard as well as others which are prototypal concepts. All the different materials and combinations are introduced and described in the next paragraphs.

### 4.2.1 Braking Discs (BDs)

Three different typologies of BDs were used in this investigation, involving both series and prototypal products: *i)* cast iron BDs from two different producers; *ii)* coated BDs from three different producers; and *iii)* carbon-ceramic BDs from one producer. Figure 4.1 reports a visual comparison between the three different typology of braking rotors involved in this study.



**Figure 4.1:** a) GCI BD; b) coated BD; and iii) Carbon-ceramic BD.

Cast-iron BDs represent the current market standard and the widest diffuse braking rotor worldwide for the automotive industry: they are commonly used on all the private and commercial vehicles from all the market segments. More in detail, standard cast iron BDs are usually made by pearlitic and lamellar grey cast iron (GCI). Therefore they are made by an Iron-based alloy, characterized by excellent castability and machinability, as well as relatively low production costs. In turn, GCI suffers of poor corrosion resistance

and relatively modest mechanical and thermal properties, such as hardness, tensile strength and thermal conductivity. Representative microstructure and chemical composition of the GCI BDs employed for this study are reported in Figure 4.2 and Table 4.1, respectively. As can be observed in Table 4.1, the elemental composition of GCI for BDs production is usually characterized by relatively high concentrations of Carbon and Silicon, while all the other elements are found in minor or trace amounts, typically lower than 0.5 wt%. These elements are in general ubiquitous impurities of Iron (such as Mn, Cr and Cu) or can be voluntarily added in the production phase as alloying elements in order to modify the microstructure, thus increasing GCI physico-mechanical properties such as hardness, wear resistance and corrosion resistance (Al, Ti, V, Nb, Mo).<sup>[9-13]</sup>

Element	C	Si	Mn	Cu	Cr	Fe	Others
wt%	3.8	1.8	0.5	0.2	0.1	balance	traces

**Table 4.1:** Elemental composition of a GCI typically used for braking discs production.

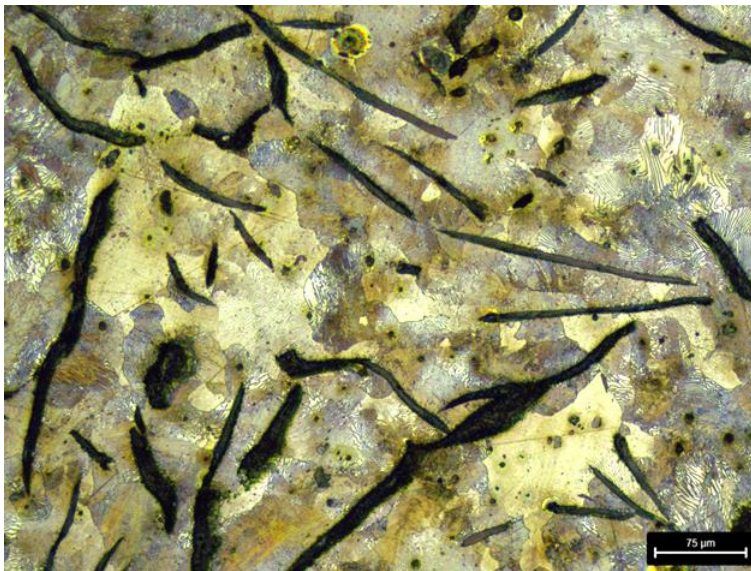


**Figure 4.2:** Microstructure of pearlitic GCI after Nital etching at the metallographic microscope. Detail of the different phases composing the alloy (ferrite, cementite, lamellar graphite and precipitates such as intermetallics and sulfides).

Coated discs are GCI BDs whose braking surfaces are covered with coatings being composed by a wide range of different materials with the specific aim of improving functional properties of the BDs, such as wear and corrosion resistance. Notably, since the overall wear of the brake device is strictly related to its emission level, coated discs are nowadays considered as one of the most promising hardware solution to reduce

particulates generated by brakes.<sup>[3,8,14]</sup> They are a relatively young technology, which in most cases rarely dates back more than 10-15 years and is currently positioned between the prototypal and the small pre-series production stage. However, coated discs are expected to diffuse very quickly into the market in the next years, mainly due to possible future legislation targeting NEE in the road transport sector. Since they are more expensive in respect with the uncoated counterpart, they will likely diffuse first in the medium to high BD market segments. The coatings for BDs can be single layer as well as ensemble of more layers with the most external one representing BD side of the tribological interface. Their thickness is calibrated in order to endure the working life of the BDs, and depending on the material composing the coating, can vary between few tenth to few hundreds of microns. They can be deposited with a wide range of different techniques, such as cold-spraying, high-velocity air/oxygen fuel (HVOF or HVAF) depositions, laser cladding or laser melting deposition. An example of BD coating can be observed in Figure 4.2.

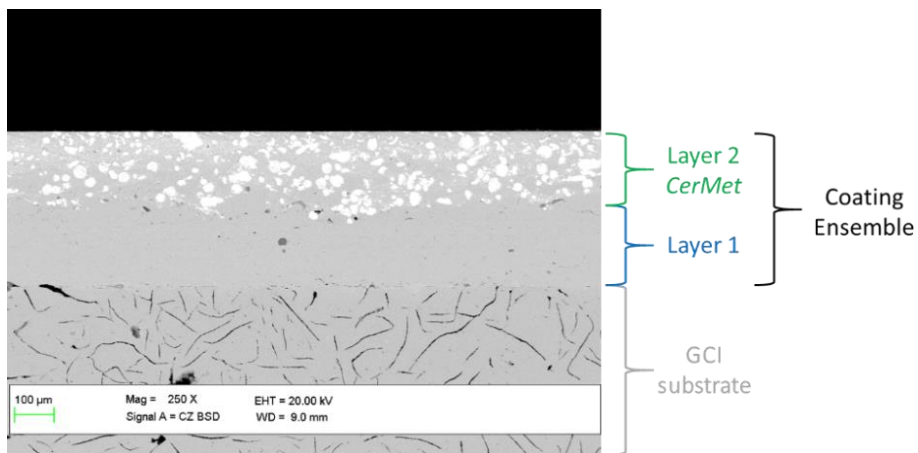


**Figure 4.2:** SEM section image of a coated BD. Detail of the coating ensemble, composed by two different layers deposited on the GCI braking surface.

The materials deposited on the braking surface must exhibit superior physico-mechanical properties in respect to the GCI. In particular, higher hardness, wear resistance and corrosion resistance are specific targets for BD coatings. At the same time, they are required to closely match the thermal properties of the substrate to avoid thermal shock or thermal stress –induced cracking of the braking surface, eventually leading to delamination of the structure and potential safety failure of the braking system. For the same reason, they must assure optimal adhesion with the substrate, with the linking interface able to sustain significant compressive and shear forces. Therefore, materials typically suitable to be applied as BDs coatings are *CerMet* composites, *i.e.* dispersions of ceramic powders (carbides and oxides) in a metallic or

intermetallic matrix, with relative ratio between *Cer* and *Met* fractions suitably tuned to match all the desired functional properties. In particular, the *Cer* components typically provide high hardness and wear resistance to the braking surface, while the *Met* fraction assure the overall integrity of the ensemble and the adhesion to the GCI substrate.

Carbon-ceramic discs are rotors made by infiltrating carbon fiber based preforms with metallic Silicon at very high temperatures. Therefore they are composites featuring the coexistence of the three following main phases: *i*) a Silicon carbides –based matrix; *ii*) elemental Carbon in form of Carbon fibers; and *iii*) unreacted Silicon from the infiltration process, constituting a minor component of the matrix. Figure 4.3 shows a SEM image of the braking surface of a carbon ceramic BD.

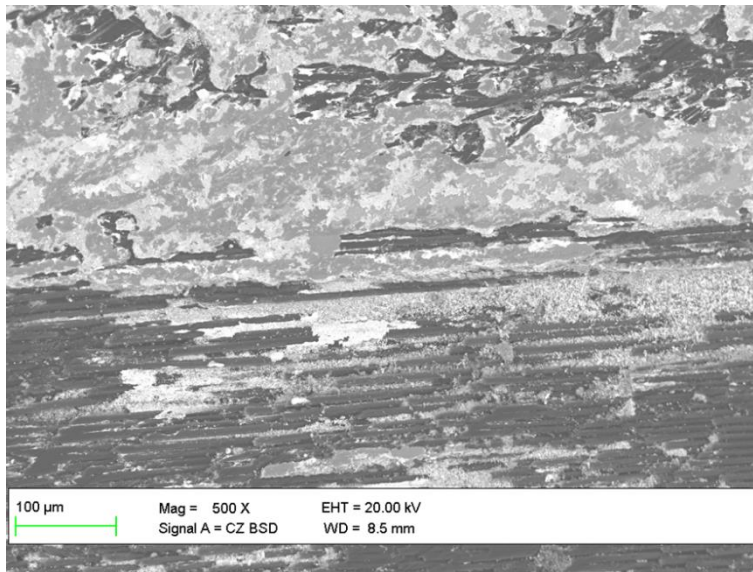


**Figure 4.3:** SEM image of the braking surface of a carbon-ceramic disc. Back-scattered electrons (BSE) are used in order to highlight phase contrast between the Carbon fibers and the SiC/Si matrix.

Silicon carbides, the main matrix component, assures great hardness for the composite material, while carbon fibers guarantee high mechanical strength resistance and providing fracture toughness required for braking rotors. Thus, these discs are characterized by having overall superior mechanical and thermal properties (hardness, wear resistance, thermal shock resistance) and significantly lower weight in respect with the GCI counterpart. At the same time, they exhibit peculiar tribological characteristics.<sup>[15,16]</sup> However, all these excellent functional properties are obtained through expensive production and surface refinement processes. Therefore, they find natural application in high-performance braking systems, such as for racing and high-end vehicles.



#### 4.2.2. Friction Materials (FMs)

Three different typologies of FMs were used in this investigation: and *i*) Non Asbestos Organic (NAO) FMs from three producers; *ii*) Low Steel and Low Metallic (LS/LM) FMs from four different producers; and *iii*) Inorganic (IN) FMs from two different producers. Also in this case, products which are current market standards are used together with prototypal formulations in advanced development stage. All the series braking pads tested are certified compliant with the ECE Regulation 90 (ECE R90)<sup>[17]</sup>, while the prototypal parts are specifically designed to be compliant to the same regulation as well.

Typical compositions for materials of the three different typologies of composites selected for the study are reported in Table 4.2, together with other parameters of interest.

wt%	NAO	LS/LM	IN
<b>Binder</b>	10-20	5-15	10-20
<b>Metals</b>	0-10	15-30	20-30
<b>Abrasives</b>	20-30	25-40	5-15
<b>Lubricants</b>	5-15	20-35	15-25
<b>Fillers</b>	20-40	5-15	0-10
<b>Hardness</b>	80-100	100-150	>150
<b>Friction Coefficient</b>	0.33-0.35	0.35-0.38	0.38-0.42
<b>Normalized Emission</b>	0.2-0.3	1	0.8-0.9

**Table 4.2:** Compositional detail and mechanical properties of different typology of friction materials. Hardness is reported in . Friction coefficient ( $\mu$ ) is reported considering the coupling with standard GCI braking discs.

As can be observed in the table, NAO friction materials exhibit overall higher content of binder and lower content of friction modifiers (strong abrasives and lubricants) in respect with the LS/LM formulations. In particular, metals are frequently absent and, where present, they are always non-ferrous. Conversely, NAO friction materials usually contain significantly higher amount of compounds which can be classified as fillers or mild abrasives. All these compositional features are well coherent with overall slightly lower friction coefficient values (0.33-0.35) and gentler tribological behavior showed by these formulations when coupled against standard GCI BDs. LS/LM and IN formulations are in general characterized by slightly higher binder content and significantly higher metals and friction modifiers concentrations. The larger presence of metals and strong abrasives determines a more aggressive tribological behavior towards the standard GCI braking discs. Thus, more lubricants are usually needed in these formulations in order to stabilize and module their friction coefficient ( $\mu = 0.35-0.38$ ). Finally, IN formulations share overall similar characteristics with the LS/LM family, with a couple of main differences. In particular, these composites are currently being developed in order to

minimize the emissions of organic compounds, thus they are not bound with soft organic resins. On the contrary, inorganic binders such as glasses, cements and geopolymers, are most frequently used. Notably, these binders show in general also significant abrasive capability at the same time. For this reason, they usually contain low amounts of strong abrasives and fillers, while maintaining significant concentrations of lubricants.<sup>[18]</sup>

Differently from the case of the braking discs, the diffusion of the various typologies of friction materials is far more dependent on the geography than the market segment. In spite of a recent general feeling of the brake linings producers oriented towards a higher degree of standardization, regional legislations and historical customer preferences still remain pivotal in determining the distribution of the different categories of friction composites. Therefore, NAO formulations, characterized by lower efficiency, wear and thermal degradation resistance, are extremely diffused in markets where road speed limits are lower, vehicles are lighter and there exist a particular attention to the cleanliness of the rim (North America and Asia). Conversely, LS/LM formulations, which in general exhibit higher braking efficiencies and thermal degradation resistance, are largely diffused in markets where speed limits and vehicle inertias are higher and the customer attention is more shifted towards the braking performance (Europe). Nevertheless, the market segment still retains a minimal influence: for example, high-performance and high-end vehicles mounting Carbon-ceramic BDs cannot be equipped with NAO FMs, since these formulations typically cannot withstand significant thermal and pressure loads for prolonged times. Finally, IN friction materials are products already available only for the car racing market, while they are in developing and prototypal stages for standard applications. Since they are in general characterized by excellent braking performances and thermal stability, they are likely expected to enter the same LS/LM markets once ready for series production.

#### 4.2.3. Friction Couples

The tribological interface and the transfer layer are composed by material arising from both the braking disc and the friction composite. Consequently, the brakes emission composition is fundamentally related to the starting composition of the objects constituting the friction couple (FC). Therefore, it is modulated by the tribological characteristic of the couple itself (relative wear ratio between components) and the interactions with the local environment (tribo-chemical reactions). Since BD and FM materials belonging to a specific category share similar compositional features, the hypothesis underlying this study is that emissions produced by friction couples composed by similar materials share similar compositional characteristic, *i.e.* similar chemical profiles. In order to verify this hypothesis, the elemental composition of PM<sub>10</sub>

particulates produced by thirty eight different friction couples is analyzed and discussed in detail in the next paragraphs. The selected friction couples are divided in five different categories, representing realistic couplings of materials following geographical, market and technological considerations reported in the previous sections. More in detail, the five FCs selected combinations are composed as follows: *i) Category 1*: grey cast-iron (GCI) BDs + LS/LM FMs, representative for the current standard EU market; *ii) Category 2*: grey cast-iron (GCI) BDs + inorganic (IN) bound prototypal FMs, representative of possible short to medium term EU market development; *iii) Category 3*: grey cast-iron (GCI) BDs + non asbestos organic (NAO) FMs, representative of the current standard US and Asian markets; *iv) Category 4*: coated BDs + specially developed LS/LM FMs, representative of the short to medium term EU market development; and *v) Category 5*: Carbon-Ceramic (CC) BDs + specially developed LS/LM FMs, representing the high-end market. Table 4.3 summarizes all the different FCs categories reported in this chapter, together with the corresponding labels adopted along the text.

Category	BDs	FMs	n° of FCs	Label
1	Grey Cast-Iron (GCI)	Low Steel/Low Metallic (LS/LM)	10	LS/LM
2	Grey Cast-Iron (GCI)	Inorganic Bound (IN)	10	IN
3	Grey Cast-Iron (GCI)	Non Asbestos Organic (NAO)	5	NAO
4	Coated (CTD)	Low Steel/Low Metallic (LS/LM)	10	CTD
5	Carbon-Ceramic (CC)	Low Steel/Low Metallic (LS/LM)	3	CC

**Table 4.3:** Summary of the selected FCs categories, number of FCs analyzed for each category, corresponding materials combinations and labels.

### 4.3. Experimental

All the PM<sub>10</sub> samples analyzed in this chapter were collected during emission tests performed in controlled laboratory conditions (see *Chapter 2* for further details) and following the WLTP-Brake cycle.<sup>[19]</sup> The elemental composition of the investigated PM<sub>10</sub> particulates was characterized by the mean of the Energy Dispersive X-Ray Spectroscopy (EDXS), following the protocol described in detail in *Chapter 2* and briefly summarized in the next lines. Each measurement was performed with the following power parameters: V = 20 kV, I<sub>beam</sub> = 300 pA. Real acquisition time was set to 500 s, with detector deadtime never exceeding the 20%. The samples surfaces were always positioned at the ideal working distance for the employed system (WD = 8.5±0.1 mm). For each investigated PM<sub>10</sub> sample, five different areas of approximatively 400 x 300 μm

are analyzed. Elemental concentration results are then averaged and reported always together with the corresponding standard deviations (SD).

## 4.4. Results

The following section summarizes all the obtained results in terms of elemental composition of the investigated brake emissions powders. For each sample, only average results and corresponding standard deviations are reported in the next paragraphs. All the results from each single measurement can be found in *Appendix 4*.

### 4.4.1. Category 1: GCI BDs + LS/LM FMs (LS/LMs)

*Category 1* regroups all the investigated emissions generated by the coupling of standard GCI braking discs with ECE R90 LS/LM friction materials. These emissions arise from ten different FCs, combining mainly series products on both side of the friction couple. Nevertheless, two prototypal GCI BDs and one prototypal FM specifically developed for emission reduction were also used. Selected BDs were from two different producers, while FMs from three different producers. As already described in the previous paragraph, this category represents a good picture of the material couplings currently dominant in the EU market, with the only exception of the high-end segment. Figure 4.4 reports an EDXS spectrum for each analyzed sample, while the following Table 4.4 summarizes the average elemental concentrations. As can be observed, it is clearly evident that all these investigated PM<sub>10</sub> samples have elemental composition dominated by three main elements, *i.e.* with concentration always higher than 10 wt%: they are Iron, Oxygen and Carbon, accounting together for about the 90% of the total PM<sub>10</sub> mass in most of the cases. On the other side, the remaining minority part of the emissions is composed by a wide range of secondary (concentration between 10 and 1 wt%), minor elements (concentration between 1 and 0.01 wt%) and trace elements (frequently or always found close or below the estimated quantification limit for the EDXS probe (0.01 wt%). In between these elements, some of them are always found, such as Magnesium, Aluminum, Silicon, Sulfur, etc., and therefore are referred along the text as ubiquitous. Conversely, other elements appear with lower frequencies, such as Potassium, Titanium and Barium. Looking at the main elements, Iron is a clear marker for the wear of the GCI BDs. However, significant amount of Fe has to be ascribed also to the friction material consumption, since LS/LM formulations typically contain appreciable amounts of Iron powders and steel fibers. Oxygen is due to the consumption of both sides of the friction couple as well as the interaction of the worn material with the local environment. On one side, tribo-oxidation occurring at the BD surface represents a significant contribution. At the same time, inorganic oxides contained in the FM as abrasives and fillers are a clear source of this element. Carbon is a main marker for the wear of the

friction materials, since LS/LMs usually contain significant amounts of organic compounds (resins and organic fibers) as well as C-based lubricants (graphites and cokes); in addition, secondary amounts of strong abrasives (carbides) and fillers (carbonates) are also, in general, always present. At the same time, minor but not negligible contribution of Carbon is due to the consumption of the GCI graphite lamellae. Finally, secondary and minor elements are mainly due to the formulation of the specific friction material and are in general due to minor components or impurities. Similarly, trace elements are mainly due to impurities coming from the raw materials of the friction composites as well as from the cast-iron alloys.

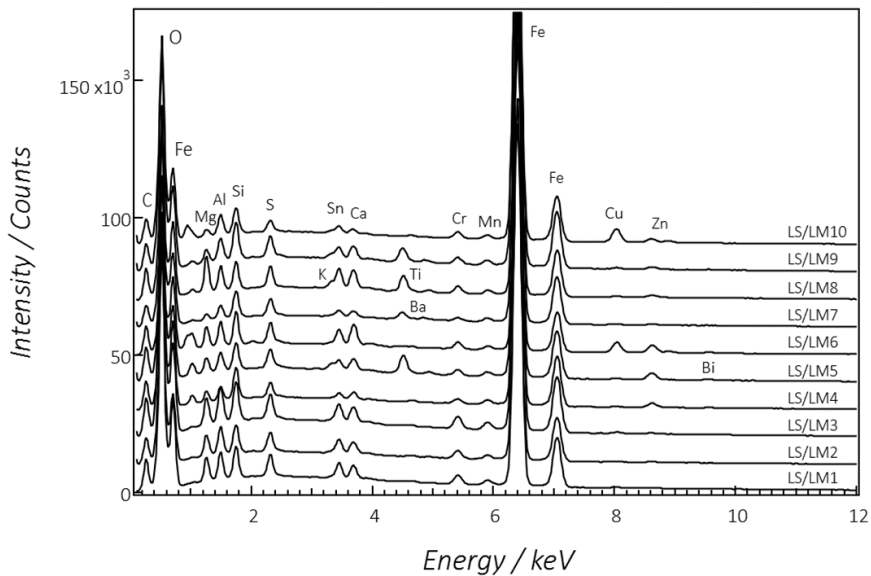


**Figure 4.4:** Comparison between EDXS spectra for each PM<sub>10</sub> sample collected during emission tests of FCs belonging to the *Category 1* (GCI BDs + LS/LM FMs).

#### 4.4.2. *Category 2: GCI BDs + IN FMs (INs)*

*Category 2* regroups all the investigated emissions generated by the coupling of standard GCI braking discs with inorganic bound friction materials. FMs reported in this category are mostly prototypal products, with only one material being currently on the market (for racing applications). All the materials belonging to this category come from the same producer. Since these FMs formulations do not contain any organic binder, their overall content of Carbon is significantly lower in respect to the LS/LMs counterpart and exclusively due to elemental (Graphites and Cokes) or inorganic Carbon (carbides and carbonates). They represent a possible future development of FCs for the European market, specifically voted to the reduction of volatile organic compounds (VOCs) emissions due to the oxidation of the FMs organic binders.

Category 1: GCI BDs + LS/LM FMs

	LS/LM1		LS/LM2		LS/LM3		LS/LM4		LS/LM5		LS/LM6		LS/LM7		LS/LM8		LS/LM9		LS/LM10	
	wt%	SD	wt%	SD	wt%	SD	wt%	SD	wt%	SD	wt%	SD	wt%	SD	wt%	SD	wt%	SD	wt%	SD
<b>Fe</b>	54.6	1.7	53.3	0.9	51.9	0.6	58.4	1.1	52.6	0.8	56.7	1.8	61.5	1.0	52.3	2.5	55.5	1.2	53.5	1.0
<b>O</b>	27.4	1.2	27.2	0.7	29.5	0.3	22.8	0.7	25.1	0.4	17.3	0.9	20.4	0.7	24.2	1.7	24.6	1.3	25.8	0.9
<b>C</b>	10.1	0.8	9.0	0.3	10.0	0.4	11.2	0.7	11.6	0.8	11.2	1.2	10.2	0.4	11.0	0.7	10.2	0.4	9.6	0.6
<b>Sn</b>	1.7	0.2	2.26	0.03	1.73	0.01	0.7	0.2	0.89	0.05	1.84	0.04	0.94	0.04	2.41	0.04	1.11	0.03	1.01	0.06
<b>Si</b>	1.30	0.08	1.42	0.01	1.25	0.03	1.49	0.06	1.24	0.03	1.78	0.08	1.54	0.05	1.3	0.1	1.60	0.04	1.31	0.04
<b>Mg</b>	1.24	0.05	1.84	0.03	1.29	0.01	0.83	0.02	1.11	0.05	1.26	0.09	0.54	0.02	2.5	0.1	0.89	0.02	0.56	0.04
<b>Al</b>	1.15	0.07	1.64	0.05	1.32	0.04	0.75	0.02	1.01	0.04	1.18	0.06	0.86	0.02	1.23	0.06	1.05	0.05	1.20	0.08
<b>S</b>	0.73	0.06	0.95	0.06	0.77	0.02	0.70	0.02	0.83	0.02	0.90	0.02	0.94	0.02	0.98	0.05	0.86	0.05	0.55	0.01
<b>Cr</b>	0.63	0.05	0.91	0.02	0.85	0.02	0.42	0.01	0.49	0.02	0.75	0.05	0.37	0.03	0.67	0.05	0.56	0.02	0.61	0.02
<b>Mn</b>	0.43	0.02	0.41	0.02	0.64	0.02	0.46	0.03	0.41	0.02	0.37	0.01	0.47	0.03	0.39	0.02	0.43	0.02	0.43	0.01
<b>Zn</b>	0.26	0.03	0.28	0.03	0.23	0.01	1.6	0.1	2.37	0.05	2.7	0.1	0.45	0.03	0.86	0.05	0.75	0.06	1.34	0.05
<b>Cu</b>	0.22	0.04	0.13	0.02	0.18	0.01	0.15	0.04	0.23	0.06	3.1	0.2	0.23	0.05	0.31	0.03	0.29	0.04	3.89	0.08
<b>Ca</b>	0.17	0.04	0.38	0.01	0.29	0.01	0.4	0.2	0.45	0.02	0.74	0.02	0.22	0.01	0.60	0.02	0.44	0.00	0.00	-
<b>Mo</b>	0.00	-	0.22	0.08	0.00	-	0.00	-	0.00	-	0.00	-	0.00	-	0.00	-	0.00	-	0.00	-
<b>V</b>	0.00	-	0.09	0.01	0.00	-	0.00	-	0.00	-	0.00	-	0.00	-	0.00	-	0.00	-	0.00	-
<b>Ti</b>	0.00	-	0.00	-	0.05	0.00	0.00	-	1.33	0.04	0.06	0.01	0.00	-	1.14	0.04	0.57	0.01	0.02	0.02
<b>Bi</b>	0.00	-	0.00	-	0.00	-	0.16	0.02	0.00	-	0.00	-	0.00	-	0.00	-	0.00	-	0.00	-
<b>K</b>	0.00	-	0.00	-	0.00	-	0.00	-	0.37	0.01	0.00	-	0.00	-	0.00	-	0.00	-	0.00	-
<b>Ba</b>	0.00	-	0.00	-	0.00	-	0.00	-	0.00	-	0.00	-	1.38	0.05	0.00	-	1.04	0.04	0.00	-
<b>P</b>	0.00	-	0.00	-	0.00	-	0.00	-	0.00	-	0.15	0.01	0.03	0.01	0.00	-	0.00	-	0.05	0.02
<b>Na</b>	0.00	-	0.00	-	0.00	-	0.00	-	0.00	-	0.00	-	0.00	-	0.00	-	0.00	-	0.08	0.06
<b>Ni</b>	0.00	-	0.00	-	0.00	-	0.00	-	0.00	-	0.00	-	0.00	-	0.00	-	0.00	-	0.00	-

**Table 4.4:** Summary of elemental composition as obtained for the investigated FCs from *Category 1*. Average results are reported together with the corresponding standard deviations (SD) over five measurements, in red. Main elements are highlighted in grey. Ubiquitous elements are highlighted in blue, while frequent elements in green. Finally, infrequent elements are highlighted in orange.

Category 2: GCI BDs + IN FMs

	IN1		IN2		IN3		IN4		IN5		IN6		IN7		IN8		IN9		IN10	
	wt%	SD	wt%	SD	wt%	SD	wt%	SD	wt%	SD	wt%	SD	wt%	SD	wt%	SD	wt%	SD	wt%	SD
Fe	68.28	1.54	66.73	0.86	64.85	0.51	67.24	0.49	64.15	0.78	63.23	0.39	67.18	0.90	59.21	0.61	57.94	0.61	64.23	0.37
O	18.95	1.02	22.31	0.45	23.94	0.27	22.44	0.67	25.21	0.57	23.64	0.30	20.08	0.72	26.09	0.24	26.80	0.34	19.23	0.30
C	6.42	0.55	4.46	0.60	4.20	0.22	4.78	0.31	3.00	0.83	6.90	0.44	6.40	0.78	6.16	0.67	5.65	0.55	12.43	0.65
Si	2.12	0.07	2.67	0.04	2.81	0.11	2.39	0.02	2.99	0.09	2.47	0.05	2.50	0.07	3.35	0.04	3.72	0.07	2.37	0.08
Al	0.90	0.06	1.12	0.04	1.06	0.03	0.81	0.04	1.15	0.05	0.97	0.03	0.97	0.04	1.52	0.02	1.66	0.03	0.04	0.01
Zn	0.57	0.06	1.05	0.09	0.93	0.07	0.86	0.05	1.23	0.11	1.00	0.10	1.06	0.08	0.02	0.04	0.00	-	0.28	0.04
Mn	0.56	0.02	0.54	0.02	0.48	0.04	0.54	0.04	0.46	0.03	0.45	0.03	0.53	0.02	0.45	0.02	0.44	0.00	0.51	0.01
K	0.49	0.01	0.60	0.01	0.86	0.02	0.42	0.03	0.88	0.01	0.61	0.01	0.62	0.01	1.16	0.02	1.32	0.01	0.00	-
S	0.44	0.04	0.16	0.01	0.20	0.02	0.10	0.01	0.07	0.01	0.07	0.01	0.11	0.00	0.27	0.01	0.21	0.01	0.11	0.01
Sn	0.20	0.05	0.00	-	0.00	-	0.00	-	0.00	-	0.00	-	0.00	-	0.94	0.02	1.43	0.03	0.29	0.02
Cu	0.16	0.03	0.19	0.02	0.20	0.05	0.27	0.04	0.27	0.09	0.21	0.03	0.24	0.08	0.20	0.03	0.19	0.03	0.24	0.04
Cr	0.15	0.02	0.18	0.01	0.13	0.02	0.15	0.02	0.15	0.03	0.14	0.01	0.14	0.00	0.12	0.01	0.12	0.02	0.21	0.01
Mo	0.74	0.13	0.00	-	0.00	-	0.00	-	0.00	-	0.00	-	0.00	-	0.00	-	0.00	-	0.00	-
Mg	0.01	0.01	0.00	-	0.00	-	0.00	-	0.00	-	0.00	-	0.00	-	0.00	-	0.00	-	0.00	-
Ca	0.01	0.00	0.00	-	0.00	-	0.00	-	0.00	-	0.00	-	0.00	-	0.00	-	0.00	-	0.00	-
Ti	0.00	-	0.00	-	0.33	0.03	0.00	-	0.51	0.02	0.29	0.02	0.19	0.01	0.52	0.02	0.50	0.01	0.00	-
P	0.00	-	0.00	-	0.00	-	0.00	-	0.00	-	0.00	-	0.00	-	0.00	-	0.03	0.01	0.04	0.01
V	0.00	-	0.00	-	0.00	-	0.00	-	0.00	-	0.00	-	0.00	-	0.00	-	0.00	-	0.02	0.01

**Table 4.5:** Summary of elemental composition as obtained for the investigated FCs from *Category 2*. Average results are reported together with the corresponding standard deviations (SD) over five measurements, in red. Main elements are highlighted in grey. Ubiquitous elements are highlighted in blue, while frequent elements in green. Finally, infrequent elements are highlighted in orange.

Figure 4.5 reports an EDXS spectrum for each analyzed PM<sub>10</sub> sample, while Table 4.5 summarizes their average elemental concentrations. As can be observed in both the graph and the composition summary table, the overall chemical profiles of FCs from *Category 2* are similar to those from *Category 1*. About the 90-95% of the total particulate mass is usually composed by three elements only, which also in this case are Iron, Oxygen and, secondary, Carbon. However, the overall amount of Iron is significantly higher in respect to the LS/LMs counterpart, while the Carbon concentration is lower, rarely approaching the 10 wt%. The remaining 5-10% of these particulates is therefore composed by a dispersion of minor ubiquitous or frequent elements. Finally several minor and trace elements are observed more infrequently, frequently at the edge between the quantification and the detection limits. The presence of all these elements depends alternatively on the specific FM formulation as well as the impurities in the BD cast-iron.

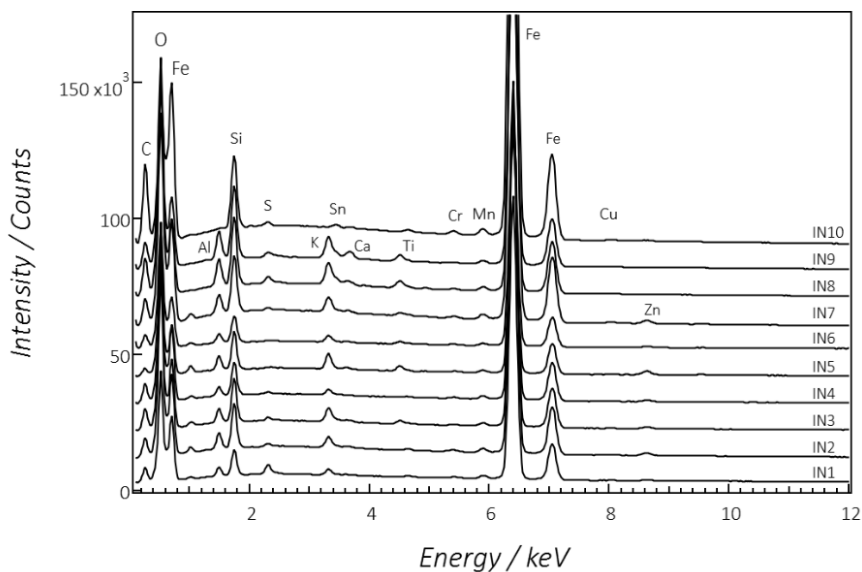


**Figure 4.5:** Comparison between EDXS spectra for each PM<sub>10</sub> sample collected during emission tests of FCs belonging to the *Category 2* (GCI BDs + IN FMs).

In these emissions, Iron still remain a not specific marker for the wear of both sides of the tribological interface. Indeed, inorganic bound FMs exhibit higher hardness and more aggressive tribological behavior towards the GCI BDs. Therefore, a major part of the Iron is likely expected to be produced by mechanical abrasion. Still, the inorganic bound FMs formulations contain appreciable amounts of Iron based species (15-25 wt%). Oxygen is also a not specific marker, since it can arise from both the tribo-oxidation of the GCI BD braking surfaces as well as from the inorganic oxides composing the FM mix



(abrasives, fillers and inorganic binder). Carbon arises as well from both sides of the friction couple, since it is contained in the friction mix (graphites and cokes lubricants) and, secondary in the GCI alloy. Secondary and trace elements are mainly due to the consumption of the friction material or impurities in the GCI alloy and FMs raw materials. Among these elements, Silicon is most frequently found in relatively high concentrations (2-4 wt%), since commonly used inorganic binders are cements, geopolymers and pyrolyzed Silicon resins.

#### 4.4.3. Category 3: GCI BDs + NAO FMs (NAOs)

*Category 3* collects the emissions generated by the coupling of standard GCI braking discs with NAO friction materials. All the materials belonging to this category are series products. In particular, NAO formulations are commercialized as automotive original equipment products in the US and Asian markets. Therefore, the emissions collected from these friction couples are specifically representative for these areas. Since NAO friction materials typically produces lower emissions in respect with the LS/LM counterpart when coupled against standard GCI braking discs, they are currently under preliminary scrutiny for possible application also in the EU. Thus, the chemical composition of these emissions might eventually represent a possible evolution of the current EU emissions composition (which is nowadays more similar to what is reported for *Category 1*). Within *Category 3*, two similar GCI BDs from a single producer are coupled against five different friction composites from three producers.

Figure 4.6 shows the comparison between the EDXS spectra acquired for each friction couple (one spectra per FC). Table 4.6 summarizes the average elemental concentration as obtained from the elemental analysis. As can be immediately observed, the emissions produced by GCI BDs and NAO FMs have elemental composition profile which is significantly different in respect with the emissions from *Category 1* and *2* couples. Iron, Oxygen and Carbon, still represent the major fraction of the particulate mass. However, they sum up about the 60 to 75% of the PM<sub>10</sub> emissions. This is mainly due to the overall significantly lower content of Iron, which is determined by the combination of the two following causes: *i*) NAO FMs typically do not contain any Fe-based compounds; and *ii*) NAO FMs show in general a gentler tribological behavior towards the GCI braking surfaces, *i.e.* they cause lower abrasion of the rotor, while being characterized by a more pronounced tribo-oxidative wear mechanism. Notably, the first point leads also to the observation that Iron is a specific marker for the wear of the BDs in emissions from *Category 3*. Conversely, the Oxygen remain a not specific marker for the consumption of both sides of the tribological interface. On one side, the amount of inorganic oxides, carbonates, sulfates, etc., is typically higher in NAO formulations in respect with the LS/LM counterpart. On the other hand, a significant contribution arising from the tribo-

oxidation of the cast-iron cannot be neglected. Finally, Carbon is a preferential marker for the consumption of the friction material, since it typically causes low wear of the BDs, thus limiting the contribution of the graphite lamellas from the GCI. Between the secondary elements, three of them are always found with concentrations higher than 4 wt%: Zirconium, Barium and Titanium. The significant presence of these elements is well coherent with the typical NAO composition, always characterized by significant concentration of Zirconium oxides and silicates (abrasives), titanates (abrasives and reinforcements) and Barium sulfate (filler). Copper is also always found in the observed emissions, but with bimodal dispersion: secondary amounts when the starting FMs is a Copper-full or Copper-less formulation (two cases out of five) or minor amounts when the starting friction composite is a Copper-free formulation (three cases out of five).

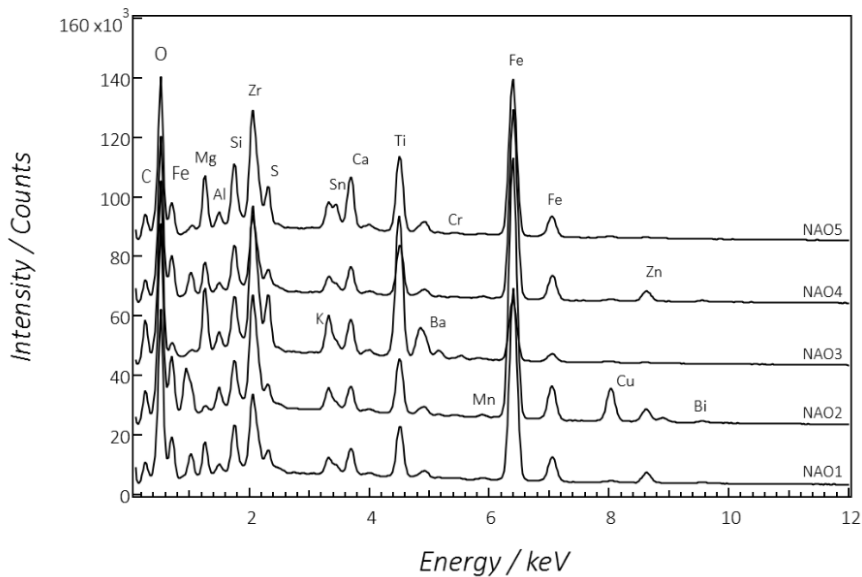


**Figure 4.6:** Comparison between EDXS spectra for each PM<sub>10</sub> sample collected during emission tests of FCs belonging to the *Category 3* (GCI BDs + NAO FMs).

Other ubiquitous secondary elements are Silicon, Aluminum, Sulfur and Magnesium, which are mainly due to the consumption of the friction material. Potassium, Zinc and Tin are also found in secondary amounts, but with lower frequency: their presence is dependent on the specific FM formulation. Finally several minor and trace elements are observed, such as Sodium, Calcium, Manganese and Bismuth. They are due to minor components of the friction materials and/or to impurities of the FM raw materials or the GCI.

Category 3: GCI BDs + NAO FMs

	NAO1		NAO2		NAO3		NAO4		NAO5	
	Average	SD	Average	SD	Average	SD	Average	SD	Average	SD
O	34.3	0.6	29.1	0.6	34.1	0.5	24.6	0.6	34.8	0.4
Fe	28.6	0.5	30.4	0.5	8.1	0.3	37.2	0.8	22.5	0.4
C	11.1	0.3	6.0	0.4	18.7	0.6	18.2	0.7	9.6	0.4
Zr	7.9	0.1	9.9	0.1	10.1	2.3	3.9	0.1	11.4	0.1
Ti	3.22	0.03	2.84	0.05	7.1	2.5	2.90	0.07	4.7	0.1
Ba	1.99	0.09	2.51	0.05	11.8	0.3	4.2	0.1	3.7	0.1
Mg	1.91	0.03	0.35	0.03	2.7	0.1	0.44	0.01	3.24	0.04
Si	1.89	0.03	1.54	0.04	1.41	0.06	1.56	0.02	2.44	0.03
Al	0.48	0.02	0.90	0.03	0.61	0.03	0.28	0.02	0.70	0.01
S	0.87	0.02	0.87	0.02	2.06	0.08	1.17	0.02	1.84	0.02
Cu	0.43	0.06	7.4	0.1	0.18	0.04	3.45	0.09	0.42	0.03
Cr	0.14	0.01	0.13	0.01	0.15	0.01	0.13	0.01	0.17	0.10
Ca	1.31	0.02	0.00	-	1.59	0.05	0.89	0.03	2.62	0.05
Zn	3.62	0.09	3.6	0.2	0.17	0.02	0.00	-	0.39	0.03
Sn	1.01	0.02	2.54	0.03	0.00	-	0.00	-	1.04	0.05
K	0.94	0.01	1.33	0.02	1.36	0.02	0.90	0.03	0.00	-
Mn	0.19	0.03	0.21	0.02	0.00	-	0.24	0.01	0.00	-
Bi	0.00	-	0.41	0.05	0.00	-	0.00	-	0.00	-
Na	0.00	-	0.00	-	0.00	-	0.00	-	0.36	0.12

**Table 4.6:** Summary of elemental composition as obtained for the investigated FCs from *Category 3*. Average results are reported together with the corresponding standard deviations over five measurements (SD, in red). Main elements are highlighted in grey. Ubiquitous elements are highlighted in blue, while frequent elements in green. Finally, infrequent elements are highlighted in orange.

#### 4.4.4. Category 4: CTD BDs + LS/LM FMs (CTDs)

Category 4 collects the emissions generated by the coupling of coated braking discs with specially developed LS/LM friction materials. BDs inside this category are mainly products in prototypal to pre-series production stage, from three different producers. On the other hand, the friction composites are LS/LM formulations for the automotive original equipment market from five different producers. Some of them are suitably modified to withstand the coupling against braking surfaces with higher hardness and abrasive capability in respect with the GCI rotors. As previously introduced, coated discs are specifically developed in order to reduce the BD wear and the overall emission of the friction couple. This is obtained by deposition of materials harder than the cast-iron, typically *CerMet* composites, by means of several different processes. Therefore these rotors have significantly higher costs in respect with the standard GCI BDs. For this reason, they represent an evolution of the medium to the high-end BD market and they are expected to find wide distribution in the next 5 to 10 years.

Figure 4.7 and Table 4.7 report respectively a sample EDXS spectra collected for each PM<sub>10</sub> specimen generated by Category 4 FCs and their elemental composition. As can be qualitatively noticed, these emissions are characterized by a wider distribution of elements in respect with the emissions from the previous categories. This is an effect of the early development stage of these friction couples, with several different materials and modifications being investigated in order to find the most robust technological solutions.

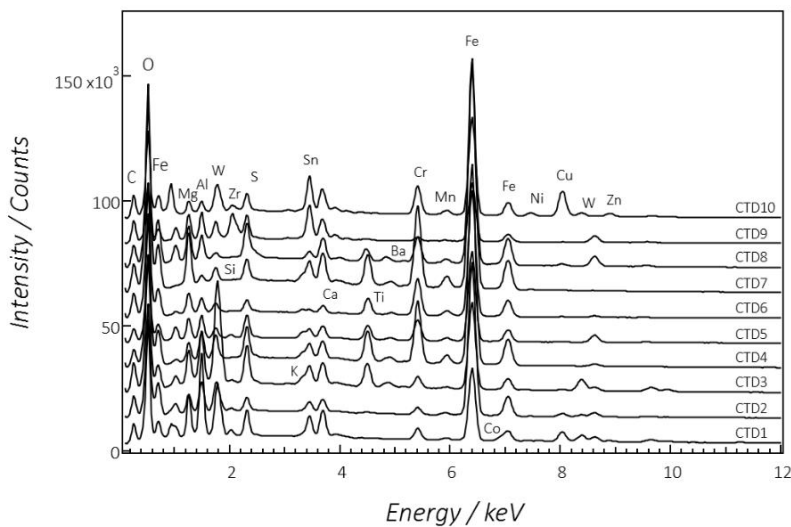


**Figure 4.7:** Comparison between EDXS spectra for each PM<sub>10</sub> sample collected during emission tests of FCs belonging to the Category 4 (CTD BDs + LS/LM FMs).

Category 4: CTD BDs + LS/LM FMs

	CTD1		CTD2		CTD3		CTD4		CTD5		CTD6		CTD7		CTD8		CTD9		CTD10	
	Average	SD	Average	SD	Average	SD	Average	SD	Average	SD	Average	SD	Average	SD	Average	SD	Average	SD	Average	SD
O	31.2	0.4	27.2	0.1	35.1	0.2	29.9	0.6	32.2	1.6	33.2	1.2	31.8	0.4	29.0	0.4	28.6	0.8	25.0	0.7
Fe	17.9	0.4	38.5	0.7	17.3	0.3	40.7	0.5	30.3	2.1	36.0	1.9	35.6	1.1	37.9	0.6	19.4	1.5	24.4	0.6
C	11.4	0.6	15.6	2.1	14.4	0.4	4.0	0.3	7.4	1.8	13.7	1.6	11.4	1.5	11.3	0.9	18.5	4.2	12.6	1.7
Al	6.1	0.1	2.6	0.2	3.20	0.03	2.12	0.04	2.98	0.04	1.35	0.03	0.39	0.02	1.66	0.06	2.7	0.2	0.98	0.05
Sn	4.99	0.06	2.3	0.2	3.00	0.02	4.41	0.05	4.96	0.32	0.29	0.07	2.59	0.12	1.43	0.02	11.1	0.7	8.9	0.2
Cu	4.38	0.09	1.4	0.1	0.50	0.03	0.21	0.02	0.28	0.06	0.18	0.04	0.21	0.02	0.65	0.06	0.18	0.04	12.2	0.3
Mg	3.86	0.05	2.0	0.2	2.44	0.02	1.78	0.05	3.37	0.04	2.45	0.05	3.6	0.1	3.0	0.1	3.2	0.2	1.50	0.01
S	2.10	0.02	1.00	0.09	2.50	0.02	1.89	0.04	2.47	0.06	0.97	0.04	1.02	0.02	1.93	0.02	2.4	0.1	1.40	0.06
Cr	1.98	0.03	1.0	0.2	1.64	0.01	8.32	0.09	4.8	0.4	7.11	0.50	8.6	0.4	3.5	0.4	0.87	0.08	5.0	0.1
Zn	2.85	0.08	2.6	0.3	1.89	0.06	1.07	0.03	6.0	0.3	1.00	0.09	0.11	0.06	4.3	0.1	5.2	0.4	0.00	-
Ca	1.63	0.02	0.75	0.08	1.18	0.03	0.00	-	0.00	-	0.69	0.03	1.22	0.06	1.27	0.03	0.51	0.03	0.53	0.02
Ti	0.00	-	0.00	-	2.37	0.04	3.08	0.05	2.6	0.2	2.30	0.16	2.41	0.10	0.19	0.04	0.18	0.02	0.00	-
Si	0.86	0.01	1.7	0.2	0.00	-	1.59	0.05	1.16	0.03	0.74	0.03	0.64	0.01	0.34	0.01	1.5	0.1	0.80	0.04
W	9.0	0.1	2.6	0.4	14.47	0.07	0.00	-	0.00	-	0.00	-	0.00	-	0.00	-	0.00	-	4.2	0.2
Co	1.24	0.04	0.00	-	0.00	-	0.00	-	0.00	-	0.00	-	0.00	-	0.00	-	0.00	-	0.00	-
Ba	0.00	-	0.39	0.06	0.00	-	0.00	-	0.00	-	0.00	-	0.00	-	2.71	0.06	0.00	-	0.00	-
K	0.00	-	0.00	-	0.00	-	0.69	0.02	1.11	0.07	0.00	-	0.00	-	0.00	-	0.00	-	0.00	-
Mn	0.14	0.02	0.33	0.02	0.00	-	0.25	0.01	0.00	-	0.00	-	0.31	0.02	0.00	-	0.00	-	0.00	-
P	0.41	0.01	0.00	-	0.00	-	0.00	-	0.38	0.01	0.00	-	0.00	-	0.00	-	0.00	-	0.00	-
Ni	0.00	-	0.00	-	0.00	-	0.00	-	0.00	-	0.00	-	0.11	0.02	0.00	-	0.00	-	1.21	0.08
Bi	0.00	-	0.00	-	0.00	-	0.00	-	0.00	-	0.00	-	0.00	-	0.80	0.03	0.00	-	0.00	-
Zr	0.00	-	0.00	-	0.00	-	0.00	-	0.00	-	0.00	-	0.00	-	0.00	-	5.7	0.3	1.24	0.05

**Table 4.7:** Summary of elemental composition as obtained for the investigated FCs from *Category 4*. Average results are reported together with the corresponding standard deviations over five measurements (SD, in red). Main elements are highlighted in grey. Ubiquitous elements are highlighted in blue, while frequent elements in green. Finally, infrequent elements are highlighted in orange.

In *Category 4*, Iron, Oxygen and Carbon represent the dominant contribution to the total PM<sub>10</sub> mass, accounting together for about the 70% of the weight. Similarly to the case of *Category 3* FCs, the concentration of Iron is significantly lower in respect with the counterpart from *Category 1* and 2. However, the vast majority of the coatings are composed also by Iron alloys (mainly steels and Fe-Cr alloys). Thus, Fe is not a specific marker for the consumption of one side of the tribological interface. Conversely, Oxygen may be expected to represent a more specific marker for the wear of the friction composite, since the Iron species composing the BD braking surfaces are significantly less oxidized in respect with the cast-iron. Similarly, the Carbon represents a more specific marker for the wear of the friction material: in spite of the frequent presence of inorganic carbides inside the BD coatings, their consumption is significantly lower in comparison with the softer friction composite. Secondary and minor elements here account typically about the 30 % of the total PM<sub>10</sub> mass. Several secondary elements are found ubiquitously, such as Al, Mg, S, Cu, Sn and Cr. Others are found frequently (such as Si, Ca, Zn, Ti) or only rarely, such as Co, W, Ni, Ba and Zr. The presence of the non-ubiquitous elements is strongly dependent by the specific coating composition and FM formulation. Finally, some other elements are found in minor and trace amounts, such as P, K and Mn. They are typically due to minor components of the friction material as well as impurity in the constituting raw materials.

#### 4.4.5. *Category 5: CC BDs + LS/LM FMs (CCs)*

The last reported category of emissions collects PM10 particulates generated by the coupling of Carbon-ceramic braking discs with specially developed LS/LM friction materials. BDs and FMs inside this category are series products for automotive original equipment for the high-end market. In particular, two CC BDs coming from the same producer and two FMs from two different produces are combined and tested.

EDXS spectra and the obtained elemental concentrations are reported in Figure 4.8 and Table 4.8, respectively. As can be observed, the three main elements characterizing all the investigated emissions, i.e. Fe, O and C, still represent the major contribution to the particulate mass (about 70%). However their distribution inside the sum is different in respect with all the previous investigated emissions. In particular, Fe and C are found in very low and high concentrations, respectively. This is well in agreement with the composition of the CC braking discs, which do not contain Iron. Consequently, Fe represents a specific marker for the consumption of FM in these friction couples. Similarly, the Oxygen can be considered as a preferential marker for the wear and tribo-oxidation of the friction material, since CC BDs typically exhibit lower wear and oxidation in respect with the GCI counterpart. For the same reason, in spite of the fact that Carbon can arise from both the side of the friction couple, the contribution from the BD side of

the tribological interface can be considered as a minor fraction. Secondary and minor elements constitute about the 30% of the particulate mass. Among them, the ones which are found ubiquitously are Cr, Sn, Cu, Zn, Al, Si, Mg, S and Ca. They arise mainly from the consumption of the friction materials. Since the overall consumption of the FM is significantly higher in respect with the CC DB wear, some of the secondary elements, such as Cu and Sn, are even locally found to have concentrations higher than 10 wt% (one sample out of three). A further evidence of the preponderant presence of material worn by the friction composite is represented by the concentration of Silicon, which is largely contained in the BD braking surface and always present in modest amounts in LS/LM FMs. Indeed, the Silicon amount is found on average around the 3 wt%: on one side, this represents the highest overall concentration for this element among all the FCs categories. On the other hand, it is a concentration value substantially not dissimilar to those observed in the emissions from the previous coupling typologies (1-2.5 wt%). Only Zirconium is found as frequent secondary elements, while Titanium and Phosphorous are registered as trace and infrequent elements. However, the number of FCs here is more lower in respect with the previous categories: thus, the statistical diffusion of secondary, minor and trace elements is more limited.

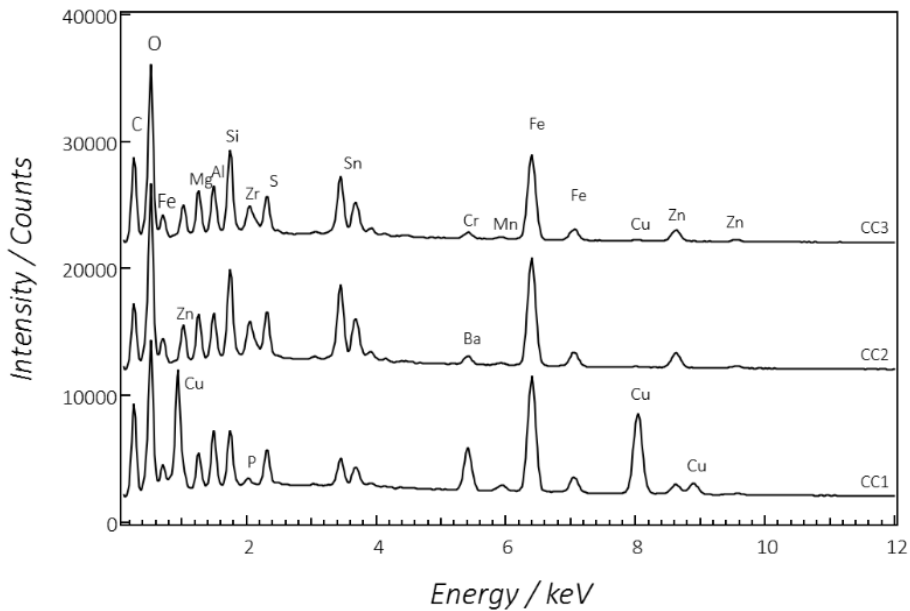


**Figure 4.8:** Comparison between EDXS spectra for each PM<sub>10</sub> sample collected during emission tests of FCs belonging to the *Category 5* (CC BDs + LS/LM FMs).

	CC1		CC2		CC3	
	Average	SD	Average	SD	Average	SD
C	25.7	1.2	18.1	0.7	27.1	3.2
O	22.4	0.5	35.8	0.3	35.5	1.0
Fe	14.3	0.5	15.6	0.5	12.6	0.9
Cu	19.4	0.6	0.19	0.03	0.23	0.02
Cr	3.7	0.2	0.89	0.03	0.68	0.06
Sn	3.51	0.06	10.5	0.3	8.1	0.6
Zn	2.8	0.1	5.1	0.2	4.0	0.3
Al	2.4	0.1	1.92	0.07	2.0	0.2
Si	2.1	0.1	3.36	0.06	3.0	0.3
Mg	1.88	0.03	2.49	0.04	2.3	0.2
S	1.1	0.1	2.01	0.03	1.54	0.08
Ca	0.26	0.04	0.33	0.02	0.30	0.06
Zr	0.00	-	3.54	0.04	2.5	0.1
Ti	0.00	-	0.11	0.01	0.09	0.02
P	0.30	0.02	0.00	-	0.00	-

**Table 4.8:** Summary of elemental composition as obtained for the investigated FCs from Category 5.

Average results are reported together with the corresponding standard deviations over five measurements (SD, in red). Main elements are highlighted in grey. Ubiquitous elements are highlighted in blue, while frequent elements in green. Finally, infrequent elements are highlighted in orange.

Since the overall consumption of the FM is significantly higher in respect with the CC DB wear, some of the secondary elements, such as Cu and Sn, are even locally found to have concentrations higher than 10 wt% (one sample out of three). A further evidence of the preponderant presence of material worn by the friction composite is represented by the concentration of Silicon, which is largely contained in the BD braking surface and always present in modest amounts in LS/LM FMs. Indeed, the Silicon amount is found on average around the 3 wt%: on one side, this represents the highest overall concentration for this element among all the FCs categories. On the other hand, it is a concentration value substantially not dissimilar to those observed in the emissions from the previous coupling typologies (1-2.5 wt%). Only Zirconium is found as frequent secondary elements, while Titanium and Phosphorous are registered as trace and infrequent elements. However, the number of FCs here is more lower in respect with the previous categories: thus, the statistical diffusion of secondary, minor and trace elements is more limited.

#### 4.5. Summary

All the elemental characterization results previously reported are summarized in the tables and figures showed in the following paragraphs, with the aim of providing visual and direct evidences for the comparative assessment of the elemental composition of the investigated emissions.



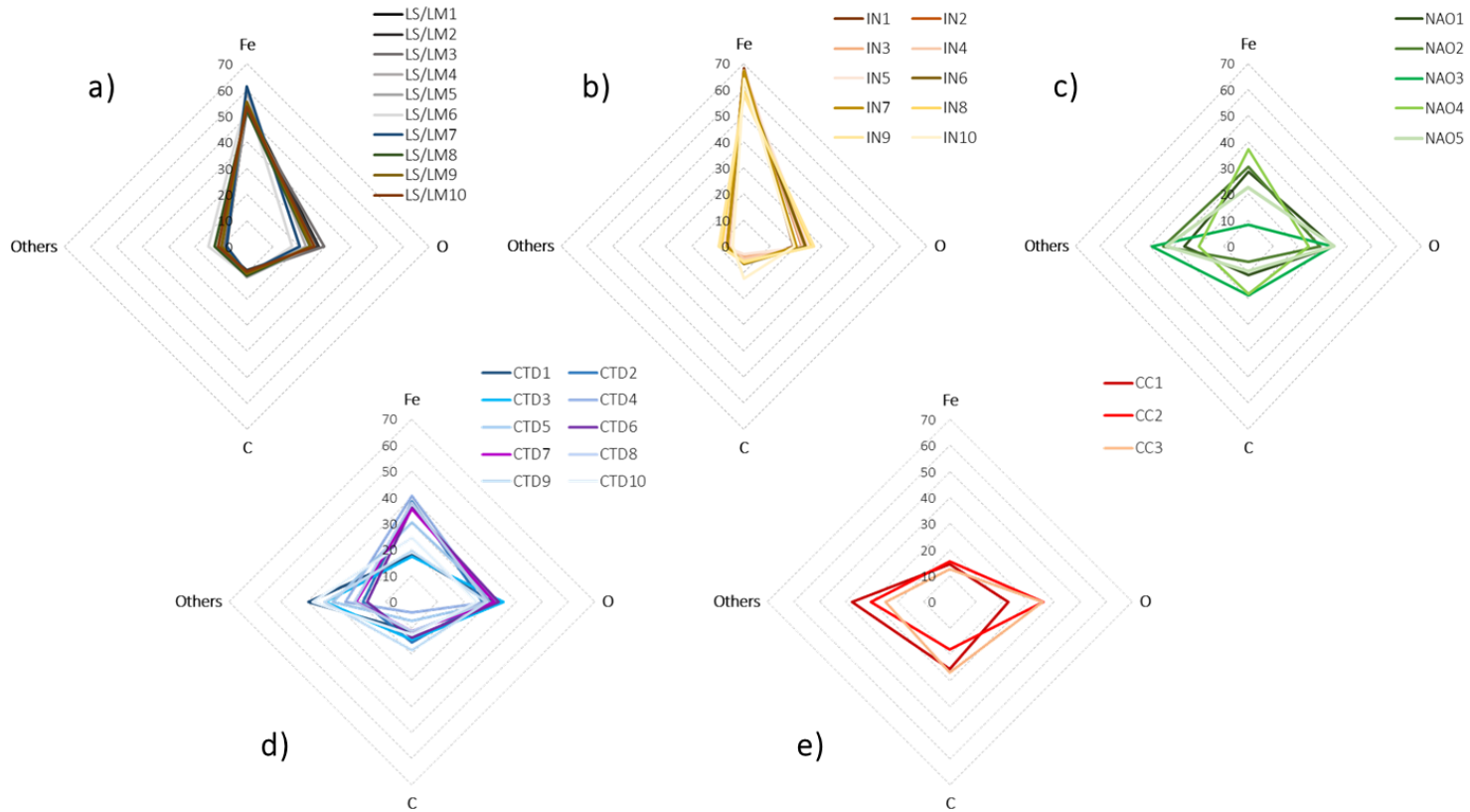


**Figure 4.10:** Kiviat plots for main components distribution in PM<sub>10</sub> emissions from each category of friction couple. Grey, green, red and blue bars indicate respectively the content of Iron, Oxygen, Carbon and Other elements. **a)** *Category 1:* GCI BDs + LS/LM FMs; **b)** *Category 2:* GCI BDs + IN FMs; **c)** *Category 3:* GCI BDs + NAO FMs; **d)** *Category 4:* Coated BDs + LS/LM FMs; and **e)** *Category 5:* CC BDs + LS/LM FMs.

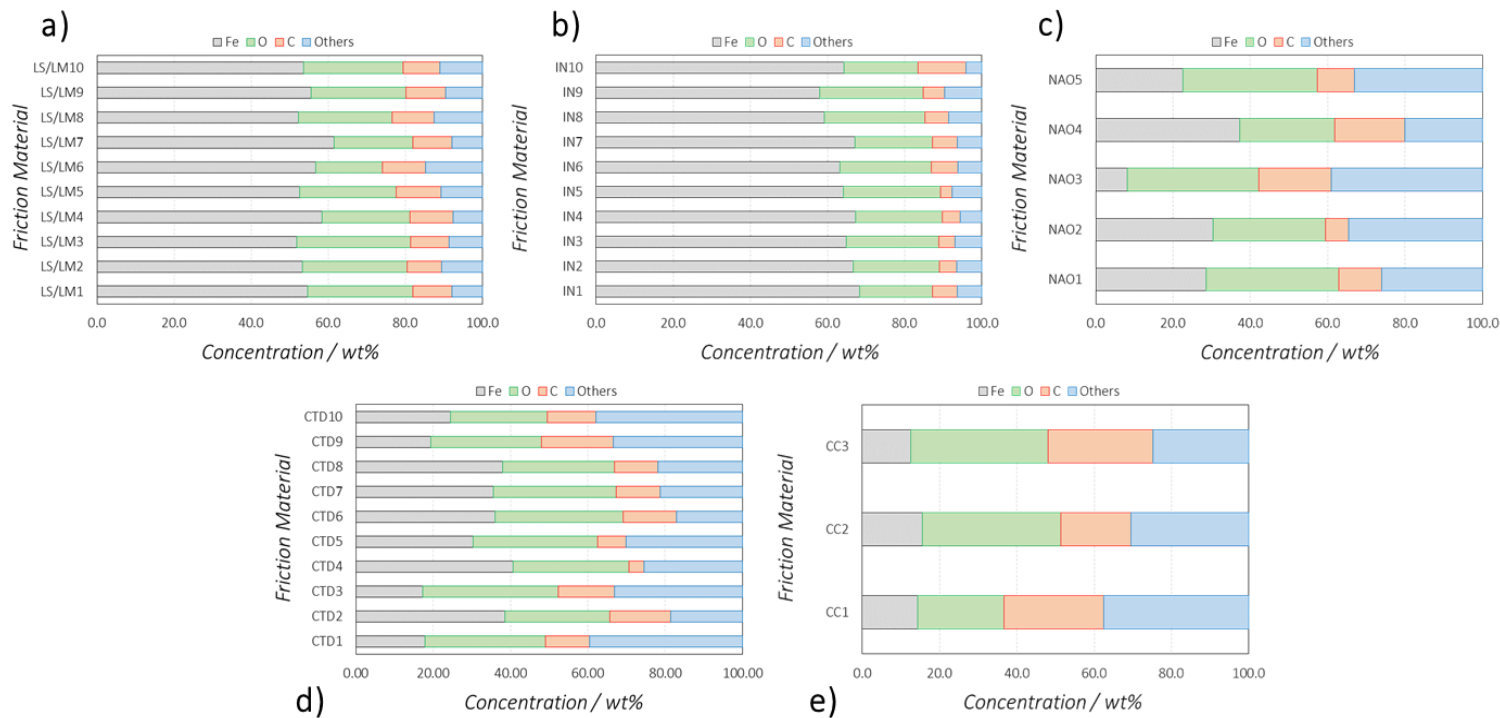


**Figure 4.10:** Distribution of the main components for PM<sub>10</sub> emissions from each category of friction couple. Grey, green, red and blue bars indicate respectively the content of Iron, Oxygen, Carbon and Other elements. **a)** Category 1: GCI BDs + LS/LM FMs; **b)** Category 2: GCI BDs + IN FMs; **c)** Category 3: GCI BDs + NAO FMs; **d)** Category 4: Coated BDs + LS/LM FMs; and **e)** Category 5: CC BDs + LS/LM FMs.

#### 4.5.1. Main Elements

As clearly showed along *Paragraph 4.4.*, the elemental composition of the PM<sub>10</sub> particulates generated by brakes is in general largely dominated by three main elements, which are Iron, Oxygen and Carbon. Taking all the obtained results together, it is possible to observe that the sum of the three main elements is typically higher than the 70% of the total PM<sub>10</sub> mass, while easily reaching the 90-95% when GCI BDs are coupled against LS/LM and IN FMs. Figure 4.9 and 4.10 summarizes the distribution of the main elements in all the emissions generated by each identified category of friction couple. Dependently on the specific compositional features of the starting materials composing the FC, as well as from their tribological behavior and wear mechanism, the relative ratio of the main elements can vary significantly. For example, NAO FMs coupled with GCI BDs generate emissions with lower content of Iron and higher content of Oxygen in respect with the counterparts generated by LS/LM and IN FMs. Similar trends are observed in the PM<sub>10</sub> emissions generated by CTD BDs coupled against LS/LM FMs. Finally, PM<sub>10</sub> particulates generated by friction couples featuring CC BDs are characterized by the lowest concentrations of Iron and the highest of Carbon. Secondary and minor elements represent only an extremely modest fraction of the total weight of the PM<sub>10</sub> emissions in particulates generated by FCs belonging to *Category 1* and *2* (GCI BDs + LS/LM/IN FMs). Conversely, they represent the 25-30 % of the total mass of the emissions when PM<sub>10</sub> particulates from *Category 3, 4* and *5* are considered. All these observations are summarized in Figure 4.11, Figure 4.12 and Table 4.9.

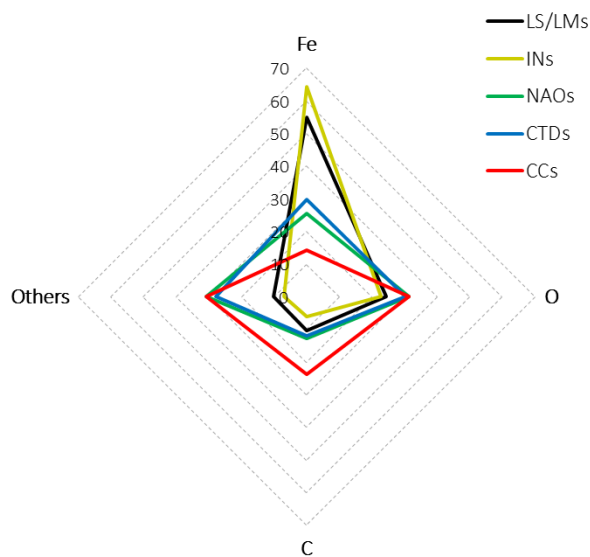


**Figure 4.11:** Overall distribution of the main components in PM<sub>10</sub> emissions from each category of friction couple.

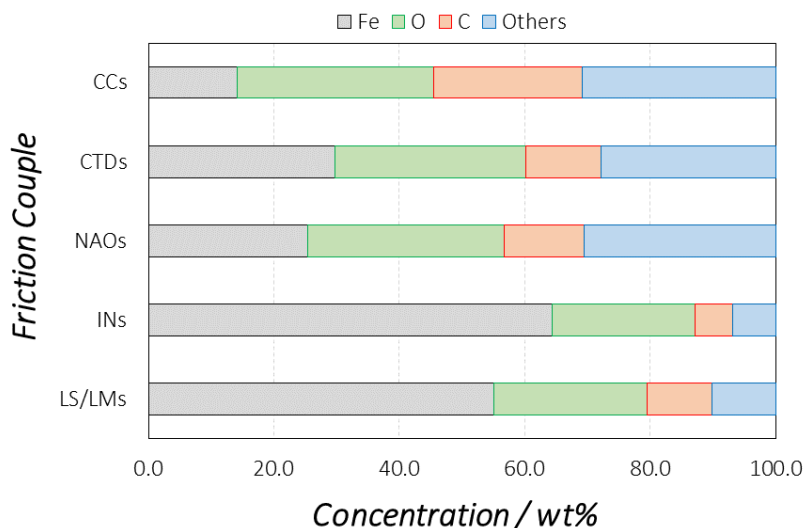


**Figure 4.12:** Overall distribution of the main components in PM<sub>10</sub> emissions from each category of friction couple.

wt%	LS/LMs	INs	NAOs	CTDs	CCs
<b>Fe</b>	55.0	64.3	25.4	29.8	14.2
<b>O</b>	24.4	22.9	31.3	30.3	31.3
<b>C</b>	10.4	6.0	12.7	12.0	23.7
<b>Others</b>	10.1	6.8	30.6	27.9	30.8

**Table 4.9:** Comparison of main elements in emissions generated by different FCs. The concentrations reported are the average of all the main elements concentrations in each category of emissions.

Taking all the results together, it is clearly possible to distinguish between characteristic elemental distribution profiles generated by different combinations of starting materials composing the friction couple. More in detail, *Category 1* friction couples (GCI BDs + LS/LM FMs) produce emissions exhibiting an elemental distribution profile strongly polarized towards the Iron. Emissions generated by *Category 2* (GCI BDs + IN FMs) friction couples share overall similar compositional features, but showing even higher concentrations of Iron and overall lower content of Oxygen, Carbon and other elements. These observations are well coherent with the overall lower content of Carbon in the inorganic bound FMs and with a higher abrasive capability of such materials towards the GCI BD, which likely play an important role in generating particulates with an overall lower oxidation level of the Iron.<sup>[20-22]</sup> In addition, it is also possible to comparatively infer

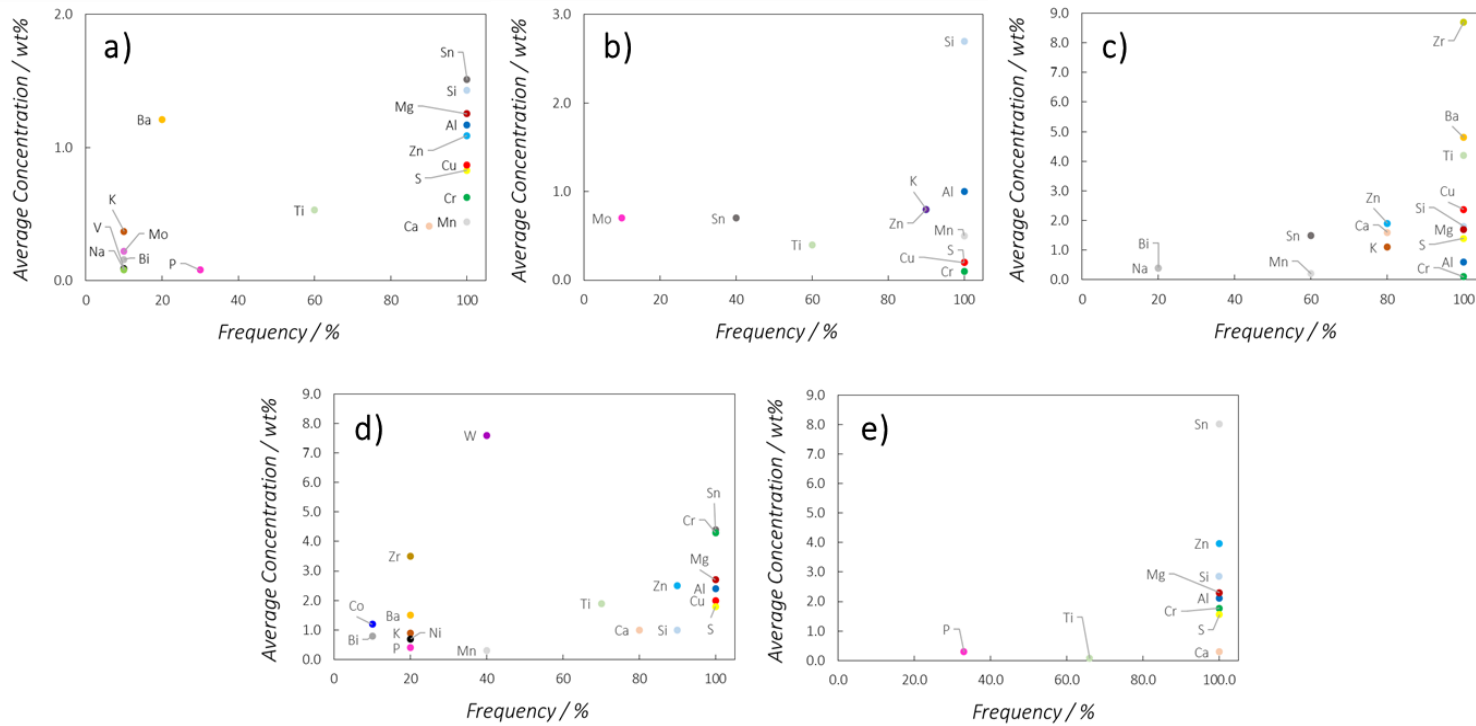
that about the 40 wt% of the Carbon produced in emissions from *Category 1* (GCI BDs + LS/LM FMs) friction couples has most likely organic origin. More detailed insights into the Carbon speciation are reported in *Chapter 5 (5. Speciation)*. Emissions produced by friction couples from *Category 3* (GCI BDs + NAO FMs) and *Category 4* (Coated BDs + LS/LM FMs) share similar elemental distribution profiles. They are characterized by significant lower amounts of Iron in respect with the counterparts from *Category 1* and *2*, while having slightly higher content of Oxygen and significantly higher amounts of other elements. Also in these cases, the characteristic elemental profile is well coherent with the tribological characteristic of these friction couples.<sup>[21,22]</sup> In particular, when looking at the *Category 3* FCs (GCI BDs + NAO FMs), it is reasonable to expect an overall lower direct abrasion of the rotor, since NAO FMs typically exhibit lower friction coefficients and are softer materials in respect with the LS/LM counterparts.<sup>[23]</sup> Therefore, the higher amount of Oxygen is due to the combination of the two following factors: *i)* higher adhesive character in the friction mechanism, therefore resulting in higher tribo-oxidation of the Iron worn by the rotor; and *ii)* higher amount of material worn from the friction composite, *i.e.* higher amount of inorganic oxides, carbonates, silicates, etc., arising from the FM side of the tribological interface. Similar influence of the specific tribological mechanism is determined when assessing the elemental distribution profile of the emissions generated by FCs from *Category 4* (Coated BDs + LS/LM FMs). More in detail, since rotor coatings are typically made by *CerMet* composites, therefore exhibiting significantly higher hardness in respect to the cast-iron, also in this case a significantly higher amount of material worn from the friction composite side of the friction couple has to be expected inside the generated particulates.<sup>[14,22,23,24]</sup> In spite of having very similar elemental distribution profiles, it is anyway possible to observe slight differences in the overall Iron concentration in emissions between *Category 3* and *Category 4*: indeed, particulates generated by NAO FMs show in general slightly lower amount of Iron in respect with the counterparts produced by Coated BDs. Notably, also this observation is good in agreement with the compositional characteristic of the tribological interface. In particular, NAO FMs typically do not contain metallic Iron species (Fe powders, steel fibers, etc.), while conversely *CerMet* coatings for rotors are in general composed by dispersions of ceramics within Fe-based alloys. Furthermore, it is possible to assume that in emissions from *Category 3* FCs, the Iron is mostly due to the wear of the braking disc, while in the emissions from *Category 4* FCs, it arises mostly from the consumption of the friction material. Finally, the emissions generated by the friction couples from *Category 5* exhibit peculiar relative abundance between the main constituents. More in detail, the elemental distribution profiles of the PM<sub>10</sub> particulates produced within this category are significantly polarized towards the Carbon corner, while exhibiting the overall lowest amount of Iron. Also in this case, the compositional and tribological characteristic of the friction couple is pivotal

in determining the elemental distribution profile.<sup>[15,16]</sup> Indeed, the extremely low content of Iron is easily explained by the Carbon-ceramic nature of the braking discs. Therefore, in these emissions Iron can be considered as a specific marker for the consumption of the friction material. In addition, the significant presence of Oxygen and other elements in these particulates can be ascribed to the higher relative consumption of the friction composite when working against a Carbon-Ceramic BD, which is significantly harder in respect with the GCI counterpart.

#### 4.5.2. Secondary and Minor Elements

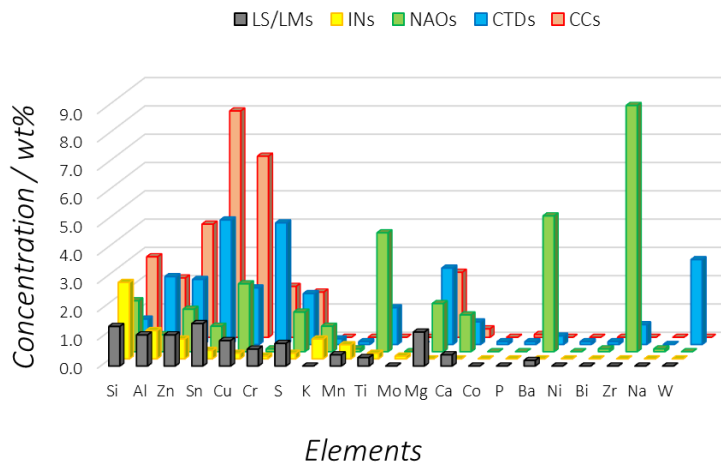
As observed in the previous paragraph, for all the investigated PM<sub>10</sub> particulates, the main elements are Iron, Oxygen and Carbon, which can be considered as characteristic constituents for the brake emissions. Nevertheless, significant amount of other elements are also found, typically ranging from 10 to 30% of the total particulate mass. These elements are usually found in far lower concentrations in respect with the principal ones and are mainly due to the consumption of the friction material. Therefore they are mostly case-specifically dependent on the friction composite formulation. Nevertheless, looking at all the collected results, it is still possible to aggregate the obtained chemical information to identify trends and draw some general conclusions. First of all, it is possible to notice that some of these elements are always found, while others appear with lower frequency. Therefore, they can be categorized on the basis of their appearance frequency as: *i) Ubiquitous*, when always found; *ii) Frequent*, when found in more than the 50% of the analyzed particulates; and *iii) Infrequent*, when appearing in less than the 50% of the investigated PM<sub>10</sub> emissions. In addition, it is also possible to further categorize them on the basis of their typical concentrations as: *i) Secondary*, when appearing with overall concentration between 10 and 1 wt%; and *ii) Minor*, when found with overall concentration between 1 and 0.01 wt%. To be highlighted that 0.01 wt% is selected as inferior limit since it represent an overall empirical quantification limit for the EDXS probe. Several additional elements can be found in concentrations lower than the 0.01 wt%, *i.e.* in **Trace** or **Ultra-Trace** amounts. These last elements are not assessed nor investigated in this work.

Figure 4.13 reports the dispersion diagrams of secondary and minor elements, as defined in the previous lines, for the PM<sub>10</sub> emissions generated by the different investigated FCs categories. In particular, the appearance frequency of a selected element within the emissions belonging to a specific category is plotted on the *x-axis*, while the *y-axis* accounts for the element concentration. Figure 4.14 summarizes the average concentration of secondary and minor elements weighted over their appearance frequency within the specific categories. Referring to *Category 1*, Mg, Al, Si, Zn and Sn are found as ubiquitous secondary elements, while only Ba is found to appear in secondary amounts with low frequency.



**Figure 4.13:** Frequency and average concentration of secondary and minor elements for PM<sub>10</sub> emissions from each investigated category of friction couple. **a)** Category 1: GCI BDs + LS/LM FMs; **b)** Category 2: GCI BDs + IN FMs; **c)** Category 3: GCI BDs + NAO FMs; **d)** Category 4: Coated BDs + LS/LM FMs; and **e)** Category 5: CC BDs + LS/LM FMs.

Mg, Al, Si are commonly contained in friction materials in forms of oxides, carbonates, silicates and alumino-silicates, mostly behaving as abrasives or fillers. Similarly, Ba can be used in form of Baryte (Barium sulphate), behaving as well as filler. Between these elements, only Si can be found also in the cast irons: it is typically used as alloying element in limited concentrations (0.1-2.0 wt%). Zn is typically used in two main forms inside the friction composite: as metal (for Fe anodic protection) or as ZnS (lubricant).



**Figure 4.14:** Average concentrations of secondary and minor elements weighted over their frequency appearance within the specific category of emission. **Grey** - Category 1: GCI BDs + LS/LM FMs; **yellow** - Category 2: GCI BDs + IN FMs; **green** - Category 3: GCI BDs + NAO FMs; **blue** - Category 4: Coated BDs + LS/LM FMs; and **red** - Category 5: CC BDs + LS/LM FMs.

Similarly, Sn is frequently used in the friction composite in metallic or sulfide forms, respectively as friction stabilizer and solid lubricant. All the other observed elements are typically found in minor amounts ( $1 < [x] < 0.01$  wt%) or rarely: they are Na, P, S, K, Ca, Ti, V, Cr, Mn, Cu, Mo and Bi. Among these elements, the vast majority is mainly due to compounds that can be typically used in the friction composites. K and Ca are due mainly to silicates, alumino-silicates and hydroxides, respectively used as fillers and pH modifiers. S is mainly due to metal sulfides, commonly used as solid lubricants, and, secondary, to insoluble sulfates that can be infrequently used as fillers. Ti can be found in alumino-silicates as well as in form of titanates, behaving respectively as fillers and friction modifiers. Bi, similarly to Zn and Sn, is used both in form of metal and sulfide, covering substantially similar functions. Cr, Cu and Mo can be found on both sides of the friction couple. In particular, they are typical alloying elements or impurities of cast-irons (and more in general of all the Fe-based alloys). At the same time, they can be used in the friction composite in form of: *i*) spinel oxides (Cr), as abrasives; *ii*) sulfides (Cu and Mo), as solid lubricants; and *iii*) metallic form (Cu), as friction stabilizer. Mn is likely the only minor element mostly due to the wear of the GCI BD, since it is a common impurity for Fe-based alloys, while is extremely rarely found in raw materials for friction








composites. Finally, Na and P are found rarely and in concentrations close to the detection limit of the EDXS probe. They are most likely due to minor components or impurities of the friction material. Among all these considerations, it is worth to highlight two main points. First of all, it is evident that the friction material contributes in secondary fashion to the overall mass of the PM<sub>10</sub> particulates generated by *Category 1* FCs. Second and most important, Cu is found to be only a secondary non ubiquitous or a minor contribution in the investigated emissions *from Category 1* FCs, which represent the current and next future standard couplings for the automotive original equipment market in EU. This observation well reflects the progressive dismissal of Cu-based raw materials in friction composites for the referenced markets, following the most recent legislations cited in the introduction of this thesis. However, minor or trace amounts of Cu can be likely expected to be always found in brakes emissions, since Cu often comprises in cast iron. Moving to the emissions generated by *Category 2* FCs, it is to be highlighted that, in spite of being treated with the main emission constituents for sake of symmetry with the other FCs categories, C is actually a secondary ubiquitous contribution in these PM<sub>10</sub> particulates. It is typically found in concentrations around 5-7 wt%, *i.e.* the lowest overall concentrations reported among all the PM<sub>10</sub> particulates generated by the different investigated typologies of FCs. Notably, this observation is extremely coherent with the absence of organic binders in the FMs of *Category 2* FCs. In addition to C, only Al and Si are found ubiquitously as secondary contributions. These two elements are indeed main constituents of several inorganic binders, such as geopolymers, cements and silicon resins. Thus, they give account of the consumption of the friction material. Other ubiquitous but minor elements are S, Mn, Cr and Cu, which mainly arise from the wear of the rotor. Finally, Zn, K, Ti, Sn and Mo are also found in minor amounts, but with progressively lower frequency. Therefore, they are likely due to some of typical compounds of the friction composite, as already described for emissions generated by FCs belonging to *Category 1*. Particulates generated by *Category 3* FCs show significantly higher amount of secondary elements, for the reasons already discussed in the previous paragraph. Zr, Ba, Ti, Cu, Si, Mg and S are found in concentrations exceeding the 1 wt% on average basis. The possible origin of the major part of these elements is already reported in the previous line with the only exception of Zr, which appear for the first time in significant amounts, thus representing a specific marker for *Category 3* emissions. Indeed, Zr is commonly used in form of oxide (ZrO<sub>2</sub>) and silicate (ZrSiO<sub>4</sub>), which are respectively used as filler with modest abrasive capability and strong abrasive in NAO FMs. Emissions generated from *Category 4* FCs show also significant amounts of secondary and minor elements, due to the specific tribological behavior. All ubiquitous elements are found in secondary amounts. They are Mg, Al, S, Cr, Cu, Sn. In particular, Mg, Al, Cu, S and Sn can be considered as specific markers for the consumption of the friction material, since they are typically found in LS/LM FMs, in

the forms already described in the previous lines. Conversely Cr is a non-specific marker. It can be found in the FMs as already reported. However, the overall higher Cr amounts found in this group of emissions are more completely justified by the fact that several BD coatings are made by at least one intermetallic/alloy component (such as steel, Fe-Cr alloys, etc.). Ca, Si, Ti and Zn are also found frequently in secondary amounts. Also these elements are mainly due to the consumption of the friction composite, since they are constituents of several raw materials already described. Zr, Ba and W are found infrequently, but with overall significant concentrations. The origin of Zr and Ba was already discussed, while W appear for the first time in brake emissions. It is a specific but not ubiquitous marker for the wear of the BD coating, since it can be found in form of carbide in some *CerMet* formulations. Finally, Co was observed rarely (one out of ten PM<sub>10</sub> samples). Also in this case, it represents a specific marker for the wear of the BD, since it can be found in some metallic alloys for *CerMet* coatings. Notably, this specific element was observed only in one single proof of concept test, featuring the presence of a coating solution which can not found way to industrialization due to both safety and economic reasons. Thus, its presence in brakes emissions is expected to be completely negligible when coated BDs will appear on the market. Finally, K, P, Mn, Ni, Bi are found in minor amounts or rarely. The origin of K, P, Mn and Bi was already discussed. As far as Ni is concerned, it is likely due to the wear of some BD coatings, since some alloys for *CerMet* coatings (steel, Ni-Cr alloys, etc.) might contain this metal. It is worth to highlight that emissions from *Category 3* and *4* were found to share similar overall elemental composition profiles when assessing the main constituents. Notably, secondary elements distribution can be used to effectively discriminate between the two emission categories. More in detail, PM<sub>10</sub> particulates generated by *Category 3* FCs were found to exhibit ubiquitously significant amounts of Zr, Ba and Ti. Conversely, these three elements are found more infrequently and with significant lower concentrations when looking at the counterparts from *Category 4* FCs. Therefore, the overall presence and relative abundance of Zr, Ba and Ti can likely be used as specific proxy for emissions generated by *Category 3* FCs. Finally, moving to emissions from *Category 5* FCs, it is possible to observe significant amounts of secondary elements, such as Mg, Al, S, Si, Cr, Cu, Zn, and minor amounts of Ti and P. All these elements, with the only partial exception of Si, are due to the wear of the friction material, which is significant in this category of FCs. Their origin compound were already reported. Conversely Si is found in several raw materials for braking pads production as well as in the Carbon-ceramic composite constituting the BD side of the tribological interface. This double origin helps to justify the overall higher concentration of Si found here in respect to all the other emissions categories. To be highlighted that *Category 5* features a limited number of investigated FCs. Thus, the overall distribution of the secondary elements here has a lower statistical value in respect to all the other emissions categories.

#### 4.5.3. Overall Summary for Introduction to Next Investigations

Table 4.10 reports all the elemental composition main characteristics of the emissions generated by the five investigated categories of FCs. The table is intended to represent an overall summary of all the observations described and discussed in the two previous paragraphs. As can be observed, the chemistry of the brake emissions is largely linked to Iron and its oxidation compounds. Indeed, Iron and Oxygen are always found to be between the main elements, with Iron being dominant (> 50 wt%) in emissions from *Category 1* and *2* FCs. Therefore, the speciation of Iron-based compounds inside brake emissions represents a pivotal point toward a more detailed chemical characterization of such particulates. For this reason, the topic will be largely discussed in the next chapter (Chapter: 5. *Speciation*). In particular, wide investigation by mean of X-Ray Diffraction (XRD) and X-Ray Absorption Near Edge Spectroscopy (XANES) probe is reported to assess the presence and the relative abundance of different Iron compounds. Notably, XANES is also used in order to investigate the oxidation states of several *d-block* metals of environmental and toxicological interest appearing in secondary or minor amounts in the brake emissions, such as Cr, Mn, Cu and Zn. In spite of being an overall minor contribution, their speciation remains of great importance when assessing the behavior of brake emissions towards environmental and biological systems, especially when they arise from species which might react and change their nature during tribo-oxidative events (*i.e.* metals and sulfides). Finally, the remaining part of secondary and minor elements are represented by alkali and alkaline-earth metals, together with Aluminum and Silicon. As previously reported, they are mainly due to materials composing the friction composites. In particular, they are contained in alumino-silicates, oxides and other materials from geological origin, typically used as fillers or mild abrasives. For this reason, they usually have high thermal stability and are not expected to modify their nature during tribo-oxidative events. Nevertheless, their interaction with liquids, in particular with water, might represent an interesting point to be investigated. For this reason, both cationic and anionic species released by brake emissions are also investigated in the next chapter by the mean of Ionic Chromatography. As already discussed in the first chapter, trace (< 0.01 wt%) and ultra-trace (down to ppm and ppb) elements are not investigated in this thesis work, since, due to their extremely low concentrations, their contribution to the overall environmental and toxicological behavior of brake emissions should likely be more limited.

	LS/LMs 	INs 	NAOs 	CTDs 	CCs 
	<i>Category 1</i>	<i>Category 2</i>	<i>Category 3</i>	<i>Category 4</i>	<i>Category 5</i>
Main	Fe, O, C	Fe, O	O, C, Fe	O, Fe, C	O, C, Fe
Secondary Ubiquitous	Mg, Al, Si, Zn, Sn	C, Si, Al	Mg, Si, S, Ti, Cu, Zr, Ba	Mg, Al, S, Cr, Cu, Sn	Mg, Al, S, Si, Cr, Cu, Zn
Secondary Frequent	-	-	K, Ca, Zn, Sn	Ca, Si, Ti, Zn	-
Secondary Infrequent	Ba	-	-	Zr, Ba, W, Co	-
Minor	Na, K, Ca, P, S, Ti, V, Mn, Cr, Cu, Mo, Bi	S, Mn, Cr, Cu, Zn, K, Ti, Sn, Mo,	Na, Bi, Al, Cr, Mn	K, P, Mn, Ni, Bi	Ti, P

**Main:** always [x] > 10 wt% (**bold** = dominant (> 50 wt%))

**Secondary:** 1.0 < [x] < 10wt%

**Trace:** [x] < 1.0 wt%

**Ubiquitous:** always found

**Frequent:** appearance frequency > 50%

**Infrequent:** appearance frequency < 50%

**Table 4.10:** Summary of the elemental composition characteristics of PM<sub>10</sub> brake emissions from different FCs categories.

#### 4.6. Elemental Composition Maps

Taking all the reported results together, it is finally possible to draw some maps of the elemental composition of PM<sub>10</sub> brake emissions. First of all, since different friction couples have preferential diffusion in specific markets, automotive brake emissions can likely exhibit different elemental composition profiles in different geographical areas. For instance, FCs belonging to *Category 1* (GCI BDs + LS/LM FMs) have wide and dominant distribution on the European markets. Conversely, FCs belonging to *Category 3* (GCI BDs + NAO FMs) are widely diffused in the North American and Asian markets. Since the overall elemental distribution profiles of PM<sub>10</sub> particulates generated from these two different FCs categories were found to be characterized by significant differences, therefore emissions produced by brakes in the cited continents are likely expected to reflect these differences. This is expected more likely when assessing the chemical composition of emissions at the local scale, such for example when comparing particulates from cities in different continents. Figure 4.15 summarizes how different elemental profiles are likely expected to find distribution in several world regions. Unfortunately, no clear information about the distribution of brakes materials are available for African and Ocean Pacific regions. Finally, it is worth to highlight that brakes emissions from Indian and South-East Asian regions might differ significantly from other countries such as China, Japan and South Korea, since the road transport in the former ones is dominated by motorbikes more than cars. Motorbikes brakes are typically made by different materials, usually steel BDs coupled against sintered FMs, *i.e.* friction composites mostly made by metals. Therefore it is important to point out that the elemental distribution profiles generated by *Category 3* FCs represent only a partial depiction of the overall chemical composition of non-exhaust emissions generated by traffic in all those areas in which motorbikes are dominant. In addition to all these considerations, it is also possible to add a further level in the analysis, *i.e.* the distribution of brakes materials in function of different market segments, as reported in Figure 4.16. As can be observed, the vast majority of the worldwide cars are expected to generate brake emissions having similar elemental distribution profiles, characteristic for specific geographic areas. However, a minor part of the worldwide fleet (luxury and high-end cars), is expected to generate emissions with significantly different elemental profiles, independently on the geography. Taking all these observations together, it appears clear how can be difficult to draw general conclusions on the overall chemical composition of the emissions generated by brakes if geography and market considerations are not taken into account. In spite of being a first and absolutely partial depiction of the global situation, the results reported in this chapter still represent a first step towards a more contextualized correlation between the diffusion of different categories of friction couples and the compositional features of their corresponding emissions.

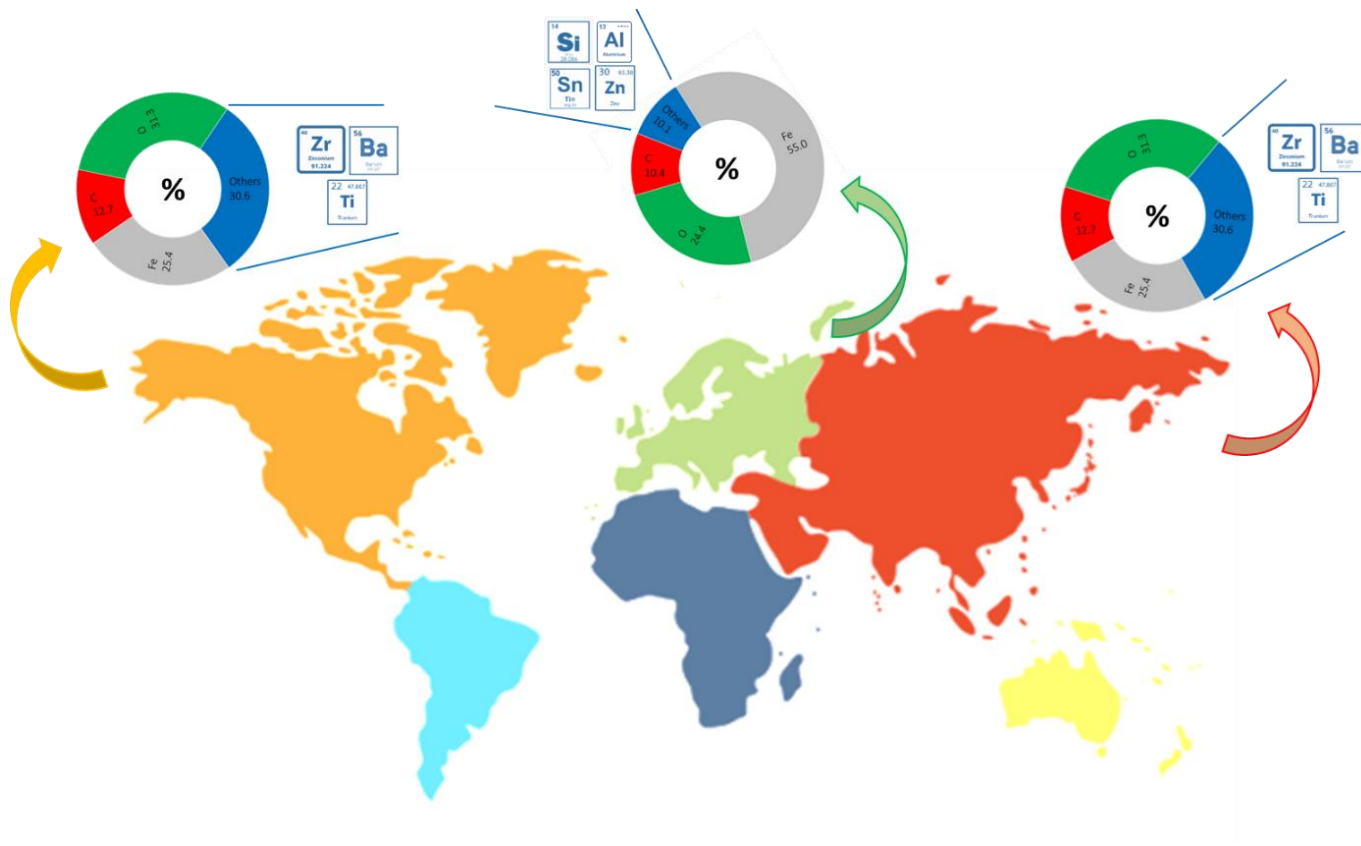


Figure 4.15: Geographical dependence of the elemental distribution profile of PM<sub>10</sub> particulates generated by car brakes.

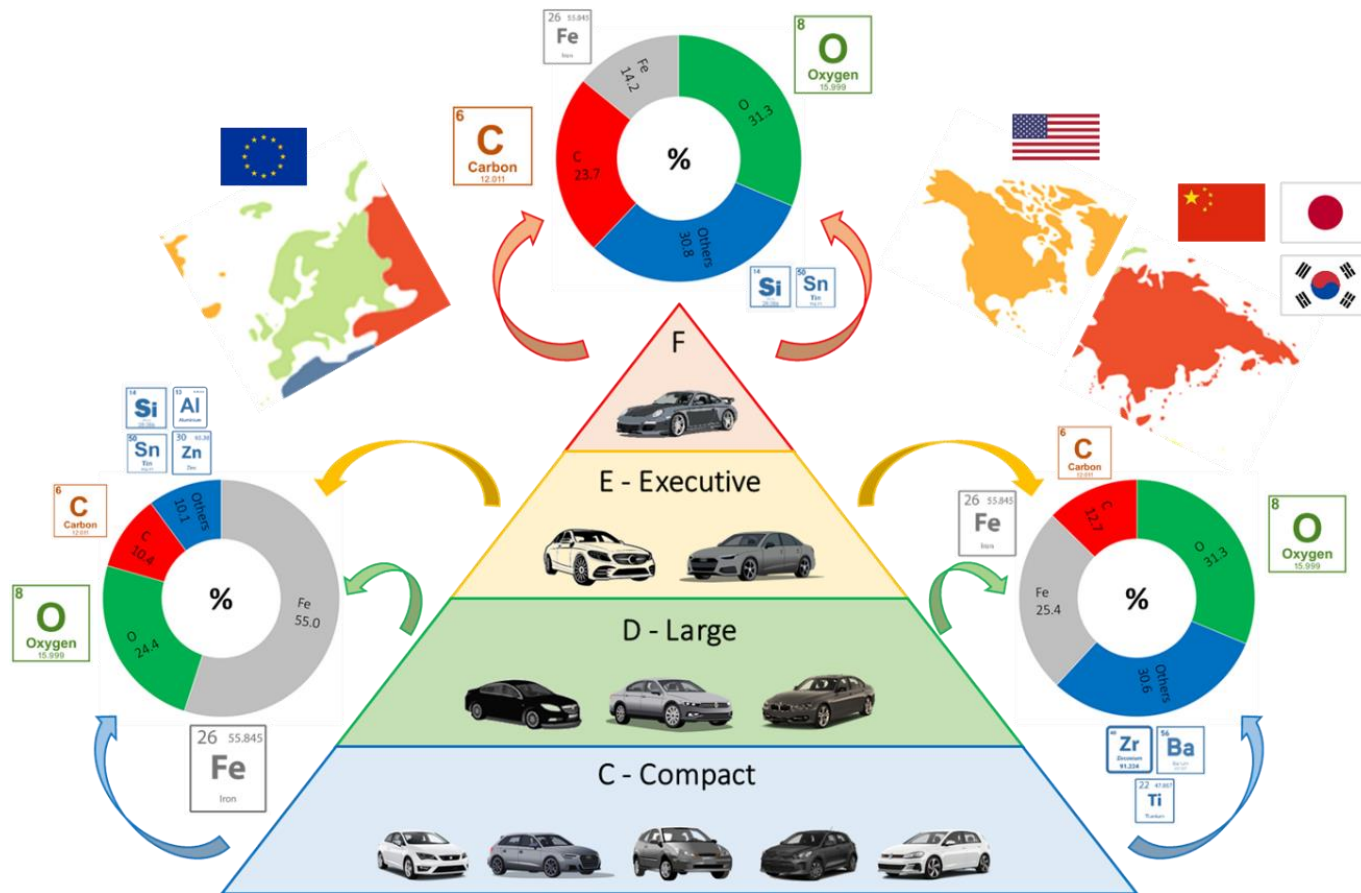
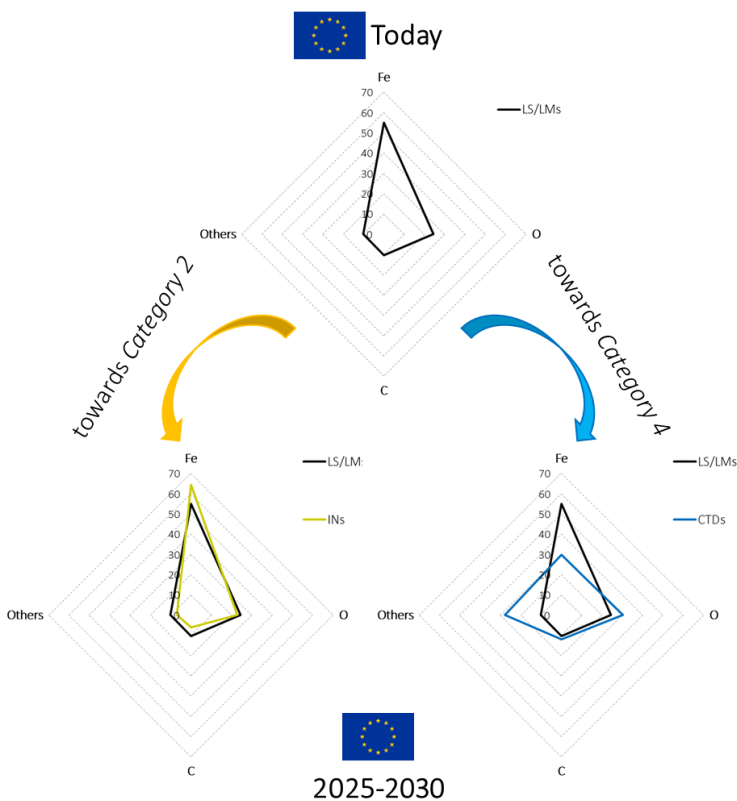


Figure 4.16: Market segment dependence of the elemental distribution profile of PM<sub>10</sub> particulates generated by car brakes.

Finally, the strong development of new materials and design solutions which is currently ongoing in the automotive brake industry is likely expected to impact the emissions elemental distribution profiles in the next years. Once new technologies such as coated BDs and inorganic bound FMs will appear diffusely on the market substituting the current FCs, elemental composition of the corresponding emissions will change accordingly to the dominant solutions. For instance, as schematically showed in Figure 4.17, *Category 1* FCs (GCI BDs + LS/LM FMs) in EU might be substituted in the next future alternatively by *Category 2* (GCI BDs + IN FMs) or *Category 4* (CTD BDs + LS/LM FMs) FCs in order to reduce brakes emission factors.



**Figure 4.17:** Possible future evolutions in elemental composition profiles of automotive brake emissions in EU.

Notably, this reduction will come together with a modification of their chemical composition, accordingly with the findings reported in the previous paragraphs. Even spurious solutions not assessed in this work, such as the combination of Coated BDs and NAO FMs will probably appear on the market. Such combination will represent a new category of FCs, whose emissions will exhibit most likely mixed character between those from *Category 3* and *Category 4*.



## References

- [1] Senate Bill (SB) 346, "California Motor Vehicle Brake Friction Material Law", California State, USA, **2013**.
- [2] RCW Disposition 70.285, "Better Brakes Law", Whashington State, USA, **2010**.
- [3] G. Perricone, V. Matějka, M. Alemani, G. Valota, A. Bonfanti, *et. al.*, "A Concept for Reducing PM10 Emissions for Car Brakes by 50%", *Wear*, 396–397, **2018**, 135–145, doi: <http://dx.doi.org/10.1016/j.wear.2017.06.018>.
- [4] Particle Measurement Programme (PMP) Informal Working Group, Informal document GRPE\_81\_12, 81st GRPE, 9-11 June 2020, Agenda Item 7.
- [5] V. Mahale, J. Bijwe, S. Sinhab, "Efforts towards Green Friction Materials", *Tribology International*, 136, **2019**, 196–206, <https://doi.org/10.1016/j.triboint.2019.03.049>.
- [6] M. Leonardi, "Development of Novel Eco-Friendly Friction Materials for Disc Brake Systems", Doctoral Thesis, 2020, Università di Trento.
- [7] N. Kalel, B. Bhatt, A. Darpe, J. Bijwe, "Copper-free brake-pads: A Break-Through by Selection of the Right Kind of Stainless Steel Particles", *Wear*, 464-465, **2021**, 203537, doi:10.1016/j.wear.2020.203537.
- [8] O. Aranke, W. Algenaid, S. Awe, S. Joshi, "Coatings for Automotive Gray Cast Iron Brake Discs: A Review", *Coatings*, **2019**, 9, 552; doi:10.3390/coatings9090552.
- [9] S.K. Rhee, "Influence of Rotor Metallurgy on the Wear of Friction Materials in Automotive Brakes", *SAE Transactions*, 80(2), **1971**, 992-998.
- [10] D.M. Stefanescu, "Classification and Basic Metallurgy of Cast Iron", *ASM Handbook*, Volume 1: Properties and Selection: Irons, Steels, and High-Performance Alloys ASM Handbook Committee, **1990**, p 3-11, doi: [10.31399/asm.hb.v01.a0009206](https://doi.org/10.31399/asm.hb.v01.a0009206).
- [11] J.M., Radzikowska, "Metallography and Microstructure of Cast Iron", *ASM International*, **2004**, 565-587, <https://doi.org/10.31399/asm.hb.v09.a0003765>.
- [12] F. Bertasi, B. Dudzik, A. Mancini, M. Bandiera, *et.al.*, "Rust Is Not a Must. Improvement of Discs Corrosion Resistance by Tuning of Grey Cast Iron Alloying Elements and Microstructure", *SAE Technical Paper 2020-01-1624*, **2020**, <https://doi.org/10.4271/2020-01-1624>.
- [13] S. Weitao, W. Bin, L. Xiaoliang, W. Yuqian, Z. Jian, "Controlling the Tribology Performance of Gray Cast Iron by Tailoring the Microstructure", *Tribology International*, 167, **2022**, 107343, <https://doi.org/10.1016/j.triboint.2021.107343>.
- [14] M. Federici, G. Perricone, S. Gialanella, G. Straffelini, "Sliding Behaviour of Friction Material Against Cermet Coatings: Pin-on-Disc Study of the Running-in Stage", *Tribology Letters*, **2018**, 66:53, <https://doi.org/10.1007/s11249-018-1004-3>.
- [15] G. Bian, H. Wu, "Friction Surface Structure of a Cf/C–SiC Composite Brake Disc after Bedding Testing on a Full-Scale Dynamometer", *Tribology International*, 99, **2016**, 85–95, doi:10.1016/j.triboint.2016.03.010.
- [16] X. Ma, C. Luan, S. Fan, J. Deng, L. Zhang, L. Cheng, "Comparison of Braking Behaviors Between Iron- and Copper-based Powder Metallurgy Brake Pads that Used for C/C–SiC Disc", *Tribology International*, 154, **2021**, 106686, <https://doi.org/10.1016/j.triboint.2020.106686>.

- [17] ECE R90 Regulation, Rev.3 "Uniform Provisions Concerning Replacement Brake Lining Assemblies and Drum Brake Linings for Power-Driven Vehicles and Their Trailers", *United Nations Economic Commission*, **2012**.
- [18] A. Sanguineti, F. Tosi, A. Bonfanti, F. Rampinelli, "Alkali-Activated Inorganic Based Brake Pads: Realization and Performances of Alternative Friction Materials for a Concrete Industrial Application," *SAE Technical Paper*, **2016**, 2016-01-1913, [doi:10.4271/2016-01-1913](https://doi.org/10.4271/2016-01-1913).
- [19] M. Mathissen, J. Grochowicz, C. Schmidt, R. Vogta, F.H. Farwick zum Hagen, *et.al.*, "A Novel Real-World Braking Cycle for Studying Brake Wear Particle Emissions", *Wear*, 414–415, **2018**, 219–226, <https://doi.org/10.1016/j.wear.2018.07.020>.
- [20] U.S. Hong, S.L. Jung, K.H. Cho, M.H. Cho, S.J. Kim, H. Jang, "Wear Mechanism of Multiphase Friction Materials with Different Phenolic Resin Matrices", *Wear*, **2009**, 266, 739–744, [doi:10.1016/j.wear.2008.08.008](https://doi.org/10.1016/j.wear.2008.08.008).
- [21] P.D. Neis, N.F. Ferreira, G. Fekete, L.T. Matozo, D. Masotti, "Towards a Better Understanding of the Structures Existing on the Surface of Brake Pads", *Tribology International*, **105**, 2017, 135–147, <http://dx.doi.org/10.1016/j.triboint.2016.09.033>.
- [22] G. Straffelini, S. Gialanella, "Airborne Particulate Matter from Brake Systems: An assessment of the Relevant Tribological Formation Mechanisms", *Wear*, **2021**, 478-479, 203883, <https://10.1016/j.wear.2021.203883>.
- [23] Y. Lyu, M. Leonardi, A. Mancini, J. Wahlström, U. Olofsson, "Tribology and Airborne Particle Emission of Laser-Cladded Fe-Based Coatings versus Non-Asbestos Organic and Low-Metallic Brake Materials", *Metals*, **2021**, 11, 1703, <https://doi.org/10.3390/met11111703>.
- [24] C. Menapace, A. Mancini, M. Federici, G. Straffelini, S. Gialanella, "Characterization of Airborne Wear Debris Produced by Brake Pads Pressed Against HVOF-Coated Discs", *Friction*, **2020**, 8, 421–432, <https://doi.org/10.1007/s40544-019-0284-4>.

## 5. Speciation in Brake Emissions

*The elemental composition of an emission sample is a necessary but still not sufficient information when assessing its behavior towards environment or biological systems. Therefore, it is of fundamental importance trying to understand which is the distribution of an element amongst different chemical species, i.e. to assess the speciation of that element. Indeed, different oxidation states and different compounds of a specific element can exhibit significantly different eco- and cyto- toxicology. However, while the elemental analysis of environmental emissions can be easily performed by the means of several chemical probes, their speciation is usually more complex and less explored. This is especially true for brakes emissions: indeed, a general assessment of their phase composition is substantially lacking in the literature. Thus, this chapter aims to provide a deeper insight into the distribution of the compounds constituting the particulates emitted by disc brake devices. In particular, the phase composition of the inorganic fraction is widely explored, since it was found in the previous chapters to be dominant in brakes emissions. To do so, a multi-technique approach is used. More in detail, X-Ray Diffraction (XRD) analysis is used to characterize the main constituents of the crystalline fraction, as already reported in previous chapters. In addition, X-Ray Absorption Near Edge Spectroscopy (XANES) probe is used to characterize more deeply the distribution of oxidation states in d-block metals usually appearing in brakes emissions, even in secondary or minor amounts.*

### 5.1. Aim of the Study

The elemental composition of a sample represents the first information needed to identify an investigated material. However, in spite of providing a fundamental characterization, the elemental analysis alone is frequently not sufficient to completely assess the chemical nature of a sample of interest. In particular, a more complete and detailed depiction of the investigated material is obtained when it is possible to merge together information from both elemental and phase composition analysis. This is especially true when: *i)* investigated materials are complex and heterogeneous mixtures; and *ii)* one or more constituting elements can arise from different sources. Notably, both these conditions are usually verified when assessing environmental emissions. As far as the particulates generated by brakes are concerned, this is particularly evident also from the results reported in the previous chapters. Therefore, it becomes frequently necessary to look at the dispersion of elements of interest amongst different chemical species (or compounds), *i.e.* to speciate them. This might be translated in a wide range of different chemical information, going from the assessment of the distribution of oxidation states of a specific element up to the identification of specific compounds containing that element of interest. These information are pivotal when assessing the

correlation between the chemical nature of a material with its environmental and biological behavior. A typical example is represented by the Chromium, which can be usually found in three different oxidation states:  $\text{Cr}^0$ ,  $\text{Cr}^{3+}$  and  $\text{Cr}^{6+}$ , with the latter one being extremely more dangerous and toxic in respect to the former species.<sup>[1]</sup> Similarly, most of the *d-block* metals exhibit fairly different toxicology in their different states. As rule of thumb for some of them, higher oxidation states often translate in higher solubility in biological media and therefore in higher bioavailability and higher activity towards biological systems, such for instance V, Mn, Cr.<sup>[1-3]</sup> Others show significantly higher eco- or cyto- toxic behavior in metallic form, while being less active in oxidized forms (Zn, Cu).<sup>[4,5]</sup> More in general, different oxidation states in metals are able to activate different toxicological paths, ranging from acute responses to chronic effects.<sup>[6,7]</sup> Therefore, it is particularly evident how a reliable speciation of the constituting elements of the brakes emissions is fundamental in order to correctly assess their behavior toward environmental and biological systems. For this reason, the investigation reported in this chapter proposes a wide characterization of the phase composition of brakes emissions generated by different friction couples. Similarly to what reported in *Chapter 4* for the elemental composition, the distribution of identified compounds is related to the different starting materials composing the friction couple.

## 5.2. Experimental Techniques

To cope with the intrinsic complexity of the chemical composition of the brakes emissions, a multi-technique approach is adopted. In particular, XRD analysis is used in order to characterize the phase composition of the crystalline fraction. The distribution of main constituents, such as the Iron and its oxides, is the main target for this analysis. Nevertheless, valuable information can be obtained also on the presence of secondary components, such as inorganic oxides and sulfides, as well as of other metals. In spite of being an extremely powerful probe, the XRD analysis suffers of two main drawbacks when applied to the chemical speciation of brakes emissions: *i)* it can assess only the crystalline fraction, therefore being blind towards amorphous compounds; and *ii)* it is characterized by relatively high detection limits, especially when modest amounts of material are available. For this reason two additional techniques are proposed to overcome these limitations. The first one is the XANES analysis, which can be applied for its nature independently on the long-range order exhibited by the investigated material, being at the same time sensible to lower amounts of analyte in respect with the XRD analysis. For this reason, XANES is used to assess the overall distribution of oxidation states of *d-block* metals present within the investigated particulates, even in secondary or minor amounts. The second technique is the Raman Spectroscopy, which can be used to qualitatively identify some chemical species such as metal oxides and sulfides as well as elemental Carbon. Similarly to the XANES probe, also Raman Spectroscopy can be

used independently on the presence of amorphous compounds. However, its application is described more in detail in *Chapter 7. Dimensional Profiles and Chemical Composition*, since it is used in this thesis only in that section and limitedly to the comparative assessment of the phase composition of the ultra-fine fractions. As far as the Carbon is concerned, its speciation is dealt assessing its presence in organic, elemental and inorganic forms. This is done by means of Carbon elemental analysis (C-EA). In particular, the investigated samples are induced to a sequential total combustion by means of the application of suitable heating ramps in Oxygen enriched environment. Therefore, the CO<sub>2</sub> generated in different temperature ranges is used as marker for assessing the relative abundance of the different Carbon compounds inside the particulates. Finally, also the ionic fraction released in water media by the investigated PM<sub>10</sub> emissions is briefly assessed by means of Ionic Chromatography. All the experimental protocols adopted for the speciation analysis are detailed described in *Chapter 2*.

### 5.3. Crystalline Fraction

From all the findings reported in *Chapter 3* and *4* it is possible to infer that the chemistry of the brakes emissions is greatly related to the chemistry of Iron. In particular, Iron oxides are generally found as main constituents of the particulates generated by brakes. In addition to the Iron, several other metals and inorganic oxides and sulfides can be frequently found in these emissions. Finally, also elemental Carbon is found to be a significant contribution. Since most of these compounds have usually crystalline character, XRD probe might represent a useful tool for their identification. For this reason, phase identification and quantification (where possible) were carried out on several PM<sub>10</sub> particulates are reported in the next sections. More in detail, XRD analysis was carried out on the same samples investigated in *Chapter 4*, when sufficient amount of material was deposited on the collection substrates. Therefore, their origin as well as their complete elemental composition can be found in that chapter. For the same reason, the results are presented and discussed in function of the different combinations of materials composing the friction couple, following the categorization previously proposed. As already reported in the paragraph of *Chapter 2* dedicated to the XRD analysis, highly disordered or even amorphous phases can be expected within the collected particulates. In addition, in spite of being selected for their non crystalline character, cellulose filters still retain some degree of short-range order, therefore exhibiting a modulated background. For all these reasons, the reported results of phase quantification have not to be considered as absolute or fully quantitative, but relatively to the crystalline fraction only.

### 5.3.1. Category 1 (GCI BDs + LS/LM FMs)

The next figures (Figure 5.1 to 5.5) report the Whole Profile Powder Fit (WPPF) refinements carried out on five particulates generated by friction couples belonging to the *Category 1*, *i.e.* combinations of GCI braking discs and Low Steel/Low Metallic friction materials. More in detail, **LS/LM1**, **LS/LM2**, **LS/LM4**, **LS/LM6** and **LS/LM10** samples were analyzed. In addition, Table 5.1 summarizes the relative abundance ratio of the identified phases relatively to the crystalline fraction. As can be immediately seen from all the reported results, the crystalline fraction of these particulates is dominated by the presence of Iron oxides. In particular, both Magnetite ( $\text{Fe}_3\text{O}_4$ ) and Hematite ( $\text{Fe}_2\text{O}_3$ ) are always found, with the latter being dominant. In addition, also metallic Iron ( $\alpha\text{-Fe}$ ) and Graphite (2H – hexagonal polymorph) are always found, but in significant lower amounts.

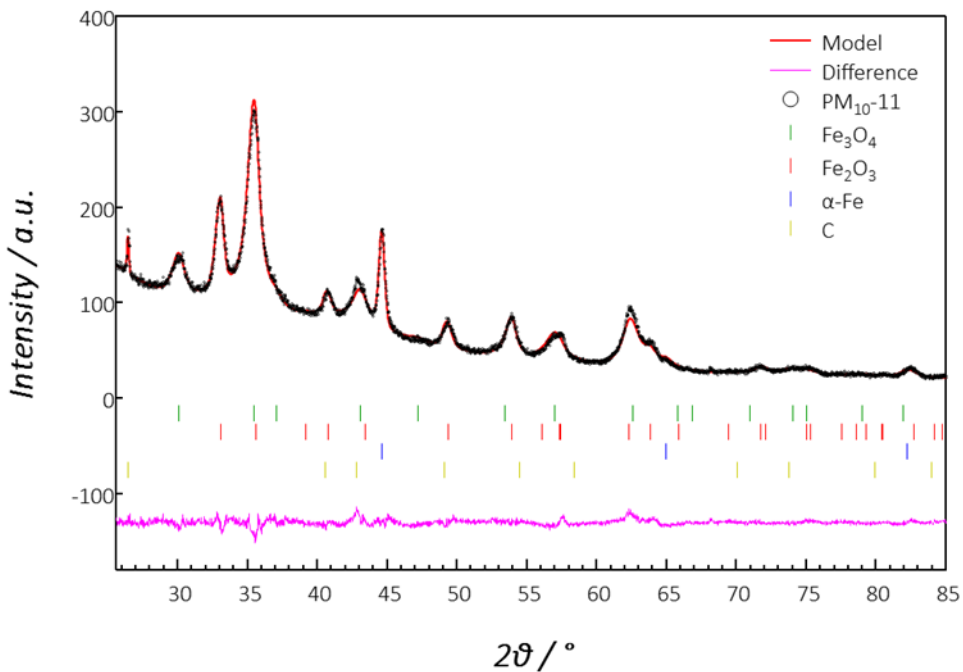


**Figure 5.1:** Refinement for PM<sub>10</sub> from LS/LM1 FC via WPPF method. *i)* Black profile: experimental pattern; *ii)* red profile: calculated model; *iii)* pink profile: residuals between experimental data and calculated model; *iv)* vertical bars: crystallographic references.  $\alpha\text{-Fe}$ ,  $\text{Fe}_3\text{O}_4$ ,  $\text{Fe}_2\text{O}_3$  and C reference bars are respectively reported in blue, green, red and yellow.

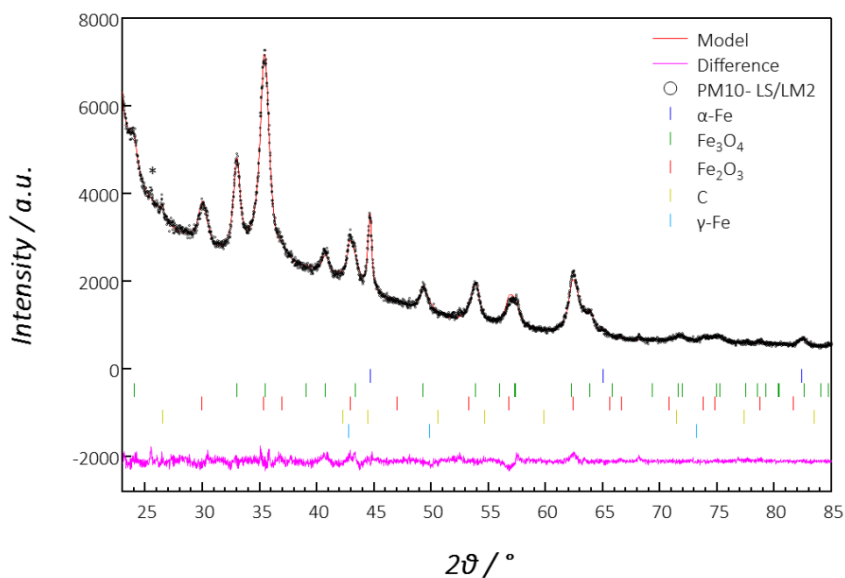


**Figure 5.2:** Refinement for PM<sub>10</sub> from LS/LM2 FC via WPPF method. *i)* Black profile: experimental pattern; *ii)* red profile: calculated model; *iii)* pink profile: residuals between experimental data and calculated model; *iv)* vertical bars: crystallographic references.  $\alpha$ -Fe, Fe<sub>3</sub>O<sub>4</sub>, Fe<sub>2</sub>O<sub>3</sub>, C and  $\gamma$ -Fe reference bars are respectively reported in blue, green, red, yellow and light blue. SnS is detected (\*) but not quantified.

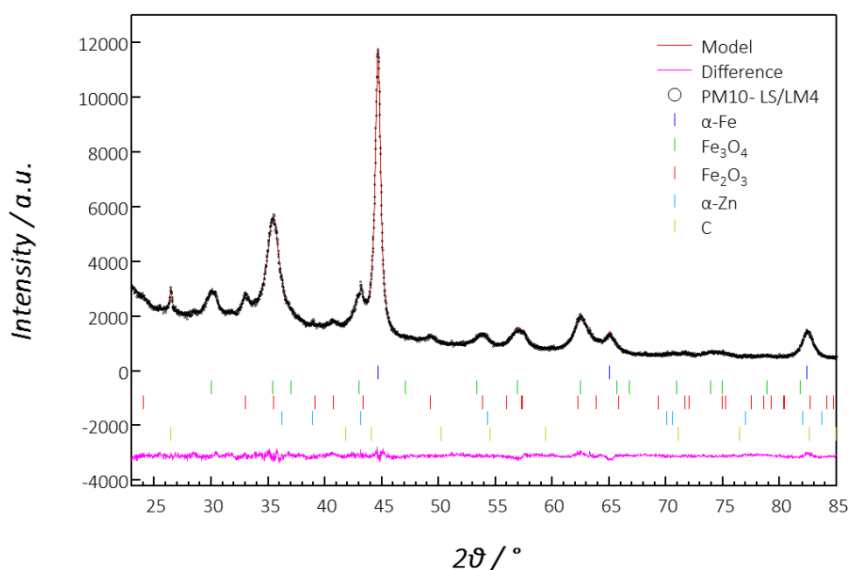


**Figure 5.3:** Refinement for PM<sub>10</sub> from LS/LM4 FC via WPPF method. *i)* Black profile: experimental pattern; *ii)* red profile: calculated model; *iii)* pink profile: residuals between experimental data and calculated model; *iv)* vertical bars: crystallographic references.  $\alpha$ -Fe, Fe<sub>3</sub>O<sub>4</sub>, Fe<sub>2</sub>O<sub>3</sub>,  $\alpha$ -Zn and C reference bars are respectively reported in blue, green, red, light blue and yellow.

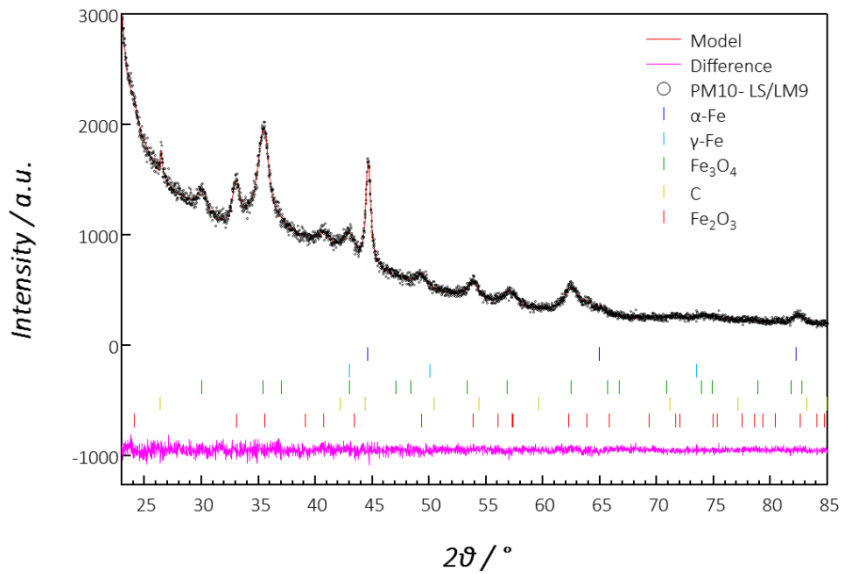


**Figure 5.4:** Refinement for PM<sub>10</sub> from LS/LM9 FC via WPPF method. *i)* Black profile: experimental pattern; *ii)* red profile: calculated model; *iii)* pink profile: residuals between experimental data and calculated model; *iv)* vertical bars: crystallographic references.  $\alpha$ -Fe,  $\gamma$ -Fe, Fe<sub>3</sub>O<sub>4</sub>, Fe<sub>2</sub>O<sub>3</sub> and C reference bars are respectively reported in blue, light blue, green, red and yellow.

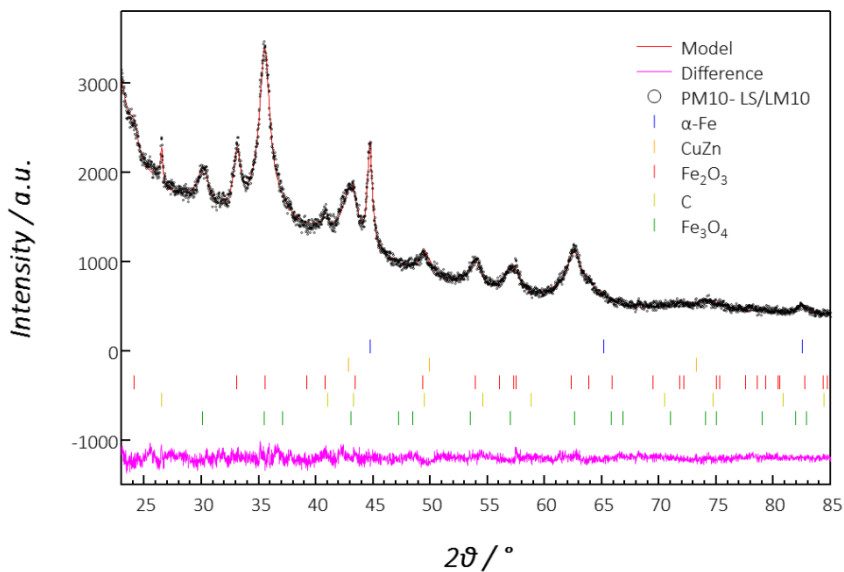


**Figure 5.5:** Refinement for PM<sub>10</sub> from LS/LM10 FC via WPPF method. *i)* Black profile: experimental pattern; *ii)* red profile: calculated model; *iii)* pink profile: residuals between experimental data and calculated model; *iv)* vertical bars: crystallographic references.  $\alpha$ -Fe, CuZn, Fe<sub>3</sub>O<sub>4</sub>, Fe<sub>2</sub>O<sub>3</sub> and C reference bars are respectively reported in blue, orange, green, red and yellow.



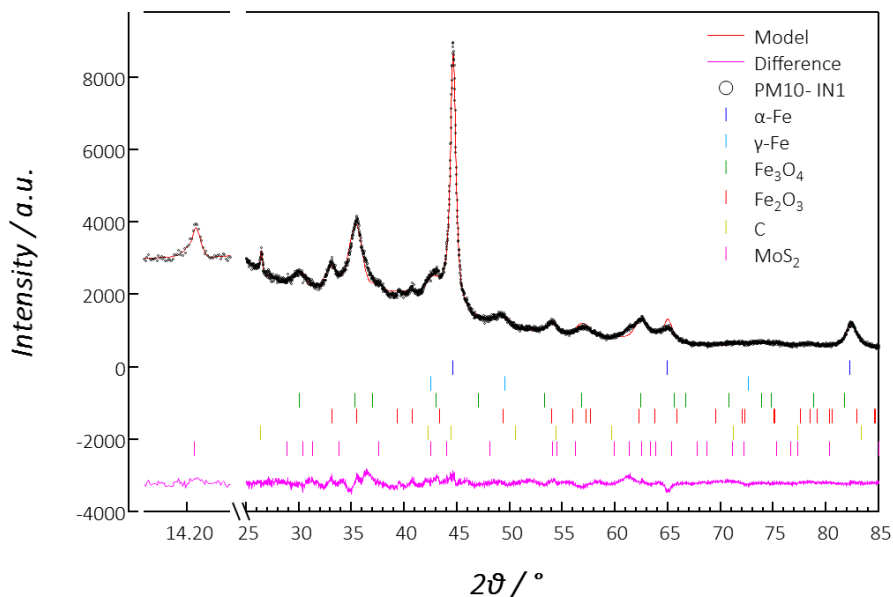
	LS/LM1	LS/LM2	LS/LM4	LS/LM9	LS/LM10
Fe <sub>3</sub> O <sub>4</sub>	51.7(3)	48.8(9)	42.7(3)	69.5(9)	54.6(9)
Fe <sub>2</sub> O <sub>3</sub>	33.9(3)	34.1(7)	22.2(5)	16.3(9)	31.1(9)
Fe (α+γ)	8.9(2)	11.2(9)	25.7(2)	9.1(8)	4.9(2)
C	5.5(2)	5.9(2)	5.4(2)	5.1(6)	4.3(4)
SnS	<i>traces</i>	<i>traces</i>	-	-	-
α-Zn	-	-	3.8(3)	-	-
CuZn	-	-	-	-	5.1(8)
R <sub>wp</sub>	3.69%	3.23%	3.56%	4.05%	3.63%
χ <sup>2</sup>	1.95	1.35	1.91	1.07	1.20

Table 5.1: Summary of relative weight ratios for identified crystalline phases in PM<sub>10</sub> emissions from *Category 1* friction couples. Estimated standard deviations (*esd*) are reported in blue within brackets and refer to the last reported significant digit. R<sub>wp</sub> and χ<sup>2</sup> are goodness of fit parameters.

Notably, all these findings are in excellent agreement with those previously reported for the elemental composition of the same category of samples. Therefore, it can be inferred that the crystalline fraction fits overall very well the elemental composition of the investigated particulates, in particular when looking at the main constituents. As far as minor components are concerned, other metals such as Zn and Brass (Cu-Zn alloy) are easily detected when contained in weight percentage higher than 1 wt% in the investigated particulate. However, these compounds are found with lower frequency in respect with the previous ones, since their presence is dependent on the specific friction material formulation. In addition, also Tin Sulfides are detected when present even in low amounts (sample from LS/LM1 and LS/LM2 FCs), thanks to their high crystallinity. However, they cannot be reliably quantified, due to the high signal to noise ratio in comparison with their diffraction peaks intensities. For this reason, they were excluded from the phase analysis and reported in Table 5.1 as “*traces*”. Finally, other two interesting considerations can arise from the reported results. First, as already pointed out in *Chapter 3*, the elemental Carbon (Graphite + Coke) concentrations found by XRD phase analysis are always lower (50-60%) in respect with their counterparts obtained from EDXS analysis. This can be explained by the two following factors: *i*) the tendency of the EDXS probe to slightly overstate light elements concentration (see *Annex 2*); and *ii*) the presence of Carbon in non-crystalline forms, such as results of thermal degradation of the organic binders. The second observation is that two different polymorphs of Iron can be observed very often at the diffraction analysis, *i.e.* α-Fe (Ferrite) and γ-Fe (Austenite). If the first one can arise from both the abrasion of the BD and FM, γ-Fe is likely more related to steel fibers eventually present in the friction composite.

### 5.3.2. Category 2 (GCI BDs + IN FMs)

Figures 5.6 to 5.10 show the WPPF refinements carried out on the experimental XRD patterns collected on five different particulates generated by friction couples belonging to the *Category 2*, *i.e.* combinations of GCI BDs and inorganic bound (IN) FMs. Table 5.2 summarizes the corresponding results of phase composition analysis. More in detail, emissions from **IN1**, **IN4**, **IN6**, **IN8** and **IN10** friction couples are analyzed (their elemental composition can be found in *Paragraph 4.4.2* in the previous Chapter). As can be observed from the reported results, also in this case Iron-related species are the dominant contribution to the crystalline fraction of the investigated emissions. However, here the overall amount of metallic Iron is higher than in the counterparts from *Category 1*. Notably, this findings is in excellent agreement with both: *i)* the results from the elemental composition characterization reported in *Chapter 4*; and *ii)* the specific tribological characteristic of this category of friction couples: indeed, IN FMs are harder and more abrasive in respect with the LS/LM counterparts; therefore, IN FMs likely generate more material by direct abrasion of GCI BD braking surfaces, in respect with that one generated by adhesive and tribo-oxidative mechanism when compared to LS/LM FMs.



**Figure 5.6:** Refinement for PM<sub>10</sub> from IN1 FC via WPPF method. *i)* Black profile: experimental pattern; *ii)* red profile: calculated model; *iii)* pink profile: residuals between experimental data and calculated model; *iv)* vertical bars: crystallographic references.  $\alpha$ -Fe,  $\gamma$ -Fe, Fe<sub>3</sub>O<sub>4</sub>, Fe<sub>2</sub>O<sub>3</sub>, C and MoS<sub>2</sub> reference bars are respectively reported in blue, light-blue, green, red, yellow and pink. The main peak of MoS<sub>2</sub> is reported on split x-axis, since it is located at lower diffraction angle in respect with the standard range.

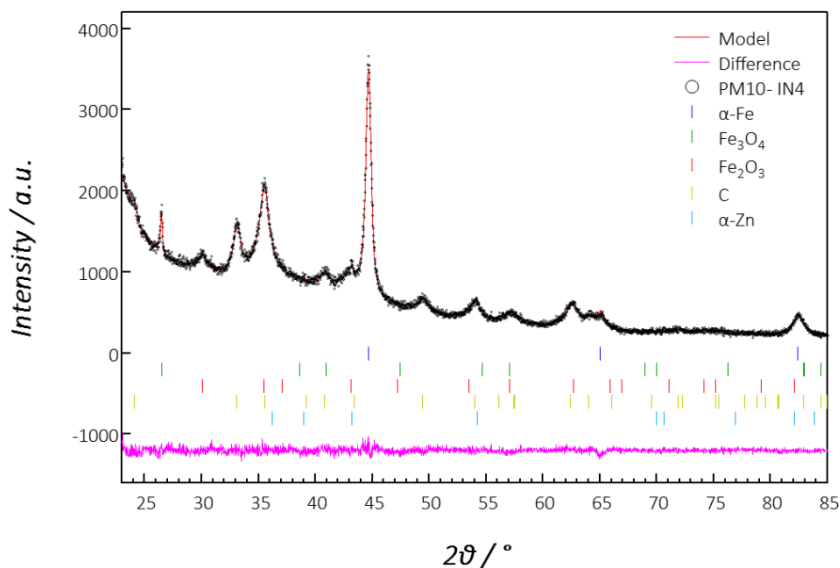


**Figure 5.7:** Refinement for PM<sub>10</sub> from IN4 FC via WPPF method. *i)* Black profile: experimental pattern; *ii)* red profile: calculated model; *iii)* pink profile: residuals between experimental data and calculated model; *iv)* vertical bars: crystallographic references.  $\alpha$ -Fe, Fe<sub>3</sub>O<sub>4</sub>, Fe<sub>2</sub>O<sub>3</sub>, C and  $\alpha$ -Zn reference bars are respectively reported in blue, green, red, yellow and light blue.

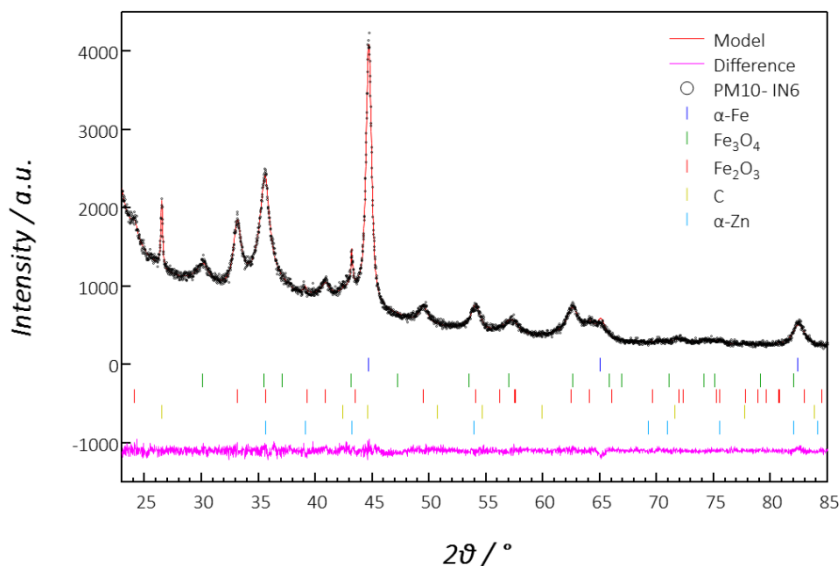


**Figure 5.8:** Refinement for PM<sub>10</sub> from IN6 FC via WPPF method. *i)* Black profile: experimental pattern; *ii)* red profile: calculated model; *iii)* pink profile: residuals between experimental data and calculated model; *iv)* vertical bars: crystallographic references.  $\alpha$ -Fe, Fe<sub>3</sub>O<sub>4</sub>, Fe<sub>2</sub>O<sub>3</sub>, C and  $\alpha$ -Zn reference bars are respectively reported in blue, green, red, yellow and light blue.

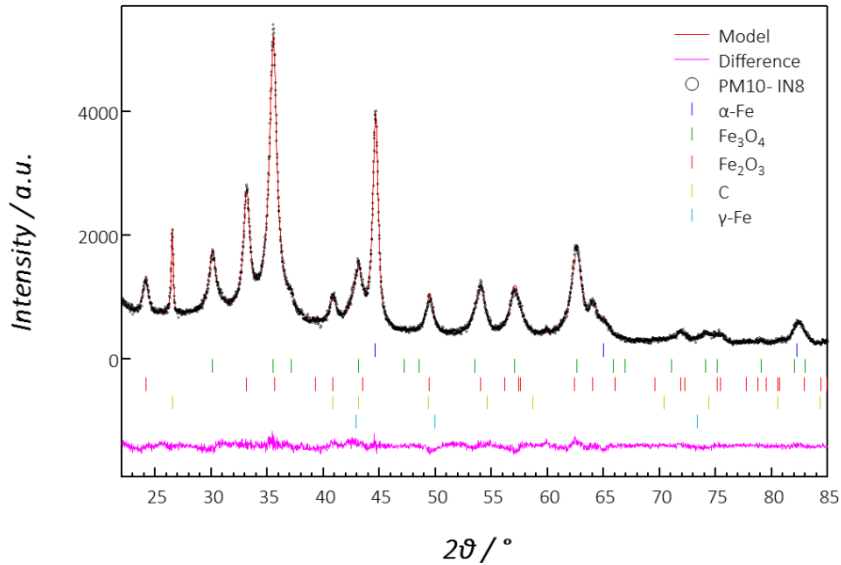


**Figure 5.9:** Refinement for PM<sub>10</sub> from IN8 FC via WPPF method. *i)* Black profile: experimental pattern; *ii)* red profile: calculated model; *iii)* pink profile: residuals between experimental data and calculated model; *iv)* vertical bars: crystallographic references.  $\alpha$ -Fe, Fe<sub>3</sub>O<sub>4</sub>, Fe<sub>2</sub>O<sub>3</sub>, C and  $\alpha$ -Zn reference bars are respectively reported in blue, green, red, yellow and light blue.

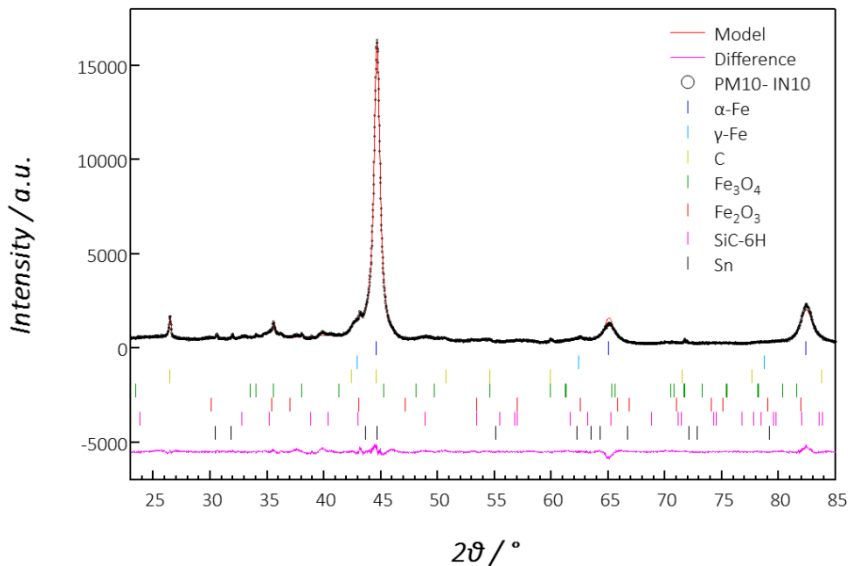


**Figure 5.10:** Refinement for PM<sub>10</sub> from IN8 FC via WPPF method. *i)* Black profile: experimental pattern; *ii)* red profile: calculated model; *iii)* pink profile: residuals between experimental data and calculated model; *iv)* vertical bars: crystallographic references.  $\alpha$ -Fe,  $\gamma$ -Fe, C, Fe<sub>3</sub>O<sub>4</sub>, Fe<sub>2</sub>O<sub>3</sub>, SiC and Sn reference bars are respectively reported in blue, light-blue, yellow, green, red, pink and black.

	IN1	IN4	IN6	IN8	IN10
Fe <sub>3</sub> O <sub>4</sub>	32.9(6)	29.0(2)	39.7(2)	47.2(3)	8.2(9)
Fe <sub>2</sub> O <sub>3</sub>	21.6(9)	44.0(2)	34.3(2)	34.0(3)	6.3(3)
Fe ( $\alpha+\gamma$ )	39.7(7)	20.2(9)	21.8(7)	15.3(8)	80.6(6)
C	4.4(3)	5.1(2)	2.7(2)	3.5(3)	2.5(9)
MoS <sub>2</sub>	1.4(2)	-	-	-	-
$\alpha$ -Zn	-	1.3(3)	1.5(2)	-	-
SiC-6H	-	-	-	-	2.2(2)
Sn	-	-	-	-	0.1(1)
R <sub>wp</sub>	4.60%	4.28%	4.06%	4.74%	4.28%
$\chi^2$	3.23	1.26	1.23	1.83	1.26

**Table 5.2:** Summary of relative weight ratios for identified crystalline phases in PM<sub>10</sub> emissions from *Category 2* friction couples. Estimated standard deviations (*esd*) are reported in blue within brackets and refer to the last reported significant digit. R<sub>wp</sub> and  $\chi^2$  are goodness of fit parameters.

This behavior is particularly evident in the particulates generated by IN10 FC, where the metallic Iron is found to be the dominant phase (80 wt%) of the PM<sub>10</sub> emission. Indeed, the friction material of this FC comes from racing application, where braking performances are maximized. In addition, this friction mix is coupled against a standard GCI BD (not for racing purposes). For this reason, the extremely high abrasive character of the friction material likely determined an emission generation mostly based on direct abrasion of the disc braking surfaces. Notably, these results highlight how the XRD probe can be a convenient probe to easily discriminate between different ratios of metallic and oxidized Iron in brakes emissions, therefore being a precious tool to investigate also the tribological mechanisms of specific friction couples.

In addition to the main phases related to the Iron, also elemental Carbon is always found (Graphite-2H, hexagonal polymorph) in all the investigated particulates. Notably, Graphite concentration is lower in these particulates than in the counterparts from *Category 1*. This observation is well in agreement with the overall fraction of material arising from the FM side of the friction couple, due to the mechanical and tribological characteristics of the IN friction materials. In addition, other minor and less frequent compounds are spotted. They are mainly dependent on the specific friction mix formulations. In particular, minor amounts of MoS<sub>2</sub> (solid lubricant, IN1), metallic Zn (friction modifier and corrosion protection, IN4 and IN6) and Silicon carbide (SiC-6H, hexagonal polymorph, abrasive, IN10) plus metallic Tin (friction modifiers, IN10) are identified. All these compounds are characterized by high electron density and/or high crystallinity; therefore, they are detected even in minor amounts.

### 5.3.3. Category 3 (GCI BDs + NAO FMs)

Figures 5.11 to 5.13 show the WPPF refinements carried out on the experimental XRD patterns collected on three different particulates generated by friction couples belonging to the *Category 3*, *i.e.* combinations of GCI BDs and NAO FMs. Table 5.3 summarizes the corresponding results obtained from the phase composition analysis. More in detail, emissions from **NAO1**, **NAO2** and **NAO4** friction couples are analyzed (their elemental composition can be found in *Paragraph 4.4.3*, in the previous Chapter). First of all it is worth to highlight that the diffraction signals are overall significantly lower in respect with the XRD patterns of the emissions generated by the first two categories of FCs. Thus, the signal to noise ratio is also significantly lower, resulting in more difficult identification and phase analysis processes, higher uncertainties and an overall lower quality of the fits. This is due to the significantly lower amounts of material generated and therefore collected during the emission tests of the FCs belonging to *Category 3*. Nevertheless, significant amount of analytical information can be extracted from the collected XRD pattern. For example, it is clearly possible to observe that all the three investigated particulates from Category 3 FCs show extremely low contents of metallic Iron. This is coherent with the compositional features of the origin FCs, as well as with their tribological characteristics. Indeed NAO friction materials are usually less prone to generate significant direct abrasion from the GCI BDs in respect to the LS/LM and IN counterparts. Thus, their tribology is in general more characterized by adhesive mechanism and tribo-oxidation. Considering this, the relative abundance of metallic Iron in respect to its oxidized forms can be reasonably expected lower. Another interesting observation is represented by the significant presence of inorganic oxides in all the investigated PM<sub>10</sub> emissions. In particular, Zirconia (ZrO<sub>2</sub>) is always detected, as extremely common abrasive for NAO formulations. In addition, also Potassium Titanate (K<sub>2</sub>Ti<sub>6</sub>O<sub>13</sub>, mild abrasive) is detected once. Where present in the origin friction materials, also other metallic species are easily identified (Zn and Cu). Notably, all these findings are in excellent agreement with the elemental composition of the investigated particulates, as well as with the already observed tendency in *Category 3* FCs to host higher relative ratio of material generated by the consumption of the friction mix when compared with LS/LM and IN counterparts. Finally, it is worth to specifically mention the particulate generated by the NAO4 friction couple, since it appears to be significantly different from most of the collected particulates, also within its category. Indeed, this emission shows two features never observed before: *i)* a significantly higher content of amorphous phase(s), testified by the broad bump observed in the 15-35° angular range; and *ii)* the presence of FeO (Wustite). In particular, the presence of FeO can be seen as an anomaly, since it is a compound stable in conditions (reducing environments), usually different from those experienced by the tribological interface. This might furthermore reflect a substantial difference in the tribology of some NAO materials.

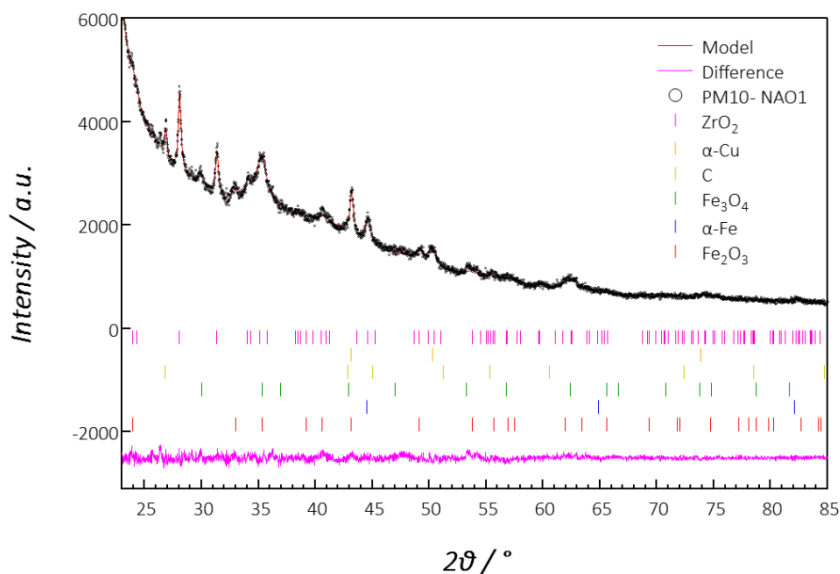


**Figure 5.11:** Refinement for PM<sub>10</sub> from NAO1 FC via WPPF method. *i)* Black profile: experimental pattern; *ii)* red profile: calculated model; *iii)* pink profile: residuals between experimental data and calculated model; *iv)* vertical bars: crystallographic references. ZrO<sub>2</sub>, α-Cu, C, Fe<sub>3</sub>O<sub>4</sub>, α-Fe and Fe<sub>2</sub>O<sub>3</sub> reference bars are respectively reported in pink, orange, yellow, green, blue and red.

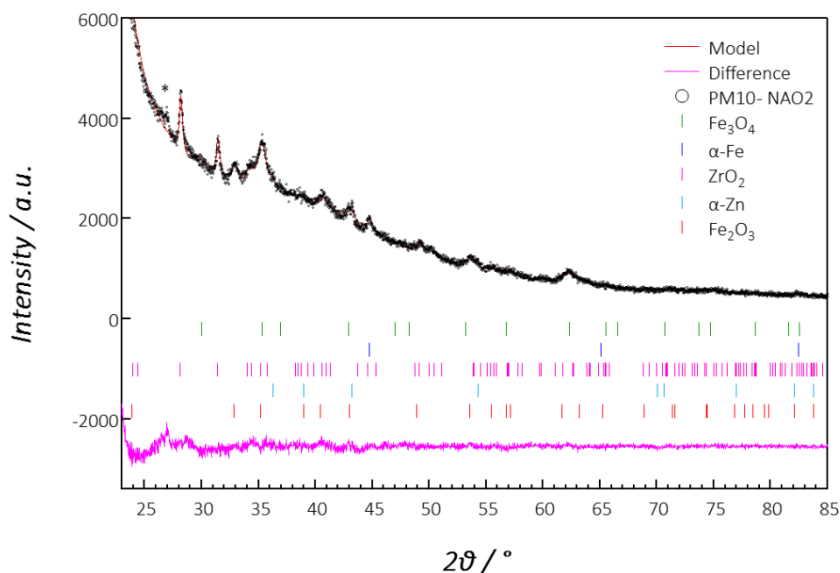


**Figure 5.12:** Refinement for PM<sub>10</sub> from NAO2 FC via WPPF method. *i)* Black profile: experimental pattern; *ii)* red profile: calculated model; *iii)* pink profile: residuals between experimental data and calculated model; *iv)* vertical bars: crystallographic references. Fe<sub>3</sub>O<sub>4</sub>, α-Fe, ZrO<sub>2</sub>, α-Zn and Fe<sub>2</sub>O<sub>3</sub> reference bars are respectively reported in green, blue, pink, light blue and red. C (\*) is detected but not quantified.

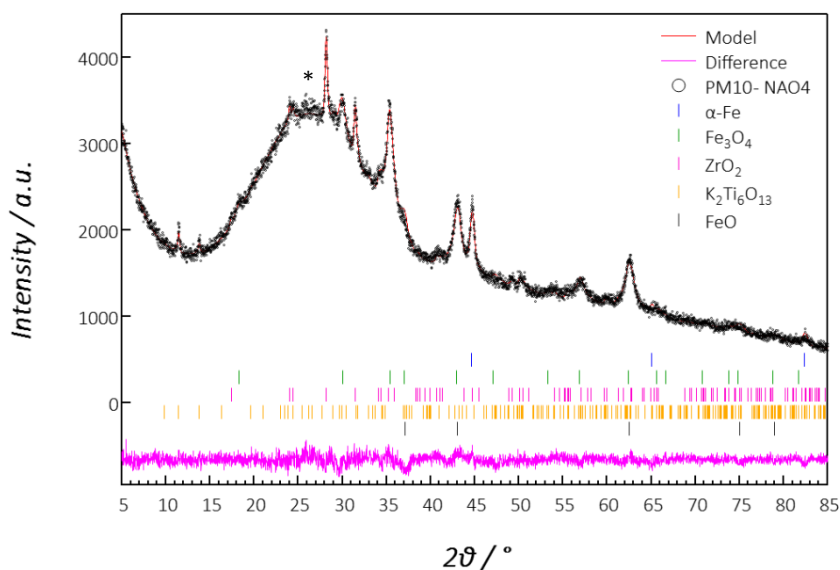


**Figure 5.13:** Refinement for PM<sub>10</sub> from NAO4 FC via WPPF method. *i)* Black profile: experimental pattern; *ii)* red profile: calculated model; *iii)* pink profile: residuals between experimental data and calculated model; *iv)* vertical bars: crystallographic references.  $\alpha$ -Fe, Fe<sub>3</sub>O<sub>4</sub>, ZrO<sub>2</sub>, K<sub>2</sub>Ti<sub>6</sub>O<sub>13</sub> and FeO reference bars are respectively reported in blue, green, orange, pink and black. C (\*) is detected but not quantified.

	NAO1	NAO2	NAO4
Fe <sub>3</sub> O <sub>4</sub>	52(2)	57.2(7)	54.5(8)
Fe <sub>2</sub> O <sub>3</sub>	21(3)	23.2(7)	-
$\alpha$ -Fe	1.8(1)	1.2(1)	5.8(1)
C	5.2(3)	NQ	NQ
ZrO <sub>2</sub>	16.5(6)	16.9(4)	11.5(4)
$\alpha$ -Zn	-	2.5(2)	-
Cu	3.5(2)	-	-
FeO	-	-	20.2(2)
K <sub>2</sub> Ti <sub>6</sub> O <sub>13</sub>	-	-	8.0(4)
R <sub>wp</sub>	3.06%	3.50%	2.83%
$\chi^2$	1.42	1.93	1.37

**Table 5.3:** Summary of relative weight ratios for identified crystalline phases in PM<sub>10</sub> emissions from Category 3 friction couples. Estimated standard deviations (*esd*) are reported in blue within brackets and refer to the last reported significant digit. R<sub>wp</sub> and  $\chi^2$  are goodness of fit parameters.



Notably, in the emissions from *Category 3*, no  $\gamma$ -Fe (Austenite) Iron polymorph was observed. This observation is well in agreement with the compositional features of NAO friction materials, which typically do not contain steel fibers.

#### 5.3.4. *Category 4 (CTD BDs + LS/LM FMs)*

Figures 5.14 and 5.15 show the WPPF refinements carried out on the experimental XRD patterns collected on two different particulates generated by friction couples belonging to the *Category 4*, *i.e.* combinations of Coated BDs and LS/LM FMs. Table 5.4 summarizes the corresponding results obtained from the phase composition analysis. More in detail, emissions from **CTD4** and **CTD10** friction couples are analyzed (their elemental composition can be found in *Paragraph 4.4.4*, in the previous Chapter). These are the only two filters from the *Category 4* whose collected diffraction intensities were sufficient for the phase analysis. In addition, Figure 5.16 shows the comparison of the experimental XRD pattern collected on three additional PM<sub>10</sub> emissions from *Category 4*. For these particulates, only the phase identification is reported, together with a qualitative assessment of the relative abundance of the identified compounds.

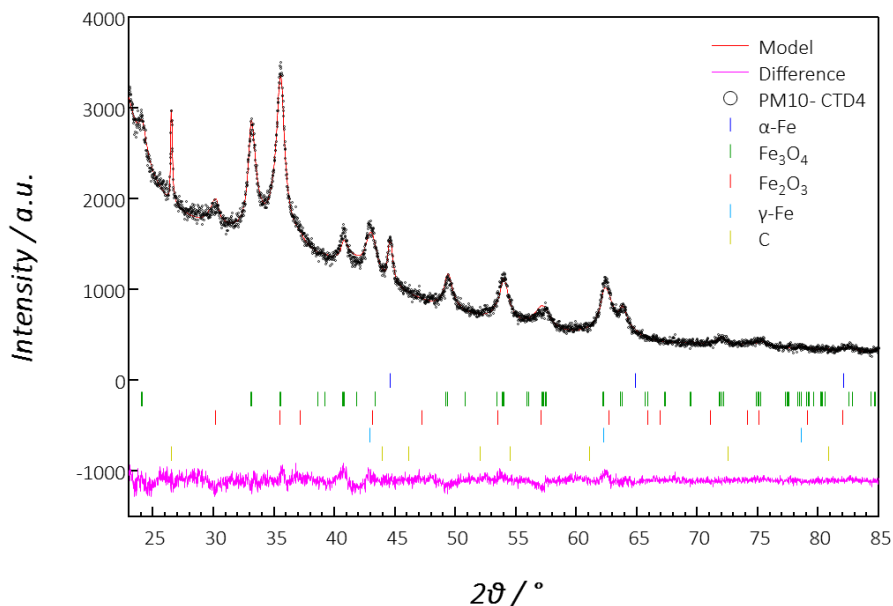


**Figure 5.14:** Refinement for PM<sub>10</sub> from CTD4 FC via WPPF method. *i)* Black profile: experimental pattern; *ii)* red profile: calculated model; *iii)* pink profile: residuals between experimental data and calculated model; *iv)* vertical bars: crystallographic references.  $\alpha$ -Fe,  $\gamma$ -Fe, Fe<sub>3</sub>O<sub>4</sub>, Fe<sub>2</sub>O<sub>3</sub>, and C reference bars are respectively reported in blue, light blue, green, red and yellow.

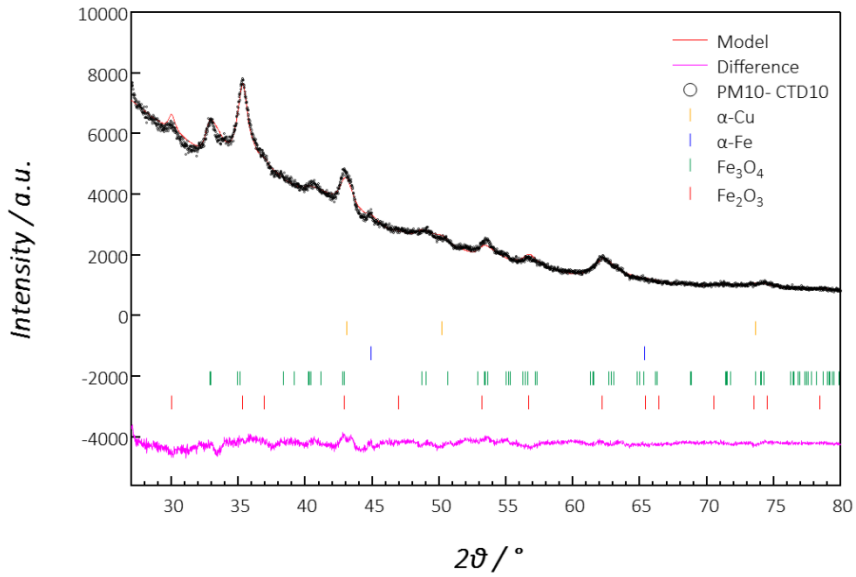


**Figure 5.15:** Refinement for PM<sub>10</sub> from CTD10 FC via WPPF method. *i)* Black profile: experimental pattern; *ii)* red profile: calculated model; *iii)* pink profile: residuals between experimental data and calculated model; *iv)* vertical bars: crystallographic references.  $\alpha$ -Cu,  $\alpha$ -Fe, Fe<sub>3</sub>O<sub>4</sub>, Fe<sub>2</sub>O<sub>3</sub>, are respectively reported in orange, blue, green, and red.

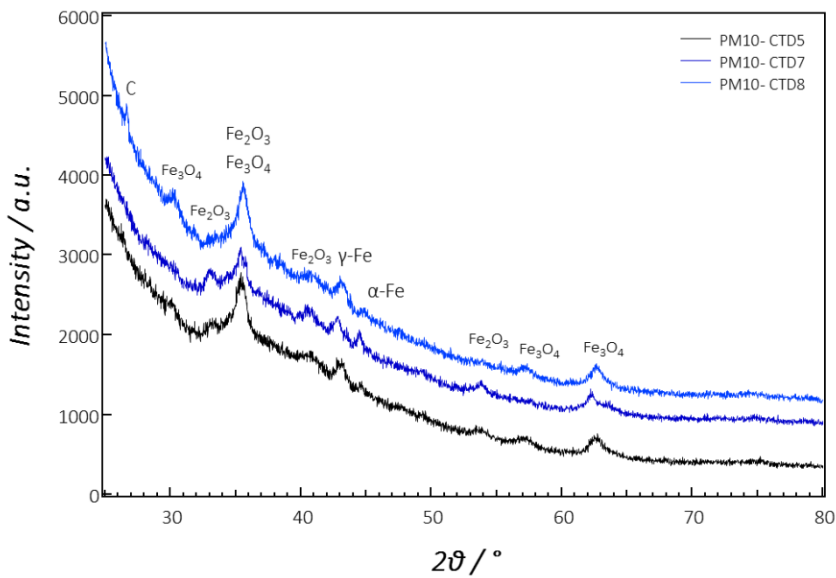


**Figure 5.16:** Experimental XRD pattern collected for PM<sub>10</sub> samples from CTD5, CTD7 and CTD8 FCs. The phase identification is reported close to each observed peak

	CTD4	CTD10	CTD5	CTD7	CTD8
Fe <sub>3</sub> O <sub>4</sub>	32.9(4)	14.2(2)	main	main	main
Fe <sub>2</sub> O <sub>3</sub>	49.6(5)	54.9(2)	main	main	main
Fe ( $\alpha$ + $\gamma$ )	14.1(7)	17.0(2)	secondary	secondary	secondary
C	3.4(5)	-	minor	-	minor
Cu	-	13.6(9)	-	-	-
R <sub>wp</sub>	3.93%	3.69%			
$\chi^2$	1.57	4.10			

**Table 5.4:** Summary of relative weight ratios for identified crystalline phases in PM<sub>10</sub> emissions from *Category 3* friction couples. Estimated standard deviations (*esd*) are reported in blue within brackets and refer to the last reported significant digit. R<sub>wp</sub> and  $\chi^2$  are goodness of fit parameters. For emission samples from CTD5, CTD7 and CTD8 FCs, only a qualitative assessment of the relative abundance is reported for the identified compounds.

As can be observed from the reported results, the dominant presence of oxidized Iron species is confirmed also in the PM<sub>10</sub> emissions described in this paragraph. Conversely, metallic Iron is found in lower amount, usually in both ferritic and austenitic forms. Looking at the relative abundance between the two polymorphs (relative ratio in main peaks reported in Figure 5.16) it is evident that  $\gamma$ -Fe is dominant in these particulates. This observation is in good agreement with the tribological characteristics of the friction couple belonging to *Category 4*, since they are expected to produce emission with higher relative ratio of material generated by the consumption of the friction composite. Similarly, when present, metallic Copper ( $\alpha$ -Cu) is easily identified and quantified. Notably, its concentration is in extremely good agreement with the corresponding results from the elemental analysis. Conversely, the overall low concentrations of Carbon combined with the low signal to noise ratio in the collected XRD patterns, makes the identification and therefore the quantification of its crystalline compounds extremely difficult.

### 5.3.5. *Category 5 (CC BDs + LS/LM FMs)*

As previously reported, the friction couples belonging to the *Category 5*, *i.e.* carbo-ceramic BDs coupled against LS/LM FMs, generate the lower amount of emissions in respect to the counterparts from all the other categories. The very low amount of material collected on the corresponding filters is detrimental for the XRD analysis, since it becomes impossible to obtain more than few and very weak diffraction features for the corresponding emissions. Figure 5.17 reports as example the experimental diffraction patterns obtained for the **CC2** sample, together with the phase attribution of the observed diffraction peaks. As can be seen in the graph, the collected intensities are extremely low. Nevertheless, some qualitative information can still be obtained. In

particular, looking at the relative ratio between the diffraction peaks for each phase, it is possible to see that, for the first time, the Graphite main peak at about  $26.5^\circ$  has higher intensity in respect with the counterpart for the Magnetite (at about  $36^\circ$ ). This is in good agreement with both the results from the elemental analysis and the compositional features of the friction couple. More in detail, being the BD made by carbo-ceramic composite, the emissions of FCs belonging to *Category 5* are richer in Carbon and poorer in Iron in respect with the counterparts from all the previous categories. In addition, no clear evidences of the presence of the Hematite ( $\text{Fe}_2\text{O}_3$ ) are observed, while weak signals from metallic Iron are detected. Finally, other two broad features are observed: *i*) a shoulder at lower diffraction angles in respect with the main Magnetite peak; and *ii*) a peak at about  $40^\circ$ . Both this two signals are compatible with the presence of Silicon carbides, and, more in detail, with the SiC-6H (hexagonal) polytype. Notably, this compound can be present on both sides of the friction couple: as constituent of the carbo-ceramic composite and eventually as abrasive in the friction mix.

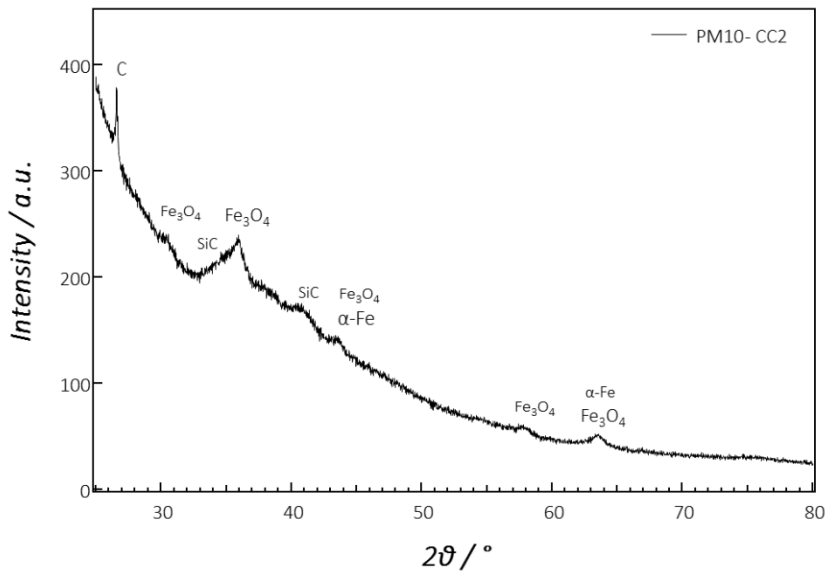


**Figure 5.17:** Experimental XRD pattern collected for PM<sub>10</sub> sample from CC2 FC. The phase identification is reported close to each observed peak.

### 5.3.6. Crystalline Fraction Summary





As testified from all the results reported in the previous paragraphs, the XRD probe can be used as convenient tool to characterize the crystalline fraction of the brake emissions. At a first level, the identification of several crystalline compounds composing the investigated particulates, together with qualitative assessments of their relative

abundance, can be obtained even when PM<sub>10</sub> samples are collected in extremely limited amounts. When more material is available for the analysis, semi-quantitative information can be obtained thanks to the phase analysis carried out by means of WPPF refinement methods. Notably, all the results obtained are in excellent agreement with the corresponding ones from the elemental analysis. Therefore, it can be inferred that the crystalline fraction of the brake emissions represents a good first description of their phase composition, especially when evaluating the main constituents. With specific reference to the Fe/O ratio already diffusely discussed in the previous chapter, it is found that the Iron contained inside the PM<sub>10</sub> brakes emissions has usually more oxidized than metallic character, with very few exceptions. However, different ratio between metallic and oxidized Iron are unveiled, depending on the materials composing the starting friction couple and accordingly with their tribological properties. Thus, it is possible to conclude that the XRD probe can be conveniently used also to understand more in detail the tribological behavior of a specific FC.

When minor components are considered, more limited but still valuable information can be obtained. This is due to the combination of two main factors: *i)* the relatively high detection limits of the XRD probe; and *ii)* the low amounts of material typically available for the analysis. Nevertheless, several compounds characterized by high electron density and/or high crystallinity can be easily detected and possibly quantified in semi-quantitative fashion. This is especially true for metals (such as Cu, Zn and their alloys), for inorganic oxides (ZrO<sub>2</sub>, titanates) and inorganic sulfides. Interestingly, the XRD phase analysis can be used also to qualitatively assess the relative abundance between crystalline compounds (Graphites, cokes, inorganic carbides) and amorphous forms (organic binders) of Carbon inside the emissions. Similarly, it can be used to evaluate the relative ratio between different Iron polymorphs ( $\alpha$ -Fe and  $\gamma$ -Fe): depending on the compositional features of the specific friction couples, this can be used to assess more in detail the relative contribution of the two FC sides to the generation of the investigated particulate.

Finally, taking all the reported results together, it is possible to summarize the relative abundance of several typologies of crystalline compounds depending on the materials composing the friction couple (Table 5.5). As already discussed in the previous chapter, the chemistry of the brakes emissions can be closely related to the chemistry of Iron, as first approximation. More in detail, Iron oxides (mainly Magnetite and Hematite) are frequently the dominant constituents, while metallic Iron represents a secondary contribution. Other metals (mainly Cu and Zn) are unfrequently found in appreciable amounts and their presence is dependent on the specific formulation of the friction material. Other inorganic oxides are usually found in appreciable amounts only in particulates generated by FCs belonging to *Category 3*, while being an overall minor

contributions in the other categories. Crystalline compounds of Carbon are ubiquitously found, but in secondary or minor amounts. Finally, other compounds, such as inorganic sulfides and carbides are rarely detected in trace amounts.

	LS/LMs 	INs 	NAOs 	CTDs 	
	Category 1	Category 2	Category 3	Category 4	General
Fe <sub>3</sub> O <sub>4</sub>	Main	Main	Main	Main	Main
Fe <sub>2</sub> O <sub>3</sub>	Main	Main	Secondary	Secondary	
α-Fe/γ-Fe	Secondary	Main	Minor	Minor	
Metals (Cu, Zn)	Minor	Minor	Minor	Minor	Minor
Graphite	Secondary	Minor	Secondary	Minor	Secondary
Inorganic Oxides	-	-	Secondary	-	Minor
Others	Traces	Traces	Traces	Traces	

**Table 5.5:** Summary of relative abundance for crystalline compounds identified in the investigated PM<sub>10</sub> particulates.

#### 5.4. Oxidation States in *d-Block* Metals

In spite of being a convenient tool for the phase composition investigation, as already reported, the XRD probe suffers of two main drawbacks: *i)* relatively high detection limits, most of all when limited amount of material is available for the analysis; and *ii)* complete insensibility to amorphous materials. In the next paragraphs, XANES analysis is proposed as convenient tool in order to overcome these limitations. In particular, the distribution of oxidation states of several *d-block* metals of environmental and biological interest is assessed, especially when they are present in the PM<sub>10</sub> emissions in minor/trace amounts and not detected in the XRD analysis. For this reason, Ti, V, Cr, Mn, Cu and Zn K-edges in several collected particulates are reported and analyzed. A detail of all the measured spectra is summarized in Table 5.6, together with the corresponding element concentration within each investigated particulate. In addition, also an investigation on the X-Ray absorption of Iron at the K-edge is reported, in order to look more in detail at the local structure of this element, since it is recognized as the most characterizing element for brakes emissions. The analysis reported in the next paragraphs are carried out based on two levels. For each element, a first qualitative

assessment is always reported, by means of comparison between the X-Ray Absorption (XAS) spectra of investigated brakes emissions and others from representative standards for specific oxidation states. When sufficient quality of the experimental spectra is obtained and wide range of standards spectra are available, Linear Combination Fit refinement of the latter ones is used to match the experimental data and obtain a more quantitative information on the relative abundance of the oxidation states.

	Ti / wt%	V / wt%	Cr / wt%	Mn / wt%	Fe / wt%	Cu / wt%	Zn / wt%
LS/LM1			0.63(0.05)	0.43(0.02)	54.6(1.7)	0.22(0.04)	0.26(0.03)
LS/LM2		0.09(0.01)	0.91(0.02)	0.41(0.02)	53.3(0.9)		0.28(0.03)
LS/LM3			0.85(0.02)	0.64(0.02)	51.9(0.6)		0.23(0.01)
LS/LM4			0.42(0.01)	0.41(0.01)	58.4(1.1)		
IN3			0.13(0.02)	0.48(0.04)	64.8(0.5)		
IN10					64.2(0.4)		
NAO1	3.22(0.03)		0.14(0.01)	0.19(0.03)	34.3(0.6)		
CTD3			1.64(0.01)		17.2(0.3)		

**Table 5.6:** Summary of investigated K-edges and corresponding elemental concentrations in analyzed PM<sub>10</sub> particulates (from *Chapter 4*).

#### 5.4.1. Titanium K-edge

XAS spectrum for Titanium is acquired only for the NAO1 sample, which was previously found to contain about 3.2 wt% of the element. Figure 5.18 shows the experimental XAS spectrum acquired at the Ti K-edge, together with standard references. In particular, metallic Ti (Ti foil) and three different Ti(IV) compounds are reported. The three Ti(IV) compounds differ for coordination and structure: *i*) K<sub>2</sub>Ti<sub>2</sub>O<sub>5</sub> is composed by [(TiO)O<sub>4</sub>] trigonal bipyramid units<sup>[8]</sup>, in which Ti exhibits coordination 5 (<sup>5</sup>Ti); *ii*) TiO<sub>2</sub>, Anatase polymorph, is composed by [TiO<sub>6</sub>] octahedral units, in which Ti exhibits coordination 6; and *iii*) TiO<sub>2</sub>, Rutile polymorph, composed by [TiO<sub>6</sub>] octahedral units and Ti exhibits coordination 6.<sup>[8]</sup> As can be observed from the inset reported in Figure 5.18, all the spectra are characterized by a pre-edge structure, which is commonly associated in literature to transitions from 1s to 3d energy levels.<sup>[8]</sup> This transition is usually forbidden from selection rules, but becomes allowed when *p-d* orbital mixing occurs in sites without a center of symmetry, such as in [TiO<sub>4</sub>] tetrahedral or [(TiO)O<sub>4</sub>] pyramid coordination. The intensity and the position of the pre-edge structure are reported to be directly proportional to the degree of *p-d* hybridization, the oxidation state and the coordination.<sup>[8]</sup> In particular, the normalized intensity of the feature can be used to discriminate between three main coordination domains for Titanium, *i.e.* <sup>4</sup>Ti, <sup>5</sup>Ti and <sup>6</sup>Ti.<sup>[8]</sup> More in detail, <sup>4</sup>Ti compounds usually exhibit the higher intensities, between 70

and 100% of the main absorption peak, and the lower energy shifts (around 3 eV).  $^{61}\text{Ti}$  compounds usually exhibit the lowest relative intensities, from 0 to 30% of the main peak, together with the stronger energy shifts towards the higher energies (up to 5 eV).  $^{51}\text{Ti}$  compounds show intermediate characteristics, with normalized energies in the order of the 40 to 70% of the main absorption peak and energy shifts around +4 eV.<sup>[8]</sup> Looking at the position of the pre-edge feature as measured for the NAO1 sample, it is clearly possible to observe that it is shifted towards higher energies (4970.5 eV) in respect with the metallic Ti counterpart (4966.4 eV). Therefore it is clearly possible to conclude that the oxidation state of Titanium inside the investigated particulate is 4+. However, the assessment of its coordination is less straightforward: the shift of the pre-edge peak (4.1 eV) is closer to the common range for  $^{51}\text{Ti}$  compounds, while the normalized intensity value (about 17%) is typical to the domain of  $^{61}\text{Ti}$  compounds. At the same time, looking at the shape of the pre-edge structure, strong differences are clearly evident when compared with the corresponding area in the  $\text{TiO}_2$  references. Conversely, the modulations of the absorption located immediately after the main peak appear more similar to those of the  $^{61}\text{Ti}$  standards in respect to the corresponding range in the potassium titanate spectrum.

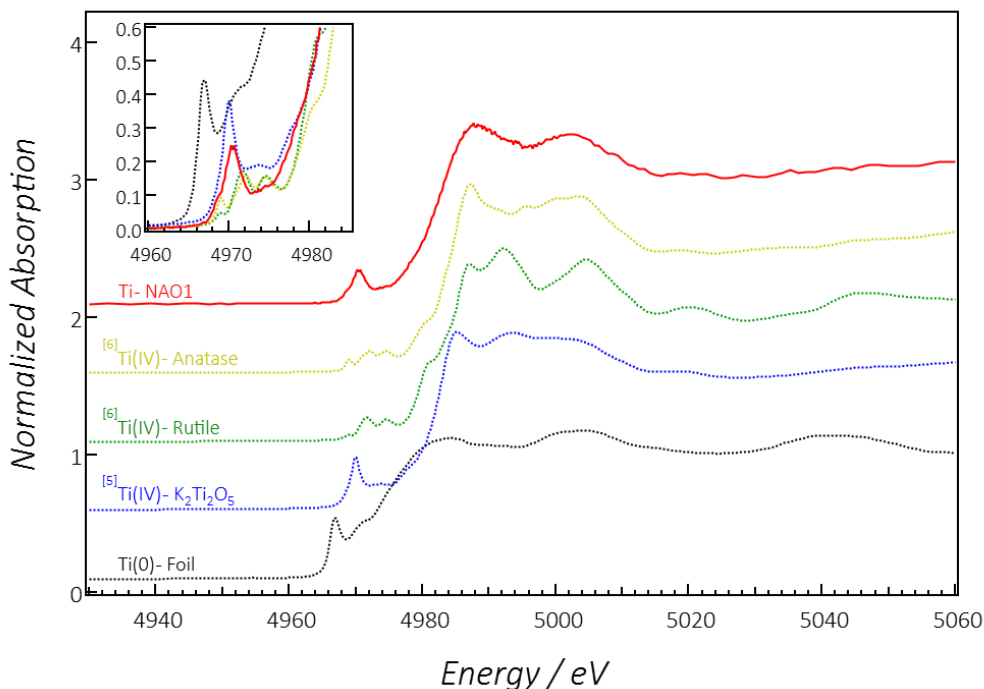


**Figure 5.18:** Experimental XAS spectrum at the Titanium K-edge for NAO1  $\text{PM}_{10}$  sample (red profile) and corresponding standard references (dotted lines). Ti foil,  $\text{K}_2\text{Ti}_2\text{O}_5$ , Rutile and Anatase are respectively reported in black, blue, green and yellow. In the top-left corner is reported a more detailed comparison of the observed pre-edge features.



For all these reasons, it is inferred that Titanium contained in NAO1 PM<sub>10</sub> sample can be due to different compounds, most likely form the titanate family and possibly exhibiting mixed coordination character. This seems reasonable since: *i*) potassium titanates are commonly used as mild abrasives and friction modifiers in NAO FM formulations; and *ii*) titanates as friction mix raw materials come usually from geological origins and are mixtures of different phases. Unfortunately, standard samples of other Potassium titanates were not available during the XAS experiment to confirm the hypothesis. Nevertheless, it seems at least corroborated by other results reported in the literature<sup>[8,9]</sup>, as well as from the linear combination fit showed in Figure 5.19. Indeed, in spite of being not completely satisfactory, this fit clearly shows on overall low affinity between the spectrum from NAO1 particulate sample and those ones from the two most common polymorphs of TiO<sub>2</sub> (Anatase and Rutile). Conversely, the Potassium Titanate appears to describe in better fashion the major features of the experimental XAS spectrum at the K-edge.

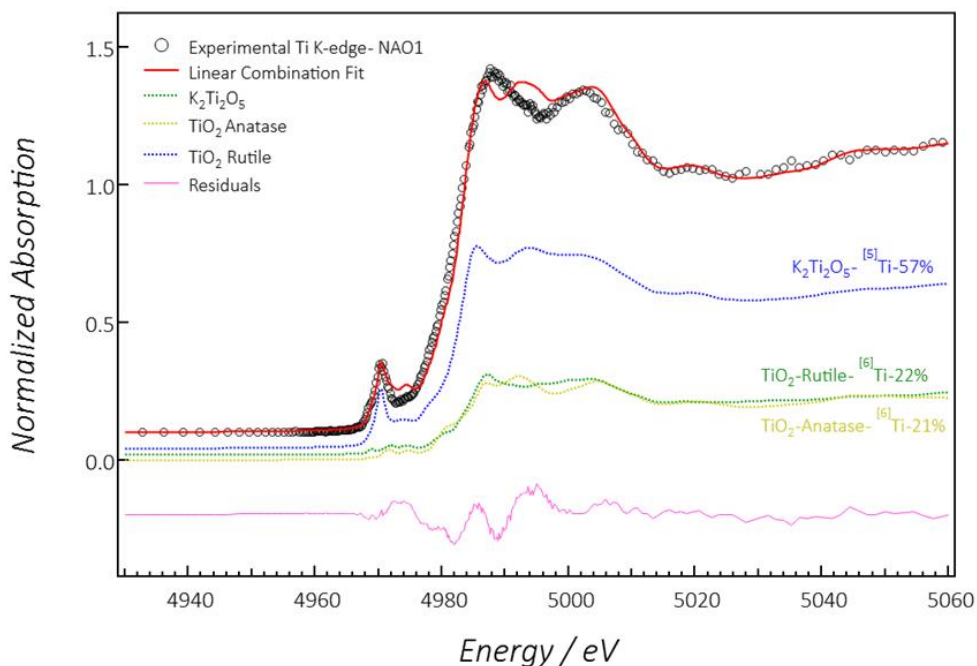


**Figure 5.19:** Linear combination fit of the experimental XAS spectrum for the NAO1 PM<sub>10</sub> sample, at the Ti K-edge. The measured points are reported as black circles, while the standard references are rendered in dotted lines. Potassium titanate, Rutile and Anatase are respectively reported in blue, green and yellow.

The overall final fit is reported as red profile, while the pink line represents the residuals between experimental data and calculated model. A R value of 2.28 is obtained for this fit.

### 5.4.2. Vanadium K-Edge

Vanadium K-edge spectrum was acquired only for the LS/LM2 PM<sub>10</sub> sample, since this is the only emission in which V has been found in amounts significantly higher (0.09±0.01 wt%) than the EDXS detection limit. In spite of the extremely low concentration of Vanadium and the consequent low signal to noise ratio, the collected XAS spectrum retains a sufficient degree of appreciable details. The spectrum is reported in Figure 5.20, together with four V-based reference compounds, *i.e.* metallic Vanadium, V<sub>2</sub>O<sub>3</sub>, VO<sub>2</sub> and V<sub>2</sub>O<sub>5</sub>. Thus, four different oxidation states are available for comparison: V(0), V(III), V(IV) and V(V). As can be observed in the graphs reported below, also Vanadium K-edge spectrum are characterized by pre-edge features. Similarly to the Titanium case, they are due to symmetry-forbidden transitions ( $1s \rightarrow 3d$ ). These features gain intensity from the mixing of  $p$  and  $d$  orbitals, following coordination geometry variations from octahedral to five-coordinate or tetrahedral or metal-ligand  $\pi$  bonding.<sup>[10]</sup> Therefore, they exhibit increasing intensity in respect with the main absorption peak moving towards the higher oxidation states.

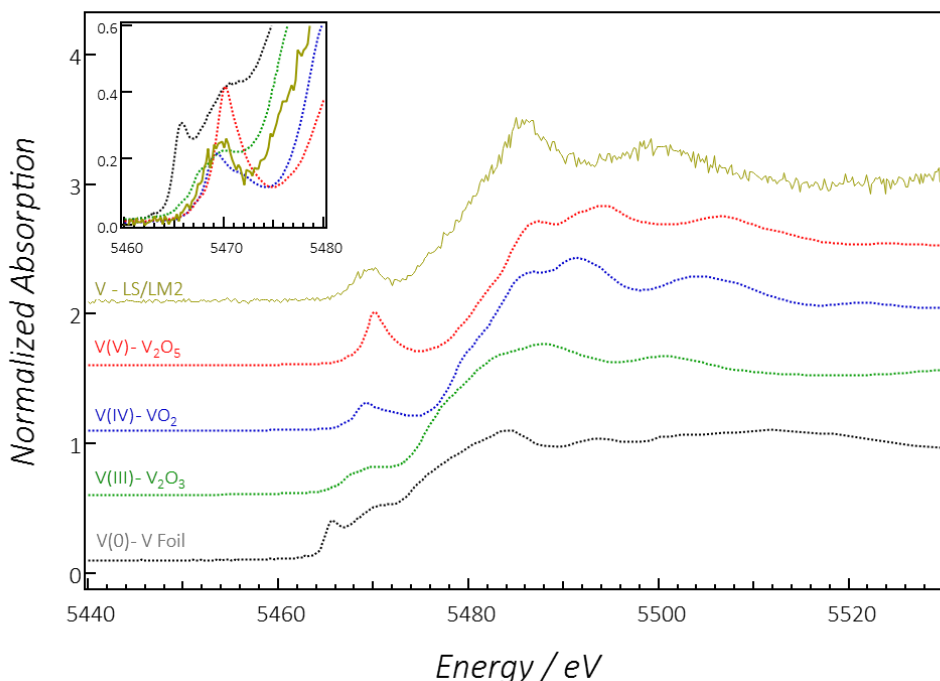


**Figure 5.20:** Experimental XAS spectrum at the Vanadium K-edge for LS/LM2 PM<sub>10</sub> sample (yellow profile) and corresponding standard references (dotted lines). V foil, V<sub>2</sub>O<sub>3</sub>, VO<sub>2</sub> and V<sub>2</sub>O<sub>5</sub> are respectively reported in black, green, blue and red. In the top-left corner is reported a more detailed comparison of the observed pre-edge features.

Looking in detail at the comparison of the pre-edge structures reported in the inset in Figure 5.20, it is possible to confirm a good matching of both the position and the relative intensity of the peak from the LS/LM2 sample with the corresponding from V(III) and V(IV) references. Conversely, V(V) pre-edge is clearly shifted towards higher energies and exhibits at the same time significantly higher intensity. These qualitative observations are also confirmed by the linear combination fit of the Vanadium references reported in Figure 5.21. As can be observed, both the metallic V and the higher oxidation state V(V) do not appear in the fit, testifying their extremely low similarity with the experimental V K-edge of LS/LM2 emission sample. The best linear combination fit is obtained when mixed V(III) and V(IV) oxidation state are considered, in 40:60 ratio. In spite of describing in good fashion the pre-edge feature, the overall fit still does not describe in completely satisfactory manner the main absorption peak and the following modulations ( $R = 2.20$ ,  $\chi^2 = 0.20$ ). Therefore, it is possible to exclude the presence of  $V_2O_3$  and  $VO_2$  oxides in the investigated particulate.

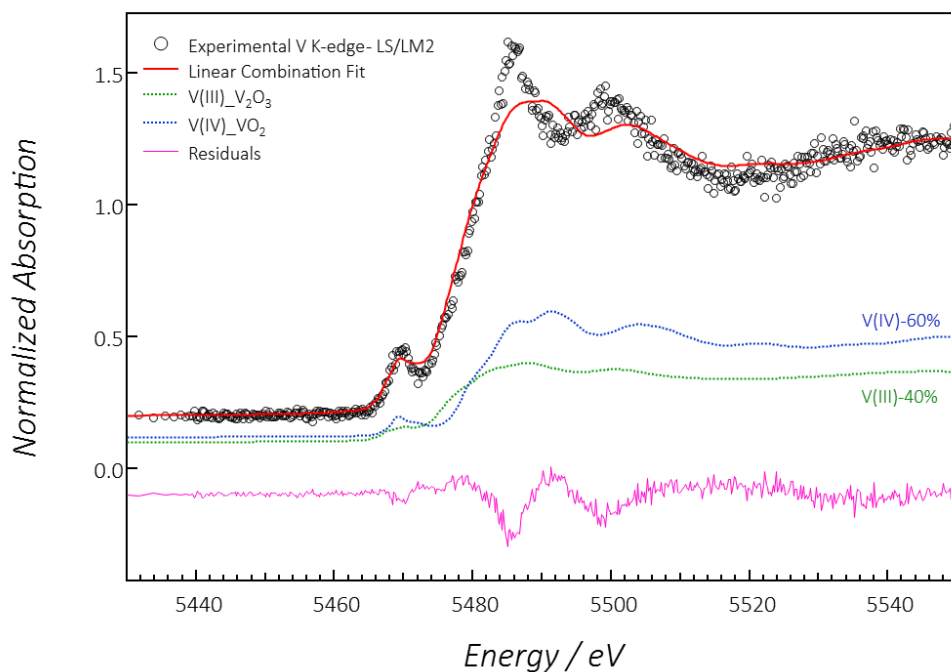


**Figure 5.21:** Linear combination fit of the experimental XAS spectrum for the LS/LM2 PM<sub>10</sub> sample, at the V K-edge. The measured points are reported as black circles, while the standard references are rendered in dotted lines.  $V_2O_3$  and  $VO_2$  are respectively reported in blue and green. The overall final fit is reported as red profile, while the pink line represents the residuals between experimental data and calculated model. A R value of 2.20 is obtained for this fit.

Differently from the Titanium case, Vanadium compounds are not typically used in friction materials formulations. Thus, attributions driven from the knowledge of the friction mix formulation are not possible. Therefore, Vanadium in LS/LM2 PM<sub>10</sub> sample is most likely a trace element/impurity in the cast-iron or in raw materials composing the friction couple. Considering the first option, Vanadium eventually surrounded by Iron might possibly generate Fe-V mixed oxides. Indeed, the overall measured profile appears to closely resemble those typical for spinel compounds, as can be seen for instance looking at the Chromite profile in *Paragraph 5.4.3* for reference, as well as in the limited available literature on XANES characterization for such typology of Vanadium compounds.<sup>[10]</sup> Considering the second possibility, Vanadium might be contained as trace elements within a wide range of different geological compounds typically used as fillers, such as for example silicates and alumino-silicates.

#### 5.4.3. Chromium K-Edge

Chromium K-edge spectra were acquired for the following six PM<sub>10</sub> particulate samples: LS/LM1, LS/LM2, LS/LM3, LS/LM4, NAO1 and IN3. Chromium concentration ranges between 0.14±0.01 (NAO1) and 0.91±0.02 (LS/LM2) wt%. All the acquired spectra are reported in Figure 5.22, together with standard references for three different Cr oxidation states: Cr(0) (Cr foil), Cr(III) (Chromite, Fe<sub>2</sub>CrO<sub>4</sub>) and Cr(IV) (Chromium trioxide, CrO<sub>3</sub>). As can be observed in the following graphs, all the measured spectra are closely similar and characterized by a sharp and intense main absorption peak, followed by strong modulations. Spectrum from sample NAO1 is characterized by an extremely low signal to noise ratio, due to the modest Cr concentration combined with a very low amount of deposited material on the corresponding collection substrate. Similarly, spectrum from IN3 sample shows low signal to noise ratio, even if the overall profile is less affected. Nevertheless, also in these two spectra, minimum level of detail is retained to assess qualitatively the Chromium speciation. As can be clearly observed from the comparison of the collected spectra with the reported standard references, all the measured Cr K-edges closely resemble that one from the Chromite (Fe<sub>2</sub>CrO<sub>4</sub>), in which Chromium exhibits 3+ oxidation state. In particular, the sharp pre-edge peak occurring at about 5993.3 eV in Cr(VI) compounds, due to the *1s* to mixed *3d/4p* hybrid orbital transition<sup>[11]</sup> is never observed. Figure 5.23 shows a detail of the pre-edge energy range for the four most resolved samples (LS/LM1 to LS/LM4), in which is clearly possible to see how a pre-edge structure indicating the same transition is always present. Nevertheless, the observed pre-edge peaks are characterized by very low intensities, never exceeding the 4% of the corresponding main absorption peak. In addition, they are localized at lower energies (5990.5-5990.7 eV) in respect with the counterpart from the Cr(VI) compounds. All these observations testify the absence of hexavalent

Chromium in the observed PM<sub>10</sub> emissions (at least at the detection capability of the XANES probe) and the only dominant presence of Cr in trivalent oxidation state.

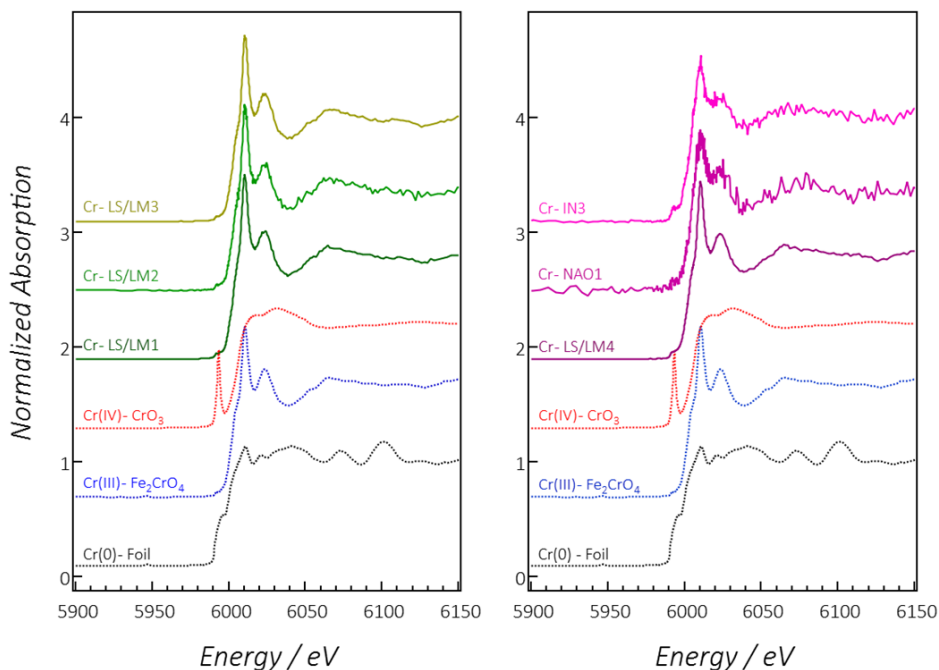


**Figure 5.22:** Experimental XAS spectrum at the Chromium K-edge for LS/LM1, LS/LM2, LS/LM3, LS/LM4, NAO1 and IN3 PM<sub>10</sub> samples (green scale and violet scale profiles). The standard references are reported in dotted lines: Cr foil, Fe<sub>2</sub>CrO<sub>4</sub> and CrO<sub>3</sub> are respectively reported in black, blue and red.

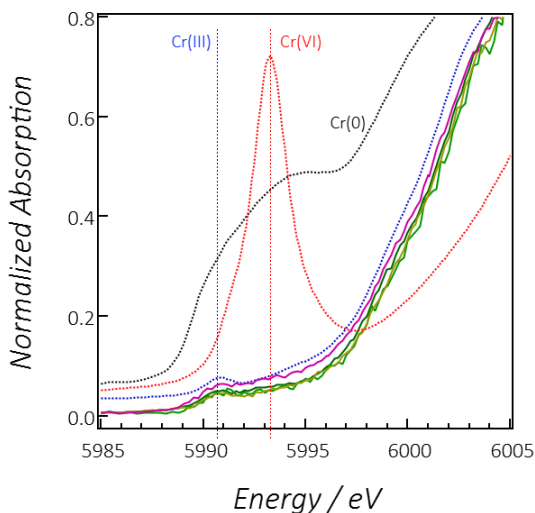


**Figure 5.23:** Comparison of the pre-edge peaks in LS/LM1, LS/LM2, LS/LM3 and LS/LM4 PM<sub>10</sub> samples with standard reference compounds.

A further confirmation of these results is obtained by linear combination fit of reference XAS spectra against the ones collected for the emissions samples. In particular, it is clearly possible to observe that the only reference needed to fit perfectly ( $R = 0.009$ ,  $\chi^2 = 0.52$ ) the experimental data is the Chromite, as can be seen reported for LS/LM1 PM<sub>10</sub> sample in Figure 5.24.

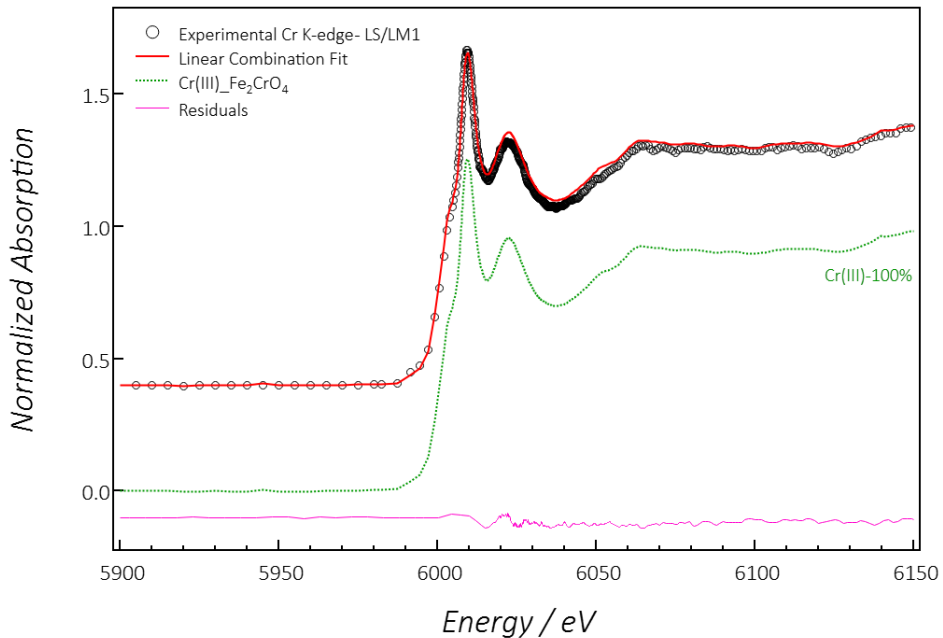
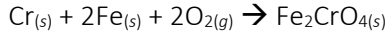


**Figure 5.24:** Linear combination fit of the experimental XAS spectrum for the LS/LM1 PM<sub>10</sub> sample, at the Cr K-edge. The measured points are reported as black circles, while the standard references are rendered in dotted lines. Fe<sub>2</sub>CrO<sub>4</sub> is reported in green. The overall final fit is reported as red profile, while the pink line represents the residuals between experimental data and calculated model. A R value of 0.009 is obtained for this fit.

The obtained results are well coherent with the compositional characteristics of the investigated friction couples. For instance, Chromites and Magnesium-Chromites from geological origin are typical mild abrasives used in LS/LM formulations. In addition, Chromium is always found in cast-irons in trace amounts as alloying element or impurity. As far as the FM raw materials are considered, both the highest temperatures possibly experienced locally at the tribological interface (500-700°C), as well as those characteristic for a standard use of disc brakes devices (below 100°C), are not sufficient to promote the Chromium oxidation from stable spinel compounds to eventual hexavalent forms. In addition, when considering traces of metallic or intermetallic Cr inside the GCI braking discs, the cast-iron can likely act as a buffer, limiting the oxidation of Cr to its trivalent form through the tribo-reactions with Iron:



Notably, this is also in agreement also with the Fe-Cr-O phase diagram, even at the highest temperatures. Similarly to what reported before, Figure 5.25 shows the detail of the pre-edge energy range for the remaining two samples (NAO1 and IN3). As already highlighted, the XAS spectra of these two samples are significantly less defined, due to: *i)* low amounts of particulate collected during the corresponding emission tests; and *ii)* low Cr concentrations. In spite of a significantly lower degree of confidence, it is anyhow possible to guess similar trend to that reported for the previous four particulates. More in particular, even if broad and noisy, Cr(III) pre-edge features seems to appear at about 5990.7 eV, while no clear evidences of peaks at 5993 eV from Cr(VI) compounds can be spotted. Thus, combining these observations with the previous considerations on the stability of Cr-bearing compounds in the friction couples, it is possible to conclude that also for particulates generated by GCI BDs coupled against IN or NAO FMs the completely dominant form of Chromium is Cr(III).

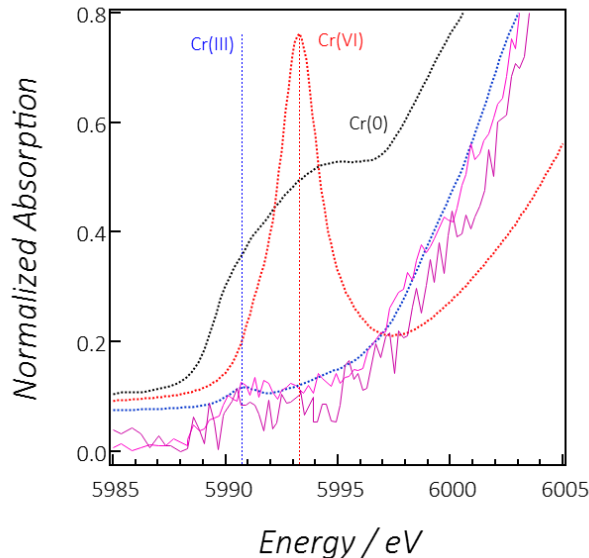


**Figure 5.25:** Comparison of the pre-edge peaks in NAO1 and IN3 PM<sub>10</sub> samples with standard reference compounds.

#### 5.4.4. Manganese K-Edge

Manganese K-edge spectra were acquired for the following six PM<sub>10</sub> particulate samples: LS/LM1, LS/LM2, LS/LM3, LS/LM4, NAO1 and IN3, with Manganese concentration ranging between 0.19±0.03 (IN3) and 0.64±0.02 (LS/LM3) wt%. All the acquired spectra are reported in Figure 5.26, together with standard references for

different Mn-bearing compounds exhibiting four different oxidation states: Mn<sup>(0)</sup> (Mn foil), Mn<sup>(II)</sup> (Manganese Oxide, MnO), Mn<sup>(III)</sup> (Manganese trioxide, Mn<sub>2</sub>O<sub>3</sub>) and Mn<sup>(IV)</sup> (Manganese dioxide, MnO<sub>2</sub>).

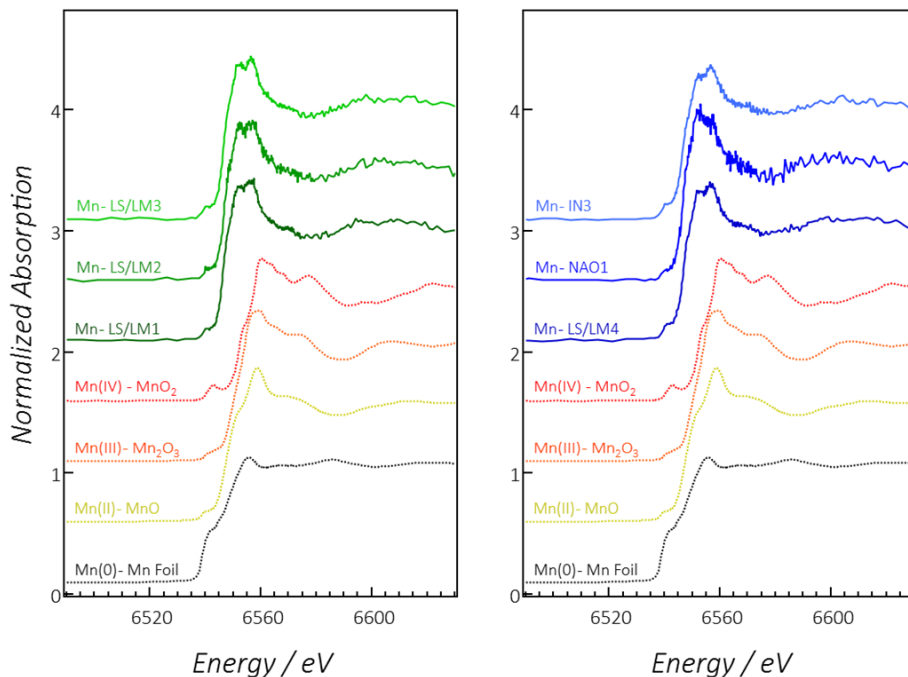


**Figure 5.26:** Experimental XAS spectrum at the Manganese K-edge for LS/LM1, LS/LM2, LS/LM3, LS/LM4, NAO1 and IN3 PM<sub>10</sub> samples (green scale and blue scale profiles). The standard references are reported in dotted lines: Mn foil, MnO, Mn<sub>2</sub>O<sub>3</sub> and MnO<sub>2</sub> are respectively reported in black, yellow, orange and red.

As for all the other considered *d-block* metals, the Manganese K-edge shifts towards higher energies with increasing oxidation states. This is true for both the main edge peak and the pre-edge structures eventually present. In the case of Manganese, the position of the main absorption peak position is reported to be sensitive with interferences between atomic absorption and multiple-scattering features from distant neighbors.<sup>[12]</sup> Conversely, the pre-edge region, located 15-20 eV before the main absorption peak, is reported to be much less influenced by medium and long -range structures. Its appearance is related to transitions from *1s* to empty *3d* levels, more or less hybridized with *4p* levels from Mn ligands. Thus, several empirical methods based on the evaluation of the intensity and position of pre-edge feature to assess the Mn oxidation state are reported<sup>[12]</sup>, since the transitions become progressively more allowed moving towards the higher Mn valences. In particular, higher Mn oxidation states (Mn<sup>(V)</sup>, Mn<sup>(VI)</sup> and Mn<sup>(VII)</sup>) usually generate pre-edge peaks with normalized intensities between 30 and 100% of



the main absorption peak, localized above 6542 eV. Conversely, lower valences ( $\text{Mn}^{(II)}$ ,  $\text{Mn}^{(III)}$  and  $\text{Mn}^{(IV)}$ ) are characterized by relative intensities typically below the 10%, with pre-edge peaks laying below 6542 eV.<sup>[12]</sup> As can be observed qualitatively already at the visual inspection of the reported XAS spectra, all the Mn K-edge reported have significant affinity with the range of the lower oxidation states. This is further corroborated in Figure 5.27, reporting the detail comparison of the pre-edge features of three investigated samples together with the corresponding ones from reference standard materials. Looking at the graphs reported, it is evident that the normalized pre-edge peak intensities of the investigated samples are well below the 10% of the main absorption peak and their positions lay below 6452 eV.

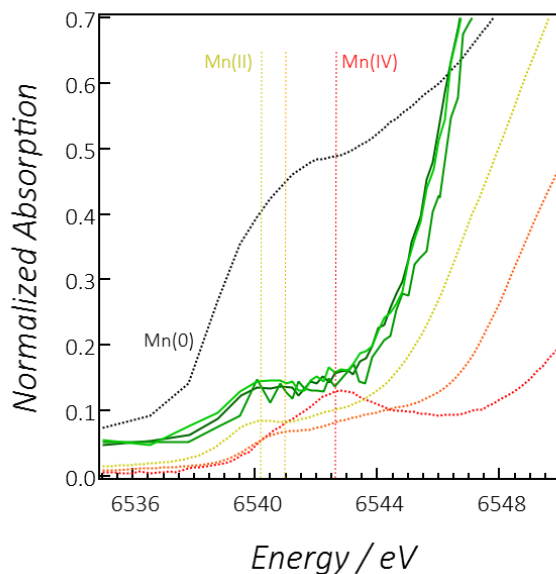


**Figure 5.27:** Comparison of the pre-edge peaks in LS/LM1, LS/LM2 and LS/LM3  $\text{PM}_{10}$  samples (green scale profiles) with standard reference compounds (dotted lines).

All these qualitative observations are finally confirmed in more quantitative fashion also by linear combination fit of standard references Mn K-edges. As can be observed in Figure 5.28, which reports the fit for the LS/LM4 particulate as example, the overall XAS spectrum profile is well described ( $R = 0.057$ ,  $\chi^2 = 1.54$ ) when assuming the presence of Manganese in three oxidation states. In particular,  $\text{Mn}^{(III)}$  is the dominant oxidation state,  $\text{Mn}^{(III)}$  and  $\text{Mn}^{(0)}$  are minor contributions, while  $\text{Mn}^{(IV)}$  is not appearing. These results are coherent with the compositional features of the starting materials generating the investigated brakes emissions. Looking at the rotor, Mn is always contained in minor amounts in grey cast-irons, mainly in form of  $\text{MnS}$  precipitates. Conversely, Mn compounds not commonly used or reported as raw materials for friction composites.

Therefore Mn in FMs can likely be present as impurity of other metallic/intermetallic species (Fe powders, steel fibers, etc.) or as trace/minor element in materials from geological origin (alumino-silicates, silicates, etc.) typically used as fillers. In all of these cases, the temperatures typically experienced at the tribological interface are hardly sufficient to promote the oxidation of Manganese to its higher oxidation states. Moreover, similarly to what proposed for the Chromium case, the large excess of Fe from grey cast-iron BD can likely act as buffer to limit the oxidation of Mn to lower states, forming mixed Fe-Mn oxides also at the highest temperatures.

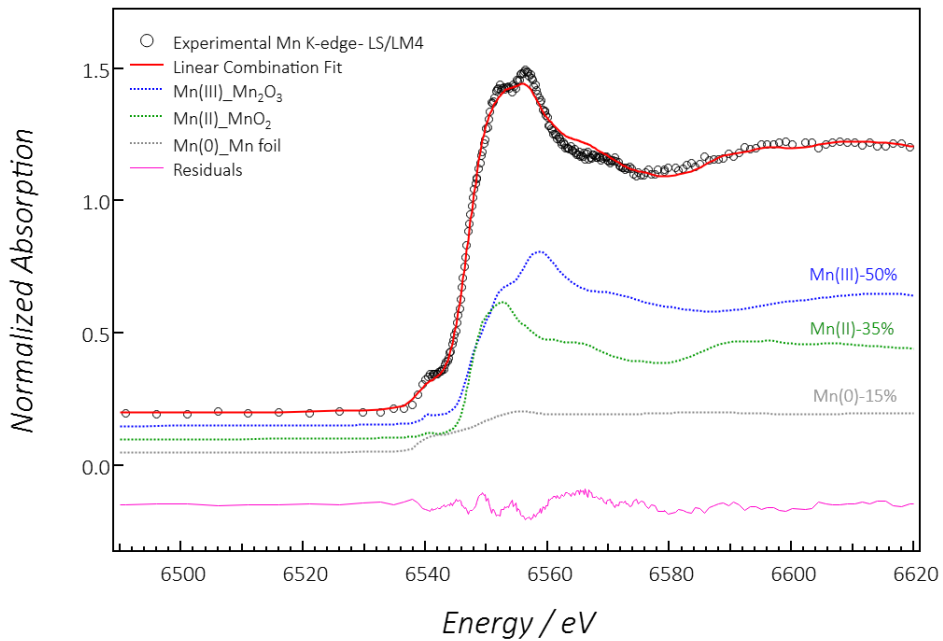


**Figure 5.28:** Linear combination fit of the experimental XAS spectrum for the LS/LM4 PM<sub>10</sub> sample, at the Mn K-edge. The measured points are reported as black circles, while the standard references are rendered in dotted lines. Mn foil, MnO and Mn<sub>2</sub>O<sub>3</sub> profiles are reported respectively in grey, green and blue. The overall final fit is reported as red profile, while the pink line represents the residuals between experimental data and calculated model. A R value of 0.057 is obtained for this fit.

#### 5.4.5. Iron K-Edge

Iron K-edge spectra were acquired for the following six PM<sub>10</sub> particulate samples: LS/LM2, LS/LM3, LS/LM4, NAO1, IN3 and IN10, with Iron concentration ranging between  $34.3 \pm 0.6$  (NAO1) and  $64.8 \pm 0.05$  (IN3) wt%. All the acquired spectra are reported in Figure 5.29, together with standard references for different Fe compounds exhibiting different oxidation states and coordination: metallic Fe (both foil and from the GCI cast iron), Fe<sup>(II)</sup> (Wustite, FeO), Fe<sup>(II,III)</sup> (Magnetite, Fe<sub>3</sub>O<sub>4</sub>), Fe<sup>(II,III)</sup> (Maghemite,  $\gamma$ -Fe<sub>2</sub>O<sub>3</sub>) and

Fe<sup>(III)</sup> (Hematite,  $\alpha$ -Fe<sub>2</sub>O<sub>3</sub>). As can be observed in comparative graph, all the reported spectra for the PM<sub>10</sub> emissions look qualitatively similar. In particular, the XAS spectra are characterized by weak pre-edge features at about 7114 eV and sharp main absorption peaks occurring between 7130 and 7134 eV. In addition, a shoulder of the main peak is always found at higher energies (at about 7145 eV) together with following broad modulations. The only major exception is represented by the K-edge recorded for sample IN10, which resembles closely the XAS spectra acquired at the Fe K-edge for the pristine grey cast-iron composing the braking disc. Another minor difference is observed in LS/LM4 and IN3 PM<sub>10</sub> sample, where the pre-edge structure exhibit slightly higher intensity and lower energy in respect to the counterparts from other LS/LM and NAO samples.

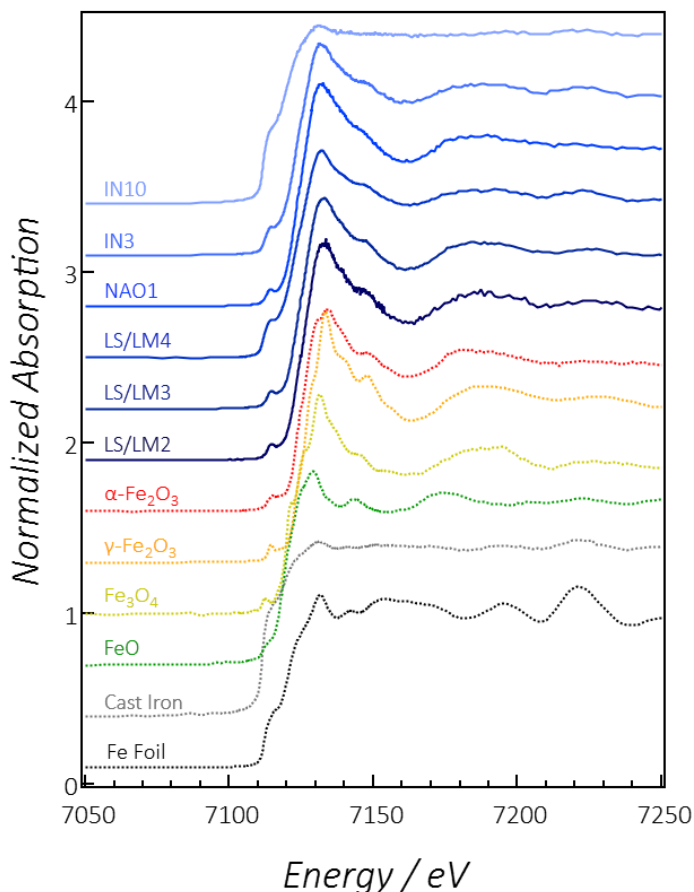


**Figure 5.29:** Experimental XAS spectrum at the Iron K-edge for LS/LM2, LS/LM3, LS/LM4, NAO1 IN3 and IN10 PM<sub>10</sub> samples (blue scale profiles). The standard references are reported in dotted lines: Fe foil, pristine GCI, FeO, Fe<sub>3</sub>O<sub>4</sub>,  $\gamma$ -Fe<sub>2</sub>O<sub>3</sub> and  $\alpha$ -Fe<sub>2</sub>O<sub>3</sub> are respectively reported in black, grey, green, yellow, orange and red.

The linear combination fits carried out for LS/LM3, LS/LM4 and IN10 samples (Figures 5.30 to 5.32) further confirms the qualitatively observed differences in terms of relative abundance of Fe-bearing compounds (or oxidation states), which are summarized in Table 5.7. For LS/LM3 sample, the best fit ( $R = 0.001$ ,  $\chi^2 = 0.04$ ) is obtained when describing the experimental spectrum only with Iron oxides. In particular, the Hematite ( $\alpha\text{-Fe}_2\text{O}_3$ ) is observed to describe the major part of the features (50%), while Magnetite ( $\text{Fe}_3\text{O}_4$ ) and Maghemite ( $\gamma\text{-Fe}_2\text{O}_3$ ) contribute in similar minor proportion (25%). Interestingly, these observations shed a new light into the local structure of the Iron composing this brake emissions. For the first time, XANES analysis unveiled the presence of the  $\gamma\text{-Fe}_2\text{O}_3$  polymorph within the range of Iron oxides characterizing the non-exhaust emissions from brakes. Maghemite is characterized by the same spinel ferrite structure as Magnetite, and, similarly to  $\text{Fe}_3\text{O}_4$ , is ferrimagnetic. Indeed, it can be considered as a Fe(II)-deficient Magnetite in the octahedral site, generated by low-temperature oxidation of the Magnetite itself. Therefore, the similar crystal structure leads to extremely similar characteristic diffraction patterns. Thus, these two Iron oxides can hardly be distinguished at the XRD probe, especially when broad peaks are observed, such as reported for the investigated brakes  $\text{PM}_{10}$  emissions (see *Paragraph 5.3*).

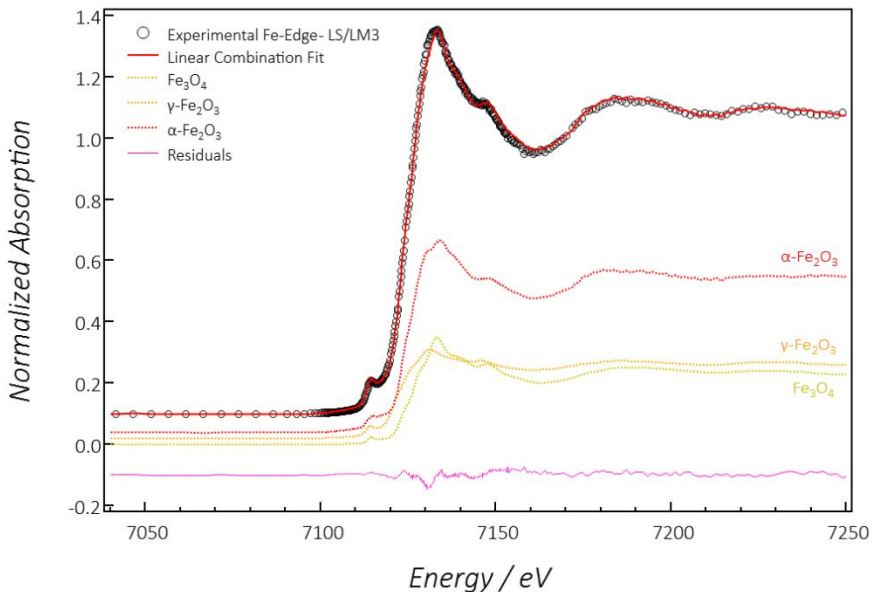


**Figure 5.30:** Linear combination fit of the experimental XAS spectrum for the LS/LM3  $\text{PM}_{10}$  sample, at the Fe K-edge. The measured points are reported as black circles, while the standard references are rendered in dotted lines.  $\text{Fe}_3\text{O}_4$ ,  $\gamma\text{-Fe}_2\text{O}_3$  and  $\alpha\text{-Fe}_2\text{O}_3$  profiles are reported respectively in yellow, orange and red.

The overall final fit is reported as red profile, while the pink line represents the residuals between experimental data and calculated model. A R value of 0.001 is obtained for this fit.

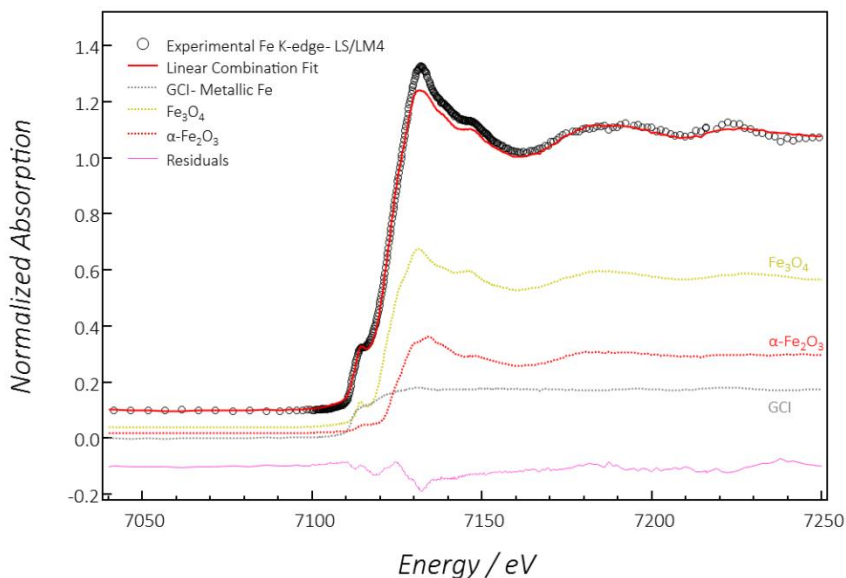


**Figure 5.31:** Linear combination fit of the experimental XAS spectrum for the LS/LM4 PM<sub>10</sub> sample, at the Fe K-edge. The measured points are reported as black circles, while the standard references are rendered in dotted lines: pristine GCI, Fe<sub>3</sub>O<sub>4</sub> and  $\alpha$ -Fe<sub>2</sub>O<sub>3</sub> profiles respectively in grey, yellow and red. The overall final fit is reported as red profile, while the pink line represents the residuals between experimental data and calculated model. A R value of 0.009 is obtained for this fit.

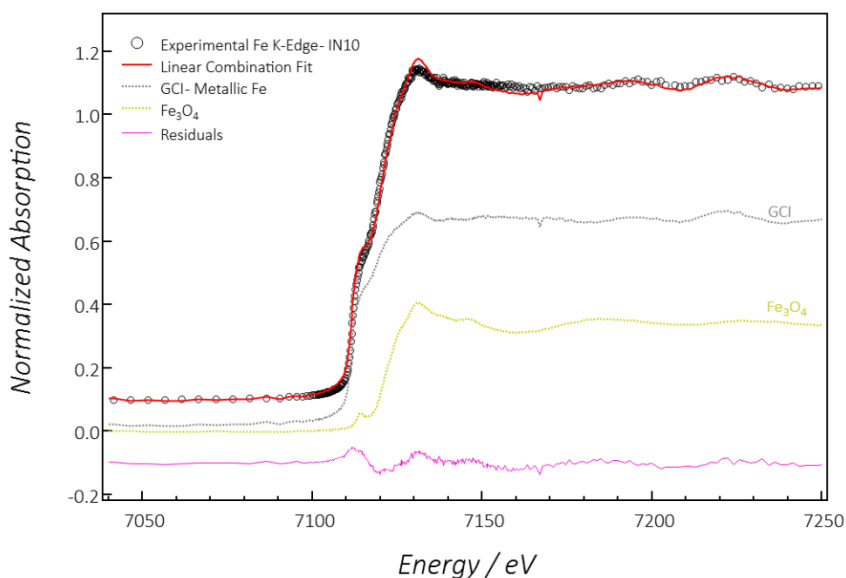


**Figure 5.32:** Linear combination fit of the experimental XAS spectrum for the IN10 PM<sub>10</sub> sample, at the Fe K-edge. The measured points are reported as black circles, while the standard references are rendered in dotted lines: pristine GCI and Fe<sub>3</sub>O<sub>4</sub> profiles respectively in grey and yellow. The overall final fit is reported as red profile, while the pink line represents the residuals between experimental data and calculated model. A R value of 0.002 is obtained for this fit.

	GCI	FeO	Fe <sub>3</sub> O <sub>4</sub>	$\alpha$ -Fe <sub>2</sub> O <sub>3</sub>	$\gamma$ -Fe <sub>2</sub> O <sub>3</sub>	R-factor	$\chi^2$
LS/LM3	-	-	25	50	25	0.001	0.04
LS/LM4	20	-	25	25	-	0.009	0.55
IN10	70	-	30	-	-	0.002	0.10

**Table 5.7:** Summary of relative abundance of Iron-based species in the investigated PM<sub>10</sub> particulates, as obtained from LCF analysis of the corresponding measured XAS spectra. The relative abundances are expressed in terms of weight percentage. The results are approximated to 5% of confidence level.

Conversely, particulates generated by LS/LM4 and IN10 friction couples show a progressive decrease of the overall amount of oxidized Iron and an increase of Iron exhibiting metallic character. In particular, the best fit ( $R = 0.009$ ,  $\chi^2 = 0.55$ ) for the LS/LM4 sample is obtained when using as reference standards the XAS spectrum of the pristine GCI composing the braking discs (20%), Hematite (Fe<sub>2</sub>O<sub>3</sub>, 25%) and Magnetite (Fe<sub>3</sub>O<sub>4</sub>, 55%). When looking at the IN10 sample, the GCI contribution is even higher (70%), while only secondary contribution of Magnetite (Fe<sub>3</sub>O<sub>4</sub>, 30%) is observed. Notably, all these trends are in excellent agreement with the observations previously reported in the XRD analysis as well as with the tribological characteristic of the different investigated categories of FCs. For instance, inorganic bound FMs usually exhibit higher direct abrasion towards the GCI BDs, therefore producing more metallic Iron in respect with the LS/LM counterparts. This behavior, justified by their specific mechanical properties (higher hardness) and already observed in the XRD characterization of the corresponding PM<sub>10</sub> emissions, is confirmed also at the XANES analysis. Interestingly, the reported XAS study indicate that significant variability of the tribological mechanism can exist also within the same category of FCs. For example, looking at the comparison between the Iron-based species composing the PM<sub>10</sub> emissions generated by LS/LM3 and LS/LM4, it is clearly possible to spot important differences. On one side, LS/LM4 is characterized by an overall higher degree of metallic Iron, testifying a corresponding higher degree of BD consumption due to direct abrasion. On the other hand, LS/LM3 particulate show significantly higher content of oxidized, with even the indication of a partial further oxidation of Magnetite to Maghemite. Thus, LS/LM3 FC tribology is clearly characterized by a higher level of adhesive wear and tribo-oxidation. Taking all the obtained results on a more general level, it is clearly possible to state that the combination of XRD and XANES Fe K-edge analysis of the PM<sub>10</sub> emissions produced by brakes represents an extremely powerful tool for: *i*) the accurate speciation of Iron within the investigated particulates; *ii*) the comparative assessment of the tribological behavior of specific friction couples; and *iii*) the characterization and the study of the emissive mechanisms of investigated FCs.

### 5.4.6. Copper K-Edge

Copper was found in appreciable amounts (higher than 0.5 wt%) only in a limited number of emissions, *i.e.* those generated by friction couples having copper-content FMs. When it is the case, XRD analysis unveiled the presence of metallic Cu or, with minor frequency, of some of its alloys (brass). In most of all the other investigated particulates, trace amounts of Copper are always detected, typically in the 0.1-0.3 wt% range. Cu is in fact a common trace element/impurity of Iron, thus it can be typically found in minor amounts the cast-iron composing the BD, as well as in some raw materials for friction composites (Fe powders, steel fibers, etc.). The XAS spectrum of only one sample was acquired at the Cu K-edge, as representative for the case of FCs from *Category 1* with Cu-free FMs. In particular, PM<sub>10</sub> emission from LS/LM1 was measured ([Cu] = 0.22 ± 0.04). It is reported in Figure 5.33, in comparison with three standard reference materials exhibiting Cu in different oxidation states: Cu<sup>(0)</sup> (Cu foil), Cu<sup>(I)</sup> (Cu<sub>2</sub>O, Cuprite) and Cu<sup>(II)</sup> (CuO, Tenorite).

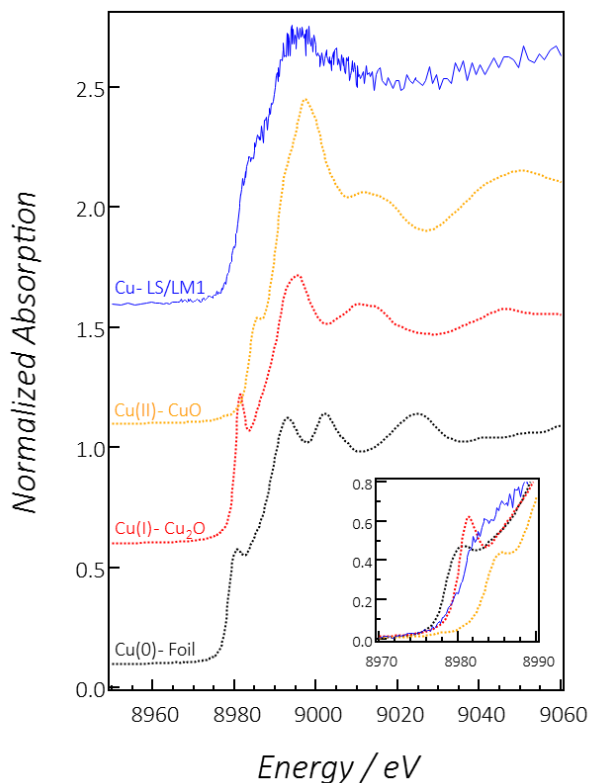


**Figure 5.33:** Experimental XAS spectrum at the Copper K-edge for LS/LM1 PM<sub>10</sub> samples (blue profile). The standard references are reported in dotted lines: Cu foil, Cu<sub>2</sub>O and CuO are respectively reported in black, grey, red and orange.

As can be observed, in spite of the high number of acquired spectra integrated together, the resolution of the final merged spectrum is barely sufficient to assess qualitatively the features of the profile. In particular, looking at the energy shift of the K-edge as well as its overall profile shape, Cu<sup>(I)</sup> looks to match better the spectrum from LS/LM1 sample. Although the refinement has to be used only as qualitative indication due to its low reliability ( $R = 0.020$ ,  $\chi^2 = 0.88$ ), the previous observation seems to be confirmed also by the linear combination fit showed in Figure 5.34, from which it is possible to observe the contemporary presence of all the three oxidation states, even if Cu(0) and Cu(II) appear in significant lower amounts (respectively 25 and 15%). Therefore, the reported results depicts a situation of partial oxidation for the Copper, when contained in trace amount in brakes emissions.

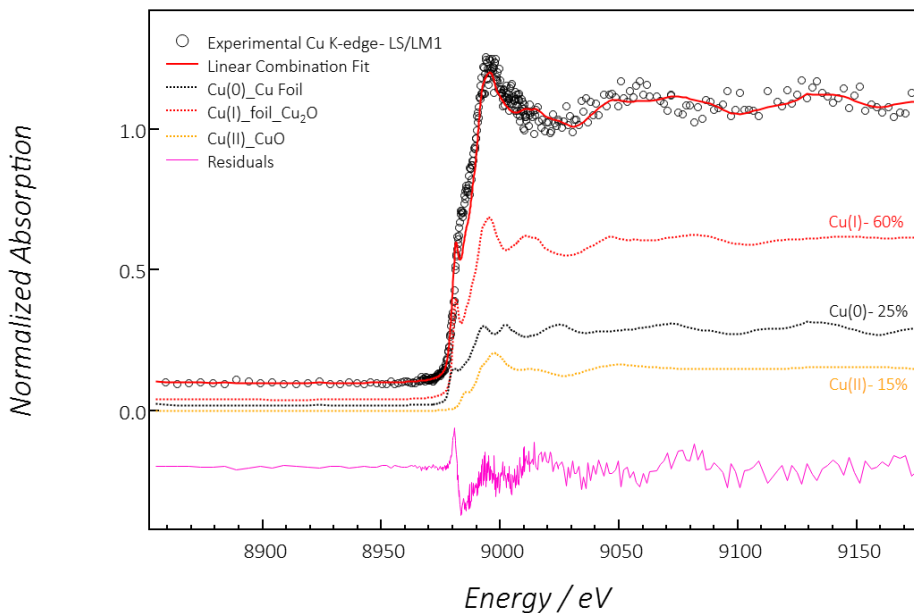


**Figure 5.34:** Linear combination fit of the experimental XAS spectrum for the LS/LM1 PM<sub>10</sub> sample, at the Cu K-edge. The measured points are reported as black circles, while the standard references are rendered in dotted lines: Cu foil, Cu<sub>2</sub>O and CuO profiles are reported respectively in black, red and orange. The overall final fit is reported as red profile, while the pink line represents the residuals between experimental data and calculated model. A R value of 0.020 is obtained for this fit.

#### 5.4.7. Zinc K-Edge

Differently to Copper, Zinc was found more frequently in appreciable amounts (higher than 0.5 wt%). Several Zn-compounds are indeed typically used in the friction materials, ranging from metallic forms (Zn, brass), to oxides and sulfides respectively



used as mild abrasives and solid lubricants. When present in metallic form and in secondary amount, it is typically detected at the diffraction analysis. However, it is also found in minor amounts ( $<0.5$  wt%) in some of the investigated particulates. In such cases, no information are obtainable on its speciation by means of the XRD probe. For this reason, three XAS spectra collected at Zn K-edge are reported and analyzed in the following lines. In particular,  $PM_{10}$  emissions from LS/LM1, LS/LM2 and LS/LM3 are measured, where Zn concentration ranges from  $0.23\pm 0.01$  and  $0.28\pm 0.03$  wt%. The corresponding spectra are showed in Figure 5.35, together with spectra from selected Zn-compounds used as standard references. As can be observed, Zn XAS spectra are not characterized by the presence of any pre-edge peak. The three profiles from the investigated samples are very similar. However they differ significantly form the reported standard compounds, *i.e.* metallic Zn(0) (Zn foil), and two different forms of Zn(II), *i.e.* ZnS and ZnO.

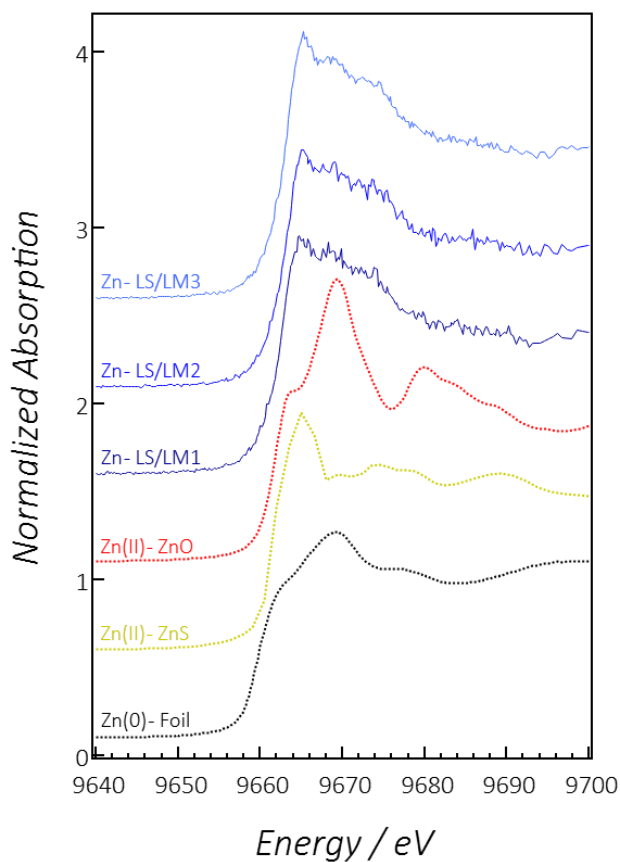


**Figure 5.35:** Experimental XAS spectrum at the Zn K-edge for LS/LM1, LS/LM2 and LS/LM3  $PM_{10}$  samples (blue-scale profiles). The standard references are reported in dotted lines: Zn foil, ZnS and ZnO are respectively reported in black, yellow and red.

In particular, all the three spectra from the investigated samples exhibit the presence of a triple peak after the absorption edge, which is particularly evident in the particulate from LS/LM3 FC. The only indication that can be obtained, due to shift towards higher energies of PM<sub>10</sub> samples Zn K-edge in respect with the corresponding from standard Zn foil, is that Zinc appears to have oxidation state of +2. As expected from the observed poor level of affinity with the standards, the attempt of a linear combination fit using the XAS spectra from the available reference materials ended in completely unsatisfactory results. However, from the comparison with spectra from several other standard materials reported in the literature<sup>[13]</sup>, it is possible to obtain some additional hints about the speciation of the Zinc inside the collected emissions. In particular, the only compounds showing similar triplet appear to belong to the family of Zn-based spinel oxides, such as the Heterolite (ZnMn<sub>2</sub>O<sub>4</sub>), the Franklinite (ZnFe<sub>2</sub>O<sub>4</sub>) and the Gahanite (ZnAl<sub>2</sub>O<sub>4</sub>). Therefore it seems reasonable to hypothesize that, similarly to what happens in the case of the Chromium, Zn eventually present in the PM<sub>10</sub> emissions in minor or trace amount can react with the excess of surrounding Iron to form mixed oxides.

#### 5.4.6. Summary of Oxidation States in d-Block Metals

As testified from all the results reported in the previous paragraphs, the XANES probe appears to be a convenient tool for the non-destructive characterization of the oxidation states of several *d-block* metals which can be found in the brakes emissions. The technique becomes fundamental when those metals are contained within the collected particulates in very low amounts, since no other options are available to assess their speciation.

Taking all the results together, it is possible to summarize that, on global basis, d-block metals appear frequently to be oxidized when contained in minor or trace amounts within the investigated emission. However, most of them are not found in their higher oxidation states. For instance, Vanadium is found to show intermediate V(III) and V(IV) character, possibly compatible with mixed forms with the Iron. Chromium is always detected in its trivalent form. More in detail, extremely matching fits are obtained with the Chromite (Fe<sub>2</sub>CrO<sub>4</sub>) structure. Similarly to the Vanadium, Mn is also found to exhibit mixed character, well described by the compresence of Mn(II) and Mn(III) forms. Finally, also Cu is found to exhibit partially oxidized character, with Cu(I) being the most matching oxidation state. This finding appear coherent with other observations reported in literature.<sup>[14]</sup> Finally, Zinc is observed in Zn(II) form, most likely related to mixed Fe/Zn oxides. Notably, for all these metals, Iron appears as a sort of sequestering/buffer agent. Conversely, Titanium is found in Ti(IV) form and exhibiting mixed 5/6 coordination. This finding is coherent with its possible presence in the friction mixes in form of Potassium titanate.

Finally, it is worth to highlight that in the case of the Iron, the obtained XANES results strongly confirm the previous observation based on XRD analysis. Indeed, Iron is confirmed to be mostly found in oxidized form, mainly related to the Magnetite ( $\text{Fe}_3\text{O}_4$ ) and the Hematite ( $\alpha\text{-Fe}_2\text{O}_3$ ). At the same time, in those cases in which the prevalence of direct abrasion wear is stated by XRD analysis, XANES probe also replicates and further confirms the observation. Most interestingly, XANES analysis helped in identify also the presence of the Maghemite ( $\gamma\text{-Fe}_2\text{O}_3$ ) in particulates which were already identified as to be generated by prevalent tribo-oxidative action. Finally, as already observed by the reported XRD characterizations, the Wustite oxide ( $\text{FeO}$ ) represent a negligible contribution.

## References

- [1] Environmental Protection Agency, "Toxicological Profile for Chromium", *EPA*, **2012**.
- [2] U.S. Department of Health and Human Services, "Toxicological profile for Manganese", *Agency for Toxic Substances and Disease Registry*, **2012**.
- [3] U.S. Department of Health and Human Services, "Toxicological profile for Vanadium", *Agency for Toxic Substances and Disease Registry*, **2012**.
- [4] C.A. Flemming, J.T. Trevors, "Copper Toxicity and Chemistry in the Environment: a Review", *Water, Air, and Soil Pollution*, 1989, 44, 143–158, <https://doi.org/10.1007/BF00228784>.
- [5] R. Eisler, "Zinc Hazards to Fish, Wildlife, and Invertebrates: A Synoptic Review", *Contaminant Hazard Reviews Report 26 ; Biological Report 10*, 1993, U.S. Department of the Interior, Fish and Wildlife Service, <https://pubs.er.usgs.gov/publication/5200116>.
- [6] E. Merian, M. Anke, M. Ihnat, M. Stoeppler, "Elements and their Compounds in the Environment: Occurrence, Analysis and Biological Relevance", 2<sup>nd</sup> edition, 2004, Wiley, [doi:10.1002/9783527619634](https://doi.org/10.1002/9783527619634).
- [7] K.S. Egorova, V.P. Ananikov, "Toxicity of Metal Compounds: Knowledge and Myths", *Organometallics*, **2017**, 36(21), 4071–4090, <https://doi.org/10.1021/acs.organomet.7b00605>.
- [8] F. Farges, G.E. Brown, J.J. Rehr, "Coordination Chemistry of Ti(IV) in Silicate Glasses and Melts: I. XAFS Study of Titanium Coordination in Oxide Model Compounds", *Geochim. Et Cosmochim. Acta*, 60(16), **1996**, 3023-3038, [doi:0016-7037/96](https://doi.org/10.1016/0016-7037(96)00163-0).
- [9] J. Kanchanawarin, W. Limphirat, P. Promchana, *et.al.*, "Local Structure of Stoichiometric and Oxygen-Deficient  $\text{A}_2\text{Ti}_6\text{O}_{13}$  (A = Li, Na, and K) Studied by X-Ray Absorption Spectroscopy and First-Principles Calculations", *J. Appl. Phys.*, 124, **2018**, 155101, <https://doi.org/10.1063/1.5052032>.
- [10] A. Levina, A.I. McLeod, P.A. Lay, "Vanadium Speciation by XANES Spectroscopy: a Three-Dimensional Approach", *Chem. Eur. J.*, 20, **2014**, 12056-12060, [doi:10.1002/chem.201403993](https://doi.org/10.1002/chem.201403993).
- [11] A. Ohta, "Speciation Study of Cr in a Geochemical Reference Material Sediment Series Using Sequential Extraction and XANES Spectroscopy", *Geostandards and Geoanalytical Research*, 39(1), **2014**, 87-103.

- [12] E. Chalmin, F. Farges, G.E. Brown Jr., "A Pre-Edge Analysis of Mn K-Edge XANES Spectra to Help Determine the Speciation of Manganese in Mineral Glasses", *Contrib. Mineral. Petrol.*, 157, **2009**, 111-126, [doi:10.1007/s00410-008-0323-z](https://doi.org/10.1007/s00410-008-0323-z).
- [13] E. Castorin, E.D. Ingall, P.L. Morton, D.A. Tavakolic, B. Laid, "Zinc K-Edge XANES Spectroscopy of Mineral and Organic Standards", *J. Synchrotron Rad.*, 26, **2019**, 1302–1309, <https://doi.org/10.1107/S160057751900540X>.
- [14] J. Kukutschova, P. Filip, "Review of Brake Wear Emissions, in: F. Amato (Ed.), Non Exhaust Emissions: an Urban Air Quality Problem for Public Health", *Academic Press*, Elsevier, San Diego, **2018**.

## 6. Size Distributions

*Most of the emissions investigated in this work are PM<sub>10</sub> particulates. This means that the particles are characterized by having maximum dimension not higher than 10 µm. However, below this limit, different dimensional distributions might be present. In the previous chapters it was demonstrated that different categories of materials composing the friction couple are characterized by different tribological mechanisms, leading to different compositional profiles. Similarly, the compositional properties and the tribological characteristics of a specific friction couple are fundamental in determining its emissive pathway. On the other hand, it is well known that decreasing particulates dimensions shows detrimental effects towards human toxicology, since smaller particles are increasingly able to penetrate deeper the respiratory apparatus. Therefore, this chapter reports an investigation specifically meant to assess the eventual correlation between the different materials composing the friction couple and the dimensional distribution profiles of the corresponding particulates.*

### 6.1. Aim of the Study

All the brakes emissions samples observed up to this chapter are PM<sub>10</sub> particulates, meaning dispersion of particles exhibiting aerodynamic diameter lower than 10 µm. Indeed, all these emissions samples are voluntarily collected in this form by means of suitable devices (cyclones) in order to specifically simulate and therefore characterize those particulates which, once emitted, can stay in air for prolonged times due to their small dimensions and weight.<sup>[1]</sup> However, independently of the upper limit, particulates generated in different conditions can likely exhibit different size distributions. The results reported in the previous chapters demonstrated how compositional and tribological characteristics of a specific friction couple are pivotal in determining the compositional profile of the corresponding PM<sub>10</sub> emissions. At the same time, it appears reasonable that different friction couples, characterized by different tribological mechanisms, can produce PM<sub>10</sub> particulates with intrinsically different dimensional profiles. For instance, it is well recognized in the literature that increasing the temperature at the disc brake tribological interface typically causes an increasing emissions of finer particles.<sup>[2-5]</sup> Accordingly, PM<sub>10</sub> emissions from friction couple characterized by more pronounced adhesive wear mechanisms are characterized by higher fraction of smaller particles.<sup>[5]</sup> Conversely, more direct abrasion can likely produce coarser dimensional distributions.<sup>[5]</sup> Therefore, the study reported in this chapter is aimed at corroborating these hypothesis and, more in detail, to seek eventual correlations between different distribution profiles in PM<sub>10</sub> particulates generated by friction couples belonging to different coupling categories. This is of particular interest, since part of the toxicology of a particulate is determined and modulated by its

dimensional profile. Smaller particles are indeed capable to progressively penetrate deeper into biological systems, such for example the human respiratory apparatus (see Table 1.2 in *Chapter 1*).<sup>[6-8]</sup> In addition, due to their higher surface area, smaller particles of a specific material are in general far more reactive, soluble and bio-available in respect with counterparts with bigger dimensions, thus being more capable of inducing inflammation, oxidative stress and several other negative biological effects.<sup>[6-8]</sup> For all these reasons, a deeper characterization of the eventual correlations between brakes materials, tribological mechanisms and dimensional profiles of the corresponding particulates can be a further tool to improve the environmental and toxicological impact of brake emissions. Indeed, it can be used to: *i)* design friction couples specifically capable to maximize the size distribution of the emitted particles; and *ii)* provide to final customers scientific evidences for a more informed assessment or choice of friction couples of interest.

## 6.2. Experimental

The PM<sub>10</sub> particulates used in this study are a selection of those reported in *Chapter 4*. In particular, several emissions generated by FCs belonging to *Category 1* to *Category 4* are investigated, as reported in Table 6.1. Unfortunately, due to the very low amount of collected material, the characterization of the dimensional profile of particulates generated by *Category 5* FCs was not possible (all the available material was dedicated to the chemical characterization).

<i>Category 1</i>		<i>Category 2</i>		<i>Category 3</i>		<i>Category 4</i>	
FC	Particles/#	FC	Particles/#	FC	Particles/#	FC	Particles/#
LS/LM1	> 15000	IN3	> 3500	NAO1	>3500	CTD2	>3500
LS/LM4	> 10000	IN4	> 5000	NAO2	>5000	CTD3	>5000
LS/LM9	>5000	IN5	> 7000	NAO4	>5000	CTD5	>5000
LS/LM10	>5500	IN6	> 5000	NAO5	>5000	CTD8	>5000

**Table 6.1:** Summary of the PM<sub>10</sub> samples investigated for their particle size distribution.

Since the investigated samples are exactly the same as reported in *Chapter 4*, the detailed description of the experimental details for their collection can be found in that section. Nevertheless, a short summary of the most important experimental detail is reported in the next lines. All PM<sub>10</sub> particulates are collected at the same dynamometric bench, during emission tests following exclusively the metric imposed by the WLTP-Brake braking cycle and using the same geometry for all the components of the braking device.<sup>[9-11]</sup> In particular, the braking corner is composed as follows: *i)* a four pistons fixed Aluminum caliper, with pistons diameter of 44 mm; *ii)* a vented braking disc with diameter of 342 mm and thickness of 32 mm; and *iii)* a couple of brake pads with surface

of 89.1 cm<sup>2</sup>. All the tests are performed with simulated vehicle inertia of 72.67 kg m<sup>2</sup>. For each investigated sample, PM<sub>10</sub> powder spared from the chemical analysis is resuspended in isopropyl alcohol by sonication. Then, diluted resuspension of particulate is gently deposited on a 47 mm polycarbonate filters (Sartorius™ 23006) by means of a micro-pipette in order to maximize the particles dispersion on the substrate. The obtained filter is then cut in small pieces, which are then deposited on Aluminum stubs covered by Carbon tape for electron microscopy. Several SEM images are acquired for each filter, to obtain statistically meaningful datasets (number of particles > 3500, at least). SEM images are finally binarized, segmented and analyzed to obtain the particle size distribution (PSD) profile for each investigated sample by means of ImageJ<sup>[12]</sup> software.

### 6.3. Particle Size Distribution (PSD)

The following paragraphs report the results obtained for the PSD characterization of the investigated samples listed in Table 6.1. Results are aggregated in terms of typology of friction couple to seek correlations and trends between specific materials and the dimensional profile of the corresponding particulates. As already proposed in *Chapter 3*, PSD results are showed as histograms distributions, following the dimensional fractions characteristic of particulate collection carried out by ELPI+ impactor. Particles from the finer fractions are merged all together in dimensional the range characterized by  $D_{\max} < 170$  nm.

#### 6.3.1. Category 1 (GCI BDs + LS/LM FMs)

The first category assessed is represented by the coupling of GCI BDs and LS/LM FMs, *i.e.* the standard friction couple for the automotive original equipment market in EU. Figure 6.1 shows the PSD profiles as obtained for the four investigated PM<sub>10</sub> samples: LS/LM1, LS/LM4, LS/LM9 and LS/LM10. The first two samples are characterized by statistically wider datasets in respects to all the other samples, since the corresponding particulates are sampled in multiple tests and used also for other studies reported in this thesis. Finally, Figure 6.2 shows the comparison of the four obtained PSD profiles, while Table 6.2 summarizes all the results obtained in terms of appearance frequency for each dimensional range. As can be observed in the reported graphs, the four profiles look in general very similar. In particular, more than 95% of the independent observations are constituted by particles exhibiting  $D_{\max}$  parameter lower than 2.5 μm in all the four analyzed particulates. In general, the dimensional most populated range is between 0.6 and 1.6 μm, with peak at 0.6 μm. Three samples out of four exhibit frequency appearance of particle from finer fractions (< 170 nm) around the 5%, with sample LS/LM1 representing the only significant exception (almost 15%).

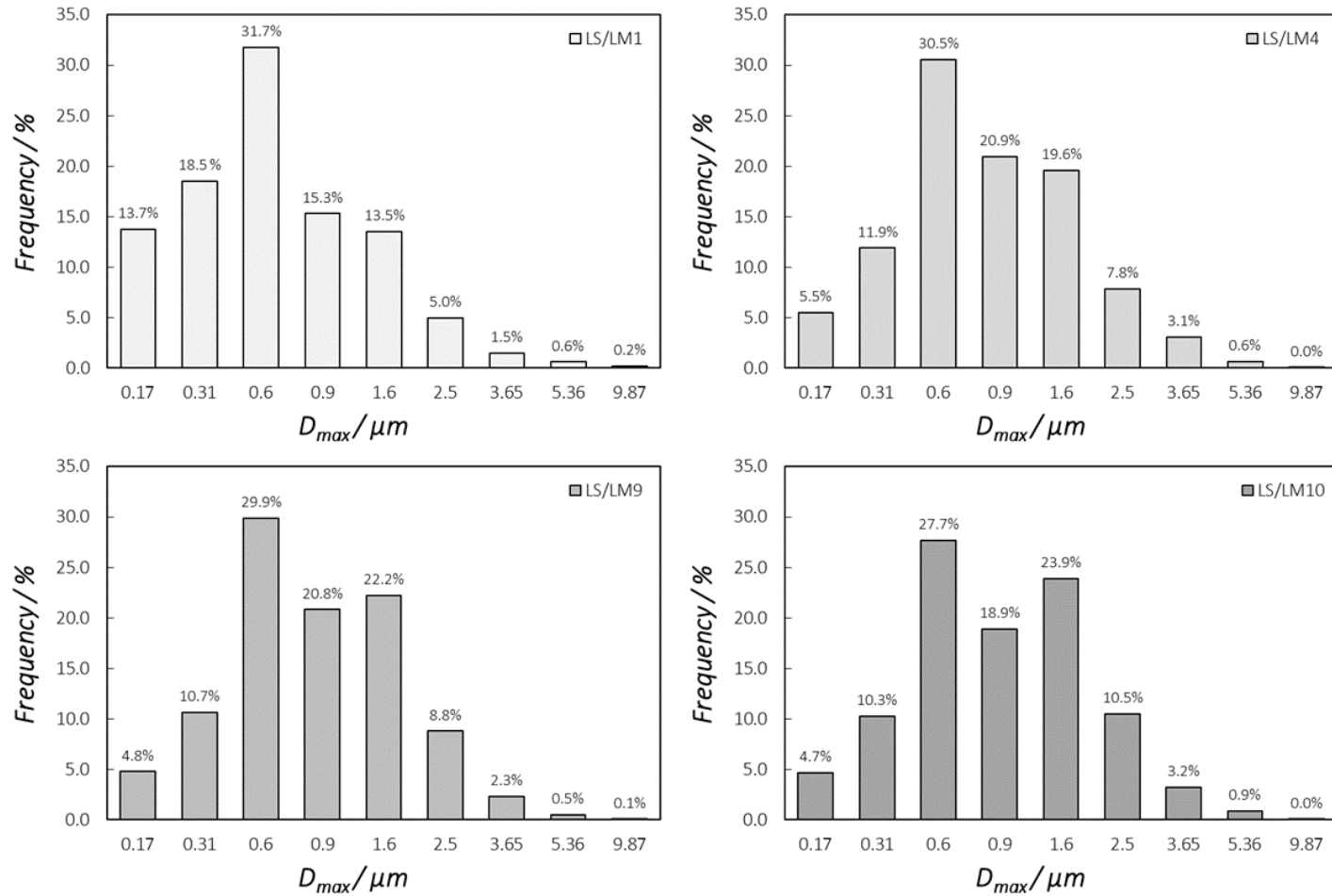
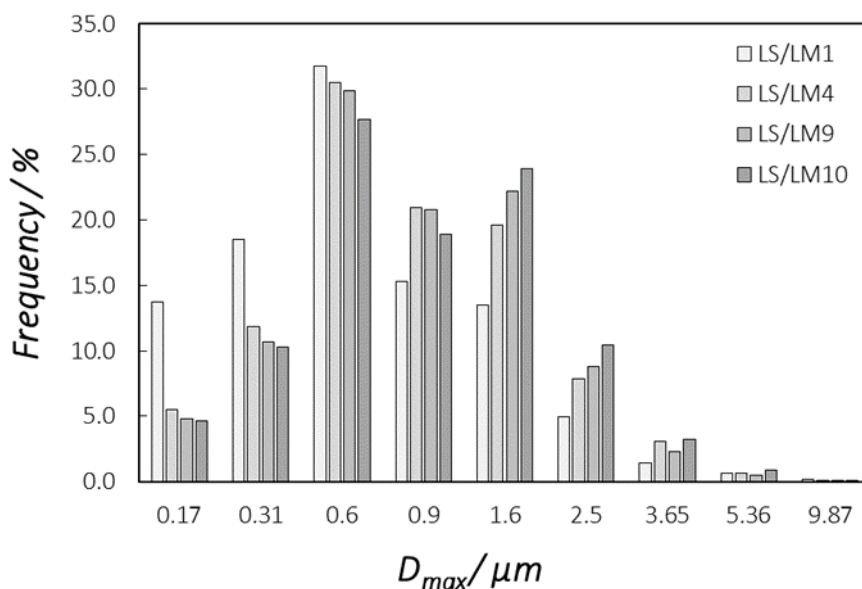


Figure 6.1: PSD profiles as obtained for the investigated PM<sub>10</sub> samples from Category 1 FCs.





**Figure 6.2:** Comparison of PSD profiles as obtained for the investigated PM<sub>10</sub> samples for *Category 1* FCs.

$D_{max}/\mu m$	LS/LM1	LS/LM4	LS/LM9	LS/LM10	Average	SD
0.17	13.7	5.5	4.8	4.7	7.2	3.8
0.31	18.5	11.9	10.7	10.3	12.8	3.3
0.6	31.7	30.5	29.9	27.7	30.0	1.5
0.9	15.3	20.9	20.8	18.9	19.0	2.3
1.6	13.5	19.6	22.2	23.9	19.8	3.9
2.5	5.0	7.8	8.8	10.5	8.0	2.0
3.65	1.5	3.1	2.3	3.2	2.5	0.7
5.36	0.6	0.6	0.5	0.9	0.7	0.1
9.87	0.2	0.0	0.1	0.0	0.1	0.1

**Table 6.2** Frequency appearance % of particles in the investigated PM<sub>10</sub> samples from *Category 1* FCs. The last two columns report the category average and the corresponding index of variability (standard deviation - SD), respectively.

More in general, the whole PSD profile of the particulate from LS/LM1 sample appears significantly shifted towards finer dimensional fractions in respect with the counterparts from the other three samples, showing consistently significant different particles frequency appearance in all the assessed ranges. The overall high variability reported are mostly caused by these dimensional differences showed by the LS/LM1 sample.

### 6.3.2. Category 2 (GCI BDs + IN FMs)

The second category assessed is represented by the coupling of GCI BDs and IN FMs, *i.e.* prototypal friction materials in which the organic binder is substituted with inorganic compounds. Figure 6.3 shows the PSD profiles as obtained for the four investigated PM<sub>10</sub> samples: IN3, IN4, IN5 and IN6. Figure 6.4 reports the comparison of the four obtained PSD profiles, while Table 6.3 summarizes all the results obtained in terms of appearance frequency for each selected dimensional range. As can be observed in the reported graphs, the four profiles share some similarities. In particular, also in this case, about the 95% of the independent observations are constituted by particles exhibiting  $D_{max}$  parameter lower than 2.5  $\mu\text{m}$  in all the four analyzed particulates. Similarly as reported for *Category 1* particulate, the most populated dimensional ranges are between 0.6 and 1.6  $\mu\text{m}$ . However, two samples out of four (IN3 and IN4) have frequency peak at 0.6  $\mu\text{m}$ , while the other two (IN5 and IN6) exhibit frequency peak at 1.6  $\mu\text{m}$ . In general, the peak frequency is always lower in respect with the counterparts from *Category 1*, thus resulting in overall broader profiles. In spite of the existence of two slightly different couples of profiles, the overall variability along the whole dimensional range remains lower in respect with particulates from the previous category, testifying an overall higher degree of intra category similarity in the PSD of particulates generated by *Category 2* FCs.

$D_{max}/\mu\text{m}$	IN3	IN4	IN5	IN6	Average	SD
0.17	6.9	5.6	1.3	2.0	4.0	2.4
0.31	11.1	8.2	11.6	12.6	10.9	1.7
0.6	28.7	27.2	20.5	23.2	24.9	3.2
0.9	18.3	20.6	22.7	22.6	21.0	1.8
1.6	21.1	22.8	25.2	23.6	23.2	1.5
2.5	9.4	10.7	12.7	10.9	10.9	1.2
3.65	3.4	3.8	4.6	3.7	3.9	0.5
5.36	1.1	1.0	1.2	1.3	1.1	0.1
9.87	0.1	0.1	0.2	0.0	0.1	0.1

**Table 6.3:** Frequency appearance % of particles in the investigated PM<sub>10</sub> samples from *Category 2* FCs. The last two columns report the category average and the corresponding index of variability (standard deviation - SD), respectively.

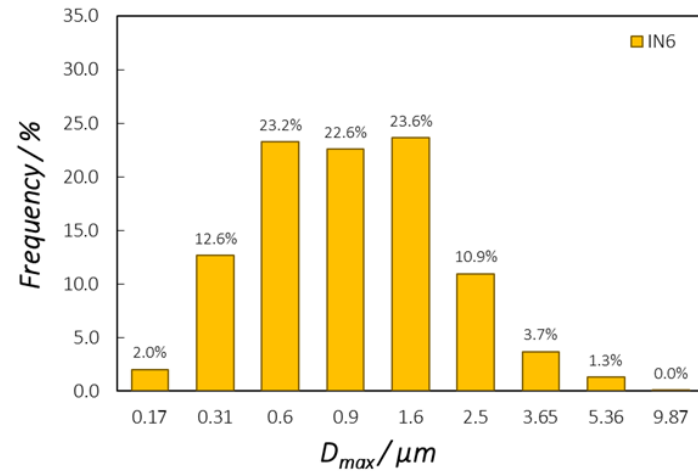
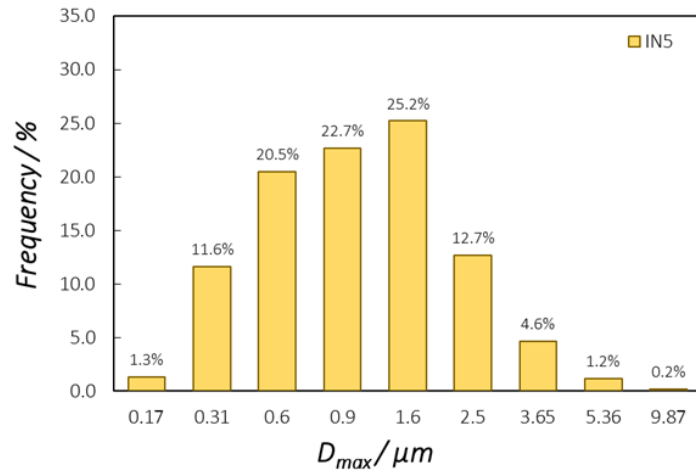
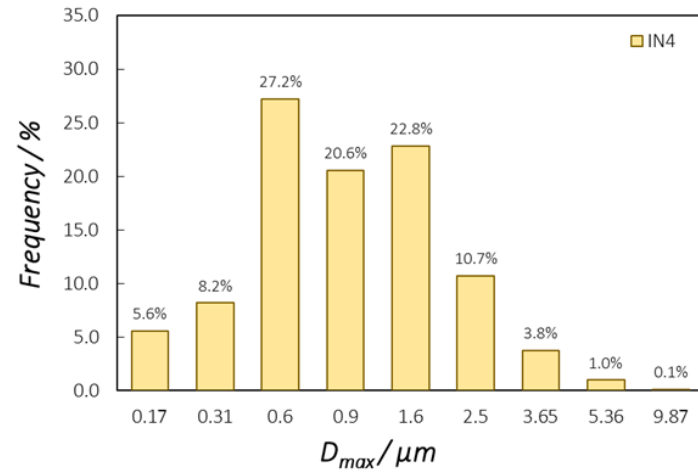
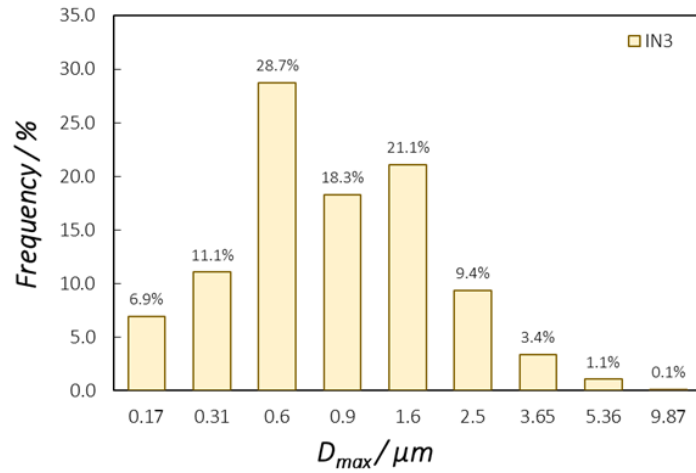
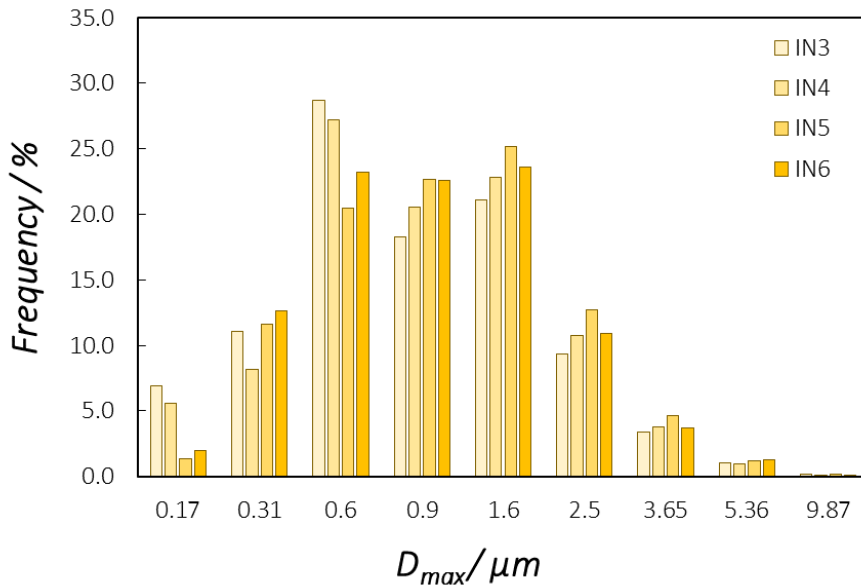


Figure 6.3: PSD profiles as obtained for the investigated PM<sub>10</sub> samples from Category 2 FCs.



**Figure 6.4:** Comparison of PSD profiles as obtained for the investigated PM<sub>10</sub> samples for *Category 2* FCs.

### 6.3.3. *Category 3 (GCI BDs + NAO FMs)*

The third category assessed is represented by the coupling of GCI BDs and NAO FMs, *i.e.* standard materials coupling for the automotive original equipment market in the North America and Asia region. Figure 6.5 shows the PSD profiles as obtained for the four investigated PM<sub>10</sub> samples: NAO1, NAO2, NAO4, NAO5. Figure 6.6 reports the comparison of the four obtained PSD profiles. In addition, Table 6.4 summarizes all the results obtained in terms of appearance frequency for each selected dimensional range.

$D_{max}/\mu m$	NAO1	NAO2	NAO4	NAO5	Average	SD
0.17	8.9	6.1	4.2	6.1	6.3	1.7
0.31	10.4	10.0	9.8	10.2	10.1	0.2
0.6	29.2	27.9	28.4	31.0	29.1	1.2
0.9	23.6	22.0	20.6	22.1	22.1	1.1
1.6	21.6	23.6	25.3	21.1	22.9	1.7
2.5	5.3	7.9	9.0	7.1	7.3	1.3
3.65	0.8	2.2	2.3	1.9	1.8	0.6
5.36	0.1	0.3	0.4	0.4	0.3	0.1
9.87	0.0	0.0	0.0	0.1	0.0	0.0

**Table 6.4:** Frequency appearance % of particles in the investigated PM<sub>10</sub> samples from *Category 3* FCs. The last two columns report the category average and the corresponding index of variability (standard deviation - SD), respectively.

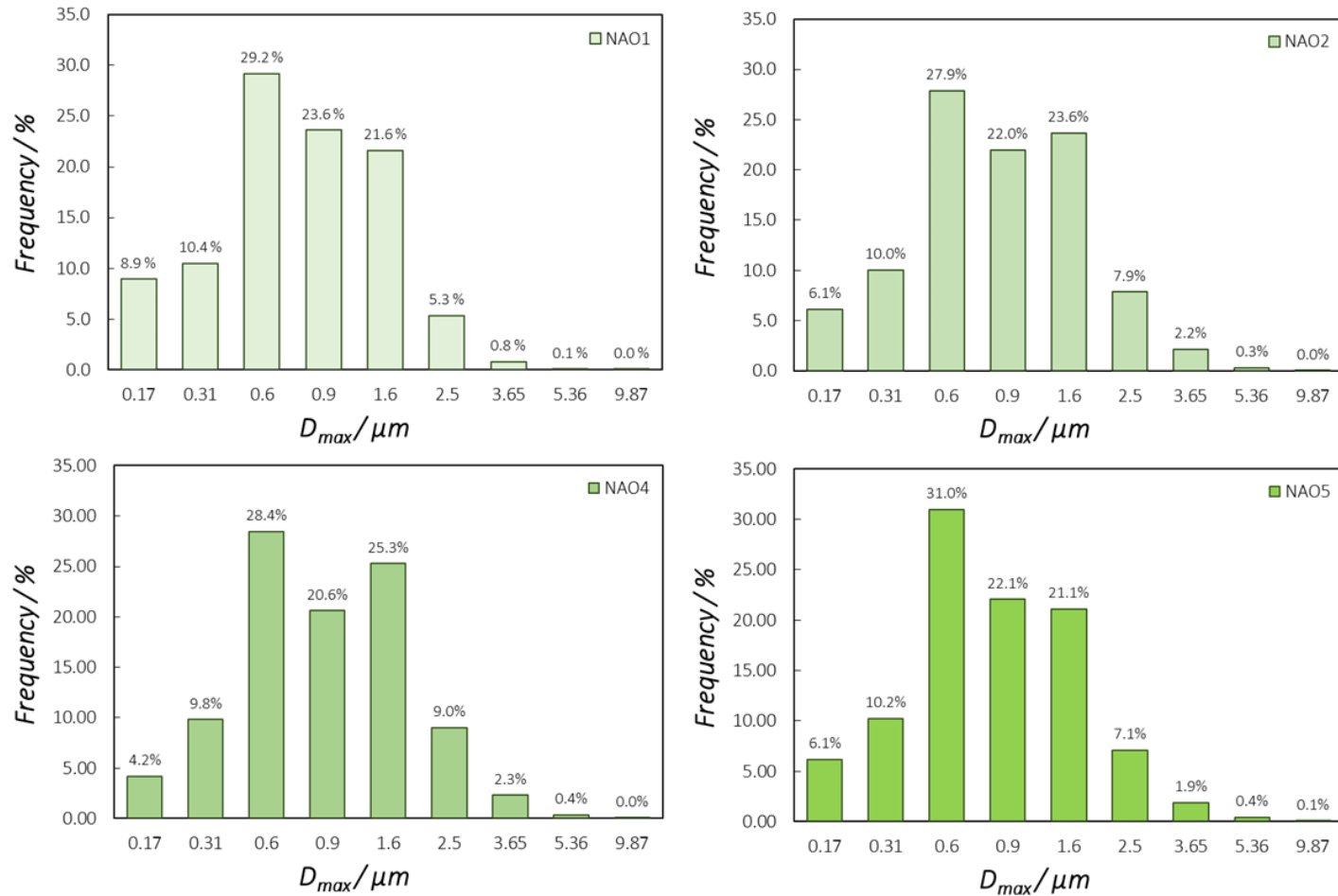
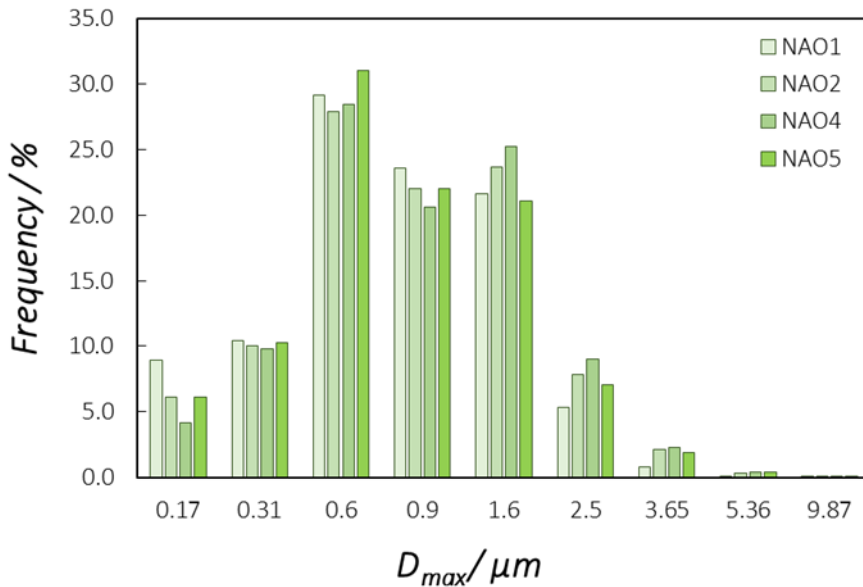


Figure 6.5: PSD profiles as obtained for the investigated PM<sub>10</sub> samples from *Category 3* FCs.



**Figure 6.6:** Comparison of PSD profiles as obtained for the investigated PM<sub>10</sub> samples for *Category 3* FCs.

Once again, in all four samples, about 95% of the particles exhibit Feret diameter lower than 2.5  $\mu m$  and the most populated dimensional range is comprised between 0.6 and 1.6  $\mu m$ . Similarly to particulates from *Category 1*, also in *Category 3* the frequency peak is observed at 0.6  $\mu m$ , with asymmetry of the distribution on its right side. The variability along the whole dimensional range is limited, testifying a good homogeneity of results inside the specific FC category.

#### 6.3.4. *Category 4 (CTD BDs + LS/LM FMs)*

The fourth considered category is represented by the coupling of CTD BDs and LS/LM FMs, *i.e.* prototypal and pre-series FCs with coated braking discs. Figure 6.7 shows the PSD profiles as obtained for the four investigated PM<sub>10</sub> samples of this specific category: CTD2, CTD3, CT5, CTD8. Figure 6.8 reports the comparison of the four obtained PSD profiles, while Table 6.4 summarizes all the results obtained in terms of appearance frequency for each selected dimensional range. As already observed in all the previous particulates, also in all the samples from *Category 4* about the 95% of the particles exhibit Feret diameter lower than 2.5  $\mu m$ . Similarly, the most populated dimensional range is comprised between 0.6 and 1.6  $\mu m$ . However, in this case the frequency peak is always observed at 1.6  $\mu m$ , with asymmetry of the distribution towards lower dimensions. The variability along the whole dimensional range is limited, testifying a good homogeneity of results inside the specific FC category.

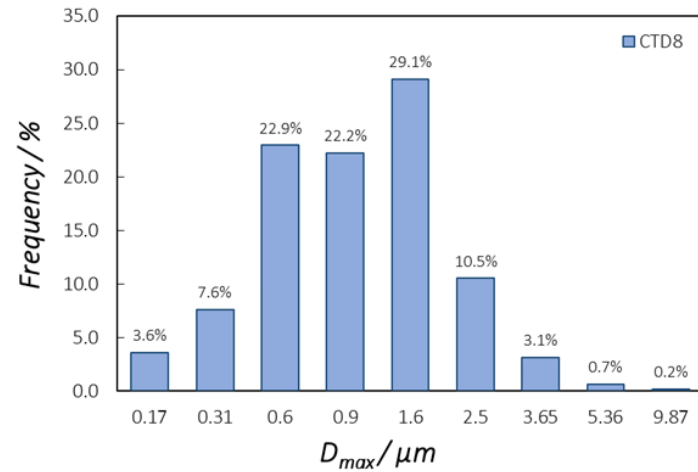
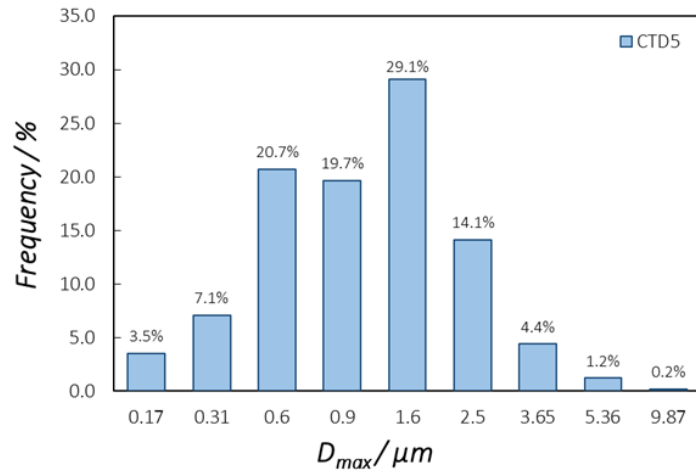
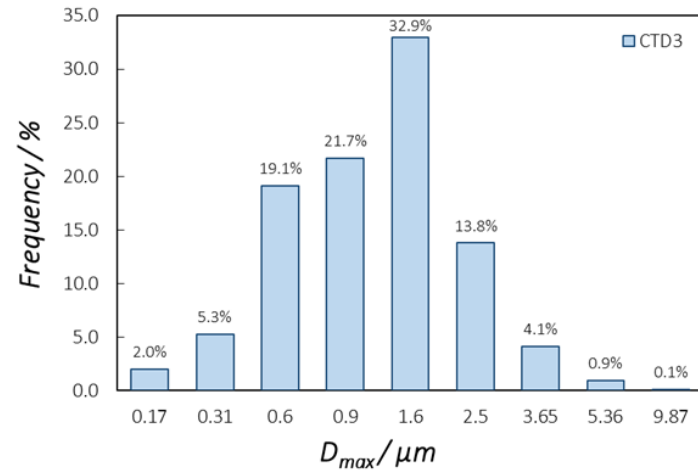
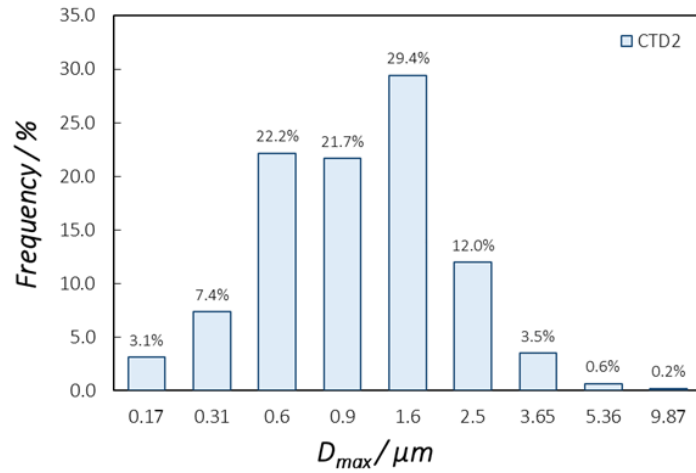
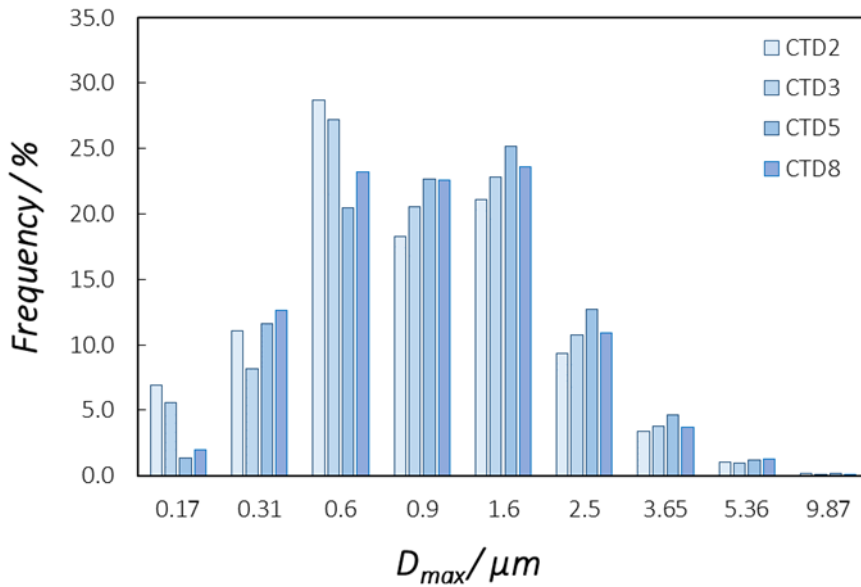


Figure 6.7: PSD profiles as obtained for the investigated PM<sub>10</sub> samples from Category 4 FCs.



**Figure 6.8:** Comparison of PSD profiles as obtained for the investigated PM<sub>10</sub> samples for *Category 4* FCs.

$D_{max}/\mu m$	CTD2	CTD3	CTD5	CTD8	Average	SD
0.17	3.1	2.0	3.5	3.6	3.1	0.6
0.31	7.4	5.3	7.1	7.6	6.8	0.9
0.6	22.2	19.1	20.7	22.9	21.2	1.5
0.9	21.7	21.7	19.7	22.2	21.3	1.0
1.6	29.4	32.9	29.1	29.1	30.1	1.6
2.5	12.0	13.8	14.1	10.5	12.6	1.4
3.65	3.5	4.1	4.4	3.1	3.8	0.5
5.36	0.6	0.9	1.2	0.7	0.9	0.2
9.87	0.2	0.1	0.2	0.2	0.2	0.0

**Table 6.5:** Frequency appearance % of particles in the investigated PM<sub>10</sub> samples from *Category 4* FCs. The last two columns report the category average and the corresponding index of variability (standard deviation - SD), respectively.

### 6.3.5. Summary

The average appearance frequencies as obtained for each category of particulate are compared together in Figure 6.9 and Table 6.6. As can be observed from the reported results, particulates from *Category 1* (GCI BDs + LS/LM FMs) show the higher frequency of particles from smaller fractions. Particulates from *Category 3* (GCI BDs + NAO FMs) show similar trends and behavior. Considering the higher variability



highlighted in the results from the first typology of coupling due to the peculiar behavior of sample LS/LM1, the overall PSD profiles from *Category 1* and *Category 3* PM<sub>10</sub> samples can be considered very similar. Conversely, particulates from *Category 2* and *Category 4* exhibit in general particles characterized by higher dimensions. In particular, *Category 2* emissions show lower ratio in the frequency between particles from the finer fractions (< 600 nm) in respect to the intermediate and higher ones. Finally, particulates generated by *Category 4* FC differ significantly from all the others, since they show the same tendency to host lower percentages of finer particles in respect to the counterparts from *Category 2*, while exhibiting in addition the frequency peak around dimensions 1 μm bigger than all the other observed PM<sub>10</sub> particulates.

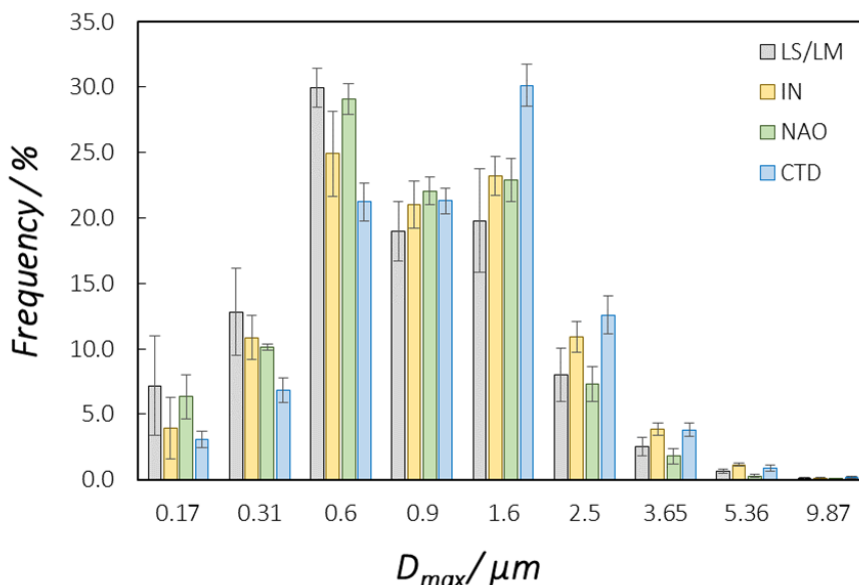


**Figure 6.9:** Comparison of PSD profiles as obtained for the investigated PM<sub>10</sub> samples for *Category 4* FCs.

$D_{max}/\mu m$	LS/LM		IN		NAO		CTD	
	Average %	SD	Average %	SD	Average %	SD	Average %	SD
0.17	7.2	3.8	4.0	2.4	6.3	1.7	3.1	0.6
0.31	12.8	3.3	10.9	1.7	10.1	0.2	6.8	0.9
0.6	30.0	1.5	24.9	3.2	29.1	1.2	21.2	1.5
0.9	19.0	2.3	21.0	1.8	22.1	1.1	21.3	1.0
1.6	19.8	3.9	23.2	1.5	22.9	1.7	30.1	1.6
2.5	8.0	2.0	10.9	1.2	7.3	1.3	12.6	1.4
3.65	2.5	0.7	3.9	0.5	1.8	0.6	3.8	0.5
5.36	0.7	0.1	1.1	0.1	0.3	0.1	0.9	0.2
9.87	0.1	0.1	0.1	0.1	0.0	0.0	0.2	0.0

**Table 6.6:** Comparison of particle frequency appearance % vs. selected dimensional fractions in the investigated PM<sub>10</sub> samples from the four reported categories. Corresponding index of variability (standard deviation - SD) are reported in blue.

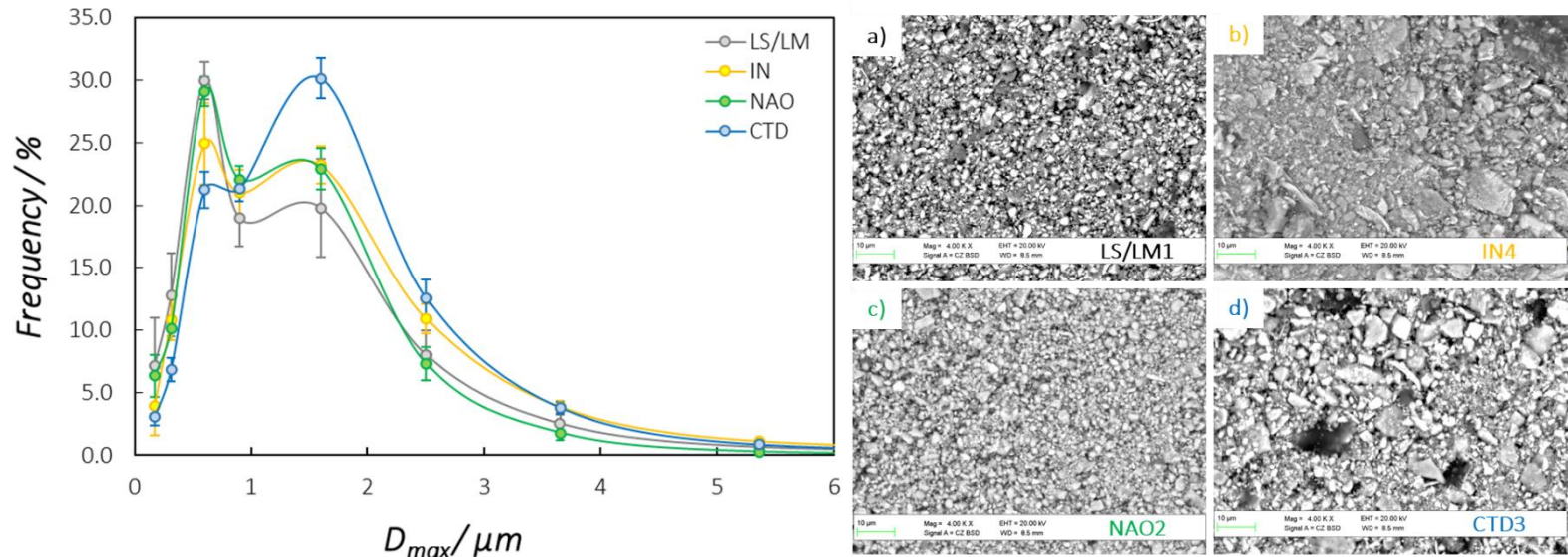


**Figure 6.10:** Comparison of PSD average profiles for  $\text{PM}_{10}$  emissions generated by different typologies of FC (left side) and SEM images representative for the investigated particulates (right side). In the PSD graph, grey, yellow, green and blue profiles represent respectively average results obtained for  $\text{PM}_{10}$  samples from *Category 1* (GCI + LS/LM FMs), *Category 2* (GCI BDs + IN FMs), *Category 3* (GCI BDs + NAO FMs) and *Category 4* (CTD BDs + LS/LM FMs) friction couples. Error bars represent the *intra* category observed variability (standard deviation). Referring to the SEM images, samples from LS/LM1 (a), IN4 (b), NAO2 (c) and CTD3 (d) are showed. They are labeled in grey, yellow, green and blue, accordingly to the belonging family. All the SEM images reported are acquired at magnification of 4000x, using back scattered detector to sample ideal working distance of 8.5 mm.

Finally, Figure 6.10 reports the comparison between the obtained average PSD profiles and SEM images collected on particulates investigated in this study. In particular, one SEM image for particulate from each category is acquired at magnification of 4000x using the back scattered detector to sample ideal working distance of 8.5 mm. As can be observed by the comparative visual inspection of the PSD profiles and the images reported, it is possible to further confirm the trends described in the previous lines. More in detail, is particularly evident that PM<sub>10</sub> emissions collected from *Category 2* and *Category 4* host an higher relative ratio of particles with bigger dimensions in respect to the counterparts of smaller dimensions. Conversely, PM<sub>10</sub> samples from *Category 1* and *Category 3* exhibit more homogeneous dispersion of small particles with dimensions in the order of or below 1 μm.

## 6.4. Conclusions

The results reported in the previous paragraphs show that some correlations between the typology of the materials composing the friction couple and the dimensional profile of the corresponding particulates actually exist. In spite of an overall dominant presence of particles with observed Feret diameter lower than 2.5 μm (about the 95% of the independent observations) in all the analyzed particulates, different dimensional distributions are observed. More in detail, PM<sub>10</sub> samples generated by friction couples belonging to *Category 1* (GCI FMs + LS/LM FMs) and *Category 3* (GCI BDs + NAO FMs) are observed to be composed by an overall higher fraction of finer particles ( $D_{\max} < 600$  nm). Conversely, PM<sub>10</sub> emissions generated by FCs belonging to *Category 2* (GCI BDs + IN FMs) and *Category 4* (GTD BDs + LS/LM FMs) exhibit PSD profiles characterized by higher amounts of coarser particles. In particular, FCs from *Category 4* are found to generate particulates with the highest fraction of coarser particles among all the observed samples.

Notably, when looking at the tribological mechanism, FCs from *Category 2* and *4* share a pronounced tendency of abrasion wear, due to their specific compositional characteristics. More in detail, IN friction materials are significantly harder in respect with the GCI of the rotor and exhibit higher friction coefficient when compared to the LS/LM counterparts. On the other hand, coated BDs are in general significantly harder than the coupled friction FMs, usually generating more abrasion in the friction composite. In both cases, the mismatch between the mechanical properties of the materials composing the friction couple makes the generation of a diffuse friction layer more difficult, thus favoring the direct abrasion more than the adhesive wear mechanism. Conversely, LS/LMs friction composites are in general able to create more diffuse transfer layer at the tribological interface, most of all when they are specifically designed to maximize comfort characteristics. Similar behavior is also observed in NAO FMs, which are furthermore characterized by gentler behavior towards the cast iron

braking surfaces of the rotors.<sup>[5,13]</sup> Therefore, it is possible to infer that FCs characterized by more pronounced direct abrasion wear mechanism usually produce coarser particulates in respect with the counterparts in which the tribological event is more characterized by adhesive wear and tribo-oxidation.

Most importantly, all the reported results confirm that it is possible to design friction couples at the specific aim of shifting the PSD profile of the corresponding emissions through the selection of suitable materials and couplings, as well as modifying or taking advantage of their tribological behavior. Therefore, this can be used as further a tool, in association with chemical considerations, in order to voluntarily tune the physico-chemical properties of the brakes emissions in order to limit their environmental and toxicological impact.

## References

- [1] U. Pöschl, "Atmospheric Aerosols: Composition, Transformation, Climate and Health Effects", *Angew. Chem. Int. Ed.*, **44**, **2005**, 7520 – 7540, <https://doi.org/10.1002/anie.200501122>.
- [2] J. Kukutschova, P. Filip, "Review of Brake Wear Emissions, in: F. Amato (Ed.), Non Exhaust Emissions: an Urban Air Quality Problem for Public Health, Academic Press, Elsevier, San Diego, **2018**.
- [3] B.S. Joo, Y.H. Chang, H.J. Seo, H. Jang, "Effects of Binder Resin on Tribological Properties and Particle Emission of Brake Linings", *Wear*, **2019**, 434–435, 202995, <https://doi.org/10.1016/j.wear.2019.202995>.
- [4] Z. Men, X. Zhang, J. Peng, J. Zhang, T. Fang, *et.al.*, "Determining Factors and Parameterization of Brake Wear Particle Emission", *Journal of Hazardous Materials*, **2022**, 434, 128856, <https://doi.org/10.1016/j.jhazmat.2022.128856>.
- [5] J. Kukutschová, P. Moravec, V. Tomásek, V. Matejka, J. Smolík, *et.al.*, "On Airborne Nano/Micro-sized Wear Particles Released from Low-Metallic Automotive Brakes", *Environmental Pollution*, **159**, **2011**, 998-1006, [doi:10.1016/j.envpol.2010.11.036](https://doi.org/10.1016/j.envpol.2010.11.036).
- [6] G. Oberdörster, E. Oberdörster, J. Oberdörster, "Nanotoxicology: An Emerging Discipline Evolving from Studies of Ultrafine Particles", *Environmental Health Perspectives*, **113**(7), **2005**, 823-839, <https://doi.org/10.1289/ehp.7339>.
- [7] A.D. Maynard, D.B. Warheit, M.A. Philbert, "The New Toxicology of Sophisticated Materials: Nanotoxicology and Beyond", *Toxicological Sciences*, **120**(S1), **2001**, 109–129, [doi:10.1093/toxsci/kfq372](https://doi.org/10.1093/toxsci/kfq372).
- [8] A.V. Singh, P. Laux, A. Luch, C. Sudrik, S. Wiehr, *et.al.*, "Review of Emerging Concepts in Nanotoxicology: Opportunities and Challenges for Safer Nanomaterial Design", *Toxicology Mechanisms and Methods*, **29**(5), **2019**, 378–387, <https://doi.org/10.1080/15376516.2019.1566425>.
- [9] G. Perricone, J. Wahlstrom, U. Olofsson, "Towards a Test Stand for Standardized Measurements of the Brake Emissions", *Proc. I. Mech. E., Part D: J. Automobile Engineering*, **2015**, 1–8.
- [10] M. Mathissen, J. Grochowicz, C. Schmidt, R. Vogta, F.H. Farwick zum Hagen, *et.al.*, "A Novel Real-World Braking Cycle for Studying Brake Wear Particle Emissions", *Wear*, **2018**, 414–415, 219–226, <https://doi.org/10.1016/j.wear.2018.07.020>.

[11] Particle Measurement Programme (PMP) Informal Working Group, Informal document GRPE\_81\_12, 81st GRPE, 9-11 June **2020**, Agenda Item 7.

[12] J. Schindelin, I. Arganda-Carreras, E. Frise, V. Kaynig, M. Longair, *et.al.*, "Fiji: an open-source platform for biological-image analysis", *Nature Methods*, 9(7), **2019**, 676–682, [doi:10.1038/nmeth.2019](https://doi.org/10.1038/nmeth.2019).

[13] J. Wahlström, A. Söderberg, L. Olander, A. Jansson, U. Olofsson, "A Pin-on-Disc Simulation of Airborne Wear Particles From Disc Brakes", *Wear*, 268, 2010, 763-769, <https://doi.org/10.1016/j.wear.2009.11.014>.

## 7. Dimensional Profiles and Chemical Composition

*Most of the emissions investigated up to this chapter are PM<sub>10</sub> particulates. This means that the particles contained in the investigated emissions are characterized by having maximum dimension not higher than 10 µm. As demonstrated in the previous chapter, below this limit, different dimensional distributions might be present depending on the characteristics of the tribological interface. On the other hand, when looking at a specific friction couple, it can produce emissions characterized by a wide dimensional dispersion, ranging from ultra-fine particles having nanometric dimensions up to millimetric scaled objects. Depending on the dimensional fractions considered, different paths of emission in environment can be guessed. For instance, once emitted, PM<sub>10</sub> particulates can stay longer in air in respect with particles with higher dimensions, which conversely are more likely subject to fall directly to the ground. Therefore, different distribution of materials emitted in environment from braking devices can preferentially populate different environments (air vs. soil/water) on the basis of the dimensional fraction in which they are generated. Thus, particulates produced by the same friction couple, but in different dimensional segments, can interact preferentially with different biological systems. At the same time, since emissions from different dimensional fractions are likely generated by different wear mechanisms (abrasive vs. adhesive), this might possibly have an influence also on their chemical composition. For this reason, this chapter investigates the influence of the emissions dimensions on their overall compositional features. For this reason, two separate but related studies are reported, assessing eventual compositional differences in various dimensional fractions produced by the same friction couple. In particular, the following paragraphs report the comparative assessment of the chemical composition between: i) PM<sub>2.5</sub> emissions and ultra-fine particulates; and ii) coarse debris materials and PM<sub>10</sub> emissions.*

### 7.1. Aim of the Study

The major part of the investigations reported in this thesis work are based on non-exhaust brakes PM<sub>10</sub> particulates, *i.e.* powder samples having controlled size distributions exhibiting maximum dimensions lower than 10 µm. The choice of a specific dimensional cut is a necessity due to concomitant factors, such as the need to produce results directly referencing and matching to the existent body of knowledge<sup>[1,2]</sup> in the research field of the air quality as well as to collect reproducible particulate samples with commercially available instrumentation. As demonstrated in the previous chapter, when assessing brakes NEE, different size distributions can exist below the selected limit of 10 µm. These distributions are influenced and modulated by the materials composing the friction couple and their tribological characteristics. At the same time, in real world scenario, materials emitted in environment by the disc brake device can have even

wider dimensional distribution, ranging from nanometric particles up to millimeter-scaled objects. If the main subjects of particle emission and toxicological studies are PM<sub>10</sub> and PM<sub>2.5</sub> particulates for both historical and practical reasons, at the same time coarser and finer dimensional fractions are similarly important and interesting.

For instance, as far as the coarser fractions are concerned, brakes wear debris produced during the tribological event can easily fall directly to the ground, due to the higher dimensions and therefore superior weights (see pictures in *Annex 7*). Since the wear debris is generated more by coarse mechanical abrasion and stochastic events occurring at the tribological interface, it can most likely have different compositional features in respect with an hypothetical corresponding PM<sub>10</sub> counterpart generated by tribo-oxidative events occurring on well-formed and structured friction layer.<sup>[3-6]</sup> This seems especially reasonable when considering the overall oxidation level of the Iron (and, more in general, of all the metallic species inside the emission) or the overall amount of Carbon generated by thermal degradation of organic species.<sup>[7,8]</sup> Therefore, if the coarser debris material falling to the ground happens to have different chemical composition in comparison to the corresponding finer particulate, it appears evident that impact assessments towards different environments (soil/water vs. air) should be based on different sets of compositional data targeting the most corresponding typology of particulate pollutant. Similar considerations can be drawn for the toxicological characterization of different biological systems, for instance human body organs or apparatuses vs. aquatic or terrestrial organisms, since they might be exposed to particulates exhibiting different physico-chemical features. On the other hand, it is well known that nanoparticles can penetrate biological barriers more easily in respect to micrometric particles. Thus, they can enter cells and generate more easily different toxicological responses based on mutagenicity effects more than “simpler” contact inflammatory effects.<sup>[9-11]</sup> At the same time, different evidences are nowadays reported in literature on how nanoparticles are generated at the tribological interface. More in detail, recent results showed that they are mostly related to the degradation of the organic compounds and that their number increases exponentially with the increasing temperature.<sup>[4,7,8]</sup> Therefore, ultra-fine particles generated during braking can preferentially concentrate or segregate some of the components of the corresponding micrometric emission, thus eventually exhibiting different chemical composition. Similarly to what discussed for the differences between wear debris and PM emissions, this can potentially have profound implication on the toxicological characterization of the investigated particulate.

For all these reasons, this chapter is specifically meant to deeply investigate eventual interconnections occurring between different dimensional fractions of the brake emissions and their corresponding chemical composition. The final aim is to define the

most precise particulate targets in function of different environmental and toxicological characterizations.

## 7.2. Ultra-fine vs. Micrometric Particulates

The investigation reported in this first section are focused on the results obtained within the perimeter of activities of the nPETS project.<sup>[12]</sup> In particular, it refers to the investigation of nanoparticle emissions generated by brakes, and more in detail on their chemical characterization. Part of the reported results has been recently published.<sup>[13]</sup> In addition to the specific results of chemical composition of the brake emission ultra-fine fraction ( $D_{50} < 150$  nm), a comparative assessment with results obtained for coarser fractions is also reported, up to  $PM_{2.5}$  fraction. The obtained results will be used in the second half of the project, together with chemical evidences collected on other transport-related nanoparticle emissions, in order to investigate their ecological and toxicological behaviors as well as to perform accurate source apportionment studies.

### 7.2.1. Experimental

The following paragraph describes the materials and the analytical protocols adopted for sample collection and chemical characterization. Particular attention is devoted to the description of the procedures used to optimize the management of limited amounts of particles of nanometric dimensions. Brakes nanoparticle emissions are generated by two friction pairs composed by a fully pearlitic grey cast iron braking disc (BD) coupled against two different ECE R90 Copper-free friction materials, labeled as LS/LM-a and LS/LM-b.

The particulate samples are collected at a dynamometric bench designed for emissions collection during tests performed in controlled conditions.<sup>[14-15]</sup> The emission test procedure used to collect the particulates is the WLTP-Brake Cycle<sup>[16]</sup>. In particular, the material is collected during both the bedding cycles (5 WLTP-Brake repetitions) and during the cycle typically used for the evaluation of the emissions (*i.e.*, the 6<sup>th</sup> WLTP-Brake Cycle repetition) in order to maximize the amount of collected nano-particles. For the same purpose, three repetitions of a single emission test are carried out, each repetition with new discs and pads. For all the tests, the braking corner is composed by: *i*) a four pistons fixed Aluminum caliper with pistons diameter of 44 mm; *ii*) a vented braking disc with a diameter of 342 mm and a thickness of 32 mm; and *iii*) a couple of pads with a surface of 89.1 cm<sup>2</sup>. During the dyno-bench tests, a controlled particle-free air flux of 245 m<sup>3</sup> h<sup>-1</sup> enters the brake enclosure in order to fulfill the temperature targets as suggested by the most recent guidelines from the Particle Measurement Programme (PMP) Informal Working Group<sup>[17]</sup> (a tailored calibration run is carried out before the bedding phases). The air flux is filtered through a HEPA-H13 filter which ensures an



average filtration efficiency higher than 99.95%. The collection of the PM emissions is carried out by an isokinetic sampling-probe, equipped with sharp-ended nozzles to ensure a high efficiency sampling. The airborne particles are sampled through two specific measurement instruments: a Dekati™ Electrical Low Pressure Impactor (ELPI+) and a Dekati™ Gravimetric Impactor (DGI). For this study, the last five stages of the ELPI+ impactor are initially considered ( $d_{50} < 120$  nm), collecting the particulates on polycarbonate filters. However, in spite of all the strategies adopted for the sampling, the amount of collected material on the lower stages of the ELPI+ was extremely low and thus insufficient for a reliable chemical characterization. In order to overcome this problem, material collected on the DGI collection substrates is used for chemical analysis, sampling the collected particles in five size fractions below 2.5  $\mu\text{m}$ . A comparison of the collected amounts of materials in the two configurations and is reported for sample LS/LM-a in Table 7.1 and Figure 7.1, for sake of reference. The instrument is used at the flow rate of 95 L/min and a cyclone with a 2.5  $\mu\text{m}$  cutoff is placed before the inlet to provide the first dimensional cut. Greased aluminum substrates are used for the upper four stages, while a Teflon filter (pores diameter of 3  $\mu\text{m}$ ) is used as backup. The material collected on the first collection substrate (**S1**:  $130 < d_{50} < 150$  nm) represents the target sample for the study of the nanoparticle emissions generated by brakes. This ultra-fine particulate is then compared with material collected on the higher collection substrates (**S2**:  $400 < D_{50} < 450$  nm; **S3**:  $800 < D_{50} < 900$  nm; **S4**:  $2.1 < D_{50} < 2.2$   $\mu\text{m}$ ).

ELPI+			DGI		
Stage	$D_{50}/\mu\text{m}$	Mass/mg	Stage	$D_{50}/\mu\text{m}$	Mass/mg
S6	0.150	0.00	S4	2.10-2.20	0.67
S5	0.095	0.01	S3	0.80-0.90	5.91
S4	0.054	0.00	S2	0.40-0.45	4.71
S3	0.030	0.02	S1	0.13-0.15	0.46
S2	0.016	0.00			
S1	0.006	0.00			

**Table 7.1:** Summary table of measured weights of nanoparticles emissions collected by the mean of ELPI+ and DGI instruments for particulates generated by LS/LM-a FC.

For each particulate, one fourth of each collected substrate is used for chemical analysis, while the remaining material is spared for the eco/cyto-toxicological characterization, which will be performed in the second half of the project. For both the samples, the four investigated particulates are stripped from the collection substrates after dissolution of the collection grease in acetone and following sonication in 1 mL of isopropyl alcohol at 35 kHz for 2 minutes. The suspended particles are then recollected by centrifugation at 3000 rpm for 5 minutes and dried overnight in mild vacuum conditions (20 mbar) before the chemical analysis. Stand-alone powders are deposited on Aluminum stubs previously covered with carbon tape for electron microscopy. Particulates are always manipulated

with a small metallic yet non-magnetic spatula and stocked or deposited in glass containers in order to minimize the potential loss of sample material.

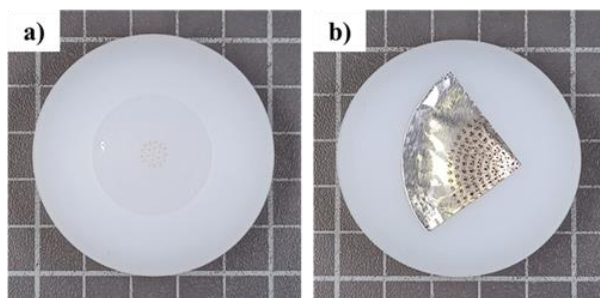


**Figure 7.1:** Comparison of: **a)** ELPI+ S6; and **b)** DGI S1 collection substrates after the performed emission tests for LS/LM-a FC. The two reported substrates collect materials with similar dimensional dispersions, centered at about 150 nm.

Scanning Electron Microscopy (SEM) imaging is used in order to verify qualitatively the granulometric profiles of the collected particulates. Energy Dispersive Spectroscopy (EDXS) analysis is coupled with the SEM probe in order to perform a comparative assessment of the elemental compositions of the materials collected from the four different DGI collection substrates. The analysis is carried out following the protocol described in *Chapter 2*, with minimal variations due to very low amount of collected material. In particular, for each powder sample, five areas of approximately 300 x 200  $\mu\text{m}$  are analyzed.

Raman Spectroscopy (RS) is used in order to obtain some information on the phase composition of the collected emissions, *i.e.* on the compounds composing the nano-powders. Raman probe is chosen after carrying out X-Ray Diffraction (XRD) analysis, which resulted in the complete absence of diffraction signals even when investigating the material from the S3 collection substrate ( $800 < d_{50} < 900$  nm). In spite of being demonstrated in the recent literature,<sup>[19-23]</sup> and in this thesis work (*Chapter 5. Speciation*) as a valuable tool for the characterization of the crystalline fraction of the PM<sub>10</sub> emissions generated by brakes, in this context the XRD probe fails to provide significant analytical signals, due to combination of the two following factors: *i)* the extremely limited amount of analyzed material; and *ii)* the mostly nanometric (and possibly amorphous) nature of the investigated samples. Raman analysis is carried out by the mean of the Horiba LabRAM HR, equipped with a solid-state laser source ( $\lambda = 473$  nm). The laser power is set nominally to 12.5 mW, since higher power values were found to damage the samples, leaving burnt micro-area after the measurements. All the spectra are acquired following analytical protocols described in the corresponding section of *Chapter 2*.

### 7.2.2. Qualitative Assessment of the PSD

SEM images of the collected particulates generated by LS/LM-a and LS/LM-b FCs are reported in Figure 7.2 and 7.3, respectively. The overall particle size distributions are coherent with the nominal  $D_{50}$  values expected as a function of the adopted flow rate, reported in Table 7.1. In particular, a progressive overall reduction in particle dimensions is apparent moving from **S4** to **S1**, with the material from the latter clearly exhibiting ultra-fine granulometry.

### 7.2.3. Elemental Composition

The elemental composition of the nanoparticle emission, in the form of material collected on the DGI **S1** collection substrate, is investigated by means of EDXS analysis. In addition, the chemical composition of the material collected on the higher collection substrates from the DGI instrument (**S2**, **S3** and **S4**) is investigated for a comparative assessment with the ultra-fine fraction. The elemental composition of the nanoparticle emission, in the form of the material collected on the DGI **S1** collection substrate ( $D_{50} < 150$  nm), is investigated by means of EDXS analysis.

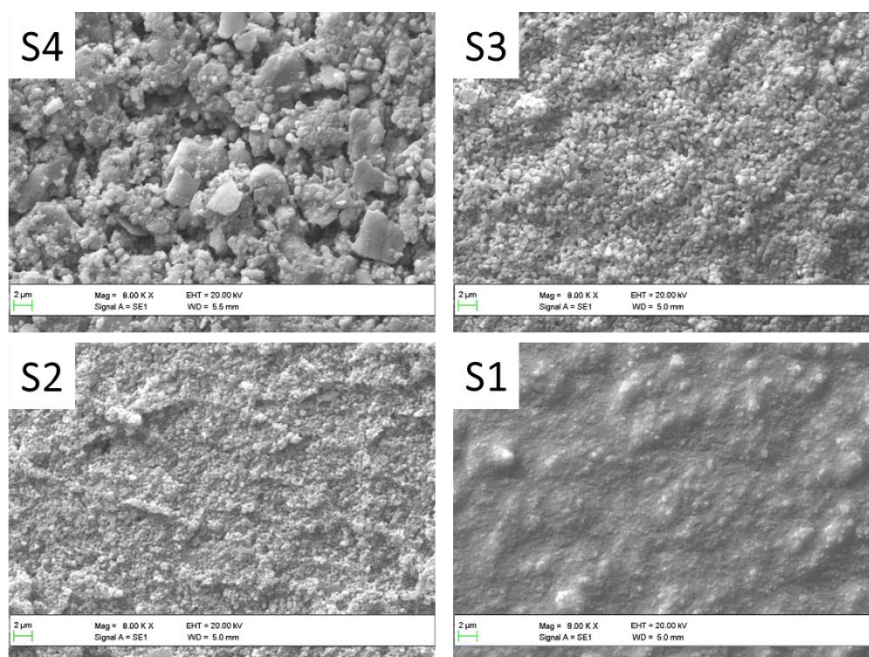


**Figure 7.2:** Comparison of SEM images acquired on the collected material for LS/LM-a sample; from top-left to bottom-right: **a)** S4; **b)** S3; **c)** S2; and **d)** S1 DGI collection substrates. **S4:**  $2.1 < D_{50} < 2.2$  m; **S3:**  $800 < D_{50} < 900$  nm; **S2:**  $400 < D_{50} < 450$  nm; **S1:**  $130 < D_{50} < 150$  nm.

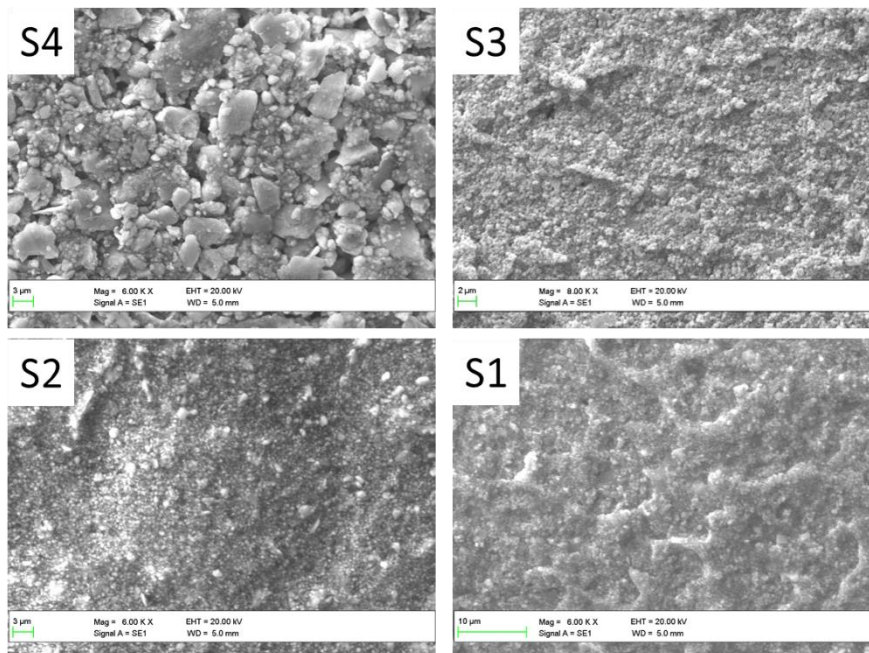


**Figure 7.3:** Comparison of SEM images acquired on the collected material for LS/LM-b sample; from top-left to bottom-right: **a)** S4; **b)** S3; **c)** S2; and **d)** S1 DGI collection substrates. **S4:**  $2.1 < D_{50} < 2.2$  m; **S3:**  $800 < D_{50} < 900$  nm; **S2:**  $400 < D_{50} < 450$  nm; **S1:**  $130 < D_{50} < 150$  nm.

Average elemental concentration values for nanoparticle emissions generated by LS/LM-a and LS/LS-b FCs are reported in Table 7.2 and 7.3. In addition, Figure 7.4 and 7.5 show the elemental distributions of the corresponding samples from **S1** substrate over five different measurements, together with the average elemental composition, in form of histograms graphs.

Element	S4		S3		S2		S1	
	Average/wt%	SD	Average/wt%	SD	Average/wt%	SD	Average/wt%	SD
Fe	50.5	1.9	46.3	2.6	44.4	2.4	37.9	1.7
O	26.0	1.2	25.3	1.0	25.4	1.9	25.5	0.7
C	9.2	0.9	14.1	2.1	16.8	3.6	24.7	1.0
Si	4.1	0.2	1.7	0.1	1.5	0.1	2.6	0.2
Sn	2.1	0.1	3.0	0.2	2.8	0.1	2.1	<0.1
Zn	1.7	0.1	2.5	0.2	2.5	0.1	1.6	0.1
Al	1.5	<0.1	1.8	0.2	1.7	<0.1	1.5	0.1
Mg	1.1	<0.1	2.2	0.2	1.9	<0.1	1.4	<0.1
S	0.8	<0.1	1.5	0.1	1.5	<0.1	1.3	<0.1
K	0.6	<0.1	0.3	<0.1	0.3	<0.1	0.3	<0.1
Cr	0.5	<0.1	0.5	<0.1	0.4	<0.1	0.3	<0.1
Cu	0.5	<0.1	0.3	<0.1	0.3	<0.1	0.3	<0.1
Mn	0.3	<0.1	0.4	<0.1	0.4	<0.1	0.3	<0.1
Others	traces	-	traces	-	traces	-	traces	-

**Table 7.2:** Summary table of measured elemental concentrations of nanoparticles emissions generated by LS/LM-a FC. The average values are reported together with the corresponding variability index (SD – standard deviation over five independent observations).

Element	S4		S3		S2		S1	
	Average/wt%	SD	Average/wt%	SD	Average/wt%	SD	Average/wt%	SD
Fe	51.8	1.5	38.9	2.2	42.7	1.7	27.0	1.8
O	25.3	0.9	22.8	3.6	25.4	1.2	21.0	1.2
C	8.5	2.2	24.1	1.3	15.7	1.1	39.7	3.8
Si	4.7	0.3	2.3	1.3	1.5	0.1	1.4	0.1
Sn	1.9	0.1	2.2	0.1	2.6	0.0	1.7	0.1
Al	1.7	0.1	0.9	0.1	0.4	<0.1	0.5	<0.1
Zn	1.4	0.3	4.6	0.2	7.3	0.8	4.7	0.5
Cu	1.0	0.1	0.6	0.2	0.2	0.1	0.4	<0.1
K	0.8	<0.1	0.4	<0.1	0.3	<0.1	0.6	<0.1
Mg	0.8	0.1	1.4	0.1	1.8	0.1	1.1	0.1
S	0.6	<0.1	0.8	0.1	1.1	<0.1	1.4	0.1
Ti	0.5	<0.1	0.2	<0.1	0.1	<0.1	0.1	<0.1
Cr	0.5	<0.1	0.4	<0.1	0.5	<0.1	0.3	<0.1
Mn	0.4	<0.1	0.3	<0.1	0.3	<0.1	0.2	<0.1
Others	traces	-	traces	-	traces	-	traces	-

**Table 7.3:** Summary table of measured elemental concentrations of nanoparticles emissions generated by LS/LM-b FC. The average values are reported together with the corresponding variability index (SD – standard deviation over five independent observations).

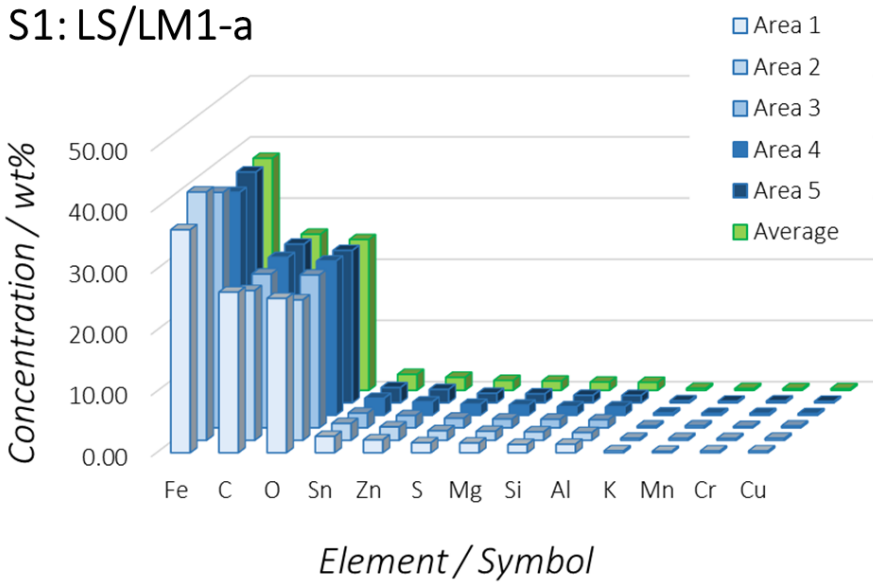


**Figure 7.4:** Distribution of elements as measured by EDXS probe for the material collected on the DGI S1 collection substrate during the emission test of the LS/LM-a friction couple. Five independent observations (blue-scale histograms) and averaged results (green histograms) are reported.

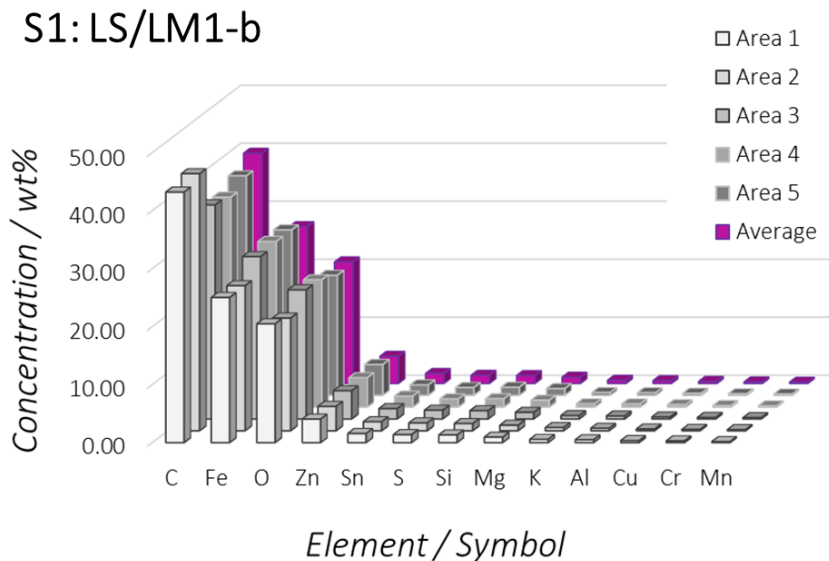


**Figure 7.5:** Distribution of elements as measured by EDXS probe for the material collected on the DGI S1 collection substrate during the emission test of the LS/LM-b friction couple. Five independent observations (gray-scale histograms) and averaged results (purple histograms) are reported.

The results reported in Table 7.2 and 7.3, as well as in Figure 7.4 and 7.5, show that the elemental composition of the nanoparticle emission is dominated by the presence of three main elements, namely Iron, Carbon and Oxygen, since they account for over 85 wt% of the total particulate mass. Iron arises from both sides of the tribological interface, *i.e.* from the wear and tribo-oxidation of the cast iron BD and from the Iron-based compounds contained inside the friction mix. In turn, Carbon is a more specific marker for the consumption of the friction material, since several Carbon-based compounds are common constituents of LS/LM friction composites: organic resins as binders, graphite and cokes as solid lubricants, inorganic carbides and carbonates as abrasives and fillers.<sup>[18]</sup> However, a minor but not negligible contribution can also be ascribed to the wear of the cast iron braking disc, due to the presence of graphite lamellae within the Iron-based alloy. The Oxygen arises from both sides of the friction couple: it is indeed a marker for the oxidation of the metallic material from both the cast iron braking disc and the friction material, as well as for the inorganic oxides, carbonates and silicates commonly used in the friction mix as abrasives and fillers.<sup>[18]</sup> However, there are strong compositional differences in the distribution of the main constituents of the two collected nanoparticle emissions. In particular, sample from LS/LM-b FC shows a significantly higher amount of Carbon; conversely, higher concentration of Iron is found in sample from LS/LM-a friction couple. Finally, both the nanoparticle emissions features the minor presence of a set of secondary and trace elements, which are typically found

in concentrations lower than 5 wt%. Together, these elements account for about the 10-15 wt% of the total particulate mass in both cases. The presence of these elements relates closely to the specific friction material formulation and, secondary, to alloying elements of the worn cast iron.

As can be spotted in Tables 7.2 and 7.3, the comparison of the results obtained for the materials collected on **S1** and from stages for higher dimensions reveals some statistically significant trends. In both cases, in all the three particulates deposited on the higher collection substrates, there are three dominant elements, namely Iron, Oxygen and Carbon. Similarly to the case of the ultra-fine emission, these elements account for about 85 wt% of the total sample mass. However, their relative distribution changes moving towards the lower dimensional fractions. In particular, a constant decrease of the Iron concentration can be observed. Conversely, the Carbon concentration increases significantly moving from particulates with bigger dimensions to their counterparts with smaller dimensions. This is in good agreement with other results recently reported in literature<sup>[8]</sup>, showing that brakes nanoparticles are preferentially and largely produced by organic compounds of the friction materials. In addition, also Graphites and Cokes might likely contribute to the same behavior, since they are extremely brittle materials. On the other hand, the overall variations of Oxygen and the secondary elements are modest (when statistically meaningful). Interestingly, the concentrations of main constituents measured in **S4** samples ( $D_{50} > 2 \mu\text{m}$ ) are very similar to those reported in *Chapter 4* for  $\text{PM}_{10}$  particulates from the same coupling typology (GCI BDs + LS/LM FMs). This is particularly meaningful, since results reported in *Chapter 6. Size distributions* showed that the previously investigated  $\text{PM}_{10}$  are mainly populated by particles having dimensions  $\leq 2.5 \mu\text{m}$ , thus not completely dissimilar from the particulates collected on **S4** stage in term of dimensional distributions. All the discussed results are graphically reported in Figure 7.6 (LS/LM-a) and Figure 7.7 (LS/LM-b).

Similarly, Figures 7.8 and 7.9 show a graphical comparison of the average concentration values for the secondary elements, respectively for LS/LM-a and LS/LM-b samples. Looking at the histogram graph for the first sample (LS/LM-a, Figure 7.8), it is possible to notice that only Silicon preferentially segregates to the dimensional fraction with the highest dimensional fraction. Notably the same trend is observed in particulates from LS/LM-b. This might be due to the nature of Si-bearing compounds in the friction couple; indeed, they typically are silicates and alumino-silicates of geological origin, *i.e.* very hard materials with low tendency to wear. All other elements show a limited decrease of average concentration moving from **S4** to **S1** (*i.e.*, from higher to lower overall particulate dimensions), which might be more likely related to the overall slight decrease of their overall amount than a real trend.

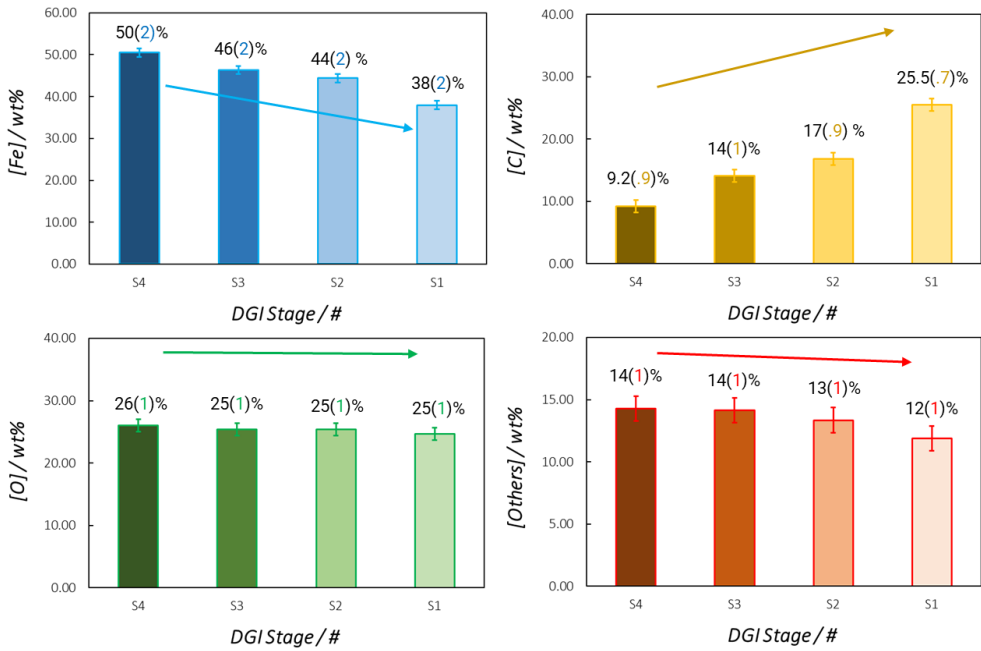


Figure 7.6: Distribution of main constituents of LS/LM-a samples along the different dimensional fractions.

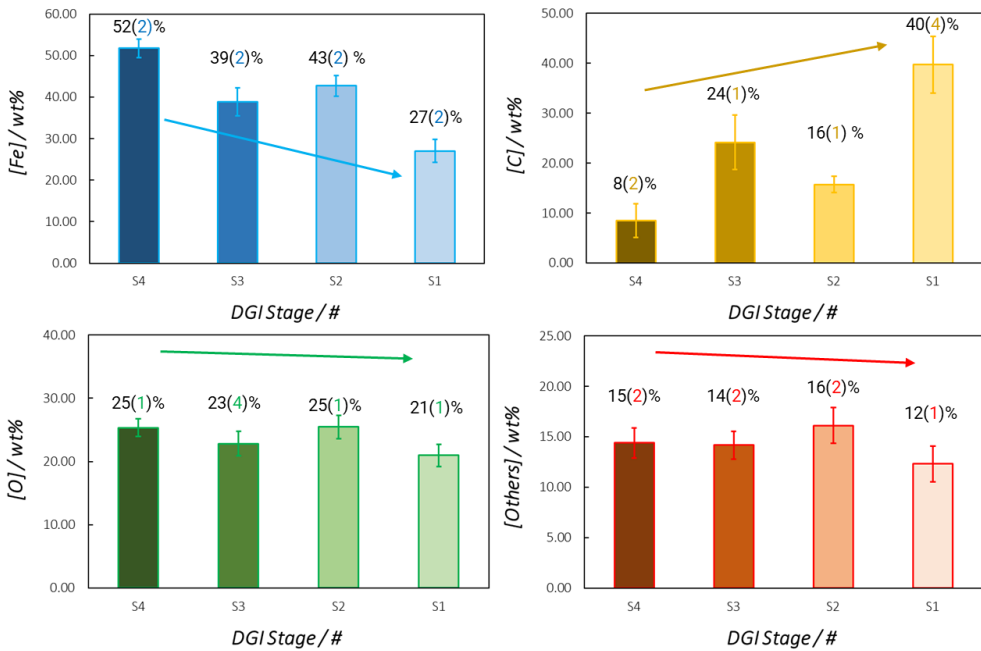
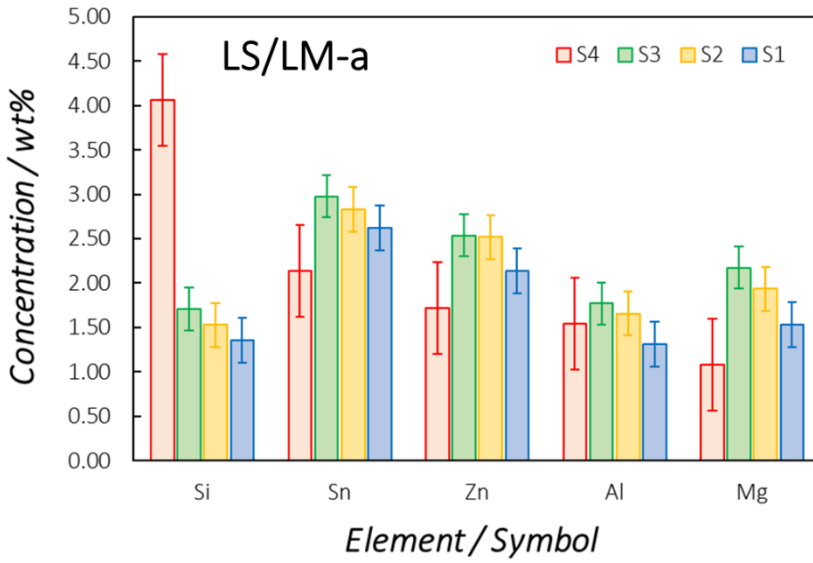
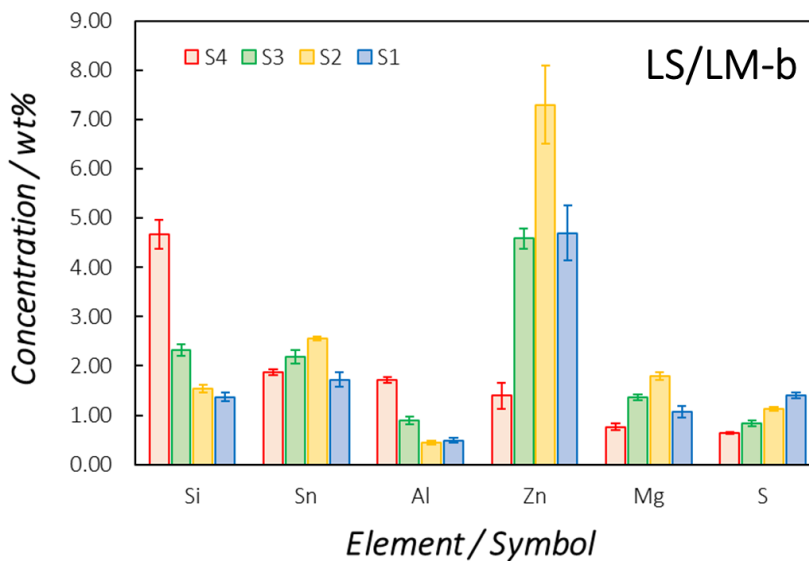


Figure 7.7: Distribution of main constituents of LS/LM-a samples along the different dimensional fractions.





**Figure 7.8:** Detail of average concentration values for secondary elements (concentration > 0.5 wt%) in LS/LM-a particulates, along the four investigated dimensional distributions. Error bars indicates standard deviations (as  $\pm\sigma$ ) around the corresponding average value.



**Figure 7.9:** Detail of average concentration values for secondary elements (concentration > 0.5 wt%) in LS/LM-b particulates, along the four investigated dimensional distributions. Error bars indicates standard deviations (as  $\pm\sigma$ ) around the corresponding average value.

Looking more in detail at the particulates from LS/LM-b samples, it is possible to observe a more variegated situation in respect with the counterparts from LS/LM-a samples, with less straightforward trends. If the Silicon decreasing trend shows similarity with that from the previous samples, other elements (Sn, Zn, Mg, S) exhibit on the contrary overall increasing trends towards the finer fractions. In addition, it is also evident a preferential (or anomalous) segregation of Zn on the **S2** stage.

#### 7.2.4. Phase Composition

Phase composition of the collected nanoparticle emissions is investigated via Raman Spectroscopy. Figures 7.10 and 7.11 show the Raman spectra acquired directly from the particulate obtained from the DGI **S1** collection substrates, together with the corresponding spectra collected from analyzing the materials sampled on the higher collection substrates (**S2-S4**), respectively for LS/LM-a and LS/LM-b samples. As can be observed, all the reported spectra look overall similar and exhibit the same main features. In particular, two characteristic frequency ranges appear populated in all measured samples: *i*) the low frequencies, from 50 to 700  $\text{cm}^{-1}$ , hosting signals from Iron oxides; and *ii*) the intermediate frequencies, from 1200 to 2000  $\text{cm}^{-1}$ , where signals from elemental Carbon typically reside.

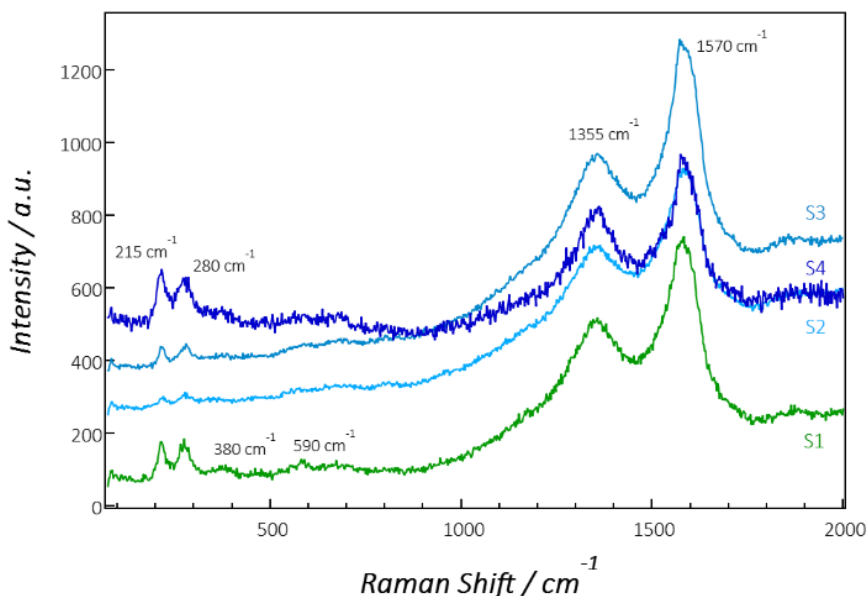


**Figure 7.9:** Comparison of Raman spectra acquired from the ultra-fine emission fraction (S1, green profile) and from coarser fractions (S2 to S4, blue-scale profiles) from LS/LM-a particulates.

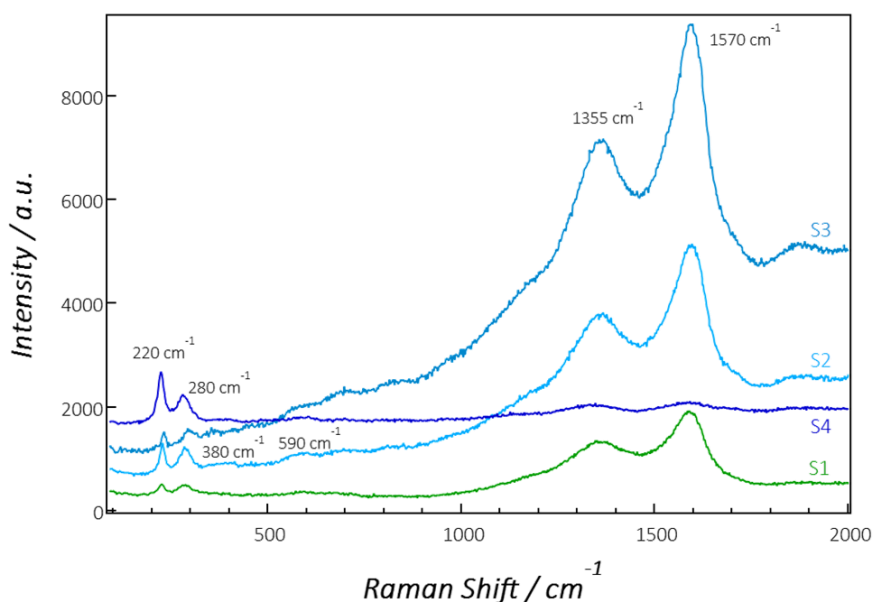


**Figure 7.10:** Comparison of Raman spectra acquired from the ultra-fine emission fraction (S1, green profile) and from coarser fractions (S2 to S4, blue-scale profiles) from LS/LM-b particulates.

All the acquired spectra exhibit two peaks at about 215 and 280  $\text{cm}^{-1}$ , which are associated with the Hematite ( $\alpha\text{-Fe}_2\text{O}_3$ ) phase. In both cases, the spectrum generated by the material collected on the **S1** substrate also hosts two additional broad features at about 380 and 590  $\text{cm}^{-1}$  which are also coherent with the Hematite identification. Moving towards the higher frequencies, all spectra exhibit two peaks at about 1355 and 1570  $\text{cm}^{-1}$ , which indicate the presence of elemental Carbon (*i.e.*, Graphites and Cokes) inside the investigated particulates. All the described peaks are extremely broad and characterized by low intensities: this observation suggests an overall low degree of crystallinity of the identified compounds, which is well coherent with the (mostly nanometric) nature of the samples. Notably, the evaluation of the phase composition qualitatively confirms the trends observed in the elemental analysis. In particular, the intensity ratio between the peaks associated with Hematite and elemental Carbon is higher in the material collected on the **S4** substrates ( $2.1 < D_{50} < 2.2 \mu\text{m}$ ), and decreases strongly in **S1** stages. As far as the Iron/Oxygen ratio is concerned, it is possible to observe more defined characteristic features of the Hematite in the spectrum from the ultra-fine fraction (**S1**) with respect to its coarser counterparts: this observation can be reasonably explained with an overall higher degree of oxidation of the Iron in Fe-based particles from the lower dimensional fractions, as recorded also from the elemental analysis reported in the previous section.

### 7.2.5 Summary

Considering all the results reported in the previous paragraphs, some interesting trends in the chemical composition of brakes emissions moving from the micrometric to the nanometric realm become apparent. In particular, at least two clear behaviors are identified: *i*) an overall decrease of the Iron/Oxygen ratio moving towards the ultra-fine particle dimensions; and *ii*) an overall increase of the Carbon-based material moving towards the lower particle size distributions.

Regarding the Fe/O ratio, it appears reasonable to expect an overall higher degree of oxidation in Iron particles with nanometric dimensions with respect to their counterparts of micrometric dimensions. This observation can be indeed well explained by considering the different surface areas generated by different particle size distributions. On the other hand, the increasing amount of Carbon-based material observed moving towards the nanoparticle emissions can be likely explained by considering the nature of the compounds which are typical sources of such element: organic resins as well as Graphites and Cokes are extremely brittle materials, which can generate exponential amounts of nanoparticles especially when exposed to increasing temperatures.<sup>[4,8]</sup> Notably, both trends presented here have been already reported and similarly discussed in the literature<sup>[19,20]</sup> when comparing the chemical composition of Debris material and PM<sub>10</sub> emissions generated by a friction couple similar to the one used in this study (GCI BD + ECE R90 Cu-Free LS/LM FM). Also in that reference cases<sup>[19,20]</sup>, moving from coarser to finer granulometric profiles resulted in decreasing Iron/Oxygen ratio and increasing concentration of Carbon. More detailed insights in the comparison of the chemical composition of wear debris and corresponding PM<sub>10</sub> emission are also reported in the next section of this chapter.

In addition to these main trends, other observational findings can be appreciated. Among the secondary and trace elements, only Silicon appears to be preferentially segregated in the highest dimensional fraction (**S4**): this can be likely explained by the specific granulometry and physical properties of its source compounds inside the friction mix. Conversely, all other elements in particulates from LS/LM-a samples are found in slightly higher concentrations in the lower dimensional size distributions (**S3**, **S2** and **S1**), with a general decreasing trend moving from sub-micrometric towards nanometric distributions. However, since this behavior is mild, it can be more likely related to the overall slight decrease of their overall amount than a real trend. On the other hand, more variegated and less straightforward behaviors are observed when assessing particulates from LS/LM-b friction couple. Among the secondary elements of this sample, Zn appear to preferentially (or anomalously) segregate in the sub-micrometric fractions more than in the nanometric distribution.

### 7.3. Debris vs. Micrometric Particulates

Similarly to the comparison reported in previous paragraphs, this section discusses the compositional differences between PM<sub>10</sub> and wear debris samples produced by the same particulates during the same emission tests.

#### 7.3.1. Experimental

The particulates used for this study are generated by six different friction couples composed by fully pearlitic grey cast iron braking discs (GCI BDs) and six different Copper-free friction materials from LS/LM and IN families. The investigated friction couples belong respectively to *Category 1* and *Category 2*, as identified in *Chapter 4*. In particular, they correspond to LS/LM1, LS/LM2, LS/LM4, IN1, IN2 and IN3 friction pairs. The choice of the friction couples was meant to assess the influence of different tribological behaviors, since IN friction materials are usually more abrasive in respect with the LS/LM counterparts.

The particulate samples are collected at a dynamometric bench designed for emissions collection during tests performed in controlled conditions.<sup>[14-15]</sup> The emission test procedure used to collect the particulates is the WLTP-Brake Cycle<sup>[16]</sup>, following the standard procedure reported in *Chapter 2*. For all the tests, the braking corner is composed by: *i*) a four pistons fixed Aluminum caliper with pistons diameter of 44 mm; *ii*) a vented braking disc with a diameter of 342 mm and a thickness of 32 mm; and *iii*) a couple of pads with a surface of 89.1 cm<sup>2</sup>. During the dyno-bench tests, a controlled particle-free air flux of 245 m<sup>3</sup> h<sup>-1</sup> enters the brake enclosure in order to fulfill the temperature targets as suggested by the most recent guidelines from the Particle Measurement Programme (PMP) Informal Working Group<sup>[17]</sup> (a tailored calibration run is carried out before the bedding phases). The air flux is filtered through a HEPA-H13 filter which ensures an average filtration efficiency higher than 99.95%. The collection of the PM emissions is carried out by an isokinetic sampling-probe, equipped with sharp-ended nozzles to ensure a high efficiency sampling. The airborne PM<sub>10</sub> particles are sampled through a 47 mm filter holder prior dimensional cut carried out by a PM<sub>10</sub> cyclone on cellulose substrates. In addition, the produced coarser fractions (Debris) is also collected, by simply positioning a metallic tray under the braking corner.

For both the samples, the investigated powders are collected and suitably manipulated following the standard procedure as described in the corresponding section of *Chapter 2*. Both the elemental and the phase compositions are assessed, respectively by SEM/EDXS and XRD analysis. Also in this case, standard procedures as adopted for all the previous studies are applied without any significant variation. In addition to the standard

analytical protocol, Laser Diffraction analysis is carried out to characterize the size distribution (PSD) of the coarser samples.

### 7.3.2. Particle Size Distributions (PSD)

The differences between the characteristic PSD profiles of PM<sub>10</sub> samples from different categories of FCs are discussed in detail in *Chapter 6*. Nevertheless, Figure 7.11 reports a comparison of typical PSD profiles for PM<sub>10</sub> samples generated by *Category 1* and *Category 2* FCs for reference. As can be observed, PM<sub>10</sub> particulates generated by IN friction materials exhibit an overall higher relative amount of coarser particles in respect with the counterparts generated by LS/LM friction composites (when coupled against GCI braking discs).

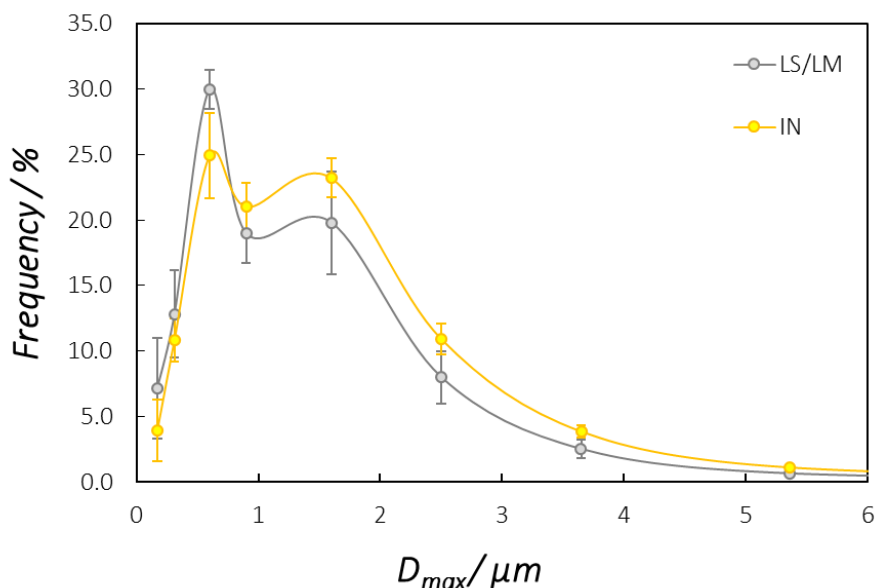


**Figure 7.11:** Comparison of PSD profiles for PM<sub>10</sub> samples generated by LS/LM and IN friction materials when coupled against GCI BDs.

Figures 7.12 shows the comparison between the PSD profile as measured from laser diffraction experiments carried out on Debris samples from LS/LM and IN friction couples, respectively. Similarly to what observed in PM<sub>10</sub> samples, also the PSD profiles of Debris materials from the two different typologies of friction couples exhibit some differences. In particular, Debris samples from *Category 2* FCs are characterized by overall significantly coarser granulometry in respect with the counterparts from *Category 1*, notably retracing the trends observed for the PM<sub>10</sub> samples.

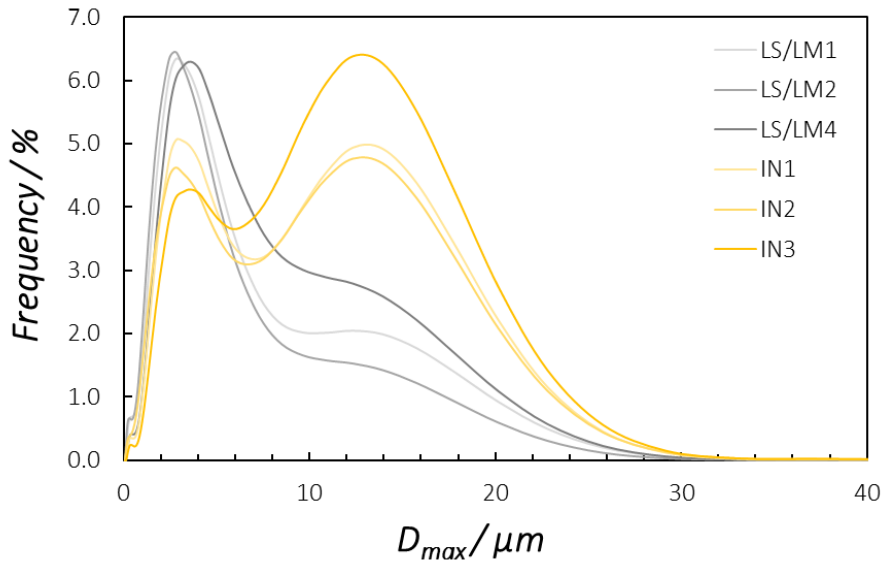


**Figure 7.12:** Comparison of PSD profiles for Debris samples generated by LS/LM and IN friction materials when coupled against GCI BDs.

### 7.3.3. Elemental Composition

Moving towards the chemical characterization, Table 7.4 summarizes all the elemental concentrations as measured for both PM<sub>10</sub> and Debris samples generated from each investigated friction couple belonging to *Category 1* (GCI BDs + LS/LM FMs). Figures 7.13, 7.14 and 7.15 report graphically the direct comparison between the elemental concentrations of both main constituents and secondary elements for all the investigated three couplings.

	LS/LM1				LS/LM2				LS/LM4					
	PM10	SD	Debris	SD	PM10	SD	Debris	SD	PM10	SD	Debris	SD		
Fe	54.6	1.7	55.3	1.0	53.3	0.9	53.7	1.8	58.4	1.1	55.2	1.0		
O	27.5	1.2	26.9	0.7	27.2	0.7	27.4	1.1	22.8	0.7	20.3	1.0		
C	10.1	0.8	9.9	0.5	9.0	0.3	8.9	0.8	11.2	0.7	12.2	1.2		
Sn	1.7	0.2	1.69	0.05	2.26	0.03	2.09	0.05	Zn	1.6	0.1	5.3	0.4	
Si	1.3	0.08	1.28	0.07	Si	1.42	0.01	1.4	0.02	Si	1.49	0.06	1.53	0.07
Mg	1.24	0.05	1.27	0.06	Mg	1.84	0.03	1.73	0.05	Mg	0.83	0.02	1.07	0.03
Al	1.15	0.07	1.1	0.1	Al	1.64	0.05	1.47	0.06	Sn	0.7	0.2	1.06	0.08
S	0.73	0.06	0.80	0.01	S	0.95	0.06	0.9	0.05	Al	0.75	0.02	0.91	0.04
Cr	0.63	0.05	0.67	0.03	Cr	0.91	0.02	0.86	0.03	S	0.7	0.02	0.86	0.04
Mn	0.43	0.02	0.44	0.02	Mn	0.41	0.02	0.40	0.01	Cr	0.42	0.01	0.53	0.07
Zn	0.26	0.03	0.16	0.05	Zn	0.28	0.03	0.37	0.02	Mn	0.46	0.03	0.43	0.02
Cu	0.22	0.04	0.22	0.04	Cu	0.13	0.02	0.13	0.03	Cu	0.15	0.04	0.20	0.02
Ca	0.17	0.04	0.25	0.01	Ca	0.38	0.01	0.38	0.01	Ca	0.4	0.2	0.31	0.02
					Mo	0.22	0.08	0.22	0.06	Bi	0.16	0.02	0.15	0.03
					V	0.09	0.01	0.09	0.01					

**Table 7.4:** Comparative summary of the elemental concentrations as measured by EDXS analysis for PM<sub>10</sub> and Debris samples obtained from LS/LM1, LS/LM2 and LS/LM4 FCs. The concentrations are average of five independent observations and are followed by the corresponding standard deviations (SD).

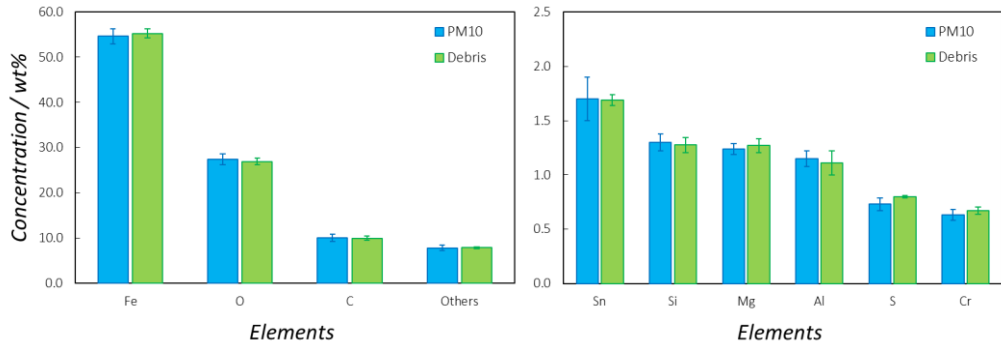


**Figure 7.13:** Comparison of elemental concentrations as measured for PM<sub>10</sub> vs. Debris samples generated by LS/LM1 friction couple. Only elements with concentration higher than 0.5 wt% are reported. Error bars refer to the observed standard deviation ( $\pm$ SD).

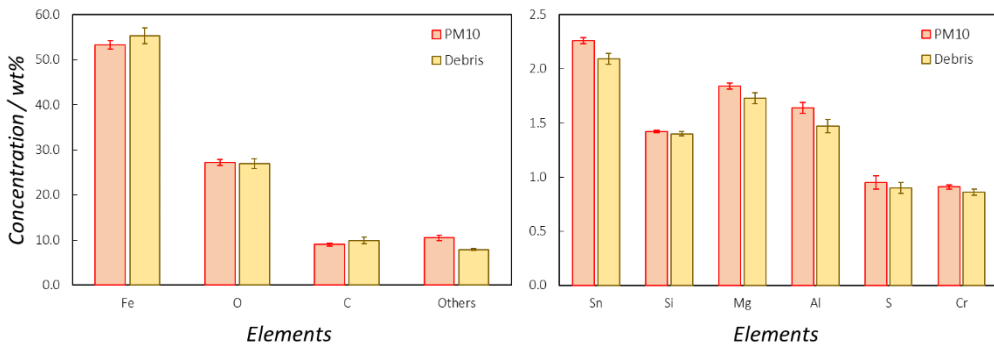


**Figure 7.14:** Comparison elemental concentrations as measured for PM<sub>10</sub> vs. Debris samples generated by LS/LM2 friction couple. Only elements with concentration higher than 0.5 wt% are reported. Error bars refer to the observed standard deviation ( $\pm$ SD).

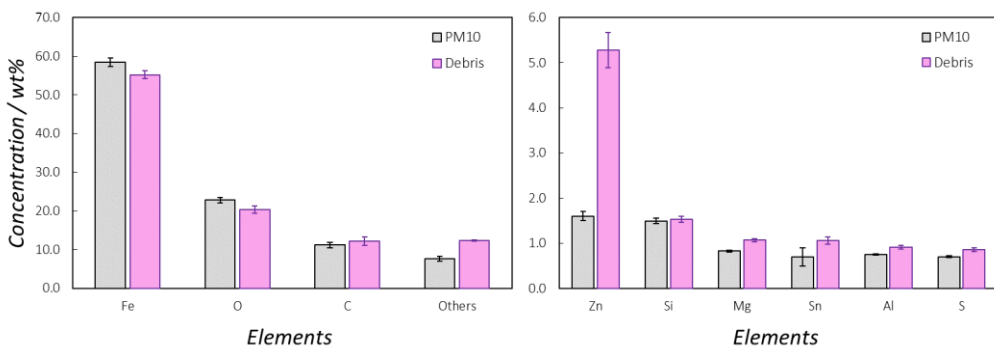


**Figure 7.15:** Comparison of elemental concentrations as measured for PM<sub>10</sub> vs. Debris samples generated by LS/LM4 friction couple. Only elements with concentration higher than 0.5 wt% are reported. Error bars refer to the observed standard deviation ( $\pm$ SD).



As far as the main constituents are concerned, no appreciable differences can be observed in the LS/LM1 samples, while only minor variability in the relative abundance of Fe, O, C and the other elements can be appreciated in samples from LS/LM2 and LS/LM3 couplings. Similarly, only limited concentration differences are detected for the secondary elements, with only one minor exception. In particular, Zn from LS/LM4 sample appears to preferentially accumulate in the coarser fraction.

Table 7.5 reports the comparison of all the elemental concentrations as measured for both PM<sub>10</sub> and Debris samples generated from each investigated friction couple belonging to *Category 2* (GCI BDs + IN FMs). Similarly to what already shown for samples from the first typology of coupling, Figures 7.16, 7.17 and 7.18 report graphically the direct comparison between the elemental concentrations of both main constituents and secondary elements for all the three investigated couplings.

	IN1				IN2				IN3					
	PM10	SD	Debris	SD	PM10	SD	Debris	SD	PM10	SD	Debris	SD		
Fe	68.3	1.5	71.2	1.5	Fe	66.7	0.9	64.5	0.7	Fe	64.8	0.5	64.7	2.3
O	19.0	1.0	15.9	1.3	O	22.3	0.5	20.7	0.5	O	23.9	0.3	21.4	1.4
C	6.4	0.6	2.2	1.1	C	4.5	0.6	6.0	0.2	C	4.2	0.2	2.7	0.7
Si	2.12	0.07	2.3	0.9	Si	2.67	0.04	2.2	0.1	Si	2.8	0.1	2.6	0.1
Al	0.90	0.06	0.9	0.1	Al	1.12	0.04	0.8	0.1	Al	1.06	0.03	1.02	0.09
Mo	0.7	0.1	0.6	0.2	Zn	1.05	0.09	4.2	0.9	Zn	0.93	0.07	5.4	1
Zn	0.57	0.06	4.8	1.0	K	0.60	0.01	0.48	0.07	K	0.86	0.02	0.86	0.05
Mn	0.56	0.02	0.54	0.01	Mn	0.54	0.02	0.51	0.03	Mn	0.48	0.04	0.50	0.04
K	0.49	0.01	0.50	0.06	Cu	0.19	0.02	0.16	0.03	Ti	0.33	0.03	0.26	0.03
S	0.44	0.04	0.41	0.08	Cr	0.18	0.01	0.16	0.02	S	0.20	0.02	0.24	0.03
Sn	0.20	0.05	0.31	0.08	S	0.16	0.01	0.18	0.01	Cu	0.20	0.05	0.22	0.08
Cu	0.16	0.03	0.17	0.02	Others	0.00	-	0.06	0.02	Cr	0.13	0.02	0.14	0.04
Cr	0.15	0.02	0.18	0.02										

**Table 7.5:** Comparative summary of the elemental concentrations as measured by EDXS analysis for PM<sub>10</sub> and Debris samples obtained from IN1, IN2 and IN3 FCs. The concentrations are average of five independent observations and are followed by the corresponding standard deviations (SD).

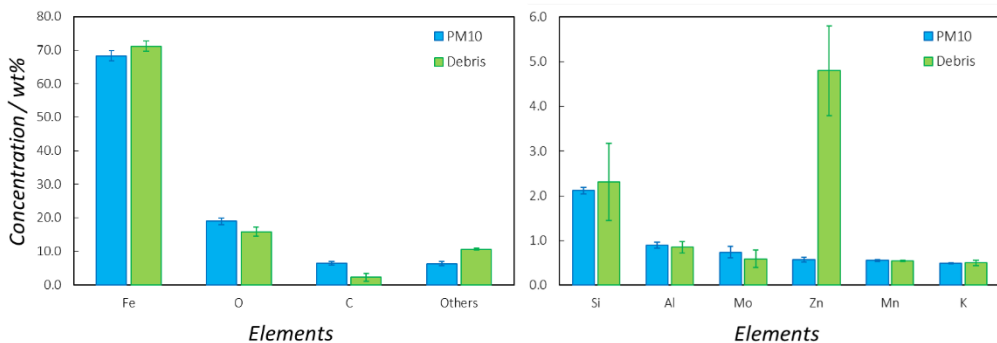


**Figure 7.16:** Comparison of elemental concentrations as measured for PM<sub>10</sub> vs. Debris samples generated by IN1 friction couple. Only elements with concentration higher than 0.5 wt% are reported. Error bars refer to the observed standard deviation ( $\pm$ SD).

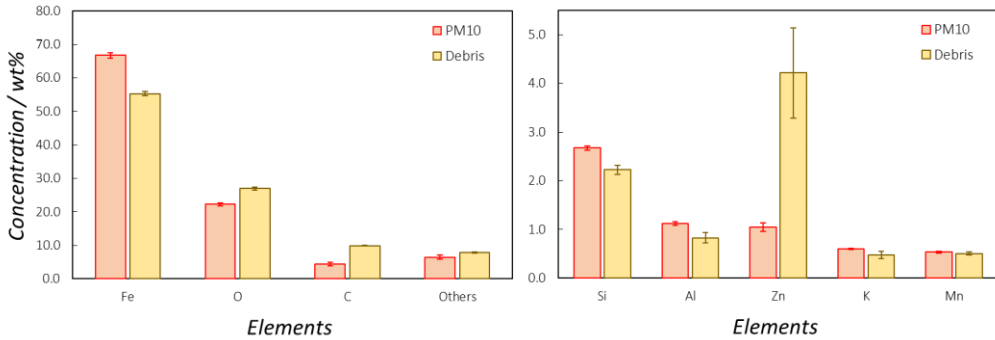


**Figure 7.17:** Comparison of elemental concentrations as measured for PM<sub>10</sub> vs. Debris samples generated by IN2 friction couple. Only elements with concentration higher than 0.5 wt% are reported. Error bars refer to the observed standard deviation ( $\pm$ SD).

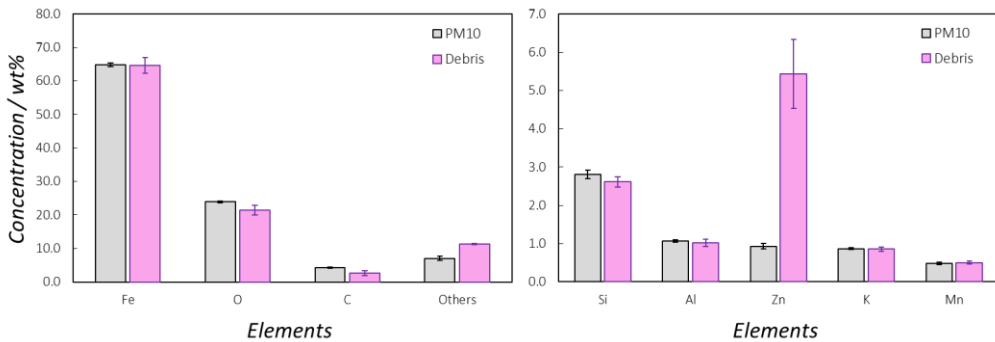


**Figure 7.18:** Comparison of elemental concentrations as measured for PM<sub>10</sub> vs. Debris samples generated by IN3 friction couple. Only elements with concentration higher than 0.5 wt% are reported. Error bars refer to the observed standard deviation ( $\pm$ SD).

Differently from what observed in samples from the previous couplings, PM<sub>10</sub> and Debris particulates generated by *Category 2* FCs show higher tendency to differ. Slightly major variability is also observed within the set of secondary and minor elements. Notably, as observed in the case of LS/LM4 samples, all three pairs of samples from *Category 2* FCs show clear evidence of preferential segregation of Zn to the coarser fractions. This behavior might be likely linked to the specific physico-chemical nature of the Zn-bearing compounds in the specific friction couples. For example, metallic Zn and brass platelets or fibers of big dimensions can reasonably be more subject to follow to the ground by direct abrasion from the tribological interface, in respect with ZnO and ZnS powders of finer granulometry. Thus, depending on the specific friction composite formulation, Zn (and other metallic species) could possibly concentrate more in the Debris fraction than in the corresponding PM<sub>10</sub> emission. This might have a direct impact on the correlation

between chemical composition of a specific friction couple emission and the corresponding toxicological behavior, since metals such Zn and Cu are well known to be hazardous towards several environment and biological systems.<sup>[21-22]</sup> For instance, assessing aquatic toxicology with the chemical composition of PM<sub>10</sub> samples with poorer concentrations of Zn in respect to the material possibly falling to the ground may lead to false negative results or underestimation errors. Conversely, assessing human cell toxicology by correlation with the chemical composition of Debris material enriched with metallic species, might lead to false positive results or overestimating errors.

As far as the main constituents are concerned, more pronounced differences in the Fe vs. O (Fe/O ratio) and main constituents vs. secondary elements (M/S ratio) are evident in particulates from *Category 2* in respect with the counterpart from *Category 1*. This can be observed more in detail in Table 7.6, which summarizes all these ratios for the six investigated samples.

	LS/LM1		LS/LM2		LS/LM4	
	PM10	Debris	PM10	Debris	PM10	Debris
Fe	54.6	55.3	53.3	53.7	58.4	55.2
O	27.5	26.9	27.2	27.4	22.8	20.3
C	10.1	9.9	9.0	8.9	11.2	12.2
Others	7.8	7.9	10.5	10.1	7.6	12.3
Fe/O	2.0	2.1	2.0	2.0	2.6	2.7
M/S	11.8	11.7	8.5	8.9	12.2	7.1

	IN1		IN2		IN3	
	PM10	Debris	PM10	Debris	PM10	Debris
Fe	68.3	71.2	66.7	64.5	64.8	64.7
O	19.0	15.9	22.3	20.7	23.9	21.4
C	6.4	2.2	4.5	6.0	4.2	2.7
Others	6.4	10.7	6.5	8.8	7.0	11.3
Fe/O	3.6	4.5	3.0	3.1	2.7	3.0
M/S	14.7	8.4	14.4	10.3	13.3	7.9

**Table 7.6:** Comparative summary of ratios of interest (Fe/O and M/S) for the investigated pairs of PM<sub>10</sub> and Debris particulates.

These differences are reasonable if considering both the tribological mechanism of the investigated friction couples and the surface areas of the corresponding collected particulates. In particular, if more direct abrasion is observed, leading to the generation of Debris particulates characterized by significantly higher amount of coarser particles (such in the case of *Category 2* FCs), overall higher Fe/O are observed. In addition, also

higher disproportion of the same Fe/O ratio is detected between a specific PM<sub>10</sub> sample and the corresponding Debris material. Conversely, when the overall emission mechanism is more characterized by adhesive wear and tribo-oxidation, leading to a more uniform distribution of finer particles in the Debris samples, lower differences are observed within the group of the main constituents: therefore both Fe/O and M/S ratios are similar in the PM<sub>10</sub> emission and in the corresponding Debris. Notably, the eventual discrepancies in the ratio between the main constituents ([Fe] + [O] + [C]) vs. the other elements (M/S ratio) can be used as index to discriminate between different tribological characteristics also within the single category of friction couple. As can be seen in the case of *Category 1* FCs, two friction couples generate PM<sub>10</sub> and corresponding Debris emissions with closely similar M/S ratios, while LS/LM4 Debris sample exhibits significantly higher amount of material arising from the FM consumption when compared to the corresponding PM<sub>10</sub> particulate. Therefore, LS/LM4 appears to be characterized by a more pronounced abrasion level in respect with the LS/LM1 and LS/LM2 friction couples. When looking at samples from *Category 2*, they all show significant differences of M/S ratios when assessing the PM<sub>10</sub> emission in comparison to the corresponding Debris material. As just discussed, this testifies a pronounced direct abrasion tendency in their wear mechanism.

#### 7.4. Summary

The investigations reported in this chapter clearly show how the dimensional fraction of brake emissions can have influence on their chemical composition. As widely discussed in *Chapter 4* the chemical composition of brakes emissions is determined in first place by the materials composing the friction couple, as well as by their tribological characteristics. However, the results here reported show how the composition can be modulated by the dimensional fraction in which a specific emission is collected and analyzed. This is particularly evident when comparing ultra-fine (nanometric) with PM<sub>10</sub> (micrometric) particulates. The reported elemental and phase analyses are in agreement in identifying two main compositional trends: *i*) a decreasing Iron/Oxygen ratio, *i.e.* an overall higher degree of Iron oxidation, when moving towards the finer fractions; and *ii*) a significantly higher concentration of Carbon in the ultra-fine particulates. These findings suggest that, in spite of presenting overall similar compositional profiles in terms of constituent elements, particulates of different dimensional ranges exhibit distinct elemental and phase compositions, mostly in terms of relative abundance of constituents compounds. In addition, it also showed how the chemical characterization of different dimensional fractions of specific emissions can bring deeper insights into the evaluation of their tribological characteristics, at least on a comparative level. Taking all the obtained results on a more general level, it is also to conclude that the chemical information arising from coarser brake emissions fractions should not be used when

specifically assessing the ecological and toxicological behavior of finer emissions generated by the same source, and *vice versa*.

## References

- [1] World Health Organization, “WHO Global Air Quality Guidelines: Particulate Matter (PM<sub>2.5</sub> and PM<sub>10</sub>), Ozone, Nitrogen Dioxide, Sulfur Dioxide and Carbon Monoxide”, *World Health Organization*, **2021**, <https://apps.who.int/iris/handle/10665/345329>.
- [2] European Environmental Agency, “Europe’s Air Quality Status - 2022”, *EEA*, **2022**, Online Version.
- [3] G. Straffelini, S. Gialanella, “Airborne Particulate Matter from Brake Systems: An assessment of the Relevant Tribological Formation Mechanisms”, *Wear*, **2021**, 478-479, 203883, <https://10.1016/j.wear.2021.203883>.
- [4] J. Kukutschova, P. Filip, “Review of Brake Wear Emissions, in: F. Amato (Ed.), Non Exhaust Emissions: an Urban Air Quality Problem for Public Health, Academic Press, Elsevier, San Diego, **2018**.
- [5] J. Kukutschova, V. Roubicek, K. Malachova, Z. Pavlickova, R. Holusa, *et.al.*, “Wear Mechanism in Automotive Brake Materials, Wear Debris and its Potential Environmental Impact, *Wear*, 267, **2009**, 807–817, <https://doi.org/10.1016/j.wear.2009.01.034>.
- [6] P. Chandra Verma, L. Menapace, A. Bonfanti, R. Ciudin, S. Gialanella, *et.al.*, “Braking Pad-Disc System: Wear Mechanisms and Formation of Wear Fragments, *Wear*, **2015**, 322– 232, 251–258, <https://doi.org/10.1016/j.wear.2014.11.019>.
- [7] B.S. Joo, Y.H. Chang, H.J. Seo, H. Jang, “Effects of Binder Resin on Tribological Properties and Particle Emission of Brake Linings”, *Wear*, **2019**, 434–435, 202995, <https://doi.org/10.1016/j.wear.2019.202995>.
- [8] Z. Men, X. Zhang, J. Peng, J. Zhang, T. Fang, *et.al.*, “Determining Factors and Parameterization of Brake Wear Particle Emission”, *Journal of Hazardous Materials*, **2022**, 434, 128856, <https://doi.org/10.1016/j.jhazmat.2022.128856>.
- [9] G. Oberdörster, E. Oberdörster, J. Oberdörster, “Nanotoxicology: An Emerging Discipline Evolving from Studies of Ultrafine Particles”, *Environmental Health Perspectives*, 113(7), **2005**, 823-839, <https://doi.org/10.1289/ehp.7339>.
- [10] A.D. Maynard, D.B. Warheit, M.A. Philbert, “The New Toxicology of Sophisticated Materials: Nanotoxicology and Beyond”, *Toxicological Sciences*, 120(S1), **2001**, 109–129, [doi:10.1093/toxsci/kfq372](https://doi.org/10.1093/toxsci/kfq372).
- [11] A.V. Singh, P. Laux, A. Luch, C. Sudrik, S. Wiehr, *et.al.*, “Review of Emerging Concepts in Nanotoxicology: Opportunities and Challenges for Safer Nanomaterial Design”, *Toxicology Mechanisms and Methods*, 29(5), **2019**, 378–387, <https://doi.org/10.1080/15376516.2019.1566425>.
- [12] nPETS Project, EU-H2020, Grant Agreement ID: 954377, [doi:10.3030/954377](https://doi.org/10.3030/954377).
- [13] A. Mancini, B. Tsyupa, M. Federici, M. Leonardi, *et.al.*, “Chemical Characterization of Nanoparticle Emissions from Brakes - The nPETS Project,” *SAE Technical Paper*, **2022**, 2022-01-1182, [doi:10.4271/2022-01-1182](https://doi.org/10.4271/2022-01-1182).
- [14] G. Perricone, J. Wahlstrom, U. Olofsson, “Towards a Test Stand for Standardized Measurements of the Brake Emissions”, *Proc. I. Mech. E., Part D: J. Automobile Engineering*, **2015**, 1–8.

- [15] G. Perricone, M. Alemani, I. Metinoz, V. Matejka, V., *et.al.*, “Towards the Ranking of Airborne Particle Emissions from car Brakes – a System Approach”, *Proc. I. Mech. E., Part D: J. Automobile Engineering*, **2016**, 1-17, 2016.
- [16] M. Mathissen, J. Grochowicz, C. Schmidt, R. Vogta, F.H. Farwick zum Hagen, *et.al.*, “A Novel Real-World Braking Cycle for Studying Brake Wear Particle Emissions”, *Wear*, **2018**, 414–415, 219–226, <https://doi.org/10.1016/j.wear.2018.07.020>.
- [17] Particle Measurement Programme (PMP) Informal Working Group, Informal document GRPE\_81\_12, 81st GRPE, 9-11 June **2020**, Agenda Item 7.
- [18] R.C. Dante, “Handbook of Friction Materials and Their Applications”, 1st Ed., Elsevier, The Woodhead Publishing, **2015**.
- [19] A. Mancini, B. Tsyupa, S. Pin, F. Bertasi, *et.al.*, “Novel Approaches for Physico-Chemical Characterization of Brake Emissions”, *EuroBrake2021 Technical Paper*, **2021**, EB2020-EBS-031.
- [20] B. Tsyupa, M. Bandiera, M. Federici, M. Leonardi, A. Bonfanti, F. Bertasi, A. Mancini, “Comparative Study of Size Distribution and Chemical Composition of Emissions from Low Steel and NAO Friction Materials”, *EuroBrake2022 Technical Paper*, **2022**, EB2022-EBS-021.
- [21] C.A. Flemming, J.T. Trevors, “Copper Toxicity and Chemistry in the Environment: a Review”, *Water, Air, and Soil Pollution*, 1989, 44, 143–158, <https://doi.org/10.1007/BF00228784>.
- [22] R. Eisler, “Zinc Hazards to Fish, Wildlife, and Invertebrates: A Synoptic Review”, *Contaminant Hazard Reviews Report 26 ; Biological Report 10*, 1993, U.S. Department of the Interior, Fish and Wildlife Service, <https://pubs.er.usgs.gov/publication/5200116>.

## 8. Influence of the Driving Conditions

*As mainly discussed in Chapter 3, the reproducible and reliable generation and characterization of non-exhaust emissions generated by brakes is of fundamental importance in order to provide correct information for source apportionment studies as well as for their toxicological and environmental assessment. Nowadays, the best option to obtain samples of  $PM_{10}$  emissions composed only by material worn from the tribological interface, i.e. the braking disc (BD) and the friction material (FM) rubbing surfaces, is to sample them on suitable collection substrates at a dedicated brake dynamometer bench, during a standard braking test cycle. In particular, the use of enclosed dyno-bench is necessary for excluding other spurious contributions from the environment, while defined test cycles are necessary to simulate standardized driving conditions. Nevertheless, different braking cycles are usually characterized by different overall temperature profiles or energy parameters, which in the end have significant influence on the wear and the oxidation of the materials involved in the tribological event. Thus, when collection is performed at the dynamometric bench, the chemical composition of the  $PM_{10}$  emissions is expected to be influenced and modulated by the overall temperature profile of a specific test cycle. At this regard, the study here reported investigates the difference in terms of chemical composition of  $PM_{10}$  samples generated by two tribo-couples (standard cast iron BD coupled respectively with standard ECE R90 FM and prototypal FM based on inorganic binder) during the 3h-LACT and the WLTP-Brake test cycles. More in detail, a wide physico-chemical characterization performed by SEM/EDXS and XRD analysis is used to unveil how braking cycles influence both the elemental and phase composition of the generated emissions. This chapter provides useful insights regarding the correlation between driving conditions, relative consumption of the tribological interface and chemistry of the emitted particulates.*

### 8.1. Aim of the study

For all the reasons already reported and discussed, in the past years, strong technological and scientific efforts have been carried out in order to study the emissions generated by brakes. In particular, reliable protocols for particulates collection and dimensional measurement have been developed, thus gaining a sound general understanding of the physico-mechanical processes involved in the generation of brakes emissions.<sup>[1-7]</sup> Recently, the chemical characterization of the brake emissions is also being more frequently and deeply investigated, representing a necessary bridging stone between emission level studies, toxicological/environmental assessments and source apportionment evaluations.<sup>[8-11]</sup> Independently of the aim of the specific researches, the most commonly adopted experimental approach to study the brake emissions, is to collect them at a suitably designed inertia dynamometric bench, during tests performed in controlled conditions.<sup>[1,2,12]</sup> Brakes dyno-benches are mechanical devices simulating

one car semi-axis corner: they represent a far less complicated experimental design than the usage of a whole vehicle, while maintaining a suitable level of complexity and representativeness of the target system. Specifically, dyno-benches are able to reproduce energy indexes of real vehicles, such as speed, inertia, pressure, kinetic energy, etc. They are commonly employed in the characterization of braking system performances via the repetition of standardized sequences of braking events. In spite of being potentially very complicated and time-consuming, these sequences, or test cycles, can be easily implemented at the dyno-bench via software control. For this reason, test cycles at the dynamometer platform usually lead to more stable and reproducible outputs in respect with road tests. In addition, as far as emission studies are concerned, dyno-benches are also necessary for looking exclusively at the particulates generated from the braking device, excluding other spurious contributions from the environment.

In order to be diagnostic, dyno-bench emission tests have to be tailored as much relatable and scalable to the real general driving conditions as possible. This is especially true when emission profiles are the main target of the study. For this reason, in recent times, several different test cycles specifically dedicated to the generation of particulates have been developed. They usually mimic overall driving conditions in ensembles of different situations, such as urban, sub-urban, rural and highway traffic situations. However, different test cycles can easily lead to incomparable results (even if tests are performed on the same friction couple, mounted on the same braking device), since the energy indexes and the temperature profiles can strongly differ from cycle to cycle. Local temperature at the tribological interface is in fact one of the main variable affecting the mechanical wear and the tribo-oxidation of the surfaces of both the braking disc and the friction material, thus having a great influence in the generation of braking emissions both in terms of particulate dimensions and emission factors.<sup>[1,2]</sup> In addition, different local temperatures experienced by the friction couple (BD+FM) might be expected to generate particulates with different chemical composition: this is especially reasonable when considering the distribution of iron oxidation compounds, as well as in the case of sulfides oxidation or carbon-based material pyrolysis. At this regard, the study here reported is meant to provide a specific insight into the differences in the chemical composition of PM<sub>10</sub> particulates generated by the same starting materials composing the friction couple, but during two different braking cycle. Thus, the results here reported are meant to underline the importance of selecting one reference test cycle in order to assure comparability also in the chemical composition of the brake emissions. This is a hard requirement especially when considering the final aim of providing reliable chemical characterization as starting point for toxicological and environmental assessments. In addition, these results are also meant to provide a first glance into the correlation between the chemistry of brake emissions and the driving, *i.e.* braking, conditions.



## 8.2. Experimental

All the experimental details as well as the materials and methodologies used in the this section are briefly summarized in the following paragraphs. More detailed information can be also found in the references reported along the experimental sections as well as in *Chapter 2*.

### 8.2.1. Materials

Two different friction couples (*i.e.* combinations of braking disc [BD] and friction material [FM]) are used as test subjects for this study. The first one, labeled FC1, is composed by a fully pearlitic grey cast-iron (GCI) braking disc (BD) and two pads of a Cu-free ECE R90 Low Steel (LS) friction material (FM1). The second one, named FC2, is made by the coupling of the same typology of BD with two pads having prototypal friction material based on inorganic binders (FM2). Nominal compositions for all the components are reported in Table 6.1. For each bench test, new braking disc and pads are used.

BD		FM1		FM2	
Element	[wt%]	Element	[wt%]	Element	[wt%]
C	3.8	C	31.3	Fe	32.6
Si	1.9	Fe	23.0	O	17.2
Mn	0.5	O	13.6	C	14.5
Cu	0.2	Zn	8.2	Si	11.0
Cr	0.1	Mg	5.5	Al	9.3
Fe	<i>balance</i>	Al	4.1	Sn	5.0
Others	<i>traces</i>	Sn	3.7	Mo	4.8
		Cr	3.0	S	4.5
		S	3.0	Bi	0.9
		Si	2.2	Mn	0.1
		Ca	1.0	Others	<i>traces</i>
		Bi	0.8		
		K	0.3		
		Mn	0.1		
		Others	<i>traces</i>		

**Table 6.1:** Nominal composition of the starting materials composing the two used friction couples.

### 8.2.2. Braking Cycles

PM<sub>10</sub> samples are collected at a dyno-bench suitably designed for emissions collection during tests performed in controlled conditions. The specific design of the dyno-bench is described in detail in the reported literature.<sup>[12,13]</sup> The two investigated particulates are respectively sampled during 3h-LACT and WLTP-Brake test routines. The two cycles are already introduced and described in *Chapter 2*. For both the tests the braking corner is composed by: *i*) a four piston fixed Aluminum caliper with pistons diameter of 44 mm; *ii*) a fully pearlitic vented cast-iron braking disc with diameter of 342 mm and 32 mm height (distance between internal and external braking surfaces); and *iii*) a couple of pads with surface of 89.1 cm<sup>2</sup>. Thus, the combination of the pads and braking disc geometry leads to an effective radius of 136.5 mm. The 3h-LACT is a temperature driven test accounting for 217 braking events performed in a run during approximately 3 hours. It is historically one of the first cycles proposed in the dedicated literature as reference cycle.<sup>[14]</sup> On the other hand, the WLTP-Brake is a time-controlled cycle composed by 303 brake events divided into ten trips. The emission test duration is about 7.5 hours, comprehensive of the cooling phases between trips. It is nowadays most commonly used for sake of reference in the study of brake emissions, since it is based on a wider database of traffic behaviors in the European region, thus being considered more representative of a global ensemble of braking profiles of standard EU driving conditions.<sup>[15]</sup> Visual comparison of the two cycles speed profiles is reported in Figure 8.1 while Table 8.2 provides additional comparative specifications.

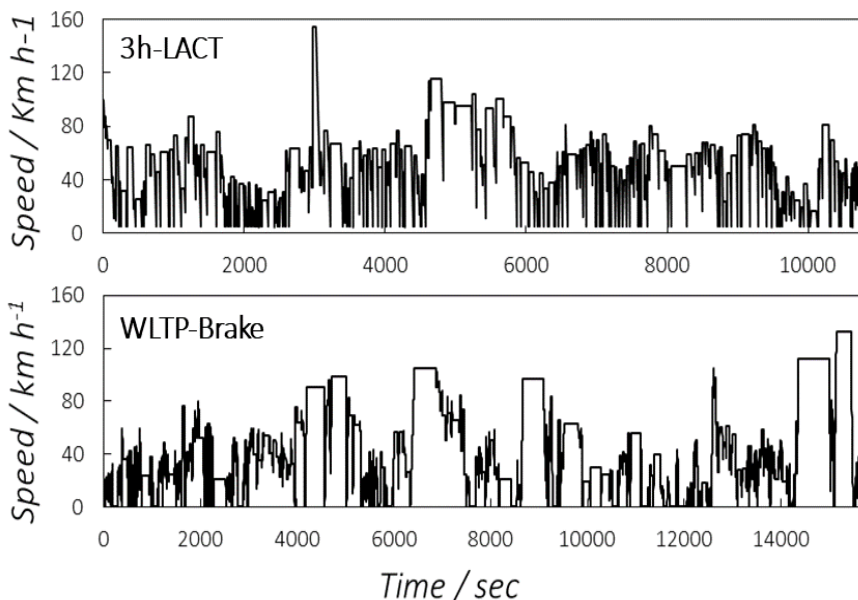


**Figure 8.1:** Speed profiles of the two braking cycle compared in this study.

	3h-LACT	WLTP-Brake
<b>Duration</b>	approx. 3h	approx. 7.5h
<b>Average Initial Speed</b>	53.6 km/h	41.5 km/h
<b>Deceleration</b>	0.2-2.9 m s <sup>-2</sup>	0.49-2.18 m s <sup>-2</sup>
<b>IBT</b>	54-187°C	30-175°C
<b>Number of Stops</b>	217	303
<b>Total Distance</b>	145 km	192 km

**Table 8.2:** Comparative summary of parameters of interest for the 3h-LACT and WLTP-Brake cycles.

As can be observed in Table 8.2, WLTP-Brake routine is overall longer than the 3h-LACT test, accounting for more stops and simulating longer run. On the other hand, 3h-LACT has globally higher decelerations, dissipating consequently more kinetic energy. In addition, due to the average lower energy indexes and the time imposed-control of the cycle, WLTP-Brake cycle provides usually more efficient cooling of the tribological interface, thus developing overall lower temperature profiles. One further minor and case specific difference between the two tests reported in this study is represented by the inertia: for the 3h-LACT test it is used an inertia of 66.80 kg m<sup>2</sup>, while for the WLTP-Brake routine it is used a slightly higher inertia of 72.67 kg m<sup>2</sup>. The WLTP-Brake test inertia is in fact calculated following the more recent guidelines from the Particle Measurement Programme (PMP) Informal Working Group<sup>[16]</sup>, *i.e.* reducing the nominal vehicle inertia by a 13% factor in order to account for the parasite losses and considering a cargo of 1.5 passengers.

### 8.2.3. Samples Collection and Preparation

During the dyno-bench tests, a controlled particle-free air flux enters the brake enclosure. The air flux was set at 850 m<sup>3</sup> h<sup>-1</sup> for the 3h-LACT and at 65 m<sup>3</sup> h<sup>-1</sup> for the WLTP-brake cycle. More in detail, the flux value for the WLTP-Brake test is chosen in order to hit the temperature targets as suggested by the more recent guidelines from the PMP Working Group<sup>[16]</sup>, prior a specifically tailored calibration run carried out before the bedding phase. For both tests, the flux is filtered through a HEPA-H13 filter which ensures an average filtration efficiency higher than 99.95%. The air flux serves a double aim: it cools down the brake system during the testing cycle and carries the particles generated during the braking test to the particles measurement and collection devices. The collection of the PM emissions is carried out by four different isokinetic sampling-probes, equipped with knife-ended nozzles to ensure a high efficiency sampling. As far as particulates analyzed in this study are concerned, a filter holder hosting a high efficiency 47 mm diameter cellulose filter is connected with one of the isokinetic probes to collect together all the particles with diameter lower than 10 μm. A Dekati<sup>TM</sup> PM<sub>10</sub>

cyclone is placed between the sampling probe and the filter holder in order to ensure the removal of the particles with diameter larger than 10  $\mu\text{m}$ . The four investigated particulates are stripped from the collection substrates by sonication in 5 mL of isopropyl alcohol at 35 kHz for 10 minutes. The suspended particles are then recollected by centrifugation at 3000 rpm for 5 minutes and finally dried overnight in mild vacuum conditions (20 mbar) before the chemical analysis (please refer to *Chapter 2* for further details).

#### 8.2.4. SEM/EDXS Analysis

After drying, the  $\text{PM}_{10}$  powders are directly deposited on Aluminum stubs covered with carbon tape for electronic microscopy, without any further manipulation. Energy Dispersive X-Ray Spectroscopy is used as probe to investigate the elemental composition of all the collected samples. The analysis is carried out by the mean of the Zeiss MA EVO10 scanning electron microscope, equipped with a 10  $\text{mm}^2$  active area INCA X-act silicon-drift detector (Oxford Instrument). For each powder sample, five areas of approximately 400 x 300  $\mu\text{m}$  are analyzed with acquisition time of 540 sec and beam intensity of 300 pA. The elemental concentrations obtained in each region of interest are statistically averaged in order to obtain final compositional results. The experimental emission spectra are acquired at the instrument ideal working distance of 8.5 mm (gun to sample surface). The elemental composition is probed by back-scattered electrons (BSE) in order to maximize the interaction volume of the incident beam with the sample.

#### 8.2.5. XRD Analysis

Phase composition of the collected samples is investigated by the mean of X-Ray Diffraction analysis, performed at the MCX beamline<sup>[17]</sup> at Elettra-Trieste synchrotron during ring operation at 2.4 GeV. XRD patterns are acquired at 15 keV and  $\lambda = 0.0826(1)$  nm, in Debye-Scherrer geometry, with beam spot kept at 1.0 x 0.3 mm. About 1 mg of  $\text{PM}_{10}$  powders are gently inserted and compacted inside standard glass Mark-tube for XRD diffraction experiments with external diameter of 0.2 mm and wall thickness of 0.01 mm (Hilgenberg), filling the capillaries for at least 15 mm in height. The capillaries are centered inside a 4-circle Huber goniometer and spinned at 3000 rpm during the measurements. The detection of the diffracted beam is carried out by a high-count rate fast scintillator counter equipped with a pair of slits with a vertical aperture of 0.3 and 0.4 mm, respectively. XRD patterns are acquired in the  $2\theta$  angular range of 3-45°, with 0.01° steps and acquisition speed of 1 sec/step. The phase identification is carried out via the PDF4+ 2022 crystallographic database (ICDD)<sup>[18]</sup>, while the phase analysis is performed by the mean of the PDXL software suite (Rigaku<sup>[19]</sup>), using as fit variables only profile and cell parameters.

### 8.3. Results

The obtained results in terms of elemental and phase composition for the collected PM<sub>10</sub> particulates, as well as their description and specific discussion, are reported in the following paragraphs. Particular attention is paid in underlining the compositional differences detected between the samples generated respectively during the two different tests.

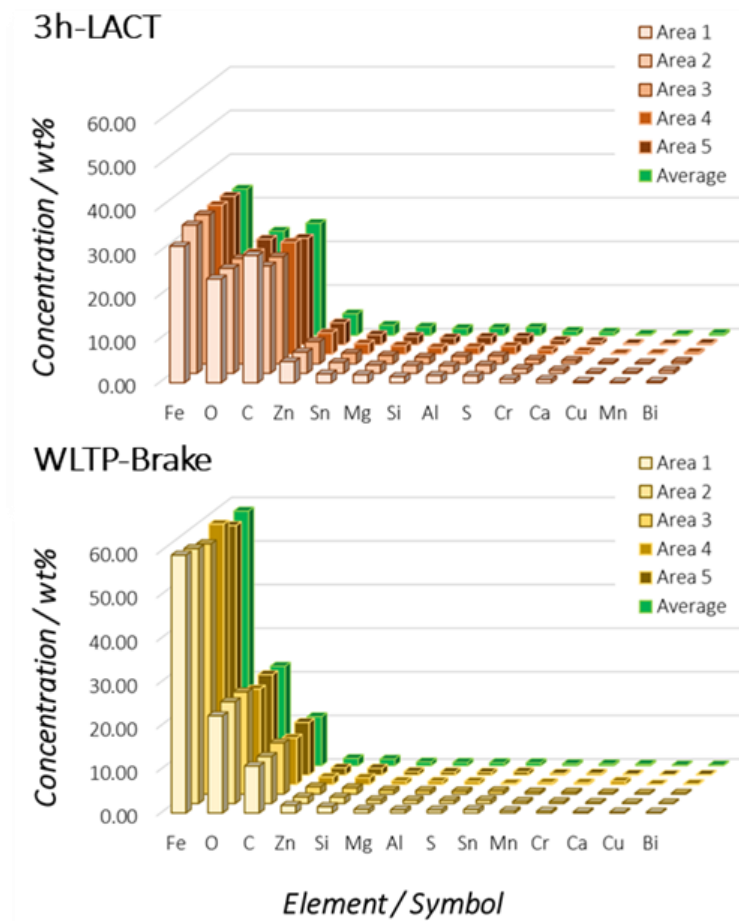
#### 8.3.1. Elemental Composition

Table 8.3 summarizes the average elemental compositions of the two PM<sub>10</sub> samples from FC1 friction couple, generated respectively during 3h-LACT and WLTP-Brake test cycles. Figure 8.2 shows the elemental distribution in the two different cases. As it is possible to see, in both the particulates the elemental composition is largely dominated by three main elements only, which are Iron, Oxygen and Carbon: they account together for about the 90 wt% of the total emission mass. This observation is in well in agreement with the results reported in *Chapter 4* for similar friction couples (*Category 1*: GCI BDs + LS/LM FMs). Iron is largely due to the consumption of the BD braking surface, but also a minor contribution from Fe-based compounds from the FM, such as Iron powders, Steel fibers, Iron Sulfides and Chromites, has to be taken into account.

FC1 Element	3h-LACT		WLTP-Brake	
	[wt%]	SD	[wt%]	SD
Fe	33.5	1.2	58.4	1.1
O	23.9	0.4	22.8	0.7
C	25.7	2.1	11.2	0.7
Zn	4.9	0.1	1.7	0.1
Sn	2.3	0.2	0.7	0.2
Mg	1.92	0.05	0.83	0.02
Si	1.6	0.2	1.49	0.06
Al	1.71	0.07	0.75	0.02
S	1.81	0.09	0.70	0.02
Cr	0.98	0.08	0.42	0.01
Ca	0.75	0.04	0.42	0.01
Cu	0.26	0.06	0.3	0.2
Mn	0.22	0.04	0.46	0.03
Bi	0.5	0.1	0.16	0.02

**Table 8.3:** Elemental composition of PM<sub>10</sub> powders from FC1 measured by EDXS (elements with concentration lower than 0.1 wt% are not listed for sake of brevity). Final composition results are

averaged over five different measurement areas for each sample. SD labels the standard deviation over the five different measurements.



**Figure 8.2:** Histogram elemental distribution graphs for the PM<sub>10</sub> particulates generated by FC1 during 3h-LACT test (top) and WLTP-Brake (bottom).

Similarly, Oxygen can be expected to be due in large extent to the tribo-oxidation of the metallic material at the tribological interface. However, minor but not negligible Oxygen contribution has to be ascribed to several compounds composing the FM composite, such as oxides, carbonates, alumino-silicates and organic resins. Finally, Carbon is largely due to the FM, which usually contains significant amounts of graphite, coke and phenolic resins, together with minor amounts of inorganic carbides and carbonates. In addition, minor contribution from graphite lamellae arising from the GCI BD worn material has also to be considered. All the other elements are detected in secondary or trace amounts, accounting together for slightly more than the 10 wt%: they are mainly due to the specific FM formulation. In spite of showing similar general compositional trends,

the two samples exhibit also important differences. Indeed, looking at the sum of the three main elements, it is clearly possible to observe that the PM<sub>10</sub> generated during the WLTP-Brake cycle has significantly higher content of Iron and lower content of Carbon in respect with its 3h-LACT counterpart. In addition, the Oxygen concentration is pretty similar in both the two particulates, making the overall Iron to Oxygen ratio higher in the case of the PM<sub>10</sub> produced in the 3h-LACT test in respect with the particulate generated during the WLTP-Brake cycle.

Table 8.4 and Figure 8.3 summarize respectively the elemental composition concentrations as measured for FC2, in similar fashion than the previously reported results for FC1. If compared with particulates generated by FC1, PM<sub>10</sub> samples produced by FC2 show significantly higher content of Iron and lower content of Carbon. This is due to the characteristics and the specific formulation of FM2: as previously described, this friction material adopts in fact an inorganic binder (silicates-based). Its Carbon content is therefore due only to the graphite and the coke lubricants, while organic Carbon from phenolic-based resins is completely avoided. In addition, the inorganic matrix of FM2 has intrinsically higher hardness in respect with the softer phenolic resin-based standard FM1 composite. Thus the higher hardness and abrasive power of the friction material generates in FC2 more direct abrasion of the disc braking surfaces, leading to an overall higher amount of Iron.

FC2 Element	3h-LACT		WLTP-Brake	
	[wt%]	SD	[wt%]	SD
Fe	54.08	1.29	68.28	1.54
O	23.71	1.03	18.95	1.02
C	6.53	0.84	6.32	0.55
Si	4.25	0.21	2.12	0.07
Al	3.02	0.13	0.90	0.06
Mo	2.40	0.24	0.74	0.13
S	1.77	0.09	0.44	0.04
K	1.51	0.03	0.49	0.01
Sn	0.80	0.07	0.20	0.05
Zn	0.72	0.08	0.57	0.06
Bi	0.45	0.11	0.12	0.03
Mn	0.42	0.04	0.56	0.02
Cu	0.20	0.07	0.16	0.03

**Table 8.4:** Elemental composition of PM<sub>10</sub> powders from FC2 measured by EDXS (elements with concentration lower than 0.1 wt% are not listed for sake of brevity). Final composition results are averaged over five different measurement areas for each sample. SD labels the standard deviation over the five different measurements.

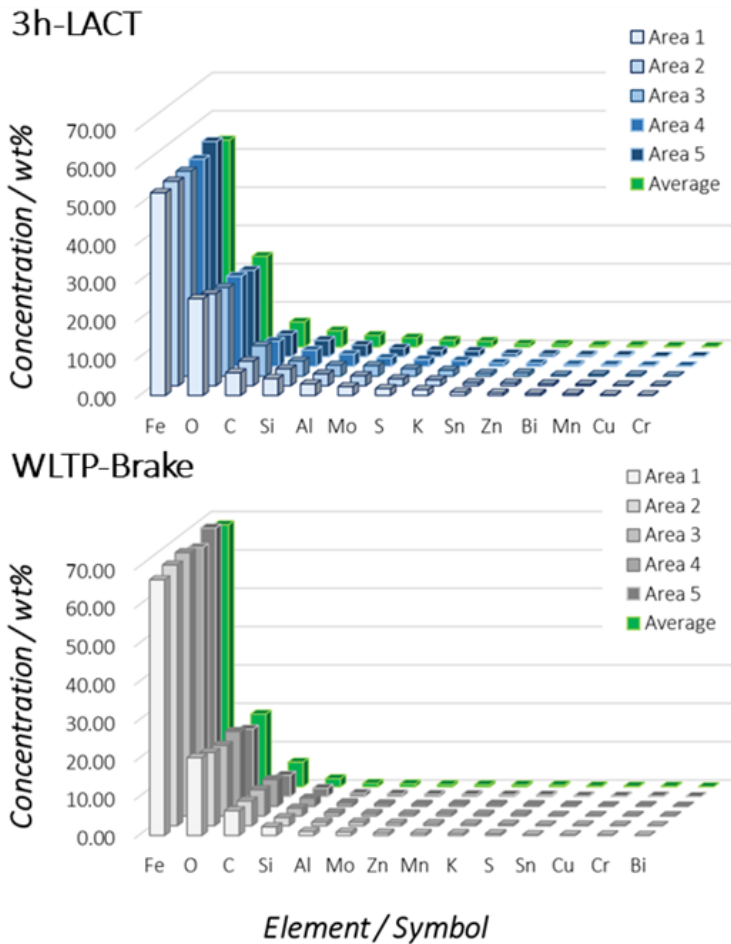


**Figure 8.3:** Histogram elemental distribution graphs for the PM<sub>10</sub> particulates generated by FC2 during 3h-LACT test (top) and WLTP-Brake (bottom).

This main difference apart, the general elemental composition of TC2 PM<sub>10</sub> samples shows similar trends than the one observed in FC1 particulates. Also in this case, the overall elemental composition is always dominated by the three main elements only: Iron, Oxygen and Carbon: they sum up for about the 90 wt% of the emission mass. Also in this case, the overall elemental distribution profile is well in agreement with those observed in *Chapter 4* for the corresponding typology of friction couples (*Category 2*: GCI BDs + IN FMs). As previously described, Iron is mainly due to the wear of the disc braking surfaces. Secondary contribution is also provided by the Iron-based compounds contained inside FM2. However, this is expected to be far lower than in FC1, due to the



higher relative consumption of BD in respect with the FC1 counterpart. Oxygen is indeed a mixed marker for the wear of both the two rubbing surfaces: it can be mutually due to the oxidation of the worn metallic material from both the tribological interface sides, than from oxides and silicates from the friction material. Finally, as previously described, Carbon arises mainly from the solid lubricants contained inside the friction material (graphite and coke) and, secondary, for inorganic carbides and carbonates eventually present inside the friction mix. Minor but not negligible contribution has also to be ascribed to the graphite lamellae inside the cast-iron composing BD. All the other elements are detected in minor or trace amounts and, also in this case, are mainly due to the specific friction material formulation. As already observed in FC1, also FC2 PM<sub>10</sub> powders show different distribution of the main elements when produced by different test cycles. In particular, Iron/Oxygen ratio is higher in the PM<sub>10</sub> sample produced during WLTP-Brake, while the overall amount of Carbon and secondary elements is higher in PM<sub>10</sub> particulate collected the from 3h-LACT test.

### 8.3.2. Phase Composition

X-Ray Diffraction analysis is used in order to investigate the phase composition of the collected PM<sub>10</sub> samples, and more in detail, to assess the crystalline fraction composing the particulates. At this regard, metallic Iron and Iron oxidized forms (namely the Magnetite-Fe<sub>3</sub>O<sub>4</sub> and the Hematite-Fe<sub>2</sub>O<sub>3</sub>) are well detected and easily identified in all the four investigated samples. The diffraction peaks of both the identified Iron oxides have always broader full width at half maximum (FWHM) in respect with the diffraction peaks from other phases, testifying their low crystallinity degree in respect with the metallic counterpart. Conversely, due to their very high crystallinity (*i.e.* sharper peaks), graphites are usually detected in all the particulates, even when contained in low amount. Since the collected and consequently analyzed particulates are of very modest amounts (about 1 mg of powder per XRD capillary), phases composed by elements in secondary or trace amount are in general hardly detectable, with the exception of the MoS<sub>2</sub> solid lubricant: this phase is composed by heavy elements, thus strongly interacting with the X-Rays, and shows in addition a very high level of crystallinity. Table 8.5 summarizes all the crystalline compounds detected through the phase identification carried out on the four investigated PM<sub>10</sub> samples, listing them together with their specific crystallographic database reference. The reported phases are consequently used as crystallographic theoretical models to fit the experimental XRD patterns in order to obtain the final phase composition of the crystalline fraction for the analyzed particulates, which is reported in Table 8.6. Examples of Rietveld refinement performed on the collected experimental data are reported in Figure 8.4, which shows the phase analysis for the FC2 PM<sub>10</sub> samples, collected respectively during the 3h-LACT and the WLTP-Brake cycles, as reference. As can be qualitatively observed in the two graphs

reported in Figure 8.4, the relative intensity ratio between the main Iron diffraction peak (at about 23.5°) and the main diffraction peaks of its oxides is higher in the case of the particulate produced during the WLTP-Brake test. As far as the Iron oxides are concerned, in both samples the Magnetite ( $\text{Fe}_3\text{O}_4$ ) is the more common polymorph, while the Hematite ( $\text{Fe}_2\text{O}_3$ ) is always detected in lower amount. In addition, secondary or trace phases, such as the Graphite or the Molybdenite, are easily observable only in the particulate generated during the 3h-LACT, while their signals remain weaker in the WLTP-Brake counterpart sample. The same considerations can be easily inferred in quantitative fashion by the observation of the phase analysis results as reported in Table 8.6. Notably, all the information arising from the analysis of the elemental composition on the four investigated samples are in excellent agreement with findings from the XRD analysis, and more in general, with all the observations previously reported in *Chapter 4* and *Chapter 5*.

Phase	Compound	Crystallographic Reference (ICDD)
$\text{Fe}_3\text{O}_4$	Magnetite	04-015-9120
$\text{Fe}_2\text{O}_3$	Hematite	04-015-7029
$\alpha\text{-Fe}$	Ferrite	04-014-0360
C	Graphite	00-041-1487
$\text{MoS}_2$	Molybdenite	01-077-1716

**Table 8.5:** Summary of the crystallographic reference used for phase identification and phase analysis (Database ICDD PDF4+ 2022).

Phase	3h-LACT / wt%	WLTP-Brake / wt%
<b>FC1</b>		
Iron ( $\alpha\text{-Fe}$ )	21.9(9)	26.6(7)
Magnetite ( $\text{Fe}_3\text{O}_4$ )	55.4(2)	48.9(9)
Hematite ( $\text{Fe}_2\text{O}_3$ )	14.5(2)	18.1(2)
Graphite (C)	8.1(2)	6.5(4)
$R_{wp}$	5.80%	4.37%
<b>FC2</b>		
Iron ( $\alpha\text{-Fe}$ )	24.6(7)	40.1(9)
Magnetite ( $\text{Fe}_3\text{O}_4$ )	55.0(2)	45.7(9)
Hematite ( $\text{Fe}_2\text{O}_3$ )	12.8(2)	9.2(7)
Graphite (C)	5.4(9)	4.7(9)
Molybdenite ( $\text{MoS}_2$ )	2.2(2)	0.4(1)
$R_{wp}$	7.93%	6.10%

**Table 8.6:** Summary results of the phase analysis.  $R_{wp}$ , is a goodness and reliability of fit parameter. Estimated standard deviations (*esd*) are reported between brackets and refer to the last significant digit. All the concentration results are reported in weight percentage [wt%].

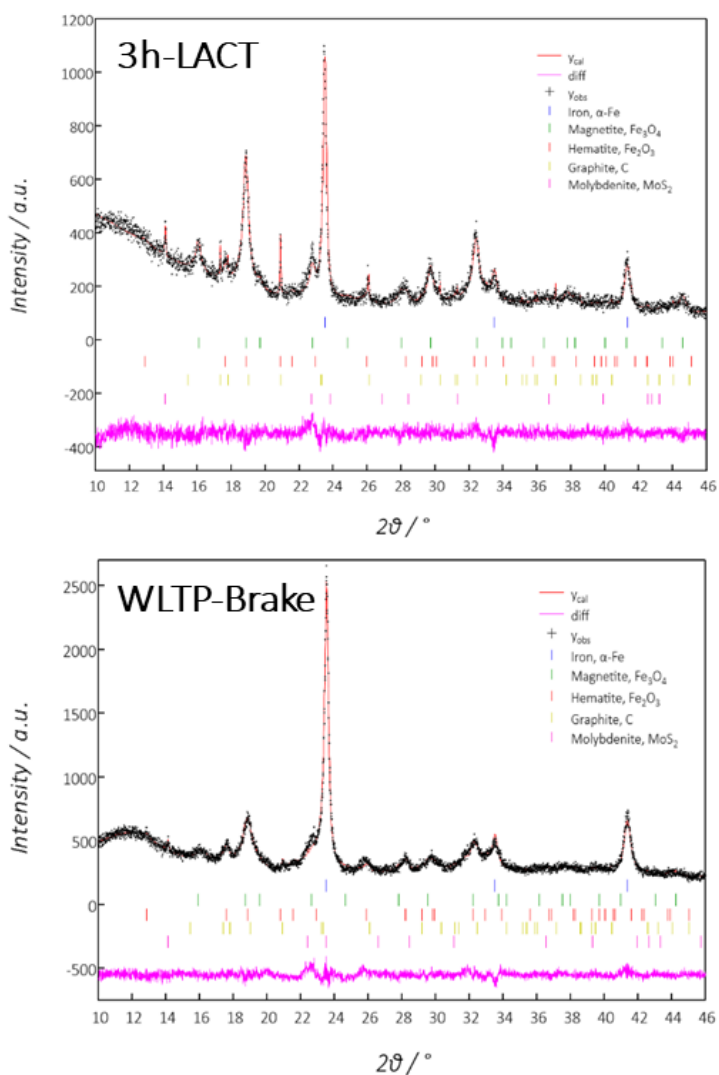


**Figure 8.4:** Rietveld refinement carried out on the experimental XRD patterns collected the FC2 particulate generated respectively during the 3h-LACT (top graph) and WLTP-Brake cycle (bottom graph). Measured points are reported in black, while the crystallographic model is in red. Their difference between calculated model and experimental pattern is showed in pink. Vertical colored bars represent the crystallographic references for the selected phases, *i.e.* metallic Iron in blue, Magnetite in green, Hematite in red, Graphite in yellow and Molybdenite in pink.

## 8.4. Discussion

All the obtained results are summarized and discussed in the following paragraph. More in detail, differences and trends in PM<sub>10</sub> chemical composition as

obtained from the performed experimental work are more widely explored with the final aim of proposing possible correlations with their origin cycle.

As previously described, both PM<sub>10</sub> samples generated by FC1 and FC2 show higher Iron/Oxygen ratio when produced during the 3h-LACT than from the WLTP-Brake test. This is a qualitative evidence of an higher level of Iron oxidation when PM<sub>10</sub> samples are produced in the 3h-LACT cycle. This trend is indeed confirmed looking also at the relative weight ratio between the metallic Iron and its oxides, as obtained from the XRD phase analysis (Table 8.6). At the same time, both FC1 and FC2 emission powders exhibit overall lower amount of Carbon and secondary/trace elements when the particulate is produced during the WLTP-Brake than the 3h-LACT cycle. All results are graphically summarized in Figure 8.5.

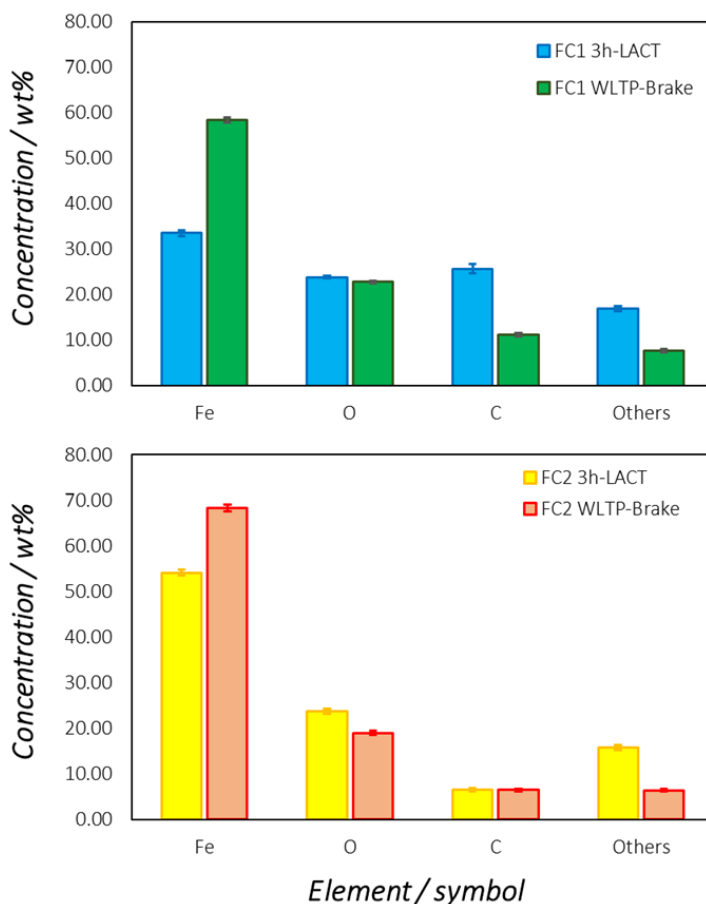


**Figure 8.5:** Summary of main contribution to the elemental composition in PM<sub>10</sub> samples from FC1 (top graph) and FC2 (bottom graph). Error bars represent the corresponding variability over the five independent measurement of concentration, expressed as standard deviation.

Since as previously described Iron and Carbon are primary markers respectively for the consumption of the BD and the FM surfaces, these findings clearly state an overall higher partial contribution of the braking disc to the total PM<sub>10</sub> mass produced during the WLTP-Brake cycle than during the LACT-3h cycle. Both these two main findings, *i.e.* the higher oxidation of the worn cast-iron and the higher consumption of the FM material during the LACT-3h cycle, fit well with the higher energy indexes, and thus the local temperatures, expected at the tribological interface during this test in respect with the WLTP-Brake counterpart. Thus, the overall more demanding energy indexes developed during the ensemble of the braking events of the 3h-LACT test represent the driving conditions producing PM<sub>10</sub> particulates which are more oxidized and have higher content of material generated by the friction material consumption. The generation of particulate at the tribological interface during the 3h-LACT cycle is expected to have a more pronounced contribution from the oxidative mechanism: higher local temperatures and friction forces have direct impact in the generation of Iron oxides as well as in the faster deterioration of the friction material composite. At this regard, it is frequently reported in the literature that increasing the contact pressure and the local temperature at the tribological interface causes significant higher production of particulate during braking, especially from the FM side of the friction couple [3,8,10,24]. Conversely, the WLTP-Brake cycle is expected to generate particulate with a relative higher contribution from the direct mechanical abrasion of the tribo-couple surfaces: this is well consistent with both the observed lower level of Iron oxidation and the overall lower consumption of the friction material. A graphical summary of all these effects is reported in the Kiviat plot Figure 8.6.

## 8.5. Summary

The study reported in this chapter offers new insights into the correlation between the chemical composition of the PM<sub>10</sub> emissions produced by brakes and their generation conditions. More in detail, it is clearly showed how two different braking test cycles, namely the 3h-LACT and the WLTP-Brake routines, have influence in determining the elemental and the phase composition of the emitted particulates. When the braking cycle is more energy demanding, as for the 3h-LACT test, the emitted particulate is characterized by an overall higher level of oxidation, especially considering the Iron arising from the BD surface and, secondary, from the FM composite. In addition, worn material from FM contributes more to the total amount of the emission. Conversely, when the cycle is less energy demanding, as in the case of the WLTP-Brake test, the emission is characterized by a significantly lower level of Iron oxidation and by a lower amount of material arising from FM. Thus, 3h-LACT test is identified to generate proportionally more particulate via oxidative mechanism in comparison to the WLTP-Brake test, where, conversely, proportionally more material is produced by direct

mechanical abrasion. A summary of the effects of the different braking cycles are reported in Figure 8.6. Notably, similar trends are observed in different tribo-couples, involving the presence of different concepts of friction materials.

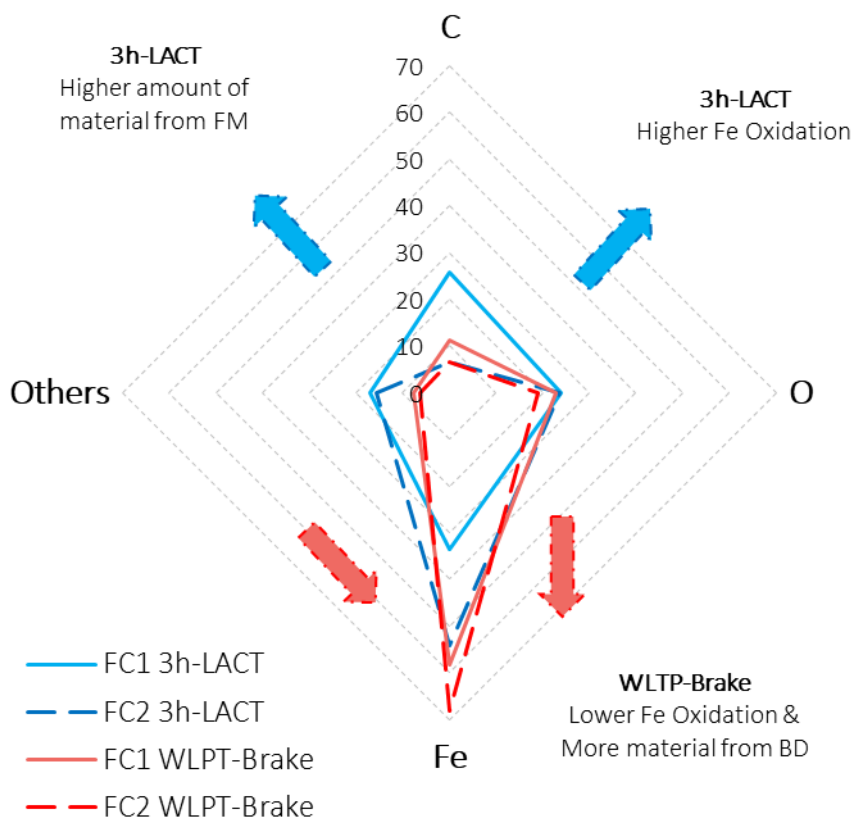


**Figure 8.6:** Effects of the cycles on the chemical composition of the generated PM<sub>10</sub> particulates. Grey dashed lines are concentrations iso-value surfaces expressed in weight percentage [wt%].

Taking all the obtained results on a more general level, it is possible to observe how different braking conditions, such as speed, deceleration and temperature, can have a strong influence in determining the final chemistry of the particulates emitted by brakes. This is particularly interesting in toxicological and environmental perspectives. Thus, the driving conditions and habits might be used in order to modulate the chemical emission profile of the emissions generated during braking. For instance, the findings here reported suggest that more or less energy demanding braking conditions can be applied in order to intentionally shift the Iron/Iron oxides ratio as well as the ratio between material produced by BD and FM. These results will become particularly powerful as soon as more detailed studies will be available in the literature dedicated to the eco-

toxicological assessment of the brake emissions. Finally, it is also demonstrated how the chemical characterization of the particulates produced by brakes is an effective tool to widen the general understanding of the mechanisms laying behind their generation.

This chapter is widely based on a technical paper published for the SAE Brake Colloquium & Expo in 2021.<sup>[20]</sup>

## References

- [1] J. Kukutschova, P. Filip, "Review of Brake Wear Emissions, in: F. Amato (Ed.), Non Exhaust Emissions: an Urban Air Quality Problem for Public Health, Academic Press, Elsevier, San Diego, **2018**.
- [2] T. Grigoratos, G. Martini, "Brake Wear Particle Emissions: a Review", *Environ. Sci. Pollut. Res.*, **22**, **2015**, 2491-2504, [doi: 10.1007/s11356-014-3696-8](https://doi.org/10.1007/s11356-014-3696-8).
- [3] B.D. Garg, S.H. Cadle, P.A. Mulawa, P.J. Groblicki, "Brake Wear Particulate Matter", *Environ. Science & Tech.*, **34**(21), **2000**, 4463-4469, [doi:10.1021/es001108h](https://doi.org/10.1021/es001108h).
- [4] M. Alemani, O. Nosko, I. Metinoz, U. Olofsson, "A Study on Emission of Airborne Wear Particles from Car Brake Friction Pairs", *SAE Int. J. Mat. and Man.*, **1**, **2016**, 147-157.
- [5] J. Kukutschova, P. Moravec, J. Tomasek, V. Matejka, *et.al.*, "On Airborne Nano/Micro-Sized Wear Particles Released from Low-Metallic Automotive Brakes", *Environmental Pollution*, **159**(4), **2011**, 998-1006, [doi:10.1016/j.envpol.2010.11.036](https://doi.org/10.1016/j.envpol.2010.11.036).
- [6] P.C. Verma, M. Alemani, S. Gialanella, L. Luterotti, *et.al.*, "Braking Pad-Disc System: Wear Mechanism and Formation of Wear Fragments", *Wear*, **322-323**, **2015**, 251-258, [doi: 10.1016/j.wear.2014.11.019](https://doi.org/10.1016/j.wear.2014.11.019).
- [7] G. Straffelini, S. Gialanella, "Airborne Particulate Matter from Brake Systems: An assessment of the Relevant Tribological Formation Mechanisms", *Wear*, **2021**, 478-479, 203883, <https://10.1016/j.wear.2021.203883>.
- [8] C. Menapace, A. Mancini, M. Federici, G. Straffelini, *et. al.*, "Characterization of Airborne Wear Debris Produced by Brake Pads Pressed against HVOF-Coated Discs", *Friction*, **8**(2), **2020**, 421-432, [doi:10.1007/s40544-019-0284-4](https://doi.org/10.1007/s40544-019-0284-4).
- [9] A. Mancini, B. Tsyupa, S. Pin, F. Bertasi, *et.al.*, "Novel Approaches for Physico-Chemical Characterization of Brake Emissions", *EuroBrake2021*, **2021**, EB2020-EBS-031.
- [10] M. Figliuzzi, M. Tironi, L. Longaretti, A. Mancini, *et.al.*, "Copper-dependent Biological Effects of Particulate Matter Produced by Brake Systems on Lung Alveolar Cells", *Archives of Toxicology*, **94**, **2020**, 2965-2979, [doi:10.1007/s00204-020-02812-4](https://doi.org/10.1007/s00204-020-02812-4).
- [11] S. Maiorana, F. Teoldi, S. Silvani, A. Mancini, *et.al.*, "Phytotoxicity of Wear Debris From Traditional and Innovative Brake Pads", *Environ. Int.*, **123**, **2019**, 156-163, [doi:10.1016/j.envint.2018.11.057](https://doi.org/10.1016/j.envint.2018.11.057).
- [12] G. Perricone, J. Wahlstrom, U. Olofsson, "Towards a Test Stand for Standardized Measurements of the Brake Emissions", *Proc.I.Mech.E., Part D: J.Aut. Engineering*, **2015**, 1-8, [doi:10.1177/0954407015616025](https://doi.org/10.1177/0954407015616025).
- [13] G. Perricone, M. Alemani, I. Metinoz, V. Matejka, *et.al.*, "Towards the Ranking of Airborne Particle Emissions from car Brakes – a System Approach", *Proc. I. Mech. E., Part D: J. Automobile Engineering*, **2016**, 1-17, [doi: 10.1177/0954407016662800](https://doi.org/10.1177/0954407016662800).

- [14] M. Mathissen, C. Evans, "Lowbrasys Brake Wear Cycle – 3h LACT", Mendeley, **2019**, [doi:10.17632/4cgs6myx9d.1](https://doi.org/10.17632/4cgs6myx9d.1).
- [15] M. Mathissen, J. Grochowicz, C. Schmidt, R. Vogt, *et.al.*, "WLTP-based Real World Brake Wear Cycle", Mendeley, **2019**, [doi:10.17632/dkp376g3m8.1](https://doi.org/10.17632/dkp376g3m8.1).
- [16] Particle Measurement Programme (PMP) Informal Working Group, Informal document GRPE\_81\_12, 81st GRPE, 9-11 June **2020**, Agenda Item 7.
- [17] L. Rebuffi, J.R. Plaisier, M. Abdellatief, A. Lausi, A., *et. al.*, "MCX: a Synchrotron Radiation Beamline for X-Ray Diffraction Line Profile Analysis", *Z. Anorg. Allg. Chem.*, **640**, **2014**, 3100-3106, [doi:10.1002/zaac.201400163](https://doi.org/10.1002/zaac.201400163).
- [18] S. Gates-Rector, T. Blanton, "The Powder Diffraction File: a Quality Materials Characterization Database", *Powder Diff.*, **34**(4), **2019**, 352-360, [doi:10.1017/S0885715619000812](https://doi.org/10.1017/S0885715619000812).
- [19] Rigaku, "PDXL Software", ver. 2.8.4.0, **2018**.
- [20] A. Mancini, B. Tsyupa, S. Pin, M. Bandiera, *et.al.*, "Chemistry of the Brake Emissions: Influence of the Test Cycle", *SAE Technical Paper*, 2021-01-1300, **2021**, [doi:10.4271/2021-01-1300](https://doi.org/10.4271/2021-01-1300).



## Annex 1: List of Abbreviations

**ANOVA** = Analysis of Variance

**BC** = Black Carbon

**BD** = Braking Disc

**BSE** = Back-Scattered Electrons

**CC** = Carbo-ceramic (typology of braking disc)

**CerMet** = Composite material made by the interplay between ceramic and metallic compounds

**CPC** = Condensation Particle Counter

**CTD** = Coated (typology of braking discs)

**DB** = Dynamometric Bench (testing bench)

**DGI** = Dekati™ Gravimetric Impactor

**EA** = Elemental Analysis

**ECE R-90** = Economic Commission for Europe - Regulation 90

**EDXS** = Energy Dispersive X-Ray Spectroscopy

**EEA** = European Environmental Agency

**EF** = Emission Factor

**ELPI+** = Electrical Low Pressure Impactor

**EPA** = Environmental Protection Agency

**EU** = European Union

**FC** = Friction Couple

**FM** = Friction Material

**GCI** = Grey Cast Iron

**GDP** = Gross Domestic Product

**HEPA** = High Efficiency Particulate Air

**HVAF** = High-Velocity Air Fuel

**HVOF** = High-Velocity Oxygen Fuel

**IA** = Image Analysis

**ICDD** = International Centre for Diffraction Data

**ICP** = Inductively Coupled Plasma

**IN** = Inorganic Bound (typology of friction material)

**IP** = Isokinetic Probe

**LC** = Laser Cladding

**LCF** = Linear Combination Fit

**LD** = Laser Diffraction

**LM** = Low Metallic (typology of friction material)

**LMD** = Laser Melting Deposition

**LS** = Low Steel (typology of friction material)

**MS** = Mass Spectroscopy

**NAO** = Non-Asbestos Organic (typology of friction material)

**NCD** = Non Communicable Disease

**NEE** = Non-Exhaust Emissions

**OE** = Original Equipment

**OES** = Optical Emission Spectroscopy

**OPC** = Optical Particle Counter

**PM** = Particulate Matter

**PC** = Polycarbonate (collection substrate)

**PDF4+** = Powder Diffraction Files (crystallographic data base)

**PM<sub>10</sub>** = PM composed by ensembles of particles having aerodynamic diameter < 10 μm

**PM<sub>2.5</sub>** = PM composed by ensembles of particles having aerodynamic diameter < 2.5 μm

**PMP** = Particle Measurement Programme (EU Informal Working Group)

**PoD** = Pin-on-Disc (testing bench)

**PSD** = Particle Size Distribution

**RC** = Regenerated Cellulose (collection substrate)

**R&D** = Research & Development

**SDD** = Silicon Drift Detector

**SE** = Secondary Electrons

**SEM** = Scanning Electron Microscopy

**SM** = Semi-Metallic (typology of friction material)

**TI** = Tribological Interface

**UFP** = Ultra-Fine Particles

**US** = United States

**VOC** = Volatile Organic Compound

**WHO** = World Health Organization

**WLTP-Brake** = Worldwide-harmonized Light-duty vehicle Test Procedure for Brakes

**WPPF** = Whole Powder Profile Fitting

**XAFS** = X-Ray Absorption Fine Structure

**XANES** = X-Ray Absorption Near Edge Structure

**XAS** = X-Ray Absorption Spectroscopy

**XRD** = X-Ray Diffraction

**μ-ED-XRF** = Micro-Energy Dispersive X-Ray Fluorescence

**μ-RS** = Micro-Raman Spectroscopy

**3h-LACT** = Abbreviated Los Angeles City Traffic (braking cycle)

## Annex 2: List of Crystallographic References

Phase	Compound	Crystallographic Reference (ICDD)
Fe <sub>3</sub> O <sub>4</sub>	Magnetite	04-015-9120
Fe <sub>2</sub> O <sub>3</sub>	Hematite	04-015-7029
α-Fe	Ferrite	04-014-0360
γ-Fe	Austenite	04-009-2090
C	Graphite	00-041-1487
MoS <sub>2</sub>	Molybdenite	01-077-1716
ZrO <sub>2</sub>	Zirconia	04-015-4188
Cu	Metallic Copper	04-009-2090
K <sub>2</sub> Ti <sub>6</sub> O <sub>13</sub>	Potassium Titanate	04-011-1358
α-Zn	Metallic Zinc	01-078-9364
SiC-6h	Silicon Carbide (Hexagonal)	01-075-8314
Sn	Metallic Tin	04-004-7747

## Annex 3: Data Sets for Reproducibility Studies

### Annex 3.1. Intra Bench Reproducibility

Fe / wt%	PM10-1	PM10-2	PM10-4	PM10-5	PM10-7	PM10-8	PM10-10	PM10-11	PM10-12	PM10-14
Area1	58.0	57.7	56.5	54.4	54.4	56.4	57.5	55.6	55.7	52.5
Area2	53.5	55.1	57.3	55.2	55.3	54.7	54.1	54.6	53.2	53.2
Area3	57.3	53.5	56.9	53.1	53.6	54.2	59.3	53.3	54.0	52.8
Area4	52.8	55.2	56.0	53.0	54.4	54.8	53.8	52.0	54.3	54.0
Area5	53.0	53.9	52.8	57.6	52.1	54.4	51.9	54.8	53.9	52.3
Average	<b>54.9</b>	<b>55.1</b>	<b>55.9</b>	<b>54.6</b>	<b>53.9</b>	<b>54.9</b>	<b>55.3</b>	<b>54.1</b>	<b>54.2</b>	<b>53.0</b>
SD	<b>2.5</b>	<b>1.6</b>	<b>1.8</b>	<b>1.9</b>	<b>1.2</b>	<b>0.9</b>	<b>3.0</b>	<b>1.4</b>	<b>0.9</b>	<b>0.7</b>

*Iron concentrations (wt%).*

O / wt%	PM10-1	PM10-2	PM10-4	PM10-5	PM10-7	PM10-8	PM10-10	PM10-11	PM10-12	PM10-14
Area1	24.9	25.4	25.5	28.0	26.9	26.6	25.6	27.4	26.2	28.1
Area2	27.0	27.3	25.9	27.5	27.0	28.3	27.6	27.2	28.2	27.4
Area3	25.0	28.3	26.0	29.2	27.8	28.4	23.9	28.1	27.8	27.5
Area4	28.1	26.9	26.6	28.8	27.4	28.2	28.2	29.6	27.3	26.9
Area5	28.9	28.5	28.8	25.9	28.7	28.2	29.8	27.1	28.0	27.9
Average	<b>26.8</b>	<b>27.3</b>	<b>26.6</b>	<b>27.9</b>	<b>27.6</b>	<b>28.0</b>	<b>27.0</b>	<b>27.9</b>	<b>27.5</b>	<b>27.5</b>
SD	<b>1.8</b>	<b>1.2</b>	<b>1.3</b>	<b>1.3</b>	<b>0.7</b>	<b>0.7</b>	<b>2.3</b>	<b>1.0</b>	<b>0.8</b>	<b>0.5</b>

*Oxygen concentrations (wt%).*

C / wt%	PM10-1	PM10-2	PM10-4	PM10-5	PM10-7	PM10-8	PM10-10	PM10-11	PM10-12	PM10-14
Area1	8.2	8.8	10.2	10.4	10.8	10.1	9.3	9.1	10.7	9.7
Area2	10.7	9.4	9.1	9.9	10.0	9.8	10.8	10.6	11.3	9.4
Area3	8.7	9.9	9.3	10.4	11.0	10.0	9.2	11.0	11.0	10.0
Area4	10.0	9.6	9.5	11.1	10.5	9.6	10.4	11.0	10.9	9.3
Area5	9.3	9.3	10.5	9.1	11.7	10.2	10.7	10.9	10.8	9.9
Average	<b>9.4</b>	<b>9.4</b>	<b>9.7</b>	<b>10.2</b>	<b>10.8</b>	<b>9.9</b>	<b>10.1</b>	<b>10.5</b>	<b>11.0</b>	<b>9.6</b>
SD	<b>1.0</b>	<b>0.4</b>	<b>0.6</b>	<b>0.7</b>	<b>0.6</b>	<b>0.2</b>	<b>0.8</b>	<b>0.8</b>	<b>0.2</b>	<b>0.3</b>

*Carbon concentrations (wt%).*

Averages	PM10-1	PM10-2	PM10-4	PM10-5	PM10-7	PM10-8	PM10-10	PM10-11	PM10-12	PM10-14	Average	Std.Dev.
Sn	2.0	1.8	1.7	1.5	1.7	1.5	1.6	1.6	1.5	2.1	<b>1.7</b>	<b>0.2</b>
Si	1.49	1.39	1.27	1.27	1.20	1.23	1.28	1.25	1.30	1.35	<b>1.30</b>	<b>0.08</b>
Mg	1.30	1.29	1.29	1.19	1.23	1.17	1.24	1.21	1.18	1.27	<b>1.24</b>	<b>0.05</b>
Al	1.31	1.21	1.17	1.06	1.17	1.05	1.09	1.13	1.14	1.16	<b>1.15</b>	<b>0.07</b>
S	0.89	0.79	0.70	0.67	0.73	0.71	0.72	0.73	0.68	0.72	<b>0.73</b>	<b>0.06</b>
Cr	0.76	0.66	0.64	0.58	0.65	0.60	0.61	0.64	0.58	0.63	<b>0.63</b>	<b>0.05</b>

*Average concentrations of secondary elements (wt%).*

Annex 3.2. Inter Benches Reproducibility

Iron			Oxygen			Carbon		
B1	B2	B3	B1	B2	B3	B1	B2	B3
58.0	55.8	55.9	24.9	26.3	24.7	8.2	10.7	11.0
53.5	54.1	54.1	27.0	27.4	25.9	10.7	11.2	11.4
57.3	53.5	53.8	25.0	28.3	25.8	8.7	11.0	11.8
52.8	53.2	53.7	28.1	27.9	25.8	10.0	11.6	11.9
53.0	56.1	53.0	28.9	25.8	26.8	9.3	10.8	11.9
57.7		53.9	25.4		26.1	8.8		11.5
55.1			27.3			9.4		
53.5			28.3			9.9		
55.2			26.9			9.6		
53.9			28.5			9.3		
56.5			25.5			10.2		
57.3			25.9			9.1		
56.9			26.0			9.3		
56.0			26.6			9.5		
52.8			28.8			10.5		
54.4			28.0			10.4		
55.2			27.5			9.9		
53.1			29.2			10.4		
53.0			28.8			11.1		
57.6			25.9			9.1		
54.4			26.9			10.8		
55.3			27.0			10.0		
53.6			27.8			11.0		
54.4			27.4			10.5		
52.1			28.7			11.7		
56.4			26.6			10.1		
54.7			28.3			9.8		
54.2			28.4			10.0		
54.8			28.2			9.6		
54.4			28.2			10.2		
57.5			25.6			9.3		
54.1			27.6			10.8		
59.3			23.9			9.2		
53.8			28.2			10.4		
51.9			29.8			10.7		
55.6			27.4			9.1		
54.6			27.2			10.6		
53.3			28.1			11.0		
52.0			29.6			11.0		
54.8			27.1			10.9		
55.7			26.2			10.7		
53.2			28.2			11.3		
54.0			27.8			11.0		
54.3			27.3			10.9		
53.9			28.0			10.8		
52.5			28.1			9.7		
53.2			27.4			9.4		
52.8			27.5			10.0		
54.0			26.9			9.3		
52.3			27.9			9.9		

Concentrations of main elements (wt%).

## Most sincere thanks to...

...all the people who mocked me, who disbelieved in me, who never supported me, who never helped me. You might not know, but you really gave me some of the most precious gifts: the fuel to pursue my objectives, the will to demonstrate you were wrong, the rage to survive hardships, the clear image of who I never want to become. I am an extremely lazy person, without all of these motivations, I simply could not make it twice. Pick your cards and try to call my bluff...

...all the colleagues and friends who supported me. You know who you are, because I stated it clearly. We shared and continue to share lots of fantastic moments, thoughts and experiences together. I have learnt (I would say, stolen) something from anyone of you and I keep it as my most precious treasure. Everyone of you saved me from prison at least once. I am so grateful for the freedom.

...to Alice, who paints most vivid colors and plays most cheerful melodies in a life full of grey and silence. If it happens I make something good in this life, that is all because of you.

...you never gonna make it...